

Technische Universität Dresden

**Investigation of Control Concepts for High-Speed
Induction Machine Drives and Grid Side Pulse-Width
Modulation Voltage Source Converters**

Kamran Jalili

von der Fakultät Elektrotechnik und Informationstechnik der Technischen Universität
Dresden

zur Erlangung des akademischen Grades eines

Doktoringenieurs

(Dr.-Ing.)

genehmigte Dissertation

Vorsitzender: Prof. Dr.-Ing. habil. F. Ellinger

Gutachter: Prof. Dr.-Ing. S. Bernet
Prof. Dr.-Ing. A. Mertens
Dr. M. Malinowski

(Leibniz Universität Hannover)
(Warsaw University of Technology)

Tag der Einreichung: 10.11.2008

Tag der Verteidigung: 26.02.2009

Kamran Jalili

**Investigation of Control Concepts for High-Speed
Induction Machine Drives and Grid Side Pulse-Width
Modulation Voltage Source Converters**

Preface

This thesis was written during my Ph.D. studies at the Power Electronics Group of Berlin University of Technology, Germany holding a DAAD scholarship.

First of all, I would like to express my gratitude to Prof. Steffen Bernet of Dresden University of Technology for his ever present supports, numerous fruitful discussions, and encouragement throughout the period of this research.

A special thank goes to Dr. Mariusz Malinowski from the Warsaw University of Technology for discussions which enhanced my knowledge.

Furthermore, I thank Niels Weitendorf for his support in preparation of the laboratory set-up. Also I wish to thank Dr. Albrecht Gensior for his excellent proof-reading service.

Finally, I am grateful to my wife Shirin and our son Mani for their love and patience.

Kamran Jalili

Berlin, February 2009

Table of Contents

Nomenclature.....	9
1 Introduction.....	19
1.1 State-of-the-art low voltage ac drives.....	19
1.1.1 Electric ac machines.....	20
1.1.2 Machine side and grid side converters.....	21
1.1.3 Dc-link capacitor.....	23
1.1.4 Grid side filter.....	24
1.1.5 Overview of control strategies of induction machine drives.....	24
1.1.6 Overview of control strategies of active front end converters.....	26
1.1.7 Industrial applications.....	27
2 Characteristics and State-of-the-art of High-Speed Drives.....	29
2.1 Characteristics of high-speed drives.....	29
2.1.1 Advantages.....	29
2.1.2 Disadvantages.....	30
2.1.3 Applications.....	30
2.1.4 Power and speed range.....	31
2.2 State-of-the-art technology of high-speed drives.....	33
2.2.1 Electric machines.....	33
2.2.2 Bearings.....	34
2.2.3 Converter.....	34
2.2.4 Control.....	36
2.3 Subject, motivation, and structure of the thesis.....	37
3 Control of High-Speed Induction Machines.....	41
3.1 Definition of an exemplary high-speed induction machine drive.....	41
3.2 Mathematical description of induction machines.....	42
3.3 Field orientation.....	45
3.3.1 Flux vector estimation using stator voltages and currents.....	48
3.3.2 Flux vector estimation using stator currents and rotor speed.....	49
3.4 Field oriented control of induction machines.....	52
3.4.1 Comparison of RFOC, MFOC, and SFOC.....	53
3.4.2 Indirect RFOC with PI current and speed controllers.....	57
3.5 Direct torque control of induction machines.....	67
3.5.1 Control of stator flux and electromechanical torque.....	69
3.5.2 Speed control loop.....	71
3.6 Comparison of indirect RFOC and DTC for the exemplary high-speed induction machine.....	72

3.6.1	Simulation results.....	72
3.6.2	Experimental investigations of the indirect RFOC.....	81
3.7	Comparison of 2L VSC and 3L-NPC VSC for the high-speed induction machine drive with RFOC.....	86
3.7.1	Converter design.....	88
3.7.2	Investigation of simulation results.....	90
3.8	Summary.....	93
4	PWM Active Front End Converters.....	95
4.1	Advantages and disadvantages of PWM active front end converters.....	95
4.2	Mathematical description of PWM active front end converters.....	96
4.3	Selection of control strategy.....	100
4.4	Voltage-oriented control of PWM active front end converters.....	103
4.4.1	d-q model of PWM active front end converters with L-filter.....	103
4.4.2	Structure of the applied PLL.....	106
4.4.3	PI-based current control.....	108
4.4.4	PI-based dc-link voltage control.....	110
4.4.5	Performance investigation of the voltage-oriented controlled PWM active front end converters at symmetrical sinusoidal grid voltage.....	113
4.4.6	Influences of the grid voltage distortions on the steady-state performance of voltage-oriented control.....	116
4.4.6.1	Performance of the current control loop of VOC for a distorted grid.....	119
4.4.6.2	Simulation and experimental results.....	122
4.5	Input filter design for PWM active front end converters.....	126
4.5.1	L-filter design procedure.....	127
4.5.2	LCL-filter design procedure.....	134
4.6	Control of PWM active front end converters with LCL-filter.....	144
4.6.1	Simulative investigations.....	150
4.6.2	Experimental investigations.....	154
4.6.3	Robustness of the current control loop.....	158
4.7	Summary.....	158
5	Conclusions.....	161
	Bibliography.....	165

Nomenclature

List of Acronyms and Names

Acronym / Name	Meaning
ACM	electric ac machine
AL-E-C	aluminium electrolytic capacitor
ARS	asymmetrical regular sampling
ARS-PWM	asymmetrical regular sampling pulse-width modulation
ARS-ZSS-PWM	asymmetrical regular sampling pulse-width modulation with added third harmonic
DCMLC	diode clamped multilevel converter
DPC	direct power control
DPF	displacement power factor
DSC	direct self control
DSP	discrete signal processor
DTC	direct torque control
DTC-SVM	direct torque control with space vector modulation
FC	film capacitor
FCMLC	flying capacitor multilevel converter
FOC	field-oriented control
GC	grid side converter
HSM	high-speed electric machine
HSIM	high-speed induction machine
HSIMD	high-speed induction machine drive
IGBT	insulated-gate bipolar transistor
IM	induction machine
MC	machine side converter
MFOC	magnetizing-flux-oriented control
N_G	grid neutral point
N_M	machine neutral point
NP	dc-link midpoint
PLL	phase-locked loop
PMSM	permanent magnet synchronous machine
PWM	pulse-width modulation
R_{ESR}	equivalent series resistance
RFOC	rotor-flux-oriented control
SFOC	stator-flux-oriented control
SM	synchronous machine
SRS	symmetrical regular sampling

List of Acronyms and Names

SRS-PWM	symmetrical regular sampling pulse-width modulation
SRS-ZSS-PWM	symmetrical regular sampling pulse-width modulation with added third harmonic
SVM	space vector modulation
THD	total harmonic distortion
UPF	unity power factor
V-DPC	voltage-based direct power control
VF-DPC	Virtual-flux-based direct power control
VFOC	Virtual-flux-oriented control
VOC	voltage-oriented control
VSC	voltage source converter
x_{MC}	terminal of machine side converter ($x = a, b, c$)
x_{GC}	terminal of grid side converter ($x = a, b, c$)
2L VSC	two-level voltage source converter
3L-NPC VSC	three-level neutral-point-clamped voltage source converter
4Q – B6C	4 quadrant thyristor converter

Generic Variable Usage Conventions

Variable Format	Meaning
x	instantaneous value of quantity x
\hat{x}	estimated value of quantity x
\bar{x}	average value of quantity x in a sampling time
X, \hat{X}	rms value and amplitude of quantity x
X_1, \hat{X}_1	rms value and amplitude of fundamental component of quantity x
X_h, \hat{X}_h	rms value and amplitude of harmonic components of quantity x
\vec{x}^Y	complex vector in Y coordinate system ($Y = S$ (stator), $Y = R$ (rotor), $Y = \vec{\psi}_S^S$ (stator flux vector), $Y = \vec{\psi}_R^S$ (rotor flux vector), $Y = \vec{\psi}_g^S$ (air gap flux vector), \vec{v}_{PCC} (grid voltage vector at PCC), $Y = K$ (arbitrary coordinate system))
\vec{x}_1^Y	complex vector of fundamental components in coordinate system of Y
x_α^Y, x_β^Y	real and imaginary components of \vec{x}^Y in a stationary coordinate system of Y
$x_{1\alpha}^Y, x_{1\beta}^Y$	real and imaginary components of \vec{x}_1^Y in a stationary coordinate system of Y
x_d^Y, x_q^Y	real and imaginary components of \vec{x}^Y in a rotating coordinate system of Y
x_{1d}^Y, x_{1q}^Y	real and imaginary components of \vec{x}_1^Y in a rotating coordinate system of Y

Specific Variable Usage Definitions

Variable	Meaning
a_{cc}	damping factor of current control loop
a_{fc}	damping factor of flux control loop
a_{PLL}	PLL damping factor
a_{sc}	damping factor of speed control loop
a_{vc}	damping factor of voltage control loop of VOC
$A_{sw,on,T}, B_{sw,on,T}$	IGBT loss coefficients for turn-on
$A_{sw,off,T}, B_{off,xT}$	IGBT loss coefficients for turn-off
$A_{sw,rec,D}, B_{sw,rec,D}$	diode recovery loss coefficients
$A_{cond,x}, B_{cond,x}$	conduction loss coefficients ($x = T, D$)
α, β	real and imaginary axes of stationary reference frame
$\cos(\varphi_M)$	induction machine power factor at nominal load
C_{dc}	dc-link capacitance
C_F	capacitance of LCL-filter
D	diode
D_{xj}	diodes, ($x = a, b, c$), ($j = 1, 2$ for anti parallel diodes of 2L VSC, $j = 1, 2, 3, 4$ for anti parallel diodes of 3L-NPC VSC, and $j = 5, 6$ for NPC diodes)
d_{ψ_s}	output of flux hysteresis controller
$d_{T_{em}}$	output of torque hysteresis controller
$E_{loss,sw,on,T}, E_{loss,sw,off,T}$	turn-on and turn-off loss energy of IGBT
$E_{loss,sw,rec,D}$	recovery loss energy of diode
$E_{loss,sw,x}$	total switching loss energy ($x = T, D$)
e_{ψ_s}	stator flux error
$e_{T_{em}}$	torque error
f_{0M}	rated input frequency of machine
$f_{0,MC}$	fundamental output frequency of machine side converter
f_C	carrier frequency
f_{res}	resonance frequency of LCL-filter
f_G	frequency of grid variables
f_s	sampling frequency
$f_{s,cc}$	sampling frequency of current control loop
$f_{s,DTC}$	sampling frequency of torque and stator flux control loop in DTC
$f_{s,fc}$	sampling frequency of flux control loop
$f_{s,sc}$	sampling frequency of speed control loop
$f_{sw}, f_{sw,average}$	switching frequency, average switching frequency
$G_{d,cc}(s)$	transfer function of current control loop delay
$G_{d,t}(s)$	transfer function of total delay (processing delay + PWM delay)
$G_{cl,cc}(s)$	closed loop transfer function of current control loop
$G_{ol,cc}(s)$	open loop transfer function of current control loop
$G_{ol,sc}(s)$	open loop transfer function of speed control loop

Specific Variable Usage Definitions

h	harmonic order
H_{ψ_s}	hysteresis band of flux controller
$H_{T_{em}}$	hysteresis band of torque controller
$I_{b,M}$	base current of machine side per unit system
$I_{b,G}$	grid base current
$i_{C_{dc}}$	current of dc-link capacitor
$I_{C,n}$	nominal collector current in IGBT
$i_{dc,GC}$	dc-link current of grid side converter
$i_{dc,MC}$	dc-link current of machine side converter
$i_{dc,ff}$	feed-forward dc current in voltage control loop of VOC
$I_{F,n}$	nominal forward current in diode
I_G	grid rms current
$i_{G,1}$	fundamental component of grid phase current
$I_{G,n}$	rated grid rms current
$i_{G,y}$	real and imaginary components of grid current vector in stationary coordinate system ($y = \alpha, \beta$)
$\hat{I}_{G,(m_f-2),0,\%}$	amplitude of the $(m_f - 2)^{\text{th}}$ grid current harmonic at no load condition in percent of rated fundamental component
$\hat{I}_{G,(m_f-2),n,\%}$	amplitude of the $(m_f - 2)^{\text{th}}$ grid current harmonic in percent of fundamental component at rated load condition
$\hat{I}_{G,(m_f-2),desired,\%}$	desired amplitude of the $(m_f - 2)^{\text{th}}$ grid current harmonic in percent of fundamental component (e.g. according to IEEE-519)
$\vec{i}_{GC,dq,h}$	grid side converter current harmonic vector in rotating reference frame
$\vec{i}_{GC,h}$	space vector of h^{th} order grid side converter current harmonic, $\vec{i}_{GC,h} = \hat{I}_{GC,h} e^{j\theta_{i_{GC,h}}}$
$\hat{I}_{GC,h}$	amplitude of h^{th} order grid side converter current
$i_{GC,x}$	phase current of grid side converter ($x = a, b, c$)
$i_{GC,y}$	real and imaginary components of grid side converter current vector in stationary coordinate system ($y = \alpha, \beta$)
$i_{G,x}$	grid phase current ($x = a, b, c$)
$i_{GC,y}^{v_{PCC}}$	direct and quadrature components of grid side converter current vector in rotating coordinate system ($y = d, q$)
$\hat{I}_{ripple,max}$	maximum amplitude of converter current ripple ($\hat{I}_{ripple,max} = \max i(t) - i_1(t) $)
I_S	rms stator current
$I_{S,n}$	rms rated stator current
$i_{S,x}$	stator current ($x = a, b, c$)
$i_{S,y}^K$	direct and quadrature components of stator current in an arbitrary coordinate system K ($y = d, q$)
$i_{S,y}^{*K}$	reference values of stator current in rotating coordination k ($y = d, q$)

Specific Variable Usage Definitions

$i_{4Q-B6C,x}$	input ac phase current of thyristor converter ($x = a, b, c$)
J	moment of inertia
$J_\mu(x)$	Bessel function of variable x
k_{ll}, α_{ll}, T_d	parameters of Lead-Lag compensator
K_P	proportional gain
$K_{P,cc}$	proportional gain of current PI controller
$K_{P,fc}$	proportional gain of flux PI controller
$K_{P,PLL}$	proportional gain of PLL PI controller
$K_{P,sc}$	Proportional gain of speed PI controller
$K_{P,vc}$	Proportional gain of voltage PI controller
K_{PWM}	proportional gain of power converter
L_F	inductance of L-filter
$L_{F,G}$	grid side LCL-filter inductance
$L_{F,G,t}$	grid side LCL-filter total inductance, $L_{F,G,t} = L_{F,G} + L_G$
$L_{F,GC}$	LCL-filter inductance of grid side converter
$L_{F,t}$	total inductance of L-filter, $L_{F,t} = L_F + L_G$
$L_{F,max}$	upper limit of L-filter inductance
L_G	grid stray inductance
L_{IS}	stator leakage inductance
L_{IR}	rotor leakage inductance in stator side
L_M	mutual inductance
L_R	rotor inductance
$L_{s,4Q-B6C}$	inductance of input L-filter of thyristor converter
L_S	stator inductance
M, M_0, M_n	modulation depth, no load modulation depth, and nominal load modulation depth ($M = \text{amplitude of reference signal} / \text{amplitude of carrier signal}$, $M_0 = 2\sqrt{2}V_{G,1} / V_{dc}$)
m_f	modulation index ($m_f = f_c / \text{frequency of reference signal}$)
n	integer coefficient
n_b	base mechanical speed
n_n	nominal speed of induction machine
n_{syn}	synchronous speed of induction machine
n_x	number of devices; $x = T$ (for IGBT), $x = D$ (for diode)
$P_{GC,PCC}$	input active power of grid side converter at PCC
$P_{loss,cond}$	total conduction loss power
$P_{loss,cond,x}$	conduction loss power of device x ($x = T, D$)
$P_{loss,sw}$	total switching power loss
$P_{loss,sw,x}$	switching power loss of device x ($x = T, D$)
$P_{mech,n}$	nominal mechanical power of induction machine
P_{sw}	switching power loss
$q_{GC,PCC}$	input reactive power of grid side converter at PCC
r	inductance split factor of LCL-filter

Specific Variable Usage Definitions

R_d	damping resistance of LCL-filter
R_F	resistance of L-filter
$R_{F,G}$	grid side LCL-filter resistance
$R_{F,GC}$	LCL-filter resistance of grid side converter
$R_{F,G,t}$	grid side LCL-filter total resistance, $R_{F,G,t} = R_{F,G} + R_G$
$R_{F,t}$	total resistance of L-filter, $R_{F,t} = R_F + R_G$
R_G	grid resistance
R_R	rotor resistance in stator side
R_S	stator resistance
$R_{th-ch,x}$	thermal resistance of case-heat sink ($x = T, D$)
R_{th-ch}	thermal resistance of case-heat sink
$R_{th-je,x}$	thermal resistance of junction-case ($x = T, D$)
$S_{GC,x}$	switching states of grid side 2L VSC ($x = a, b, c$)
$\bar{S}_{GC,x}$	average value of switching states $S_{GC,x}$ ($x = a, b, c$)
$S_{GC,y}$	real and imaginary components of grid side converter switching state vector in stationary coordinate system ($y = \alpha, \beta$)
$S_{GC,y}^{\bar{v}_{PCC}}$	direct and quadrature components of grid side converter switching state vector in rotating coordinate system ($k = \bar{v}_{PCC}, y = d, q$)
$\bar{S}_{GC,y}^{\bar{v}_{PCC}}$	average values of $S_{GC,x}^{\bar{v}_{PCC}}$ ($y = d, q$)
S_S	installed switch power
T	Transistor
T_l	fundamental time period
T_C	carrier period
T_d	time delay
T_{em}	electromechanical torque
$T_{em,av}$	average electromechanical torque
$T_{em,b}$	base electromechanical torque
$\hat{T}_{em,h}$	amplitude of h^{th} order harmonic of T_{em}
$T_{em,n}$	nominal electromechanical torque
$T_{em,pull-out}$	pull-out electromechanical torque
T_h	heat sink temperature
T_i	integrator time constant of PI controller
$T_{i,cc}$	integrator time constant of current PI controller
$T_{i,fc}$	integrator time constant of flux PI controller
$T_{i,PLL}$	integrator time constant of PLL PI controller
$T_{i,sc}$	integrator time constant of speed PI controller
$T_{i,vc}$	integrator time constant of voltage PI controller
$T_{\mu p}$	processing time
$T_{j,max}$	junction maximum temperature
$T_{s,cc}$	sampling interval of current control loop
$T_{s,DTC}$	sampling interval of torque and stator flux control loop in DTC
$T_{s,fc}$	sampling interval of flux control loop

Specific Variable Usage Definitions

$T_{s,PLL}$	sampling interval of PLL
$T_{d,PWM}$	time delay of sampled waveform in a regular sampling
$T_{s,sc}$	sampling interval of speed control loop
T_{xj}	IGBTs; ($x = a, b, c$), ($j = 1, 2$ for 2L VSC and $j = 1, 2, 3, 4$ for 3L-NPC VSC)
THD_{i_s}	total harmonic distortion of stator current
$THD_{T_{em}}$	total harmonic distortion of electromechanical torque
$V_{b,G}$	grid base voltage
$V_{b,M}$	machine base voltage
$V_{CE,n}$	nominal collector-emitter voltage (blocking capability)
$V_{CE,T}$	IGBT on-state collector-emitter voltage
V_{com}	commutation voltage
$V_{com@100fit}$	commutation voltage for a cosmic ray withstand capability of 100FIT
V_{dc}	dc-link voltage
$V_{dc,n}$	nominal dc-link voltage
$V_{F,D}$	diode on-state anode-cathode voltage
$v_{G,1}$	fundamental component of grid phase voltage
$v_{G,x}$	grid phase voltage ($x = a, b, c$)
$v_{G,y}$	real and imaginary components of grid voltage vector ($y = \alpha, \beta$)
$v_{G,ll,x}$	grid line-to-line voltage ($x = a, b, c$)
$V_{G,ll}$	rms line-to-line grid voltage
$V_{G,ll,n}$	rated rms line-to-line grid voltage
\vec{v}_G	grid voltage vector
$v_{GC,y}$	real and imaginary components of converter output voltage vector, ($y = \alpha, \beta$)
$v_{GC,x}$	output phase voltage of grid side converter ($x = a, b, c$)
$v_{GC,y}^{\bar{v}_{PCC}}$	direct and quadrature components of grid side converter output voltage vector in rotating coordinate system ($y = \alpha, \beta$)
$v_{GC,x}^*$	reference voltage of grid side converter ($x = a, b, c$)
$v_{GC,y}^{*\bar{v}_{PCC}}$	direct and quadrature components of grid side converter reference voltage vector in rotating coordinate system ($y = \alpha, \beta$)
$\bar{v}_{GC,y}^{\bar{v}_{PCC}}$	average values of direct and quadrature components of grid side converter output voltage vector in rotating coordinate system ($y = \alpha, \beta$)
$\vec{v}_{GC,h}$	space vector of h^{th} order grid side converter output voltage harmonic, $\vec{v}_{GC,h} = \hat{V}_{GC,n} e^{j\theta_{v_{GC,h}}}$
$\hat{V}_{GC,n}$	amplitude of h^{th} order grid side converter output voltage harmonic
\vec{v}_{GC}	output voltage vector of grid side converter
$\vec{v}_{GC,dq,h}$	grid side converter output voltage harmonic vector in rotating reference frame

Specific Variable Usage Definitions

$\hat{V}_{n,\mu}$	amplitude of converter output phase voltage harmonic (n is carrier band number and μ is number of side band)
$v_{PCC,x}$	phase voltage at PCC, ($x = a, b, c$)
$v_{PCC,y}$	real and imaginary components of PCC voltage vector, ($y = \alpha, \beta$)
$v_{PCC,y}^{PLL}$	direct and quadrature components of the PCC voltage vector in the rotating reference frame of PLL, ($y = \alpha, \beta$)
$\bar{v}_{PCC,y}^{pcc}$	direct and quadrature components of PCC voltage vector in rotating coordinate system ($y = \alpha, \beta$)
$V_{PCC,ll}$	rms value of line-to-line voltage at PCC
$\hat{V}_{PCC,h}$	amplitude of h^{th} order PCC voltage harmonic
$\bar{v}_{PCC,h}$	space vector of h^{th} order PCC voltage harmonic, $\bar{v}_{PCC,h} = \hat{V}_{PCC,h} e^{j\theta_{v_{PCC,h}}}$
$\bar{v}_{PCC,dq,h}$	voltage harmonic vector of PCC in rotating reference frame
V_{RRM}	rated repetitive peak reverse voltage of diodes
$v_{S,x}$	stator phase voltage ($x = a, b, c$)
$v_{S,x}^*$	reference stator voltage ($x = a, b, c$)
$v_{S,ll,x}$	stator line-to-line voltage ($x = a, b, c$)
$V_{S,ll}$	rms stator line-to line voltage
$V_{S,ll,n}$	rated rms stator line-to line voltage
$v_{S,y,control}^K$	output of current controllers of FOC in coordinate system K ($y = d, q$)
$v_{S,y,decoupling}^K$	output of decoupling circuit of FOC in coordinate system K ($y = d, q$)
$V_{o,x}$	threshold voltage ($x = T, D$)
$v_{4Q-B6C,ll,x}$	input line-to-line voltage of thyristor converter ($x = a, b, c$)
Z_p	number of pole pairs
δ	torque angle
ϕ_{pm}	phase margin
ψ_g	amplitude of air gap flux vector
$\psi_{g,n}$	nominal amplitude of air gap flux vector
$\psi_{g,x}$	phase linkage flux in air gap ($x = a, b, c$)
ψ_R	amplitude of rotor flux vector
$\psi_{R,n}$	nominal amplitude of rotor flux vector
$\psi_{R,x}$	phase linkage flux of rotor ($x = a, b, c$)
ψ_S	amplitude of stator flux vector
$\psi_{S,n}$	nominal amplitude of stator flux vector
$\psi_{S,x}$	phase linkage flux of stator ($x = a, b, c$)
σ	total leakage factor
σ_R	rotor leakage factor
σ_S	stator leakage factor
ρ_K	rotation angle of coordinate reference frame K
ρ_M	rotation angle of rotor

Specific Variable Usage Definitions

$\rho_{\bar{\psi}_s^s}$	rotation angle of the coordinate reference frame fixed on stator flux vector
$\rho_{\bar{\psi}_g^s}$	rotation angle of the coordinate reference frame fixed on air gap flux vector
$\rho_{\bar{\psi}_R^s}$	rotation angle of the coordinate reference frame fixed on rotor flux vector
$\rho_{\bar{v}_{PCC}}$	rotation angle of the coordinate reference frame fixed on fundamental component of PCC voltage vector
τ_{DTD}	approximated time constant of the torque control loop in DTC
τ_R	rotor time constant
τ_{Rl}	rotor transient time constant
τ_S	stator time constant
$\theta_{V_{PCC}}$	phase angle of $v_{PCC,a}$ at $t = 0$
$\theta_{\bar{i}_{GC,h}}$	phase angle of h^{th} order grid side converter current harmonic vector
$\theta_{0,\bar{i}_{GC,h}}$	phase angle of h^{th} order grid side converter current harmonic vector at $t = 0$
$\theta_{\bar{v}_{GC,h}}$	phase angle of h^{th} order grid side converter output voltage harmonic vector
$\theta_{0,\bar{v}_{GC,h}}$	phase angle of h^{th} order grid side converter output voltage harmonic vector at $t = 0$
$\theta_{\bar{v}_{PCC,h}}$	phase angle of h^{th} order PCC voltage harmonic vector
$\theta_{0,\bar{v}_{PCC,h}}$	phase angle of h^{th} order PCC voltage harmonic vector at $t = 0$
$\omega_{b,G}$	grid base angular frequency
ω_G	angular velocity of grid variables vector ($\omega_G = 2\pi f_G$)
ω_{ff}	feed-forward angular frequency of PLL
ω_M	rotor mechanical angular velocity
ω_{PLL}, ρ_{PLL}	angular frequency and angle of PLL rotating reference frame
ω_K	angular velocity of coordinate reference frame K
ω_{sl}	slip frequency
$\omega_{sl,n}$	nominal slip frequency
$\omega_{sl,pull-out}$	pull-out slip frequency

Chapter 1

Introduction

This opening chapter introduces state-of-the-art low voltage drives. Examples of commercially available low voltage drives are described. Different parts of an industrial low voltage drive are investigated. Industrial applications of low voltage drives are briefly addressed.

1.1 State-of-the-art low voltage ac drives

Electric drives are attractive in industrial applications because of features like controlled starting current, controlled acceleration, adjustable operating speed, adjustable torque limit, reverse operation, and saving of energy. At first, adjustable ac drives were applied in processing industries, such as plastics and textiles. AC drives equipped with field-oriented control (FOC) or direct torque control (DTC) also started to replace dc drives in industries requiring good dynamic performance, such as machine tools, robotics, and metal rolling.

Low voltage ac drives are used in widespread applications in which there are mechanical equipments powered by low voltage ac motors. Commercially available low voltage ac drives (e.g. offered by ABB and Siemens) cover a wide power range (x100 W to 5 MW) and industrial line-to-line voltages up to 690V. ABB low voltage converters vary widely from component drives (0.18 to 4 kW, 110 - 480 V) to high power drives (e.g. ACS800-07-2900-7, 2300 kW, 525-690 V) [134]. Siemens products also comprise a wide variation from low voltage low power ac converters (e.g. MICROMASTER 410, 0.12 to 0.55 kW, 100 - 120 V) to low voltage large ac converters (e.g. SINAMICS S120, 1.6 - 4500 kW, 380 - 690 V) [146].

A basic structure of a low voltage drive (nominal line-to-line voltage ≤ 690 V) with voltage-dc-link is shown in Fig. 1-1. A low voltage drive combines a low voltage electric machine (3~ ACM) connected to a machine side converter (MC), a dc-link with capacitor C_{dc} , and a grid side converter (GC). The GC can be connected to the grid through a filter to damp the current harmonics injected to the grid. Different parts of a low voltage ac drive have been investigated briefly in the following.

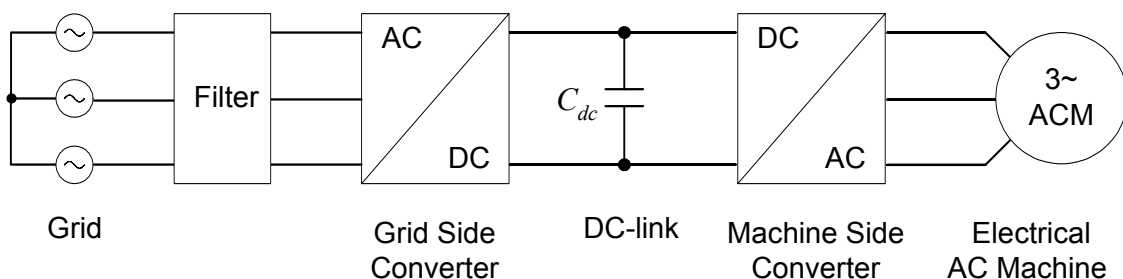


Fig. 1-1 Block diagram of a low voltage drive

1.1.1 Electric ac machines

Electric machines are the workhorse of industry which transforms electromagnetic energy into mechanical energy and vice versa. Electric ac machines are advantageous to dc machines because:

- ac machines require lower maintenance,
- ac machines are smaller and less expensive than dc machines,
- special ac machine types are more readily available at a lower cost, whenever the operating environment is wet, corrosive, or explosive.

A classification of the most common applied three-phase ac machines is shown in Fig. 1-2. Synchronous machines (SM) and induction machines (IM) are the main groups of three-phase ac machines. SMs are manufactured in forms of wound rotor and permanent magnet synchronous machines (PMSM). IMs are available with wound rotor or squirrel cage rotor and different design classes [17].

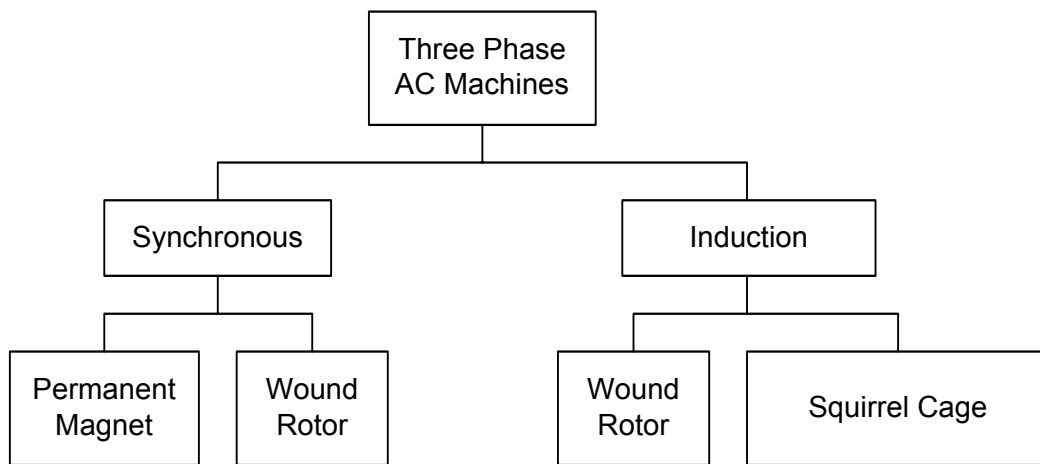


Fig. 1-2 Classification of the most common applied three-phase ac machines

Wound-Rotor SMs have a low starting torque and require dc current for excitation. Wound-rotor SMs are generally used for large motor-generator sets, air compressors and similar applications, which permits starting under a light load. These machines are used particularly in the large power systems, because of their inherent ability to improve the system power factor.

PMSMs are a type of SM with a three-phase stator and the rotor of PMSMs has surface-mounted permanent magnets. PMSMs are manufactured without a commutator, so they are more reliable than dc machines. These machines generate the rotor magnetic flux with rotor magnets so they are more efficient than IMs. Consequently, PMSMs are used in appliances which require high reliability and efficiency like refrigerators, washing machines, dishwashers, etc. PMSMs produce high torques with a relatively small diameter rotor. This yields high torque to inertia ratios and power to size ratios.

Wound-Rotor (slip ring) IMs have a three-phase stator and a three-phase rotor. Windings on the rotor are terminated to a set of slip rings for connection to external resistors. By inserting different values of resistances in the rotor circuit, various performance characteristics of IM can be obtained. The slip ring IMs enable the starting characteristics of the motor to be

controlled to suit the load. One of the disadvantages of the slip ring motors is that the slip rings and brushes need regular maintenance and the external resistors cause additional losses.

Squirrel-Cage IMs are the most simple and reliable electric machines. Squirrel-cage IMs are simple in structure and require very low maintenance. There are a number of design classifications of squirrel-cage IMs particularly applied to the rotor design. These design classifications affect the starting characteristics of the motors and are distinguished by different starting and pullout torque [17]. High production volumes for the squirrel-cage IM and lack of magnets make it considerably less expensive than the PMSM.

IMs are available with power ratings up in the megawatt range. Due to straightforward construction, low cost, reliable operation, easily found replacements, and variety of mounting styles, squirrel-cage IMs are particularly widespread.

1.1.2 Machine side and grid side converters

Conventional two-level Voltage Source Converters (2L VSC) with insulated gate bipolar transistors (IGBT) are the state-of-the-art converters of the low voltage power conversion market for machine side converters with voltage dc-link. In applications such as high-speed drives which require high switching frequencies, grid-connected and traction converters with a desire for smaller and lighter filter, three-level low voltage converters appear to be an attractive solution [74]. Three-level converters have been implemented in the form of diode-clamped multilevel converter (DCMLC) known as neutral point clamped voltage source converter and flying-capacitor multilevel converters (FCMLC). The three-level neutral-point-clamped voltage source converter (3L-NPC VSC) is preferred because of more complex start-up routine and a higher expense of capacitors of FCMLC [74]. A 2L VSC and a 3L-NPC VSC are shown in Fig. 1-3 (a) and (b), respectively. T and D are abbreviations for IGBT and diode. V_{dc} denotes the dc-link voltage.

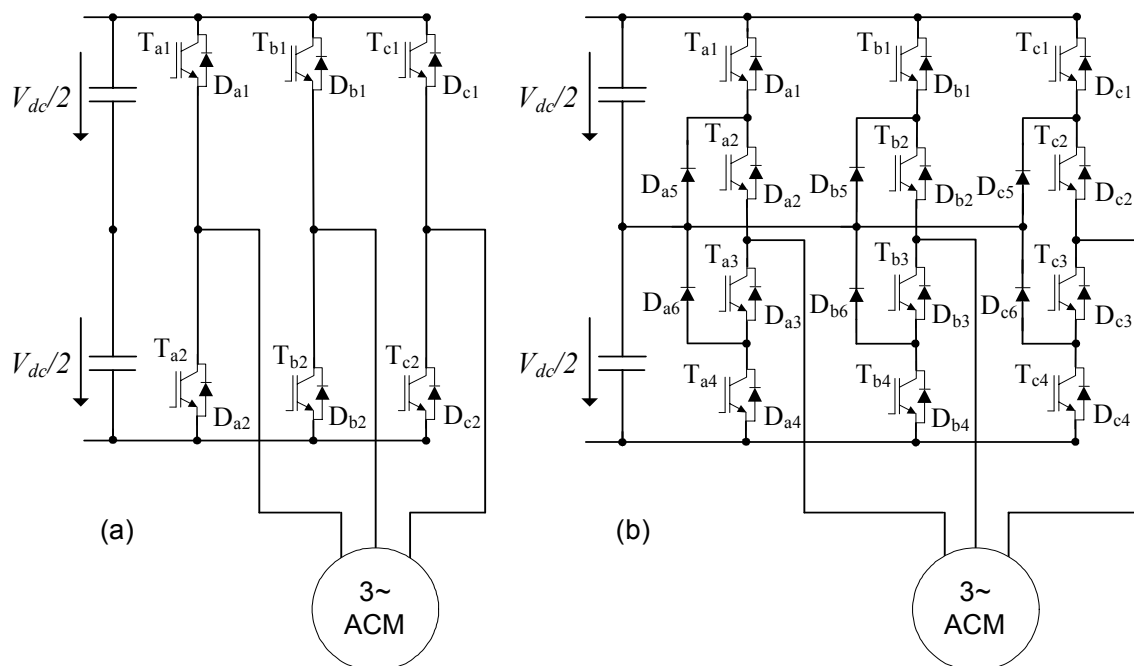


Fig. 1-3 Block diagram of machine side voltage source converters with voltage dc-link: (a) a 2L VSC; (b) a 3L-NPC VSC

The three-phase diode front end rectifier is one of the most common grid side converters which allow only unidirectional power flow. Diode rectifiers are interesting in industry due to advantages like simple structure and low cost. However, the diode rectifier results in uncontrollable power factor and low order grid current harmonics. A block diagram of the diode rectifier is shown in Fig. 1-4 (a). Active front end converters with the capability of bidirectional power flow are mainly applied in the drive applications with a high share of regenerative operation (e.g. elevators) and utility applications such as distributed power generation systems. 2L VSCs are the commonly applied topology in active front end converters. A 2L VSC active front end converter connected to the grid with a grid stray inductance of L_G and grid resistance of R_G is presented in Fig. 1-4 (b). Furthermore, the 3L-NPC VSC is an attractive topology for active front end converters in applications with

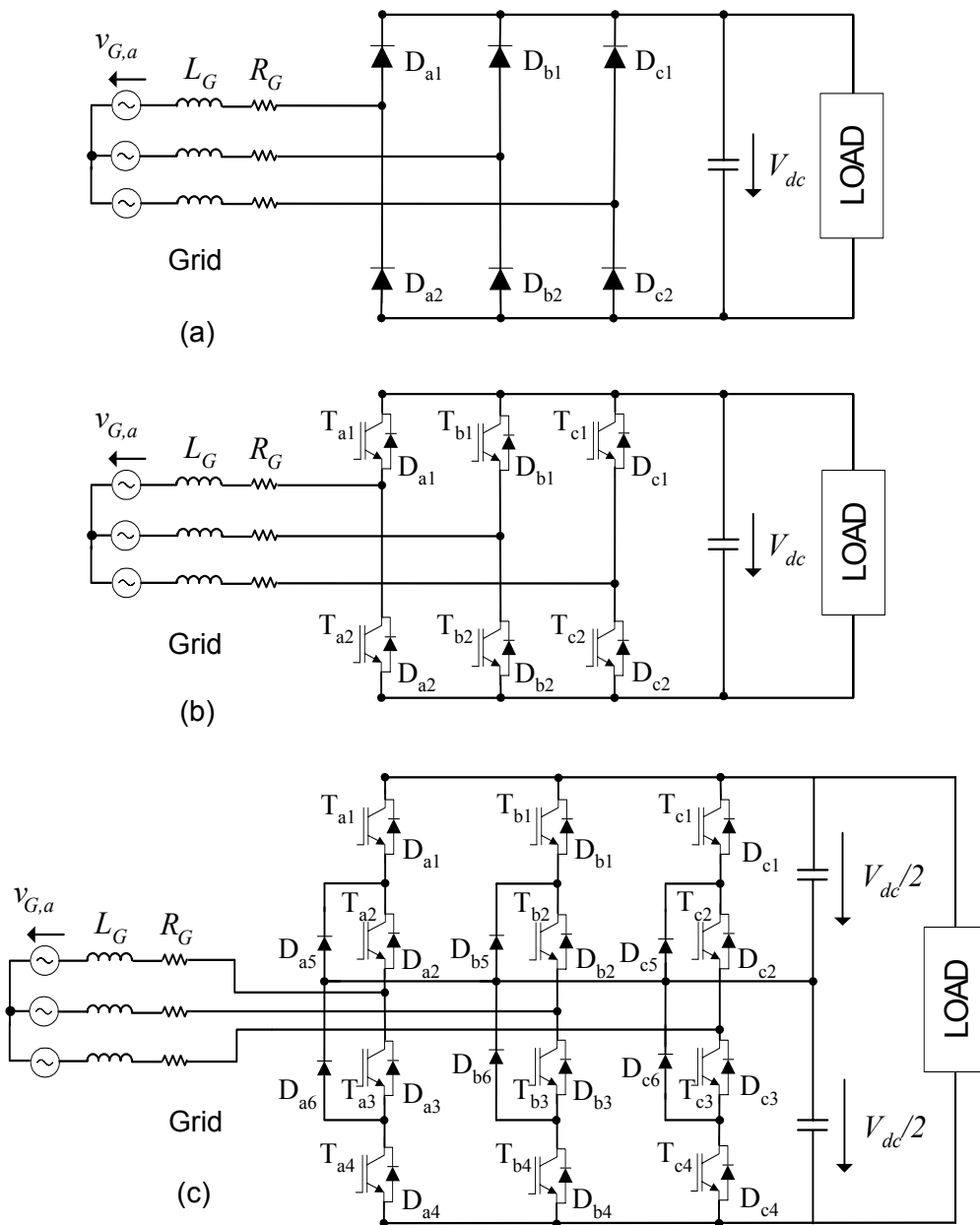


Fig. 1-4 Block diagram of grid side three-phase converters: (a) a diode rectifier (passive rectifier); (b) an active front end converter with a 2L VSC; (c) an active front end converter with a 3L-NPC VSC

Table 1.1

Common voltage levels and required IGBT voltage classes for 2L VSC active front end converters in low voltage applications

line to line rms voltage	dc-link voltage	IGBT voltage classes
200–230 V	350–400	600 V
380–460 V	700–800	1200 V
575–690 V	1000–1200	1700 V

medium to high switching frequencies [74].

An active front end converter based on a 3L-NPC VSC is shown in Fig. 1-4 (c). The grid phase voltage is denoted as $v_{G,a}$.

A classification of three-phase low voltage levels, required dc-link voltage, and corresponding IGBT voltage classes for a 2L VSC applied for the machine side converter and the grid side active front end converter is given in Table 1.1. The dc-link voltage values are determined supposing that the converter is controlled by an asymmetrical regular sampled sine-triangle modulation with one-sixth third harmonic [74].

1.1.3 DC-link capacitor

Aluminium electrolytic capacitors (AL-E-Cs) and film capacitors (FCs) are state-of-the-art power capacitors used as dc-link capacitors in industrial drives with voltage dc-link [20].

Al-E-Cs apply the oxidant of aluminium layer which provides a high dielectric constant. The anode of Al-E-Cs is formed by an aluminium foil and the cathode is a conductive liquid [137]. Dielectric properties of the oxide impose a limit to the maximum voltage of these capacitors. Al-E-Cs are practically available with nominal voltages up to 600 V [88]. For applications with higher nominal voltage, electrolytic capacitors must be connected in series. The main advantage of Al-E-Cs which has led to their wide industrial application is their high volumetric efficiency (capacitance / volume). These capacitors feature a significant variation of capacitance versus the temperature [88]. Therefore, the use of electrolytic capacitors in the equipments which operate in a wide range of temperatures (e.g. traction) might be impossible. Al-E-Cs are polar capacitors and only suitable for DC operation.

FCs are constructed using a combination of metal foils and moralized plastic films. They are used for voltages above 450 V [138]. FCs occupy considerably higher volume than equivalent Al-E-Cs. FCs feature a very good capacitance tolerance over the temperature range. FCs are not polarized capacitors and can be used for both ac and dc voltages. There are no problems like blow-up and dry-out which are typical for Al-E-Cs [88], [93]. FCs with a low-loss

Table 1.2

Qualitative comparison of aluminium electrolytic capacitors and film capacitors

	Aluminium Electrolytic Capacitors	Film Capacitors
Size, Weight	poor	good
Temperature stability	poor	good
Equivalent series resistance	good	excellent
Failure mode	poor	excellent
Cost	excellent	poor

dielectric have extremely low equivalent series resistance (R_{ESR}) [138]. This characteristic accounts for low capacitor losses and high current-handling capability. However, FCs also have some disadvantages. FCs are more expensive for lower voltages and have a much lower capacitance volume ratio than Al-E-Cs. A quantitative comparison between Al-E-Cs and FCs is presented in Table 1.2.

1.1.4 Grid side filter

The main objective of a grid side filter is to damp the current harmonics injected to the grid. Harmonic filters can be categorized into passive, active and hybrid filters [81], [107], [127].

While active filters use active power electronic components, passive components such as inductors and capacitors are used in passive filters. A hybrid filter is a combination of a passive and an active filter.

L-filters (inductance-filters) are state-of-the-art grid side passive filters which connect the diode rectifiers or active front end converters to the grid. The main advantage of L-filters is their simplicity. A single phase representation of an L-filter is shown in Fig. 1-5 (a). The voltage vectors of the grid and the grid side converter are denoted by \vec{v}_G and \vec{v}_{GC} , respectively. The total filter inductance and the total filter resistance are represented by $L_{F,t} = L_F + L_G$ and $R_{F,t} = R_F + R_G$. L_F and R_F are the inductance and resistance of the L-filter. In case of active front end converters, application of an LCL-filter (Inductance-Capacitance-Inductance-filter) can be an attractive solution. An LCL-filter is a combination of a grid side inductor, a converter side inductor, and a filter capacitor as shown in Fig. 1-5 (b). C_f is the capacitance of LCL-filter. The converter side inductance and resistance are denoted by $L_{F,GC}$ and $R_{F,GC}$. The grid side total inductance and total resistance are given by $L_{F,G,t} = L_{F,G} + L_G$ and $R_{F,G,t} = R_{F,G} + R_G$ where $L_{F,G}$ and $R_{F,G}$ are the grid side inductance and resistance of the LCL-filter. In case of L-filter, high switching frequencies are required for a sufficient attenuation of grid current harmonics at a reasonable filter size and filter voltage drop [99]. LCL-filters have an attenuation of 60 dB/decade for grid current harmonics above the resonance frequency while this attenuation is 20 dB/decade for an L-filter. The higher attenuation of LCL-filters leads to a lower filter total inductance compared to L-filters. Consequently, in the case of LCL-filters, a desirable high transient performance of the active front end converter with reasonable dc-link voltage is achievable [107]. In the industrial grids, L-filters are usually applied. In applications where grid current harmonics should be attenuated significantly to achieve compliance with the grid standards (e.g. IEEE-519), LCL-filters are more advantageous than L-filters.

1.1.5 Overview of control strategies of induction machine drives

As mentioned in Section 1.1.1, IMs, particularly squirrel cage IMs, are very popular in

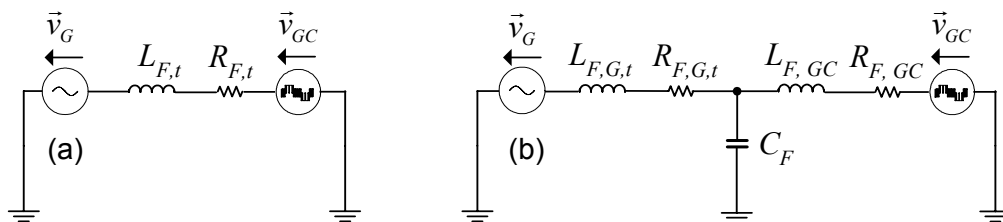


Fig. 1-5 Single phase representation of the grid side filters: (a) L-filter; (b) LCL-filter

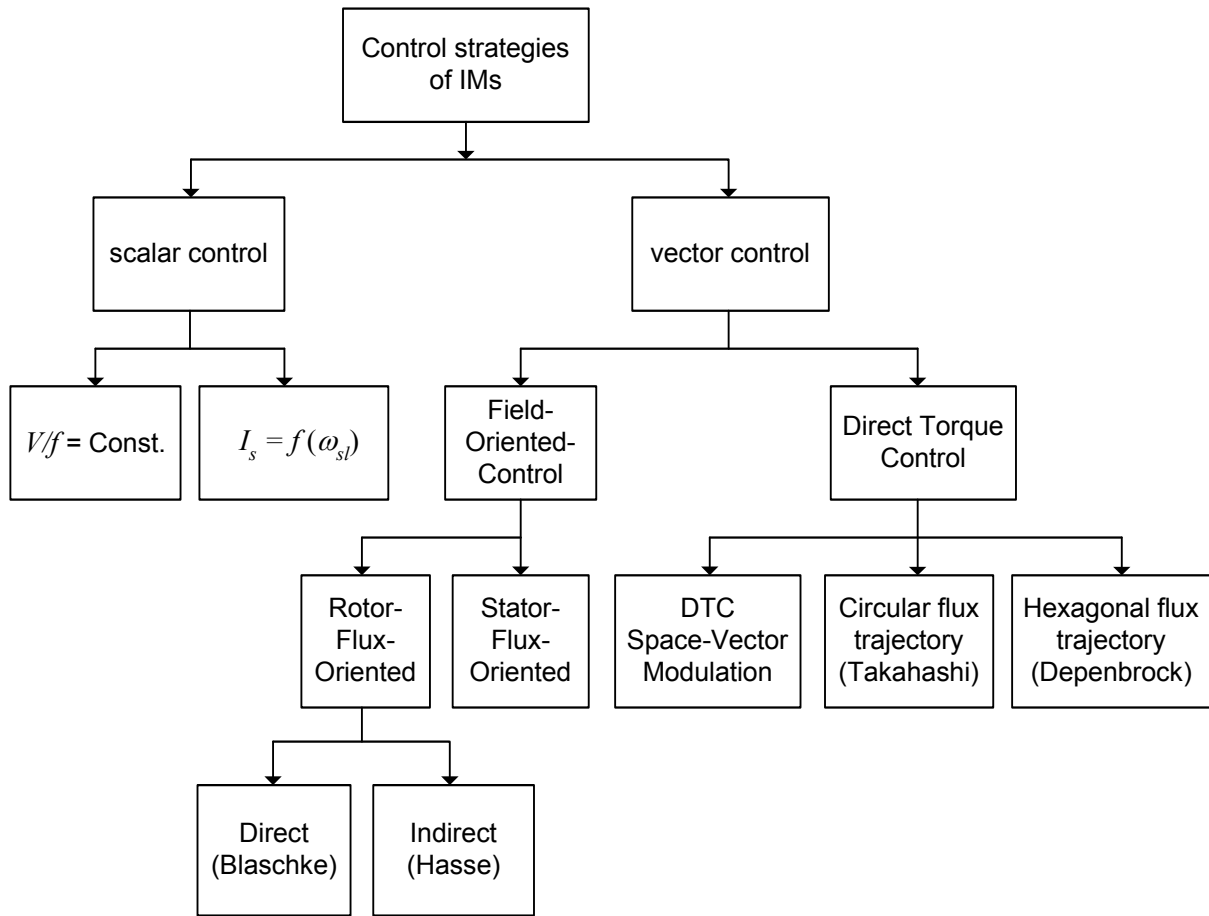


Fig. 1-6 Classification of control strategies for induction machines [47]

industrial applications because of well-known advantages like ruggedness, reliability and low cost. In this section an overview of different control strategies of squirrel cage IMs and the state-of-the-art control techniques are presented.

A classification of IMs control methods is shown in Fig. 1-6 [47]. IMs control strategies are mainly divided into two main methods: scalar control and vector control. In scalar control methods with $V/f = \text{const.}$ for drive with impressed stator voltage and $I_s = f(\omega_{sl})$ for drives with impressed stator current (I_s is the stator current and ω_{sl} denotes the slip angular frequency) amplitude and frequency of the stator voltage, stator current and linkage flux are adjusted. There is no control of the position of the flux vector. Therefore, scalar methods do not provide a high performance, especially during transients. Nevertheless these control methods are very simple to implement and popular for many applications (e.g. fans) in which no high transient performance is required.

In vector control based strategies amplitude, angular frequency and position of voltage, current and flux vectors are to be adjusted. Vector control is based on the dynamic model of IM and therefore results in a high performance dynamics of torque and speed. Vector control is implemented in different ways. FOC and DTC are often used in induction machine drives with high dynamics performance.

In FOC (proposed in the early 1970s) motor equations are usually transformed into a coordinate system that rotates in synchronism with the rotor flux vector (rotor-flux-oriented

control (RFOC)) or the stator flux vector (stator-flux-oriented control (SFOC)). In RFOC, there is a linear relationship between control variables and the motor torque [10], [19], [55] and there is no pull-out torque. Therefore RFOC is very popular in industry (e.g. high performance induction machine drives of Siemens). RFOC can be implemented by direct [46], and indirect [53] methods which will be described in chapter 3.

DTC was introduced in the mid 1980s. DTC was implemented with hexagonal flux trajectory (Depenbrock) [51] and circular flux trajectory (Takahashi) [73]. There is no coordinate transformation and linearization in DTC. Hysteresis torque and flux controllers are used instead of linear controllers. The main features of DTC are simple structure and excellent dynamic performance. In classic DTC, in which the stator flux is controlled, the control system is independent of the rotor parameters which leads to a robust behaviour. Meanwhile, variable switching frequency and required high sampling frequency are the main disadvantages of DTC. DTC has also been recently applied in electric drives with excellent dynamics (e.g. high performance induction machine drives of ABB). To overcome the disadvantages of DTC, DTC with space vector modulation (DTC-SVM) was recently proposed [21], [47]. In DTC-SVM, linear torque and stator flux controllers are applied and consequently no high sampling frequency is required. Furthermore, due to the modulator, a constant switching frequency appears in the output of the converter. However, this method needs a transformation into the stator-flux-oriented coordinates and does not provide excellent dynamic behaviour due to a lower sampling frequency.

1.1.6 Overview of control strategies of active front end converters

The main goal of the control of active front end converters is to maintain the dc-link voltage at the required set point value providing an adjustable power factor and sinusoidal grid currents. Control techniques of active front end converters can be classified into two main groups: voltage based control and virtual-flux-based control (Fig. 1-7).

Voltage-oriented control (VOC) and voltage-based direct power control (V-DPC) can be distinguished as two types of voltage based control [111]. In VOC, grid currents are transformed into a coordinate system which rotates synchronously with the grid voltage vector. Current components on direct d and quadrature q axis are used to control the dc-link

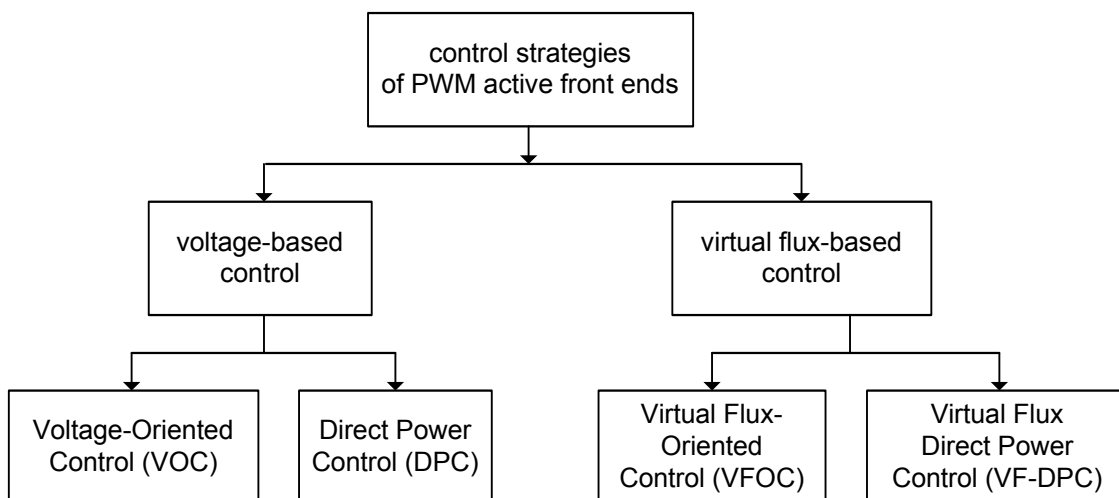


Fig. 1-7 Classification of control strategies for active front end converters [12]

voltage and the power factor. In V-DPC, active and reactive input powers are calculated based on grid voltages and currents. In a manner analogous to DTC of IMs, hysteresis controllers are used to control active and reactive power.

Virtual-flux-based control methods are based on a virtual flux defined as a time integral of the grid voltage vector [12], [110]. Virtual-flux-based control strategies have the advantage of low-pass filtering properties of the voltage integrators and are suitable for supplies with distorted voltage. These control methods are implemented in forms of virtual-flux oriented control (VFOC) and virtual-flux-based direct power control (VF-DPC). Similar to VOC, in VFOC linear controllers and a modulator (pulse-width modulation (PWM) or space vector modulation (SVM)) are applied and the converter operates with a constant switching frequency. Grid currents on q and d axis are used to control the dc-link voltage and power factor since the flux vector lags the voltage vector by 90° . In VF-DPC, active and reactive powers are estimated using the grid currents and the grid virtual flux components on the stationary reference frame. Similar to the V-DPC, hysteresis controllers are applied to control active and reactive power. A linear PI controller can be used as the controller of the dc-link voltage.

A comparative study of different control methods of active front end converters including investigations on their advantages and disadvantages is carried out in [111]. According to [111], VOC and VFOC feature a constant switching frequency and therefore require smaller grid side filter but they require a coordinate transformation and have a complex algorithm. V-DPC and VF-DPC have a simple structure and realize a good dynamic performance. On the other hand, they require a high sampling frequency and cause variable switching frequency.

1.1.7 Industrial applications

Low voltage ac drives are used in a wide range of industrial applications such as process control and automation and are poised for substantial growth. AC drives are increasingly being used by manufacturing companies in order to be energy efficient. In a basic classification, low voltage ac drives can be categorized as industrial standard drives, servo drives, and high-speed drives.

Industrial standard drives can be used in a wide range of industries. Typical applications are outlined in the following [134]:

- Air conditioning (fans, pumps, and compressors),
- Cement industry (fans, kilns, and conveyors),
- Chemical industry (pumps, fans, mixers, and processing lines),
- Food and beverage branch (mixers, conveyors, centrifuges, ovens, and bottling tables),
- Metal industry (roller tables, processing lines, and cranes),
- Oil and gas industry (fans, pumps, centrifuges, and compressors),
- Power plants (pumps, fans, and conveyors),
- Textile industry (mixers, extruders, and textile machines),
- Water treatment (pumps, compressors, and conveyors),
- Wind power.

Compared to standard drives, servo drives have some advantages like high dynamics and accuracy and compact motors with high power density. Servo drives are suitable for

applications for which very high precision, lower size and reliability are required. Some applications of servo drives are listed in the following [134], [139]

- Machine tools and metal working machinery,
- Electronics and semiconductor production machinery,
- Measuring and testing machinery,
- Packaging machinery,
- Textile machinery,
- Plastics processing machines,
- Coiling machines.

As compared to the standard drives, high-speed drives show several attractive characteristics like extensively increased power density and avoidance of mechanical gears. Replacing mechanical gears in direct high-speed drives [29] is one way to realize the market trend of a steadily decreasing ratio of cost per function in ac drives. High-speed drives are technology development with increasing importance. The power range of the high-speed drives is up to hundred kW (e.g. 500 kW) and the speed range is up to 200,000 rpm – 300,000 rpm. Typical applications of high-speed drives are:

- Machine tools,
 - Grinding and polishing machines
 - Spindle drives
- High-speed mills,
- Compressors,
 - Turbo compressors
 - Centrifugal compressors
- Pumps,
 - Centrifugal pumps
 - Turbo-molecular pumps
 - Vacuum pumps
 - Blood pumps
- Fans, blowers,
- Generators of microturbines and gas turbines for cogeneration systems,
- Flywheel energy storage systems.

Characteristics and state-of-the art of high-speed drives and the subject and motivation of this thesis are considered in the next chapter.

Chapter 2

Characteristics and State-of-the-art of High-Speed Drives

High-Speed Drives (HSDs) are a technology development with increasing importance. HSDs have interesting characteristics like increased power density and the avoidance of mechanical gears. These advantages are counterbalanced by disadvantages like strong centrifugal forces on the rotor and increased converter and machine losses. A block diagram of the power part of a low voltage high-speed drive with voltage dc-link is shown in Fig. 2-1. A low voltage high-speed drive comprises a high-speed machine (e.g. PMSM or IM), a machine side converter (e.g. 2L VSC or 3L-NPC VSC), a dc-link, and a grid side converter which has been briefly described in the previous chapter.

Advantages, disadvantages, and some details of selected applications of HSDs are investigated in this chapter. Power and speed range of HSDs are shown. Moreover, state-of-the-art technology for high-speed electric machines, converters, and control is explained. Finally, the motivations and the main subject of this work and the structure of the thesis are addressed.

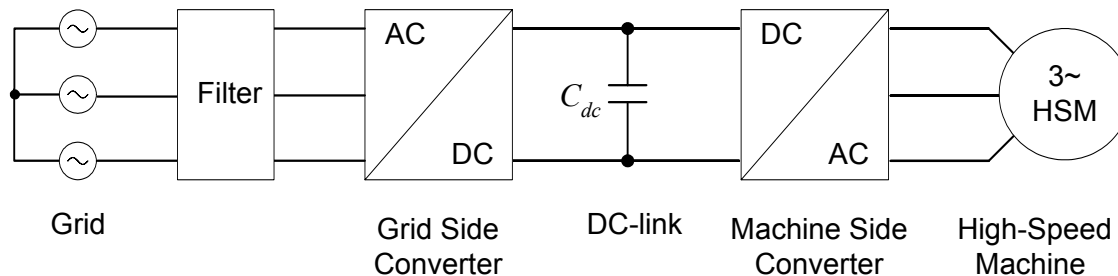


Fig. 2-1 A block diagram of the power part of a low voltage high-speed drive

2.1 Characteristics of high-speed drives

2.1.1 Advantages

The mechanical power of an electric machine is proportional to ampere conductors, magnetic flux per pole, and the mechanical speed. For a given machine size, ampere conductors, and magnetic flux per pole have limited values. Therefore, driving at high-speed is the efficient way to increase the output power. The aerospace industry (applying electric machines fed by a 400 Hz supply) is a commercial example of HSDs.

The following advantages are offered by HSDs:

- Increase of power density,
- Oil free design and less maintenance due to avoidance of mechanical gears,
- Integration of drive and process (e.g. compressors, pumps, fans, etc.).

Some quantitative values to describe the advantages of the HSDs are presented in the following:

- A 22.4 kW, 54,000 rpm drive for a centrifugal compressor is described in [34]. The HSD enables an increase of the system efficiency by more than 15% and a space and weight reduction of 80% compared to commercial compressors.
- A high-speed generator (131 kW, 60,000 rpm) for a microturbine is considered in [22]. A weight reduction of 75 % was achieved compared to a conventional diesel generator.
- A 1600 kW, 18,000 rpm generator for gas turbines has been investigated in [35]. The mass of the high-speed generator is only 30 % of the mass of a 1600 kW, 1800 rpm generator.

2.1.2 Disadvantages

HSDs have the following disadvantages compared to standard drives:

Electric Machines

- Requirement for a special rotor design because of strong centrifugal forces,
- Expensive bearings,
- Increased hysteresis and eddy current losses due to increased stator fundamental frequency and decreased stray inductance [4],
- Increased friction losses,
- Increased expense of cooling.

Converter

- High switching frequency f_{sw} or a low ratio of f_{sw} and fundamental frequency are required for an increased fundamental frequency. Increased switching frequency causes increased switching losses and consequently decreased converter efficiency. A low frequency ratio leads to higher current harmonics and therefore higher losses in the machine.

Control

- The required encoder for high-speed drives must have a high frequency response and high-speed rating. Due to reliability concerns and costs, the use of sensorless control schemes is recommended. Several sensorless control schemes have been proposed for synchronous and induction machines in the literature [22], [32].
- In control of HSDs a high sampling frequency is required. Therefore, the sampling period is short (e.g. 33.33 μ s for vector control of a high-speed PMSM with stator frequency of $f_{\omega M} = 1.2$ kHz [22]). In order to meet the required short calculation time, powerful DSPs or microcontrollers are usually required (e.g. [22], [34], [41]).
- Effects of the non-ideal switching behaviour (e.g. dead time) of semiconductors are not negligible, due to the higher fundamental and switching frequency.

2.1.3 Applications

Industrial applications of HSDs are introduced in the first chapter. In the following, some of the HSD applications are outlined with more details.

- **Microturbines** [22], [135], [147], [136]:

Microturbines are high-speed gas turbines which operate at low pressure and temperature. Microturbines cover a power range from 25 kW to 500 kW and can operate on fuels such as natural gas, oil, and biogas.

Microturbines are appropriate in applications like heat-power generations, hybrid electric vehicles, and in electric mains for peak load shaving.

Generator, turbine, and compressor are connected on one shaft in microturbines that rotate at high-speed (e.g. up to 100,000 rpm). Therefore, the high-speed drive is an essential technology for microturbines.

Microturbines enable a clean and reliable production of heat and electric power offering electric efficiency of 30%. If heat and power are utilized, system efficiency reaches 70%–90%.

- **High-speed compressors** [34], [144]:

Application of high-speed compressors offers the avoidance of mechanical gears, thus increasing reliability and efficiency. Moreover, a considerable reduction of weight and volume can be reached.

- **Machine tools** [144], [140]:

The main advantage of HSDs in machine tools is stress reduction in the part being machined, due to high metal removal with fine cuts. Furthermore, HSDs enable a wide range of speed control, including very high torque at low speed.

- **Spinning** [145]:

An evident trend towards improved economy of production is rotor spinning with HSDs. Using air bearings in speeds up to 140,000 rpm increases the lifetime and reduces the re-lubrication interval, compared to classical bearings.

2.1.4 Power and speed range

In the design of HSDs, the power and speed range is decisive. Spindle drives are used in a speed range of 10,000 rpm – 40,000 rpm up to several 10 kW. The drive power decreases to a few kW in the high-speed range (Fig. 2-2).

The power and speed range of commercially available microturbines (e.g. 30 kW – 250 kW; 30,000 rpm – 120,000 rpm) and compressors (e.g. 11 kW – 500 kW; 12,000 rpm – 90,000 rpm) are depicted in Fig. 2-2. Obviously, the speed and power range of microturbines and compressors considerably overlaps the speed and power range of spindles.

Fig. 2-3 shows the power and speed range of different high-speed electric machines (HSMs). It is evident that IMs and PMSMs dominate the considered applications. PMSMs appear to be the dominant HSMs, particularly in applications like microturbines, in which the system efficiency is very important. HSMs are usually applied in spindle drives.

However, reference [15] presents research of the investigation of HSMs for the medium power range (x10kW–x100 kW).

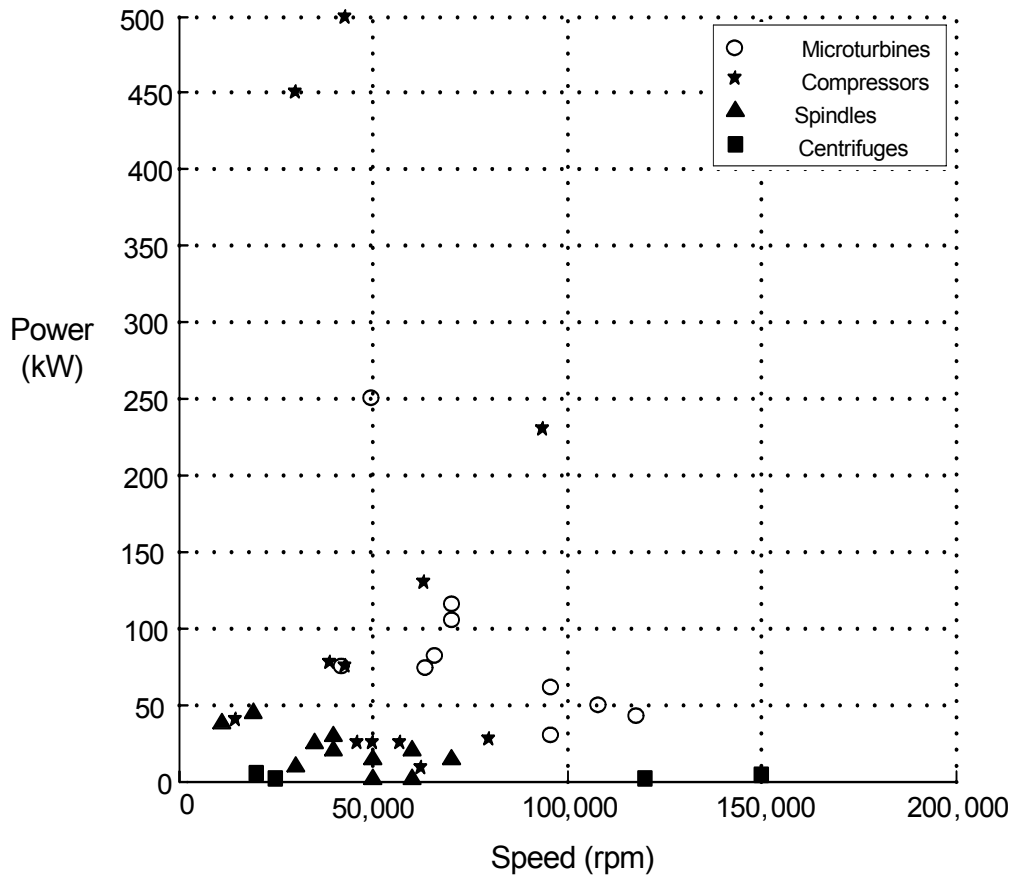


Fig. 2-2 Power and speed range of high-speed drives [22], [34], [144], [145]

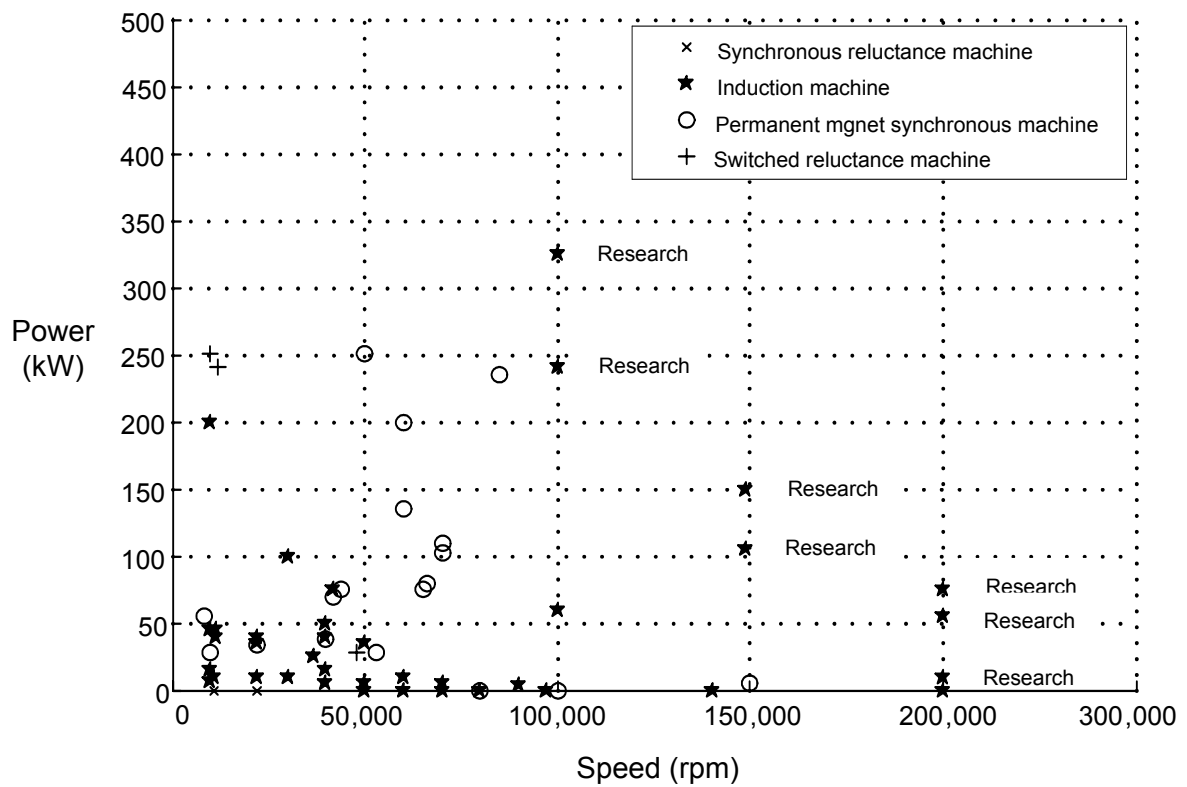


Fig. 2-3 Types of electric machines applied in high-speed drives [15], [22], [140], [144], [145]

2.2 State-of-the-art technology of high-speed drives

2.2.1 Electric machines

The main characteristics of high-speed machines are high power density and high mechanical stress of the rotor. Furthermore, fast switching frequency of the converter causes isolation stress in the stator. Low costs of material and manufacturing, a high power factor, and high reliability as general requirements are also valid for high-speed machines. Specific requirements are:

- low losses (iron, copper, and friction) at high fundamental frequency,
- low rotor losses particularly important, because of the difficulties of the rotor cooling,
- liquid cooling usually applied to manage the stator losses,
- rotor with high tolerable temperature,
- stator isolation with high withstand capacity of dv/dt (due to converter operation).

IMs and SMs are the main types of high-speed electric machines. PMSMs and switched reluctance machines (SRM) can be distinguished as the main types of high-speed SMs [23]. The resulting losses for various types of high-speed electric machines are summarized in Table 2.1.

Table 2.1
Losses of high-speed drives

	IM	PMSM	SRM
Stator copper losses	×	×	×
Excitation copper losses			
Stator iron losses	×	×	×
Rotor copper losses	×		
Rotor iron losses	×		×
Gas flow losses	×	×	×
Friction losses	×	×	×
Losses of cooling system	×	×	×

PMSMs and IMs are the most widely used high-speed drives today. In the following section, fundamental characteristics of these high-speed electric machines are presented.

IMs [34], [28], [38], [33]

Squirrel-cage IMs have been widely applied in high-speed machine tools, pumps, fans, and compressors. High-speed squirrel-cage IMs feature following advantages and disadvantage

- Advantages:
 - low manufacturing costs,
 - low maintenance,
 - high temperature withstand capacity,
 - quiet operation,
- Disadvantage:
 - Rotor iron and copper losses reduce the efficiency.

PMSMs [22], [27], [34], [39]

Using rare earth components such as samarium and neodymium as permanent magnets makes

it possible to use PMSMs in high-speed application, thus offering high efficiency and a high power factor. The high efficiency of PMSMs is the main reason to apply PMSMs in microturbines [22]. Below the advantages and disadvantages of high-speed PMSMs are summarized

- Advantages:
 - no rotor copper losses,
 - high power factor,
- Disadvantages:
 - difficult manufacturing of complex rotor structure,
 - higher material costs compared to IMs,
 - limited temperature withstand capacity,
 - difficult rotor maintenance.

2.2.2 Bearings

Mechanical bearings are a technical problem of HSDs. Bearings limit the mechanical speed and have maintenance requirements.

Air bearings and magnetic bearings are alternatives to mechanical bearings in microturbines, which enable a reliable operation at moderate costs [136]. Magnetic bearings have no mechanical contacts and therefore do not require lubrication and feature a lower bearing losses compared to mechanical bearings. The increased costs and complexity are the main disadvantages of magnetic bearings. Magnetic bearings have been applied in many commercially available high-speed drives such as spindle drives, pumps, and mills.

Another disadvantage of magnetic bearings is the increase of motor axial length. In order to reduce the axial shaft length of high-speed machines with magnetic bearings, the high-speed motor can be magnetically combined with magnetic bearings [30]. The electric machines with no separate magnetic bearings (rotor is magnetically supported by the motor itself) are called bearingless electric machines [25], [37]. High-speed IMs and high-speed PMSM are produced applying the principles of the bearingless electric machines [37], [36], [26].

The control complexity of bearingless high-speed machines is increased due to the cross coupling of electrometrical torque and radial force, compared to the control of machines with magnetic bearings [27].

2.2.3 Converter

General requirements of drive converters like low costs, high reliability and power density as well as moderate dv/dt are also important for high-speed drives.

Specific requirements of the converters of high-speed drives are:

- high fundamental frequency of converter,
- high switching frequency for asynchronous modulation (frequency ratio $m_f > 10$).

Machine side converters in high-speed drives differ from standard machine side converters, due to the extremely increased fundamental frequency of the high-speed machine. Grid side converters of high-speed drives are a standard front end converter (diode rectifiers or active front end converters).

The 2L VSC with PWM is applied as a machine side converter in high-speed drives for motor

and generator operation. However, the use of a diode rectifier for generator application has been described in several publications (e.g. [29]).

For speed ranges of $n_{syn} = 30,000$ rpm to $n_{syn} = 200,000$ rpm for a machine with one pole pair, fundamental converter frequencies of $f_{0M} = 500$ Hz to $f_{0M} = 3333$ Hz are required. The control scheme (e.g. FOC and DTC) and the control platform determine the modulation type (synchronous or asynchronous modulation). In case of asynchronous modulation, switching frequency should be considerably higher than fundamental frequency (e.g. $f_{sw} > 10 \cdot f_{0M} - 15 \cdot f_{0M}$). Therefore a 2L VSC with asynchronous modulation requires switching frequencies of $f_{sw} = 5$ kHz to $f_{sw} = 33.33$ kHz for a one pole machine and synchronous mechanical speed range of $n_{syn} = 30,000$ rpm to $n_{syn} = 200,000$ rpm.

Synchronous modulation can be used to reduce the required switching frequency and the switching losses, which can be useful especially at high speeds. Obviously the reduced switching frequency causes increased current ripple and therefore increased machine losses and torque ripple. The required switching frequency could be decreased to e.g. $f_{sw} = 3 \cdot f_{0M} - 13 \cdot f_{0M}$ applying synchronous modulation with 3-, 5-, ..., 13- pulses per fundamental cycle as shown in Fig. 2-4.

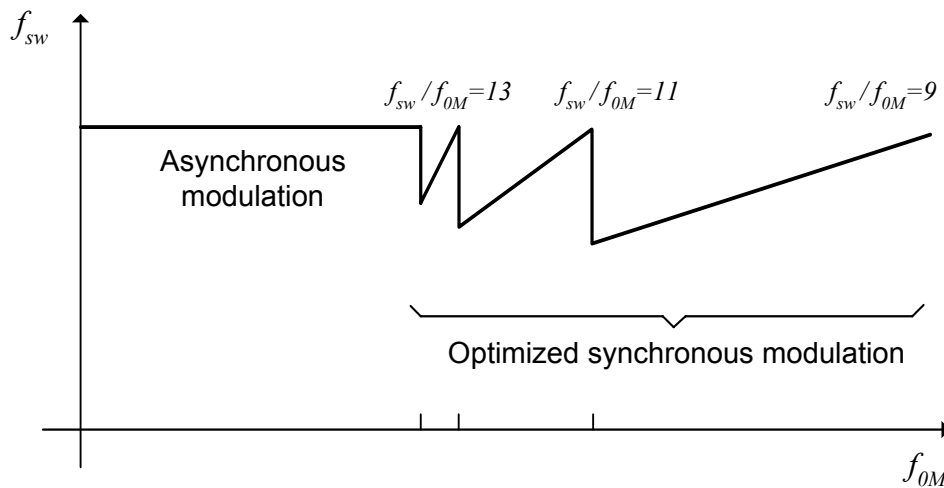


Fig. 2-4 Asynchronous and optimized synchronous PWM

The 2L-VSC is the most widely applied topology for machine side converter in high-speed drive applications. In case of a drastically increased switching frequency e.g. in high-speed asynchronous modulation, the installed switch power of IGBT increases significantly for a 2L VSC. Therefore, a 3L-NPC VSC can be an attractive solution for high switching frequencies [74], [75]. A 3L-NPC VSC is an alternative topology to reduce these effects, especially if a high switching frequency is required ($f_{sw} = 10$ kHz - 15 kHz). The 3L-NPC VSC offers several attractive features like a reduction of the installed switch power, semiconductor losses, machine losses, voltage, and current harmonics, insulation stress of the stator windings and the bearing currents [74].

Harmonics of the converter output voltage cause eddy current losses in rotor and stator, which then reduces the machine efficiency. Reference [31] shows that the efficiency of an induction machine fed by a 2L VSC decreased by about 2 %, compared to the efficiency of the machine fed by sinusoidal voltages.

The steep voltage transients of VSC stress the insulation of the electric machine particularly if long cables are used. High switching frequency required for high-speed drives worsen the problems, as compared to conventional drives due to the required fast switching transients.

The common mode voltage and currents of the PWM converter causes shaft voltage and current. Shaft currents can flow through bearings and cause damage in mechanical bearings. Common mode frequencies are critical in the range of high frequencies (e.g. 50 kHz - 5 MHz).

Application of a sine filter between converter and high-speed machine can reduce the above problems. A sine filter features the following characteristics:

- machine voltage with substantially decreased THD,
- low current and torque ripple,
- increase of machine efficiency.

2.2.4 Control

Control strategies like DTC, direct self control (DSC), and FOC have been successfully applied in industrial induction motor drives [47]. The best approach is determined according to requirements with respect to the ratio of switching frequency and output frequency as well as performance requirements.

In case of very high-speed drives (e.g. $n_{syn} > 200,000$ rpm, n_{syn} is the synchronous mechanical speed) a significantly decreased computation cycle restricts the applicable control strategies to scalar control. One main disadvantage of scalar control strategies is their poor starting dynamic performance. Modified V/f control methods are also used in control of super high-speed drives to improve the starting performance [24], [40].

In medium high-speed drive applications ($n_{syn} < 50,000$ rpm) for which high dynamic performance is required (e.g. high-speed spindle drives), DTC and RFOC are the applicable control strategies. DTC applies hysteresis controllers to realize an instantaneous torque and flux control. In case of DTC, for an excellent dynamic performance with reasonable torque ripple, a high sampling rate (e.g. $f_s = 20 \cdot f_{sw}$ where f_s and f_{sw} denote the sampling and switching frequency, respectively) is required [47]. In standard RFOC linear PI controllers are used. Torque and rotor flux are indirectly controlled with stator currents. RFOC realizes a constant switching frequency.

Instantaneous control of torque and flux in DTC requires a high sampling rate (e.g. $f_s = 10 \cdot f_{sw} - 20 \cdot f_{sw}$). Typical switching and sampling frequencies are $f_{sw} = 4$ kHz and $f_s = 40$ kHz today. If the sampling frequency can be increased to $f_s = 100$ kHz using a fast processor, DTC is realizable for a high-speed machine with fundamental frequency of $f_{0M} = 1$ kHz and an average switching frequency of $f_{sw} = 10$ kHz.

In case of very high-speed drives, sensorless speed control is usually required to avoid the mechanical sensor [22], [32], [40]. For medium high-speed drives where speed sensors are available, control strategies with speed sensor can be used. Application of a speed sensor is advantageous in the case that low-speed performance is important.

2.3 Subject, motivation, and structure of the thesis

Investigation of a low voltage high-speed induction machine drives (HSIMD) is the general subject of this dissertation. A block diagram of the investigated HSIMD is shown in Fig. 2-5.

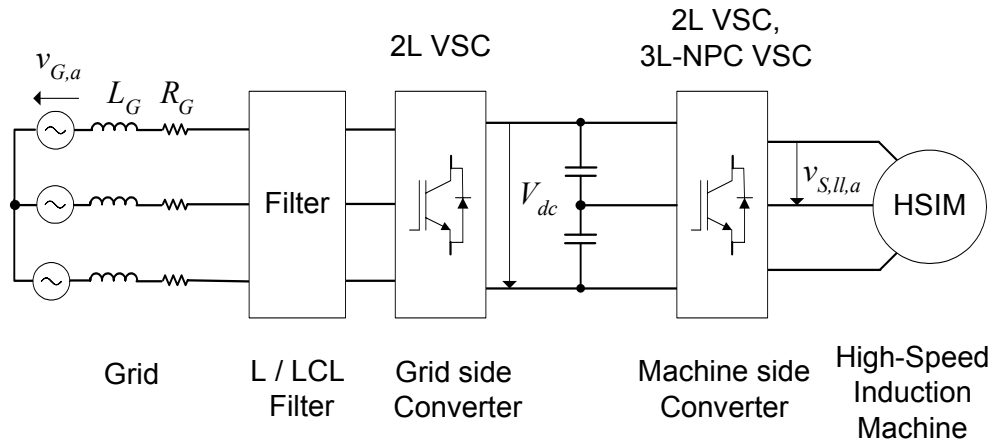


Fig. 2-5 Block diagram of the investigated high-speed induction machine drive

A low-voltage high-speed induction machine (HSIM) with nominal synchronous mechanical speed of $n_{syn} = 30,000$ rpm (one pole pair) is applied in the investigations (stator nominal line to line rms voltage $V_{S,ll,n} = 400$ V and nominal mechanical power $P_{mech,n} = 20$ kW). Such a configuration can be applied in principle in distributed power generation systems [22], [135], [136], [147]. In grid-connected microturbine or high-speed gas turbine applications, the dc-link voltage is adjusted by the grid side converter and the machine side converter regulates the mechanical speed.

Furthermore, the configuration shown in Fig. 2-5 can be used e.g. in high-speed spindle drives in the machine tool industry (specifically in the aerospace industries, due to the requirements necessary for the extremely high-speed cutting of aluminium alloy for high productivity) [140], [144], [145]. In order to obtain minimum speed and torque variations during cutting, high performance control system is required in high-speed spindle drives.

The HSIMD shown in Fig. 2-5 is investigated in two main chapters of this thesis. Chapter 3 comprises analysis and study of the HSIM control and comparison between the 2L VSC and the 3L-NPC VSC as machine side converter for the HSIMD.

In chapter 4, control of the grid side converter (2L VSC) and analytical design procedure of the grid side filter (L and LCL) are investigated.

Control of HSIMs

Scalar control is usually applied in the control of high-speed drives. In this thesis, RFOC for the exemplary HSIM ($V_{S,ll,n} = 400$ V, $P_{mech,n} = 20$ kW, $n_{syn,n} = 30,000$) is investigated for both symmetrical and asymmetrical regular sampling. The sampling rate is chosen to be equal to the switching frequency ($f_s = f_{sw}$) in a symmetrical regular sampling PWM (SRS-PWM) or twice the switching frequency ($f_s = 2f_{sw}$) in an asymmetrical regular sampling PWM (ARS-PWM) [7]. In the second step, DTC is applied to control the HSIM. Sampling frequency and the hysteresis band of torque and flux control loops are chosen so that DTC and RFOC realize the same torque total harmonic distortion (THD).

For high-speed drives in the mentioned speed range ($n_{syn,n} = 30,000$), speed sensors are available. Hence, a control system with speed measurement for both RFOC and DTC is investigated in this thesis.

Finally, the required sampling frequency as well as the dynamic performance for both control methods for the HSIM are investigated and compared.

Comparison of 2L VSC and 3L-NPC VSC for high-speed drives

A detailed comparison between 2L-VSC and 3L-NPC VSC for the mentioned HSIM with RFOC is included in this thesis. Comparison criteria comprise maximum torque ripple, torque THD, installed switch power, loss distribution, and converter efficiency.

Control of the grid side converter and design of the grid side filter

In this thesis, VOC as a common control strategy of active front end converters [12], [111] is applied for the control of the grid side converter. In many applications, active front end converters operate in parallel with diode or thyristor converters. Diode and thyristor converters cause significant current harmonics, which lead to a distorted grid voltage at the point of common coupling [98]. Steady-state performance of an active front end converter with VOC and L-filter for a notched grid (caused by a parallel thyristor converter) is investigated in this thesis. Simulation and experimental results are presented to validate the investigations which were carried out.

In case of distributed power generation, current harmonics injected to the grid are strongly limited according to standards like IEEE-519. L-filters are usually applied to damp the current harmonics. LCL-filters can also be used to damp the current harmonics effectively. Design of an LCL-filter is a complex subject and is the subject of recent literature [43], [100], [107], [129]. However, a precise analytical design procedure considering the control reserve and the amplitudes of the grid current harmonics is not presented in recent publications and the literature. In this thesis, a new iterative design procedure for L-filter and LCL-filter to fulfil the IEEE-519 limitations is proposed and investigated in detail. Design procedure is based on the analytical expression of converter voltage harmonics applying Bessel functions. Validation of the proposed design procedures are proved with simulation and experimental results.

The main problem involved with the control of active front end converters with LCL-filter is the resonance of the LCL-filter. Depending on the LCL-filter resonance frequency and the band width of the current controllers of VOC, the control system could excite the LCL filter in transitions. In order to avoid filter resonance, active damping is applied. Active damping can be realized in different methods [85], [107]. Active damping based on measurement of the filter capacitors voltage is applied in this thesis. A simple method to design the required compensator using the parameters of the current control loop is proposed. Simulation and experimental results for the transient and steady-state performance of the VOC for active front end converter with LCL-filter are presented.

Structure of the thesis

Material of this thesis is arranged in four chapters. Chapter 3 presents the control strategies of HSIMs. FOC and DTC are described for an HSIM and compared. Design of 2L VSC and 3L-NPC VSC as the machine side converter is also discussed in this chapter, and a comparison between two topologies is given.

PWM active front end converters with L-filter and LCL-filter as the grid side filter are investigated in chapter 4. Mathematical descriptions of the converter and the filter as well as the applied control strategy are presented. Furthermore, behaviour of active front end converters with L-filter in the presence of thyristor converters is analyzed.

An analytical procedure to design the grid side filter (L- and LCL- filter) is introduced and verified by simulation and experimental results.

Chapter 5 presents the conclusions of this thesis.

Chapter 3

Control of High-Speed Induction Machines

In this chapter, FOC and DTC as standard control strategies of IMs are investigated for an exemplary HSIM fed by a 2L VSC. Besides the description of both methods, a comparison is carried out, considering the required sampling frequency and dynamic performance. Furthermore, 2L VSC and 3L-NPC VSC as machine side converters are compared for the HSIM controlled with RFOC. Torque ripple, loss distribution, and converter efficiency are taken into account for a detailed comparison.

3.1 Definition of an exemplary high-speed induction machine drive

An exemplary HSIM is used to investigate the high performance control strategies (FOC and DTC) for a HSIMD. A power circuit block diagram of a HSIMD is presented in Fig. 3-1. The machine is a HSIM with rated mechanical power of $P_{mech,n} = 20$ kW and a line-to-line rms stator voltage of $V_{s,ll,n} = 400$ V. Nominal stator frequency is $f_{0M} = 500$ Hz and the machine has one pole pair. Synchronous and nominal mechanical speeds are 30000 rpm and 29820 rpm, respectively. Electrical and mechanical parameters of the HSIM and a standard IM are shown in Table 3.1. Obviously, the main and leakage inductances are decreased significantly in case of the high-speed machine. Further machine parameters and design details can be taken from [4]. A 2L VSC with dc-link voltage of 700 V is used as machine side converter (MC) for the comparison of FOC and DTC for the HSIMD. Sinus-triangle PWM with regular sampling and a carrier frequency of $f_c = 11.5$ kHz ($m_f = 23$) is used as the modulator of FOC.

2L VSC and 3L-NPC VSC are compared for HSIMD controlled with RFOC. Table 3.2 lists the basic parameters and characteristic converter data for both converters. To enable a comparison between the topologies, the converter phase current and the apparent converter powers are kept constant.

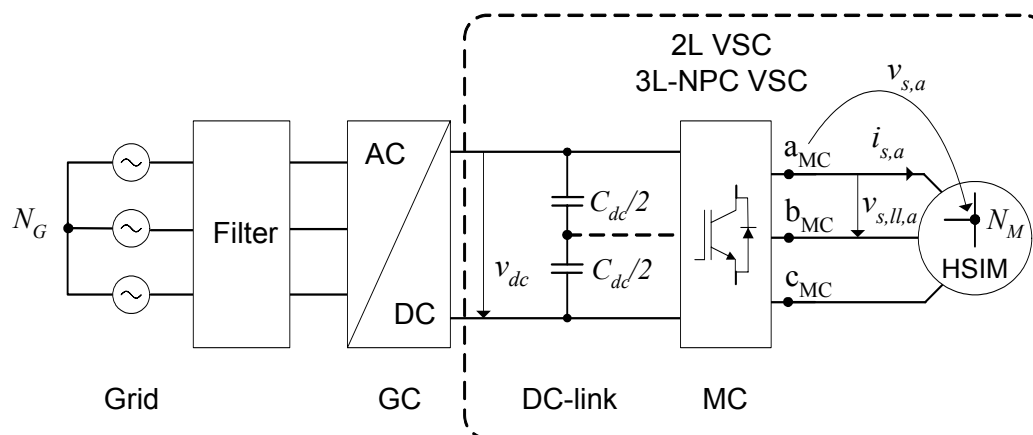


Fig. 3-1 Power circuit block diagram of a high-speed induction machine drive

Table 3.1

Data and parameters of the high-speed induction machine [4] and a standard induction machine [148]

Parameter	Value (high-speed)	Value (standard)
Nominal rms stator line-to-line voltage, $V_{s,ll,n}$	400 V (Y)	400 V (Y)
Base voltage of machine side per unit system, $V_{b,M}$	$V_{b,M} = \sqrt{2}v_{s,ll,n} / \sqrt{3}$	
Nominal rms stator current, $I_{s,n}$	38.25 A	32 A
Base current of machine side per unit system, $I_{b,M}$	$I_{b,M} = \sqrt{2} I_{s,n}$	
Rated load power factor, $\cos(\varphi_M)$	0.768	0.92
Nominal stator frequency, f_{0M}	500 Hz	50 Hz
Number of pole pairs, Z_p	1	1
Nominal synchronous speed, $n_{syn,n}$, $N_b = n_{syn,n}$	30000 rpm	3000 rpm
Nominal mechanical speed, n_n	29820 rpm	2920 rpm
Nominal mechanical power, $P_{mech,n}$	20 kW	18.5 kW
Moment of inertia, J	0.00072 Kgm ²	0.0675 Kgm ²
Nominal electromechanical torque, $T_{em,n}$, $T_{em,b} = T_{em,n}$	6.39 Nm	60.5 Nm
Nominal stator flux, $\psi_{S,n}$	0.1036 Wb	1.0206 Wb
Nominal rotor flux, $\psi_{R,n}$	0.1010 Wb	0.9819 Wb
Stator resistance, R_S	0.025 Ω	0.1437 Ω
Rotor resistance, R_R	0.022 Ω	0.1885 Ω
Stator leakage inductance L_{lS}	0.128 mH	2.16 mH
Rotor leakage inductance L_{lR}	0.128 mH	2.16 mH
Mutual inductance, L_M	3.3 mH	101.3 mH

Resolver of the high-speed induction machine: RE 3620-952-10-S, Excitation frequency: 2 to 20 kHz, Maximum speed: 100,000 rpm

Table 3.2

Basic data of converter for 2L VSC and 3L-NPC VSC

Parameter	Value
Nominal rms output line to line voltage of converter	400 V
Nominal rms converter phase current	38.25
Rated apparent output power of converter	26.5 kVA
Nominal converter output frequency	500 Hz
Nominal dc-link voltage, V_{dc}	700 V
Modulation	Sinus-triangle modulation
Carrier frequency, f_c	11.5 kHz – 23 kHz
Maximum junction temperature, $T_{j,max}$ (IGBT, diode)	125° C
Heat sink temperature, T_h	80° C

3.2 Mathematical description of induction machines

Mathematical modelling of an IM is achieved considering the following assumptions [10] :

- Windings of both stator and rotor are symmetrical with isolated neutral point.

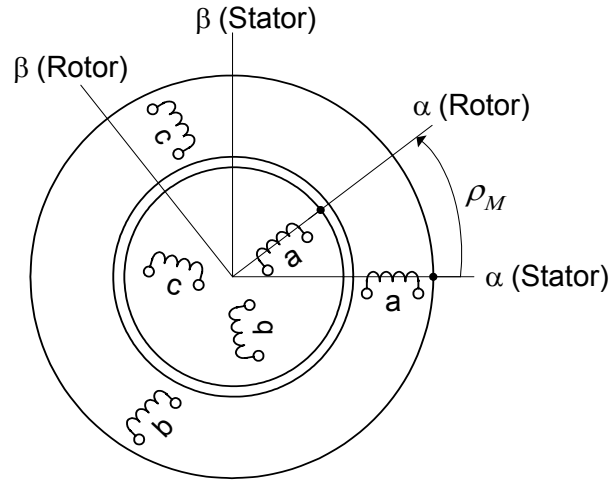


Fig. 3-2 Structure of a symmetrical induction machine [16]

- The permeability of the stator and the rotor iron is considered to be infinite.
- Saturation and iron losses are neglected.
- All rotor parameters and variable are transferred to the stator side.

Considering the above assumptions, a simple representation of a three-phase induction machine is shown in Fig. 3-2. Mechanical rotation angle of the rotor is ρ_M which is measured in the stator stationary coordinate frame. The real axis α of the stationary stator frame is fixed on the stator winding of phase a . The mechanical angular velocity of the rotor is:

$$\omega_M(t) = \frac{d\rho_M(t)}{dt}. \quad (3-1)$$

Considering the resistive voltage drop and the back electromotive force (EMF) of the windings, the stator and rotor voltage equations can be written as follows:

$$R_S i_{S,x} + \frac{d\psi_{S,x}}{dt} = v_{S,x}, \quad (3-2)$$

$$R_R i_{R,x} + \frac{d\psi_{R,x}}{dt} = v_{R,x}, \quad x = a, b, c, \quad (3-3)$$

where

R_S and R_R are the resistance of the stator and rotor windings,

$i_{S,x}$ and $i_{R,x}$ are the instantaneous phase currents of the stator and rotor,

$\psi_{S,x}$ and $\psi_{R,x}$ are the instantaneous fluxes of the stator and rotor windings of phase a, b , and c ,

$v_{S,x}$ and $v_{R,x}$ are the instantaneous phase voltages of the stator and rotor.

In order to reduce the number of equations, the space vector representation of the machine equations is applied. This representation offers the opportunity to represent the machine equations in various coordinate systems [10], [19]. In the space vector representation, the three-phase equations are projected into a two-dimensional stationary reference frame (α - β). The following equation is used for the projection:

$$\bar{x} = \frac{2}{3} (x_a(t) + \bar{a} \cdot x_b(t) + \bar{a}^2 \cdot x_c(t)), \quad (3-4)$$

where, \bar{a} and \bar{a}^2 are complex unit vectors with phase shift of $2\pi/3$ and $4\pi/3$ as follows:

$$\vec{a} = e^{j\frac{2\pi}{3}}, \vec{a}^2 = e^{j\frac{4\pi}{3}}. \quad (3-5)$$

The projection (3-4) can be represented in a matrix form as follows:

$$\begin{bmatrix} x_\alpha \\ x_\beta \end{bmatrix} = \begin{bmatrix} \frac{2}{3} & \frac{-1}{3} & \frac{-1}{3} \\ 0 & \frac{1}{\sqrt{3}} & -\frac{1}{\sqrt{3}} \end{bmatrix} \begin{bmatrix} x_a \\ x_b \\ x_c \end{bmatrix}, \vec{x} = x_\alpha + jx_\beta. \quad (3-6)$$

Using (3-6), the stator and rotor instantaneous voltage equations in (3-2) and (3-3) are projected into the following equations

$$R_S \vec{i}_S^S + \frac{d\vec{\psi}_S^S}{dt} = \vec{v}_S^S, \quad (3-7)$$

$$R_R \vec{i}_R^R + \frac{d\vec{\psi}_R^R}{dt} = \vec{v}_R^R, \quad (3-8)$$

where

\vec{i}_S^S , $\vec{\psi}_S^S$, and \vec{v}_S^S are current, flux, and voltage vectors of the stator in the stator stationary reference frame,

\vec{i}_R^R , $\vec{\psi}_R^R$, and \vec{v}_R^R are current, flux, and voltage vectors of the rotor in the rotor stationary reference frame.

The stator and rotor flux vectors were determined in the stator and rotor stationary reference frames using self and mutual inductances as described in the following [10], [16], [19]:

$$\vec{\psi}_S^S = L_S \vec{i}_S^S + L_M e^{j\rho_M} \vec{i}_R^R, \quad (3-9)$$

$$\vec{\psi}_R^R = L_R \vec{i}_R^R + L_M e^{-j\rho_M} \vec{i}_S^S, \quad (3-10)$$

$$L_S = (1 + \sigma_S) L_M, \quad \sigma_S = L_{IS} / L_M, \quad (3-11)$$

$$L_R = (1 + \sigma_R) L_M, \quad \sigma_R = L_{IR} / L_M, \quad (3-12)$$

where

L_M is the mutual inductance of IM,

σ_S and σ_R are the stator and rotor leakage factor,

L_{IS} and L_{IR} denote the stator and rotor leakage inductance,

L_S and L_R are the stator and rotor self inductances.

The stator variables and the equations (3-7) and (3-9) are represented in the stator stationary reference frame (real axes α is fixed on phase a of the stator). In a similar way, the rotor variables and the equations (3-8) and (3-10) are represented in the rotor stationary reference frame (real axes α is fixed on the phase a of the rotor). The apexes S and R are applied to identify the stationary reference frame of stator and rotor, respectively. Since the real axis of the rotor stationary reference frame is fixed on the rotor winding of phase a , the rotor stationary reference frame rotates with the rotor angular velocity ω_M . The machine electromechanical torque T_{em} can be expressed in terms of the stator and rotor current vectors as [10], [16], [19]

$$T_{em} = \frac{3}{2} Z_p L_M \text{Im} \left[\vec{i}_S^S \cdot (\vec{i}_R^R e^{j\rho_M})^* \right] \quad (3-13)$$

where Z_p denotes the number of pole pares.

Inserting the flux equations (3-9) and (3-10) in the voltage equations (3-7) and (3-8), the complete mathematical model of the symmetrical IM is derived as following:

$$R_S \vec{i}_S^S + L_S \frac{d\vec{i}_S^S}{dt} + L_M \frac{d}{dt}(\vec{i}_R^R e^{j\rho}) = \vec{v}_S^S, \quad (3-14)$$

$$R_R \vec{i}_R^R + L_R \frac{d\vec{i}_R^R}{dt} + L_m \frac{d}{dt}(\vec{i}_S^S e^{-j\rho}) = \vec{v}_R^R, \quad (3-15)$$

$$J \frac{d\omega_M}{dt} = T_{em} - T_L = \frac{3}{2} Z_P L_m \text{Im}[\vec{i}_S^S (\vec{i}_R^R e^{j\rho_M})^*] - T_L, \quad (3-16)$$

with T_L and J being the load torque and the rotor moment of inertia.

3.3 Field orientation

The equations of IM given in (3-7) to (3-13) are represented in two different reference frames. In order to simplify the mathematical model, both equations of the stator and rotor should be projected into a common coordinate system K with angular speed of ω_K . Multiplying machine voltage and flux equations by $e^{-j\rho_K}$, $\rho_K(t) = \int_0^t \omega_K(\tau) d\tau$, the mathematical model of IM has been projected into the coordinate system K [16]. Electrical and mechanical equations of IM in an arbitrary coordinate system K are:

$$R_S \vec{i}_S^K + \frac{d\vec{\psi}_S^K}{dt} + j\omega_K \vec{\psi}_S^K = \vec{v}_S^K, \quad (3-17)$$

$$\vec{\psi}_S^K = L_S \vec{i}_S^K + L_M \vec{i}_R^K, \quad (3-18)$$

$$R_R \vec{i}_R^K + \frac{d\vec{\psi}_R^K}{dt} + j(\omega_K - Z_P \omega_M) \vec{\psi}_R^K = \vec{v}_R^K, \quad (3-19)$$

$$\vec{\psi}_R^K = L_R \vec{i}_R^K + L_M \vec{i}_S^K, \quad (3-20)$$

$$J \frac{d\omega_M}{dt} = T_{em} - T_L = \frac{3}{2} Z_P \text{Im}[\vec{\psi}_S^{*K} \cdot \vec{i}_S^K] - T_L, \quad (3-21)$$

where

\vec{i}_S^K , $\vec{\psi}_S^K$, and \vec{v}_S^K are the stator current, flux, and voltage vectors in the coordinate system K , \vec{i}_R^K , $\vec{\psi}_R^K$, and \vec{v}_R^K are the rotor current, flux, and voltage vectors in the coordinate system K . K is an arbitrary coordinate system which can be chosen as a stationary coordinate system fixed on the stator ($\omega_K = 0$). This coordinate system is usually used in classic DTC, which will be discussed later in this chapter.

Electrical and mechanical equations of IM in (3-17)–(3-21) are applied to determine a state space representation of the model of an IM with the stator and rotor flux components as well as the mechanical speed as state variables. The state space representation of a squirrel-cage IM in the stator fixed stationary coordinate system (α – β) can be formulated as [16]

$$\frac{d}{dt} \begin{bmatrix} \psi_{S,\alpha}^S \\ \psi_{S,\beta}^S \\ \psi_{R,\alpha}^S \\ \psi_{R,\beta}^S \end{bmatrix} = \begin{bmatrix} -R_S/\sigma L_S & 0 & R_S L_M/\sigma L_S L_R & 0 \\ 0 & -R_S/\sigma L_S & 0 & R_S L_M/\sigma L_S L_R \\ R_R L_M/\sigma L_S L_R & 0 & -R_R/\sigma L_R & -Z_P \omega_M \\ 0 & R_R L_M/\sigma L_S L_R & Z_P \omega_M & -R_R/\sigma L_R \end{bmatrix} \begin{bmatrix} \psi_{S,\alpha}^S \\ \psi_{S,\beta}^S \\ \psi_{R,\alpha}^S \\ \psi_{R,\beta}^S \end{bmatrix} + \begin{bmatrix} 1 & 0 \\ 0 & 1 \\ 0 & 0 \\ 0 & 0 \end{bmatrix} \begin{bmatrix} v_{S,\alpha}^S \\ v_{S,\beta}^S \end{bmatrix} \quad (3-22)$$

$$J \frac{d\omega_M}{dt} = T_{em} - T_L = \frac{3}{2} Z_P (\psi_{S,\alpha}^S i_{S,\beta}^S - \psi_{S,\beta}^S i_{S,\alpha}^S) - T_L, \quad (3-23)$$

where

$$\sigma = 1 - \frac{1}{(1 + \sigma_S)(1 + \sigma_R)} = 1 - \frac{L_M^2}{L_S L_R}, \quad (3-24)$$

σ is total leakage factor,

$\psi_{x,\alpha}^S$ and $\psi_{x,\beta}^S$ denote real and imaginary components of the stator ($x = S$) and rotor ($x = R$) flux vectors in the stator fixed coordinate system (axis α fixed on phase a of stator windings),

$v_{x,\alpha}^S$ and $v_{x,\beta}^S$ are real and imaginary components of the stator ($x = S$) and rotor ($x = R$) voltage vectors in the stator fixed coordinate system (axis α fixed on phase a of stator windings),

$i_{x,\alpha}^S$ and $i_{x,\beta}^S$ denote real and imaginary components of stator ($x = S$) and rotor ($x = R$) current vectors in the stator fixed coordinate system (axis α fixed on phase a of stator windings).

Real and imaginary components of the stator and rotor currents can be expressed as functions of the stator and rotor flux as follows:

$$\begin{cases} i_{S,\alpha}^S = \frac{1}{\sigma L_S} \psi_{S,\alpha}^S - \frac{L_M}{\sigma L_S L_R} \psi_{R,\alpha}^S \\ i_{S,\beta}^S = \frac{1}{\sigma L_R} \psi_{S,\beta}^S - \frac{L_M}{\sigma L_S L_R} \psi_{R,\beta}^S \end{cases}, \quad (3-25)$$

$$\begin{cases} i_{R,\alpha}^S = \frac{1}{\sigma L_R} \psi_{R,\alpha}^S - \frac{L_M}{\sigma L_S L_R} \psi_{S,\alpha}^S \\ i_{R,\beta}^S = \frac{1}{\sigma L_R} \psi_{R,\beta}^S - \frac{L_M}{\sigma L_S L_R} \psi_{S,\beta}^S \end{cases}. \quad (3-26)$$

In field orientation, the electrical and mechanical equations of a squirrel-cage IM are projected into a rotating reference frame $\omega_K \neq 0$ [16], [19]. The electromechanical equations of a squirrel-cage IM in an arbitrary rotating coordinate system (d - q), read

$$\frac{d}{dt} \begin{bmatrix} \psi_{S,d}^K \\ \psi_{S,q}^K \\ \psi_{R,d}^K \\ \psi_{S,q}^K \end{bmatrix} = \begin{bmatrix} -R_S/\sigma L_S & \omega_K & R_S L_M/\sigma L_S L_R & 0 \\ -\omega_K & -R_S/\sigma L_S & 0 & R_S L_M/\sigma L_S L_R \\ R_R L_M/\sigma L_S L_R & 0 & -R_R/\sigma L_R & \omega_K - Z_P \omega_M \\ 0 & R_R L_M/\sigma L_S L_R & Z_P \omega_M - \omega_K & -R_R/\sigma L_R \end{bmatrix} \begin{bmatrix} \psi_{S,d}^K \\ \psi_{S,q}^K \\ \psi_{R,d}^K \\ \psi_{S,q}^K \end{bmatrix} + \begin{bmatrix} 1 & 0 \\ 0 & 1 \\ 0 & 0 \\ 0 & 0 \end{bmatrix} \begin{bmatrix} v_{S,d}^K \\ v_{S,q}^K \end{bmatrix} \quad (3-27)$$

$$J \frac{d\omega_M}{dt} = T_{em} - T_L = \frac{3}{2} Z_P \frac{L_M}{L_S} (\psi_{S,q}^K i_{R,d}^K - \psi_{S,d}^K i_{R,q}^K) - T_L, \quad (3-28)$$

where

$\psi_{x,d}^K$ and $\psi_{x,q}^K$ are direct and quadrature components of the stator ($x=S$) and rotor ($x=R$) flux vectors in the rotating coordinate system K ($\omega_K \neq 0$),

$v_{x,d}^K$ and $v_{x,q}^K$ denote direct and quadrature components of the stator ($x=S$) and rotor ($x=R$) voltage vectors in the rotating coordinate system K ,

$i_{x,d}^K$ and $i_{x,q}^K$ are direct and quadrature components of the stator ($x=S$) and rotor ($x=R$) current vectors in the rotating coordinate system K .

Direct (d) and quadrature (q) components of the stator and rotor current vector in the rotating coordinate system K are determined by using the flux components as [16]

$$\begin{cases} i_{S,d}^K = \frac{1}{\sigma L_S} \psi_{S,d}^K - \frac{L_M}{\sigma L_S L_R} \psi_{R,d}^K \\ i_{S,q}^K = \frac{1}{\sigma L_R} \psi_{S,q}^K - \frac{L_M}{\sigma L_S L_R} \psi_{R,q}^K \end{cases}, \quad (3-29)$$

$$\begin{cases} i_{R,d}^K = \frac{1}{\sigma L_R} \psi_{R,d}^K - \frac{L_M}{\sigma L_S L_R} \psi_{S,d}^K \\ i_{R,q}^K = \frac{1}{\sigma L_R} \psi_{R,q}^K - \frac{L_M}{\sigma L_S L_R} \psi_{S,q}^K \end{cases}. \quad (3-30)$$

Stator-flux orientation

In stator flux orientation ($K : \vec{\psi}_S^S$), the d axis of the rotating coordinate system is fixed on the stator flux vector $\vec{\psi}_S^S$. Therefore, $\omega_K = \omega_{\vec{\psi}_S^S}$ where, $\omega_{\vec{\psi}_S^S}$ is the angular frequency of the stator flux vector. Consequently, the direct component of the stator flux vector is equal to the stator flux amplitude $\psi_{S,d}^S = \psi_S$ and the quadrature component of the stator flux vector is zero $\psi_{S,q}^S = 0$. The apex S in $\vec{\psi}_S^S$ denotes that the direct and quadrature components of the stator flux vector are expressed in the rotating reference frame synchronous to the stator flux vector. Moreover, the apex S in $\vec{\psi}_S^S$ denotes that the stator phase a is considered as the reference to determine the stator flux vector angle.

Using (3-28), (3-29), and (3-30), the electromechanical torque can be formulated in terms of the amplitude of the stator flux and the stator current as

$$T_{em} = \frac{3}{2} Z_P \psi_S i_{S,q}^S. \quad (3-31)$$

The variable $i_{S,q}^S$ is the quadrature component of the stator current vector in the stator-flux-oriented coordinate system.

Air gap flux orientation

Air gap flux vector has been determined in the stator fixed coordinate system as presented in the following [16], [19]:

$$\vec{\psi}_g^S = L_M (\vec{i}_S^S + e^{j\rho_M} \vec{i}_R^R). \quad (3-32)$$

Apex S in $\vec{\psi}_g^S$ denotes that the stator winding of phase a is the reference to determine the angle of the air gap flux vector.

In case of air gap flux orientation ($K : \vec{\psi}_g^S$), the real axis of the coordinate system is fixed on the air gap flux vector, $\omega_K = \omega_{\vec{\psi}_g^S}$ which $\omega_{\vec{\psi}_g^S}$ is the angular frequency of the air gap flux vector. Therefore, the real part of the air gap flux vector is equal to the amplitude of air gap flux, $\psi_{g,d}^S = \psi_g$ and the imaginary part of the air gap flux vector is zero $\psi_{g,q}^S = 0$.

According to the stator flux vector expression in (3-9) and the air gap flux vector defined in (3-32), the stator flux can be expressed in terms of air gap flux and stator current vector

$$\vec{\psi}_S^S = \vec{\psi}_g^S + L_{IS} \vec{i}_S^S. \quad (3-33)$$

Using (3-33) and (3-21) the electromechanical torque can be represented in the terms of amplitude of the air gap flux and the stator current as

$$T_{em} = \frac{3}{2} Z_P \psi_g i_{S,q}^S, \quad (3-34)$$

where $i_{S,q}^{\psi_g^S}$ is the quadrature component of the stator current vector in the air gap flux oriented coordinate system.

Rotor flux orientation

In rotor flux orientation, the d axis of the coordinate system is fixed on the rotor flux vector (K : $\vec{\psi}_R^S$) and $\omega_K = \omega_{\vec{\psi}_R^S}$ where, $\omega_{\vec{\psi}_R^S}$ is the angular frequency of the rotor flux vector. The real part of the rotor flux vector equals the amplitude of the rotor flux vector, $\psi_{R,d}^{\psi_R^S} = \psi_R$ and the imaginary part of the rotor flux vector is zero $\psi_{R,q}^{\psi_R^S} = 0$. Apex S in $\vec{\psi}_g^S$ denotes that the stator winding of phase a is the reference to determine the angle of the rotor flux vector.

Considering (3-9) and (3-10), the stator flux vector in a stator fixed coordinate system can be calculated in the terms of the rotor flux vector and the stator current vector as

$$\vec{\psi}_S^S = (L_S - L_M)\vec{i}_S^S + \frac{L_M}{L_R}\vec{\psi}_R^S, \quad (3-35)$$

where $\vec{\psi}_R^S = e^{j\rho_M}\vec{\psi}_R^R$ is the rotor flux vector in the stator fixed stationary coordinate system. Using (3-35) and (3-21), the electromechanical torque is

$$T_{em} = \frac{3}{2}Z_P \frac{L_M}{L_R}\psi_R i_{S,q}^{\psi_R^S} \quad (3-36)$$

where $i_{S,q}^{\psi_R^S}$ denotes the quadrature component of the stator current vector in the rotor-flux-oriented coordinate system.

Equations of the electromechanical torque in (3-31), (3-34), and (3-36) imply that if the flux amplitude is controlled to be constant, the motor torque can be controlled independently using the imaginary component of the stator current. The real and imaginary parts of the stator current in an arbitrary coordinate system K can be determined using the following projection [10], [16], [19]

$$\begin{bmatrix} x_d^K \\ x_q^K \end{bmatrix} = \begin{bmatrix} \cos(\rho_K) & \sin(\rho_K) \\ -\sin(\rho_K) & \cos(\rho_K) \end{bmatrix} \left(\begin{bmatrix} 2/3 & -1/3 & -1/3 \\ 0 & 1/\sqrt{3} & -1/\sqrt{3} \end{bmatrix} \begin{bmatrix} x_a \\ x_b \\ x_c \end{bmatrix} \right), \quad (3-37)$$

where ρ_K is the angle of the vector (e.g. stator, rotor, and air gap flux vector) which is applied to coordinate the reference frame.

As evident from (3-37), the angle of the stator, air gap, and rotor flux vectors are required for the projection into the field-oriented coordinate system. Furthermore, the amplitude of the flux vectors is necessary for the flux control. Estimation of the flux vectors is achieved using the measured variables of the IM such as stator voltages, currents, and rotor speed. These estimation methods are carried out in direct and indirect methods [21]. Direct method [46] applies the stator voltages and currents, while the stator currents and rotor speed are used in the indirect method [53]. Both methods are investigated in the following sections.

3.3.1 Flux vector estimation using stator voltages and currents

The stator voltages and currents can be used to estimate the position and amplitude of the stator, air gap, and rotor flux vector in the stationary coordinate reference frame (α - β) [16], [19], [21]. According to (3-17), the stator flux components in the stator fixed stationary reference frame ($K = S$, $\omega_K = 0$) can be estimated as

$$\widehat{\psi}_{S,\alpha}^S(t) = \int_0^t (v_{S,\alpha}^S(\tau) - R_S i_{S,\alpha}^S(\tau)) d\tau, \quad (3-38)$$

$$\widehat{\psi}_{S,\beta}^S(t) = \int_0^t (v_{S,\beta}^S(\tau) - R_S i_{S,\beta}^S(\tau)) d\tau. \quad (3-39)$$

Using the real and imaginary parts of the estimated stator flux vector, the amplitude $\widehat{\psi}_S$ and rotation angle $\widehat{\rho}_{\widehat{\psi}_S^S}$ of the stator flux vector have been derived to:

$$\widehat{\psi}_S = \sqrt{\widehat{\psi}_{S,\alpha}^S + \widehat{\psi}_{S,\beta}^S}, \quad \widehat{\rho}_{\widehat{\psi}_S^S} = \tan^{-1} \frac{\widehat{\psi}_{S,\beta}^S}{\widehat{\psi}_{S,\alpha}^S}. \quad (3-40)$$

Applying the relationship between the air gap flux and the stator flux presented in (3-35), amplitude $\widehat{\psi}_g$ and angular frequency $\widehat{\rho}_{\widehat{\psi}_g^S}$ of the air gap flux vector can be estimated as

$$\widehat{\psi}_{g,\alpha}^S = -(L_S - L_M) i_{S,\alpha}^S + \widehat{\psi}_{S,\alpha}^S, \quad (3-41)$$

$$\widehat{\psi}_{g,\beta}^S = -(L_S - L_M) i_{S,\beta}^S + \widehat{\psi}_{S,\beta}^S, \quad (3-42)$$

$$\widehat{\psi}_g = \sqrt{\widehat{\psi}_{g,\alpha}^S + \widehat{\psi}_{g,\beta}^S}, \quad \widehat{\rho}_{\widehat{\psi}_g^S} = \tan^{-1} \frac{\widehat{\psi}_{g,\beta}^S}{\widehat{\psi}_{g,\alpha}^S}, \quad (3-43)$$

where $\widehat{\psi}_{g,\alpha}^S$ and $\widehat{\psi}_{g,\beta}^S$ are the estimated real and imaginary components of the air gap flux vector in the stator fixed coordinate system.

In the same way, amplitude $\widehat{\psi}_R$ and angular frequency $\widehat{\rho}_{\widehat{\psi}_R^S}$ of the rotor flux vector are estimated according to (3-35), (3-38), and (3-39) as presented in the following:

$$\widehat{\psi}_{R,\alpha}^S = \frac{\sigma L_S L_R}{L_M} (-i_{S,\alpha}^S + \frac{1}{\sigma L_S} \widehat{\psi}_{S,\alpha}^S), \quad (3-44)$$

$$\widehat{\psi}_{R,\beta}^S = \frac{\sigma L_S L_R}{L_M} (-i_{S,\beta}^S + \frac{1}{\sigma L_S} \widehat{\psi}_{S,\beta}^S), \quad (3-45)$$

$$\widehat{\psi}_R = \sqrt{\widehat{\psi}_{R,\alpha}^S + \widehat{\psi}_{R,\beta}^S}, \quad \widehat{\rho}_{\widehat{\psi}_R^S} = \tan^{-1} \frac{\widehat{\psi}_{R,\beta}^S}{\widehat{\psi}_{R,\alpha}^S}, \quad (3-46)$$

where $\widehat{\psi}_{R,\alpha}^S$ and $\widehat{\psi}_{R,\beta}^S$ denote the estimated real and imaginary components of the rotor flux vector in the stator fixed coordinate system.

Using (3-38)-(3-46), block diagrams of the stator, air gap, and rotor flux estimators based on the measurement of the stator voltages and currents are shown in Fig. 3-3. Obviously, the stator flux estimation is the simplest one. Other estimators, especially the rotor flux vector estimator, depend strongly on the machine parameters. In implementation, the stator voltages can be calculated applying measured dc-link voltage and the converter gate signals [47], [21].

3.3.2 Flux vector estimation using stator currents and rotor speed

Stator currents and mechanical speed can be used to estimate the flux vectors (stator, air gap, and rotor). In this method, flux vector is determined indirectly from the stator current dynamics. For the stator flux orientation, the stator current dynamics can be described as below using the electromechanical equations of an induction machine [55]:

$$\frac{d}{dt} \begin{bmatrix} i_{S,d}^S \\ i_{S,q}^S \end{bmatrix} = \begin{bmatrix} -1/\sigma\tau_R & \omega_{sl} \\ -\omega_{sl} & -1/\sigma\tau_R \end{bmatrix} \begin{bmatrix} i_{S,d}^S \\ i_{S,q}^S \end{bmatrix} + \frac{1}{\sigma\tau_R L_S} \begin{bmatrix} \psi_S + \tau_R \frac{d\psi_S}{dt} \\ \tau_R \omega_{sl} \psi_S \end{bmatrix}, \quad (3-47)$$

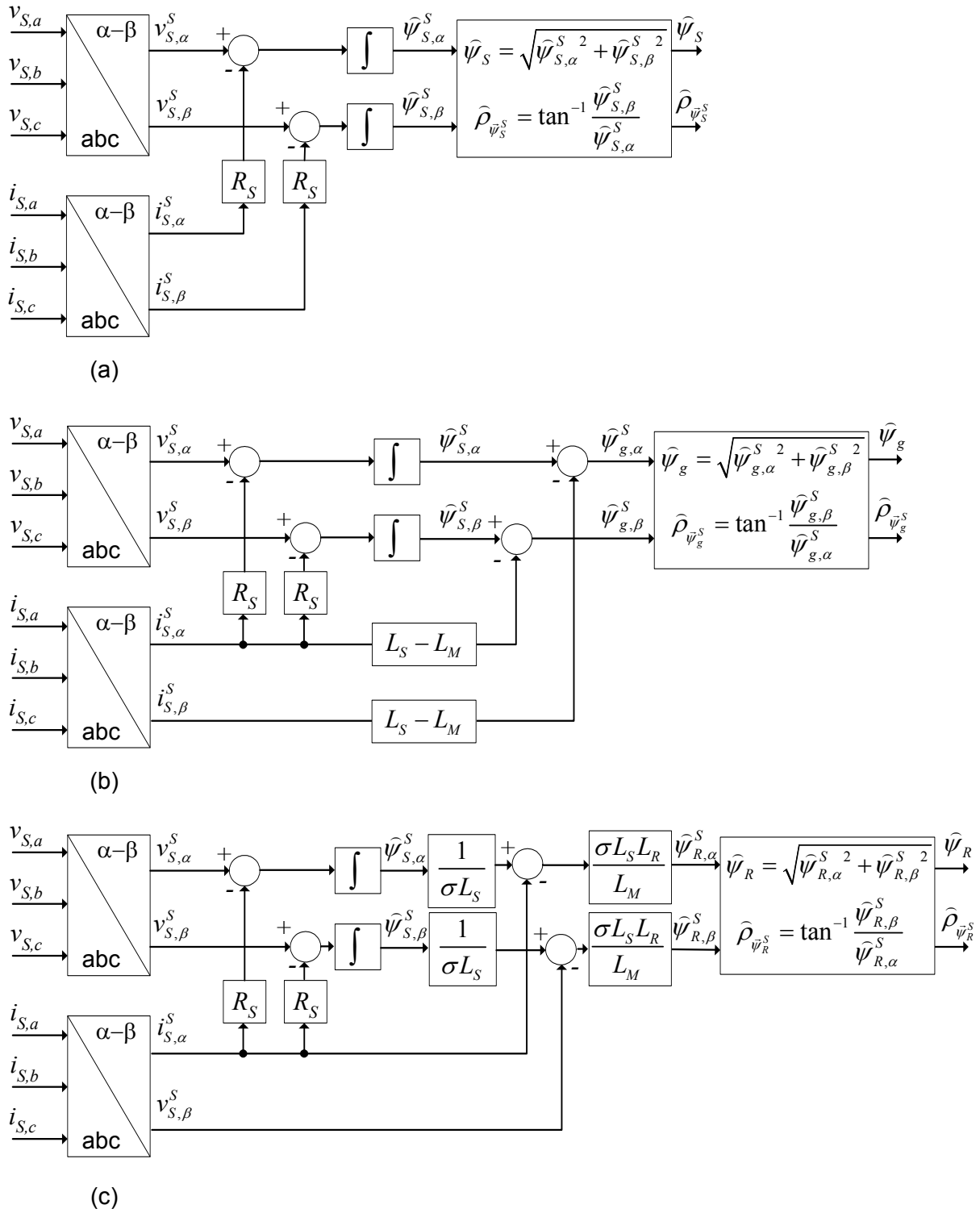


Fig. 3-3 Block diagram of flux vector estimators (flux models) in stator-fixed stationary coordinate system (α - β): (a) stator flux; (b) air gap flux; (c) rotor flux

Using (3-47) the stator flux amplitude in s -domain and the corresponding rotation angle are determined as:

$$\widehat{\psi}_S = \frac{L_S}{1 + s\tau_R} \left[i_{S,d}^S (1 + s\sigma\tau_R) - \widehat{\omega}_{sl} \sigma\tau_R i_{S,q}^S \right], \quad (3-48)$$

$$\widehat{\omega}_{sl} = \widehat{\omega}_{\widehat{\psi}_s^s} - Z_P \omega_M = \frac{i_{S,q}^{\widehat{\psi}_s^s} (1 + s\sigma\tau_R)}{\widehat{\psi}_s \tau_R / L_S - \sigma\tau_R i_{S,d}^{\widehat{\psi}_s^s}}, \quad \tau_R = \frac{L_R}{R_R}, \quad (3-49)$$

$$\widehat{\rho}_{\widehat{\psi}_s^s}(t) = \int_0^t (Z_P \omega_M(\tau) + \widehat{\omega}_{sl}(\tau)) d\tau. \quad (3-50)$$

where $\widehat{\omega}_{sl}$ is the estimated slip angular frequency and τ_R denotes the rotor time constant. Equations (3-48) - (3-50) are the stator flux model of an induction machine based on the stator currents and the rotor speed. A block diagram of this flux model is shown in Fig. 3-4 (a).

In the same way, the following stator current dynamics in the air-gap-flux-oriented coordinate system and the rotor speed are applied to estimate the air gap flux vector [55]

$$\frac{d}{dt} \begin{bmatrix} i_{S,d}^{\widehat{\psi}_g^s} \\ i_{S,q}^{\widehat{\psi}_g^s} \end{bmatrix} = \begin{bmatrix} -1/\tau_{Rl} & \omega_{sl} \\ -\omega_{sl} & -1/\tau_{Rl} \end{bmatrix} \begin{bmatrix} i_{S,d}^{\widehat{\psi}_g^s} \\ i_{S,q}^{\widehat{\psi}_g^s} \end{bmatrix} + \frac{1}{\tau_{Rl} L_M} \begin{bmatrix} \psi_g + \tau_R \frac{d\psi_g}{dt} \\ \tau_R \omega_{sl} \psi_g \end{bmatrix}. \quad (3-51)$$

The estimated amplitude of the air gap flux in s -domain and the corresponding angle are

$$\widehat{\psi}_g = \frac{L_M}{1 + s\tau_R} \left[i_{S,d}^{\widehat{\psi}_g^s} (1 + s\tau_{Rl}) - \widehat{\omega}_{sl} \tau_{Rl} i_{S,q}^{\widehat{\psi}_g^s} \right], \quad (3-52)$$

$$\widehat{\omega}_{sl} = \widehat{\omega}_{\widehat{\psi}_g^s} - Z_P \omega_M = \frac{i_{S,q}^{\widehat{\psi}_g^s} (1 + \tau_{Rl} \frac{d i_{S,q}^{\widehat{\psi}_g^s} / dt)}{\widehat{\psi}_g \tau_R / L_M - \tau_{Rl} i_{S,d}^{\widehat{\psi}_g^s}}, \quad \tau_{Rl} = \frac{L_{Rl}}{R_R}, \quad (3-53)$$

$$\widehat{\rho}_{\widehat{\psi}_g^s}(t) = \int_0^t (Z_P \omega_M(\tau) + \widehat{\omega}_{sl}(\tau)) d\tau, \quad (3-54)$$

where τ_{Rl} expresses the rotor transient time constant [19]. Structure of the corresponding air gap flux model is given in Fig. 3-4 (b).

Direct and quadrature components of the stator currents in the rotor-flux-oriented coordinate system are as follows [10], [19], [55]:

$$\begin{bmatrix} i_{S,d}^{\widehat{\psi}_R^s} \\ i_{S,q}^{\widehat{\psi}_R^s} \end{bmatrix} = \frac{1}{L_M} \begin{bmatrix} \psi_R + \tau_R \frac{d\psi_R}{dt} \\ \tau_R \omega_{sl} \psi_R \end{bmatrix} \quad (3-55)$$

Using (3-55), the estimated amplitude of the rotor flux vector in s -domain and the corresponding rotation angle are

$$\widehat{\psi}_R = \frac{L_M}{1 + s\tau_R} i_{S,d}^{\widehat{\psi}_R^s}, \quad (3-56)$$

$$\widehat{\omega}_{sl} = \widehat{\omega}_{\widehat{\psi}_R^s} - Z_P \omega_M = \frac{L_M}{\tau_R \widehat{\psi}_R} i_{S,q}^{\widehat{\psi}_R^s}, \quad (3-57)$$

$$\widehat{\rho}_{\widehat{\psi}_R^s}(t) = \int_0^t (Z_P \omega_M(\tau) + \widehat{\omega}_{sl}(\tau)) d\tau. \quad (3-58)$$

A block diagram of this rotor flux estimator is shown in Fig. 3-4 (c). Comparing the three flux estimators presented in Fig. 3-4, it is evident that the rotor flux estimator has the simplest structure if the stator currents and the rotor speed are available for the flux estimation.

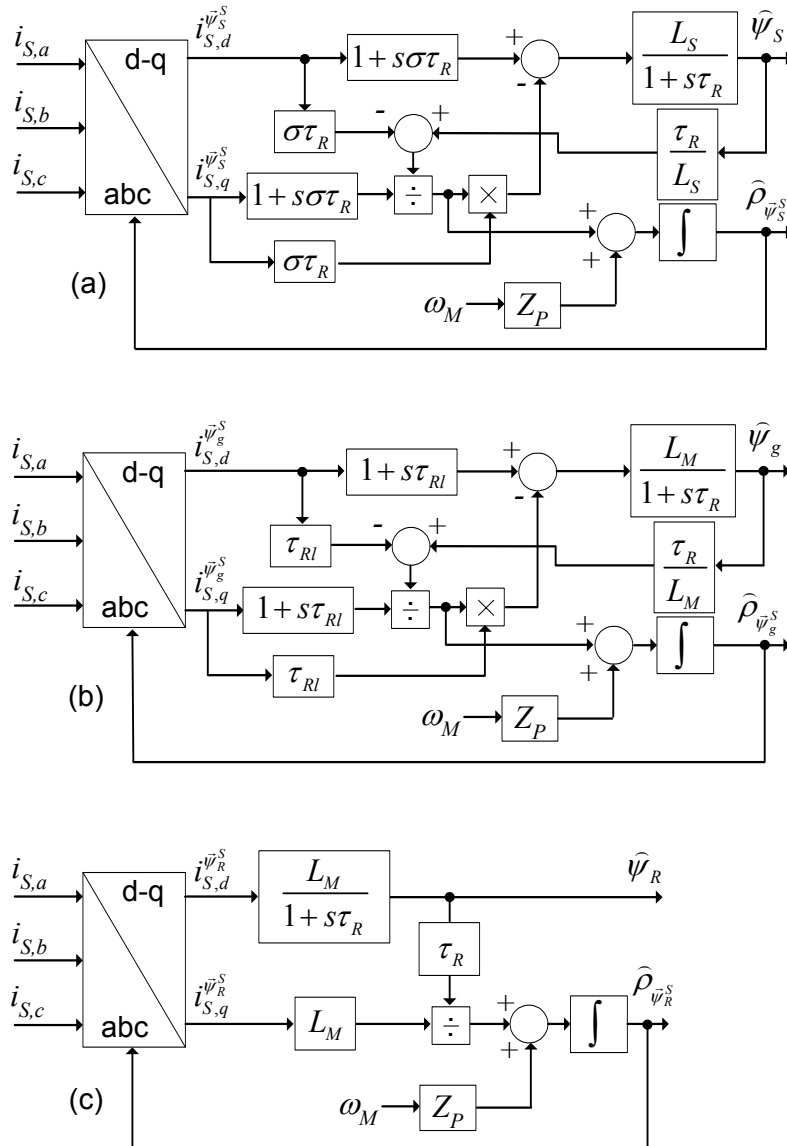


Fig. 3-4 Block diagram of flux vector estimators (flux models) in rotating coordinate system (d - q): (a) stator flux; (b) air gap flux; (c) rotor flux

The main advantage of the rotor flux estimator is that there is no requirement for derivatives in the estimator structure. Because of this, the rotor flux orientation is usually applied in the FOC of the IMs with stator currents and rotor speed measurement [10].

3.4 Field-oriented control of induction machines

The main idea of the FOC is the separate control of flux and torque of an IM similar to the control principles of a DC machine. For this propose, the mathematical model of an IM in a rotating coordinate system synchronized to the stator, air gap, or rotor flux vector is applied. All voltages and currents of IM are projected into the rotating coordinate system using the projection defined in (3-37). In steady-state, ac voltages and currents are dc signals in the rotating coordinate system and controllers like PI-regulators can be used to control flux and torque.

If the estimated stator flux vector angle $\hat{\rho}_{\vec{\psi}_S}$ is used for the projection in (3-37) and the amplitude of the stator flux and the electromechanical torque are the variables to be controlled, the control strategy is named stator-flux-oriented control (SFOC). In the same way, if the estimated air gap magnetizing flux angle $\hat{\rho}_{\vec{\psi}_g}$ is used in the projection and the air gap flux and the torque are controlled, the control method is termed air gap magnetizing-flux-oriented control (MFOC). Finally, in rotor-flux-oriented control (RFOC), the estimated rotor flux vector angle $\hat{\rho}_{\vec{\psi}_R}$ is used for the required projection in (3-37) and the rotor flux and the electromechanical torque are the controlled variables [10], [16], [19]. Flux vectors of the stator, air gap, and rotor for induction motor ($\delta > 0$) and induction generator ($\delta < 0$) operation are presented in Fig. 3-5(a) and Fig. 3-5(b), respectively. The stator and the rotor leakage flux cause differences between the flux vectors. The torque angle is denoted by δ .

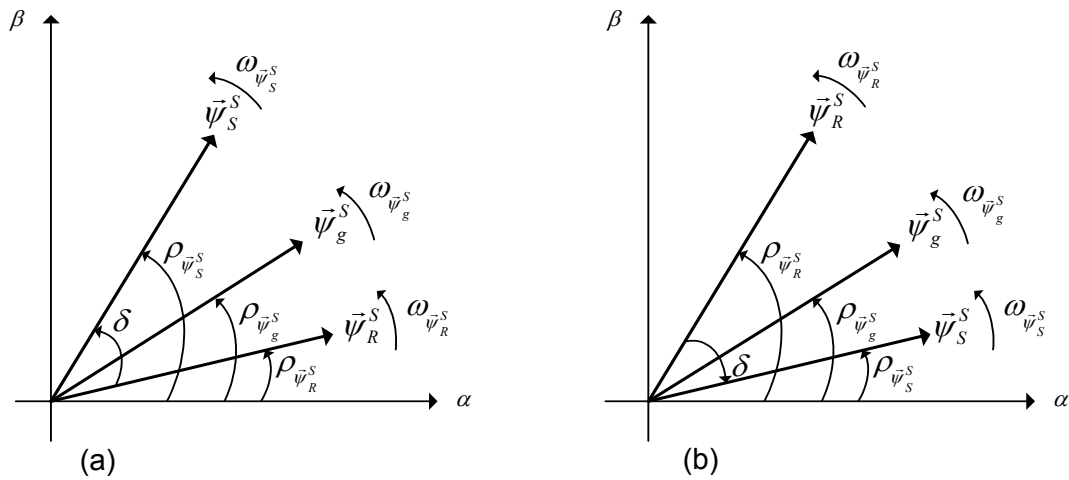


Fig. 3-5 Stator, air gap, and rotor flux vectors of an induction machine in the stator fixed stationary reference frame (α - β): (a) induction motor ($\delta > 0$); (b) induction generator ($\delta < 0$)

3.4.1 Comparison of SFOC, MFOC, and RFOC

In a comparison among SFOC, MFOC, and RFOC, it is assumed that the IM is fed by a VSC. Then the required flux estimator, stator current dynamics, required decoupling terms, and steady-state characteristic of the three vector control methods are compared.

In case that the stator voltages and the stator currents are measured, the stator flux model has the simplest structure as shown in Fig. 3-3. Furthermore, the stator flux model requires just the stator resistance value whereas the models of the air gap flux and the rotor flux contain further machine parameters like the main inductance. If the stator currents and the rotor mechanical speed are used to estimate the flux vector, the rotor flux observer is the simplest one as depicted in Fig. 3-4. However, the main inductance and the rotor time constant are required as parameters of the rotor flux estimator.

Assuming that the IM is fed by a VSC, it is necessary to use the stator voltage equations to acquire the required reference voltages for the modulator of the converter. The voltage equations expressed in the stator-flux-oriented reference frame are [19]

$$R_S i_{S,d}^{\bar{\psi}_g^S} = v_{S,d}^{\bar{\psi}_g^S} - \frac{d\psi_S}{dt}, \quad (3-59)$$

$$R_S i_{S,q}^{\bar{\psi}_g^S} = v_{S,q}^{\bar{\psi}_g^S} - \omega_{\bar{\psi}_g^S} \psi_S. \quad (3-60)$$

In the case of SFOC, the stator voltage equations become simple because there is no separate stator leakage voltage component.

Obviously, the first equation (3-59) can be used to control the stator flux. With a constant stator flux, equation (3-60) and the expression of the motor torque in (3-31) can be used to control the electromechanical torque and the rotor speed. The combination of the stator voltage equation of (3-60) and the stator flux observer presented in Fig. 3-3 (a) leads to a simple direct SFOC [21], [56], [66], [70],[79], [80].

Stator voltage equations represented in the magnetizing flux reference frame are given by [55]

$$\begin{cases} L_{IS} \frac{di_{S,d}^{\bar{\psi}_g^S}}{dt} + R_S i_{S,d}^{\bar{\psi}_g^S} = v_{S,d}^{\bar{\psi}_g^S} + \omega_{\bar{\psi}_g^S} L_{IS} i_{S,q}^{\bar{\psi}_g^S} - \frac{d\psi_g}{dt} \\ L_{IS} \frac{di_{S,q}^{\bar{\psi}_g^S}}{dt} + R_S i_{S,q}^{\bar{\psi}_g^S} = v_{S,q}^{\bar{\psi}_g^S} - \omega_{\bar{\psi}_g^S} (L_{IS} i_{S,d}^{\bar{\psi}_g^S} - \psi_g) \end{cases}. \quad (3-61)$$

Obviously, the stator voltage equations are more complicated in the magnetizing-flux-oriented coordinates due to the stator leakage inductance. If PI controllers are used to control the stator currents, appropriate decoupling terms ($v_{S,d,decoupling}^{\bar{\psi}_g^S}$ and $v_{S,q,decoupling}^{\bar{\psi}_g^S}$) should be added to the output of the current controllers ($v_{S,d,control}^{\bar{\psi}_g^S}$ and $v_{S,q,control}^{\bar{\psi}_g^S}$) as follows:

$$\begin{cases} v_{S,d}^{\bar{\psi}_g^S} = v_{S,d,decoupling}^{\bar{\psi}_g^S} + v_{S,d,control}^{\bar{\psi}_g^S}, \quad v_{S,d,decoupling}^{\bar{\psi}_g^S} = -\hat{\omega}_{\bar{\psi}_g^S} L_{IS} i_{S,q}^{\bar{\psi}_g^S} + \frac{d\hat{\psi}_g}{dt} \\ v_{S,q}^{\bar{\psi}_g^S} = v_{S,q,decoupling}^{\bar{\psi}_g^S} + v_{S,q,control}^{\bar{\psi}_g^S}, \quad v_{S,q,decoupling}^{\bar{\psi}_g^S} = \hat{\omega}_{\bar{\psi}_g^S} (L_{IS} i_{S,d}^{\bar{\psi}_g^S} - \hat{\psi}_g) \end{cases}. \quad (3-62)$$

Applying the decoupling terms in (3-62), the stator voltage equations are simplified to the following first order system

$$\frac{d}{dt} \begin{bmatrix} i_{S,d}^{\bar{\psi}_g^S} \\ i_{S,q}^{\bar{\psi}_g^S} \end{bmatrix} = \begin{bmatrix} -\frac{R_S}{L_{IS}} & 0 \\ 0 & -\frac{R_S}{L_{IS}} \end{bmatrix} \begin{bmatrix} i_{S,d}^{\bar{\psi}_g^S} \\ i_{S,q}^{\bar{\psi}_g^S} \end{bmatrix} + \begin{bmatrix} \frac{1}{L_{IS}} & 0 \\ 0 & \frac{1}{L_{IS}} \end{bmatrix} \begin{bmatrix} v_{S,d,control}^{\bar{\psi}_g^S} \\ v_{S,q,control}^{\bar{\psi}_g^S} \end{bmatrix}. \quad (3-63)$$

Magnetizing flux models presented in Fig. 3-3 (b) and Fig. 3-4 (b) can be used to realize direct SFOC and indirect SFOC by applying (3-61)–(3-63).

In the rotor-flux-oriented coordinate system, the stator voltage equations are [19], [55]

$$\begin{cases} \sigma L_S \frac{di_{S,d}^{\bar{\psi}_R^S}}{dt} + R_S i_{S,d}^{\bar{\psi}_R^S} = v_{S,d}^{\bar{\psi}_R^S} + \omega_{\bar{\psi}_R^S} \sigma L_S i_{S,q}^{\bar{\psi}_R^S} - (1-\sigma) \frac{L_S}{L_M} \frac{d\psi_R}{dt} \\ \sigma L_S \frac{di_{S,q}^{\bar{\psi}_R^S}}{dt} + R_S i_{S,q}^{\bar{\psi}_R^S} = v_{S,q}^{\bar{\psi}_R^S} - \omega_{\bar{\psi}_R^S} \sigma L_S i_{S,d}^{\bar{\psi}_R^S} - (1-\sigma) \frac{L_S}{L_M} \omega_{\bar{\psi}_R^S} \psi_R \end{cases}. \quad (3-64)$$

The following decoupling terms ($v_{S,d,decoupling}^{\bar{\psi}_R^S}$ and $v_{S,q,decoupling}^{\bar{\psi}_R^S}$) should be added to the output of current PI controllers ($v_{S,d,control}^{\bar{\psi}_R^S}$ and $v_{S,q,control}^{\bar{\psi}_R^S}$) to simplify the stator voltage equations to a first order system as follows

$$\left\{ \begin{array}{l} \mathbf{v}_{S,d}^{\bar{\psi}_R^S} = \mathbf{v}_{S,d,decoupling}^{\bar{\psi}_R^S} + \mathbf{v}_{S,d,control}^{\bar{\psi}_R^S}, \quad \mathbf{v}_{S,d,decoupling}^{\bar{\psi}_R^S} = -\hat{\omega}_{\bar{\psi}_R^S} \sigma L_S \mathbf{i}_{S,q}^{\bar{\psi}_R^S} + (1-\sigma) \frac{L_S}{L_M} \frac{d\hat{\psi}_R}{dt} \\ \mathbf{v}_{S,q}^{\bar{\psi}_R^S} = \mathbf{v}_{S,q,decoupling}^{\bar{\psi}_R^S} + \mathbf{v}_{S,q,control}^{\bar{\psi}_R^S}, \quad \mathbf{v}_{S,q,decoupling}^{\bar{\psi}_R^S} = \hat{\omega}_{\bar{\psi}_R^S} \sigma L_S \mathbf{i}_{S,d}^{\bar{\psi}_R^S} + (1-\sigma) \frac{L_S}{L_M} \hat{\omega}_{\bar{\psi}_R^S} \hat{\psi}_R \end{array} \right. , \quad (3-65)$$

$$\Rightarrow \frac{d}{dt} \begin{bmatrix} \mathbf{i}_{S,d}^{\bar{\psi}_R^S} \\ \mathbf{i}_{S,q}^{\bar{\psi}_R^S} \end{bmatrix} = \begin{bmatrix} -\frac{R_S}{\sigma L_S} & 0 \\ 0 & -\frac{R_S}{\sigma L_S} \end{bmatrix} \begin{bmatrix} \mathbf{i}_{S,d}^{\bar{\psi}_R^S} \\ \mathbf{i}_{S,q}^{\bar{\psi}_R^S} \end{bmatrix} + \begin{bmatrix} \frac{1}{\sigma L_S} & 0 \\ 0 & \frac{1}{\sigma L_S} \end{bmatrix} \begin{bmatrix} \mathbf{v}_{S,d,control}^{\bar{\psi}_R^S} \\ \mathbf{v}_{S,q,control}^{\bar{\psi}_R^S} \end{bmatrix}. \quad (3-66)$$

The stator current dynamics of (3-66) and the rotor flux observers depicted in Fig. 3-3 (c) and Fig. 3-4 (c) can be used to realize direct RFOC and indirect RFOC. Indirect RFOC with stator current control using (3-66) and applying Fig. 3-4 (c) as flux estimator is a common control strategy for IMs [10], [19].

Obviously, stator voltage equations in the stator-flux-oriented coordinate system are less complicated compared to those of the magnetizing-flux-oriented coordinate and the rotor-flux-oriented coordinate system. Furthermore, complex decoupling terms are required for independent control of direct and quadrature components of the stator currents in the cases of MFOC and RFOC. As mentioned before, the direct SFOC with flux observer depicted in Fig. 3-3 (a) is interesting because of its simplicity. However, the stator voltages are required for a direct estimation of the stator flux vector. Indirect RFOC is a more complicated control structure compared to direct SFOC. The main advantage of the indirect RFOC is that there is no requirement for the stator voltages. However, deviation of the rotor time constant leads to a detuned flux model.

The steady-state characteristics (torque versus slip frequency) are different for the control strategies of SFOC, MFOC, and RFOC [55]. The steady-state characteristic of the SFOC is derived using (3-31) and (3-47) as given in the following equation

$$T_{em} = \frac{3}{2} Z_P \frac{\tau_R (1-\sigma)}{L_S} \psi_S^2 \frac{\omega_{sl}}{\sigma^2 \tau_R^2 \omega_{sl}^2 + 1}. \quad (3-67)$$

The torque equation in (3-67) has an extreme which corresponds to the maximum pull-out torque in the SFOC and is given by

$$\frac{dT_{em}}{d\omega_{sl}} = 0 \Rightarrow T_{em,max} = \pm \frac{3}{4} Z_P \left(\frac{L_M}{L_R} \right)^2 \frac{\psi_S^2}{\sigma L_R} \quad \text{at} \quad \omega_{sl,max} = \pm \frac{1}{\sigma \tau_R}. \quad (3-68)$$

In the case of MFOC, the steady-state characteristic is determined using (3-34) and (3-51)

$$T_{em} = \frac{3}{2} Z_P \frac{\psi_g^2}{R_R} \frac{\omega_{sl}}{\tau_{Rl}^2 \omega_{sl}^2 + 1}. \quad (3-69)$$

The maximum pull-out torque in the MFOC related to the extreme point of the steady-state torque equation (3-69) is expressed as:

$$T_{em,max} = \pm \frac{3}{4} Z_P \frac{\psi_g^2}{L_{Rl}} \quad \text{at} \quad \omega_{sl,max} = \pm \frac{1}{\tau_{Rl}}. \quad (3-70)$$

The steady-state relationship between the electromechanical torque and the slip frequency for the RFOC strategy can be derived as follows using (3-36) and (3-55)

$$T_{em} = \frac{3}{2} Z_p \frac{\psi_R^2}{R_R} \omega_{sl} \quad (3-71)$$

Clearly, the electromechanical torque is proportional to the slip frequency and theoretically there is no pull-out torque for a rotor-flux-oriented controlled IM.

Fig. 3-6 shows the steady-state torque versus slip frequency characteristics for SFOC, MFOC, and RFOC for the exemplary HSIM with parameters presented in Table 3.1. Amplitudes of the stator flux, the air gap flux, and the rotor flux are equal to the nominal values.

In RFOC, the electromechanical torque is directly proportional to slip frequency at constant flux operation (Fig. 3-6 (a)) while in SFOC and MFOC there is a nonlinear relationship between electromechanical torque and slip frequency (Fig. 3-6 (b) and (c)). The torque-slip characteristic of the HSIM at nominal voltage ($V_{s,II} = 400$ V) and nominal stator frequency ($f_{0M} = 500$ Hz) is shown in Fig. 3-6 (d) which conforms to the characteristics of the SFOC.

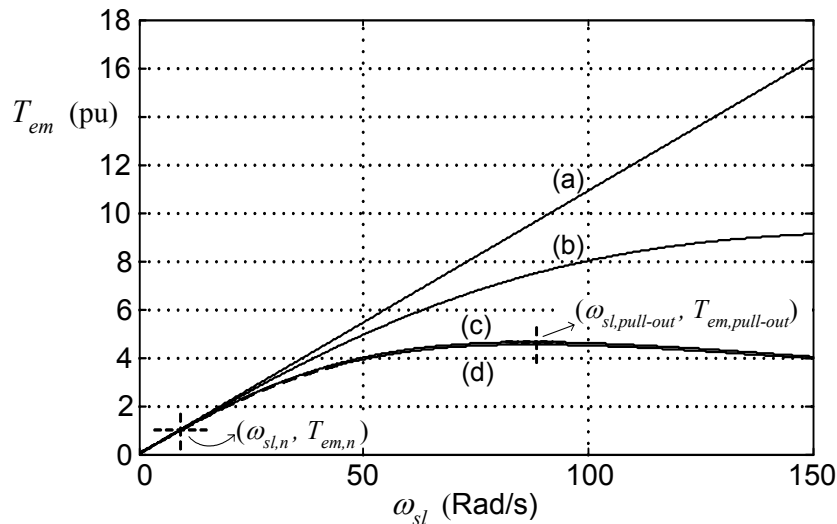


Fig. 3-6 Steady-state characteristic (torque versus slip frequency) of the exemplary high-speed induction machine: (a) RFOC; (b) MFOC; (c) SFOC; (d) torque-slip characteristic of the HSIM at stator nominal voltage ($V_{s,II} = 400$ V) and nominal frequency ($f_{0M} = 500$ Hz)

Obviously, at a slip frequency above the nominal slip frequency, the RFOC generates a higher torque compared to the SFOC and MFOC if an appropriate dc-link voltage reserve (e.g. 10% - 20%) is available. Furthermore, in RFOC, it is possible to produce considerably large torques (e.g. 6 pu) at low speeds (e.g. 0.1 pu) for a short period considering thermal limitations. However, it should be noted that independent of the control strategy there are physical limitations for the electromechanical torque, due to the limited amplitude of the dc-link voltage, thermal, and mechanical limitations [6], [72].

The fastest torque response can be achieved in the RFOC since the electromechanical torque is directly proportional to the slip frequency at constant flux operation, especially in decoupling control [55]. A brief comparison between the SFOC, MFOC, and RFOC is summarized in Table 3.3.

Table 3.3
Comparison of SFOC, MFOC, and RFOC

Control strategy	SFOC		MFOC		RFOC	
	direct	indirect	direct	indirect	direct	indirect
Flux estimator	simple	complex	moderate	complex	complex	simple
Required measurements for speed control	v_s, i_s, ω_M	i_s, ω_M	v_s, i_s, ω_M	i_s, ω_M	v_s, i_s, ω_M	i_s, ω_M
Required machine parameters	R_S	R_S, R_R, L_S, L_R, L_M	R_S, L_S, L_M	R_S, R_R, L_S, L_R, L_M	R_S, L_S, L_R, L_M	R_S, R_R, L_S, L_R, L_M
Stator voltage equations	simple		moderate		moderate	
Decoupling circuit	simple		moderate		moderate	
Steady-state torque-slip characteristic	nonlinear		nonlinear		linear	
Pull-out torque	×		×		—	

Indirect RFOC is the most common control strategy of IMs due to features such as relative simple structure, no requirement to measure the stator voltage, and linear torque-slip characteristic at steady-state. Therefore, the indirect RFOC is applied as the control strategy of the exemplary HSIM.

3.4.2 Indirect RFOC with PI current and speed controllers

A block diagram of the indirect RFOC for the exemplary HSIM with current, rotor flux, and speed control loops is shown in Fig. 3-7. The rotor flux observer constituted by (3-56) and shown in Fig. 3-4 (c) is used to estimate the rotor flux vector. The machine is fed by a

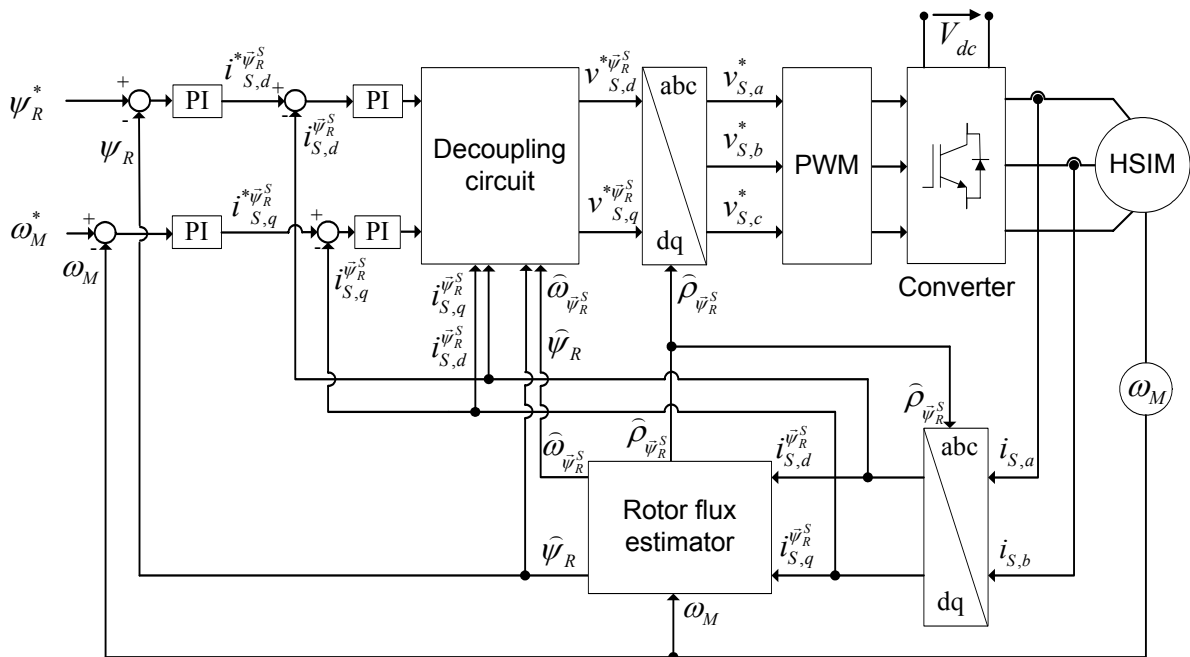


Fig. 3-7 A block scheme of the indirect RFOC

2L VSC with dc voltage link. PWM is applied as modulation strategy and the basic parameters of the converter are given in Table 3.2. All reference values are shown by an apex of *.

Stator voltage equations in (3-64) and PI-controllers are used to control the direct and quadrature components of the stator current. Decoupling terms in (3-65) are used in the decoupling circuit. In case of constant rotor flux ($d\psi_R/dt = 0$), the decoupling circuit shown in Fig. 3-8 can be applied. Thanks to the decoupling circuit, the stator voltage equations become a simple first order system as shown in (3-66).

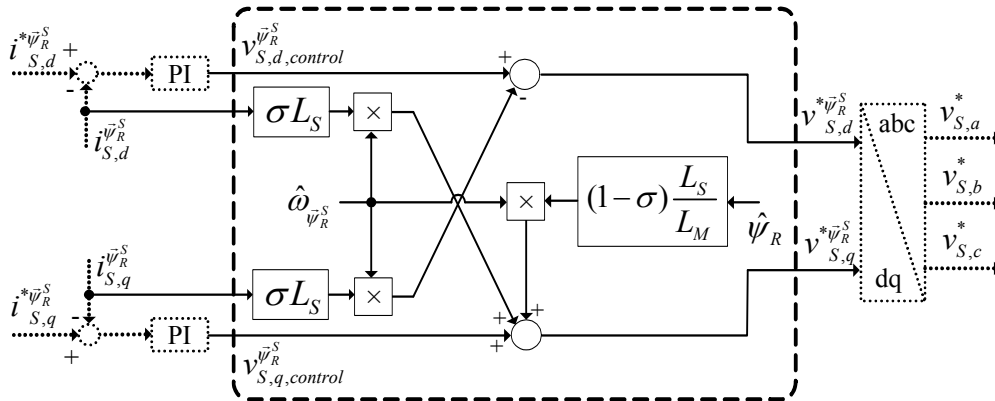


Fig. 3-8 Decoupling circuit to obtain a decoupled current control in the indirect RFOC

The indirect RFOC structure comprises an internal current control loop. Therefore, the performance of the control system strongly depends on the performance of the current control loop. PWM converters with current control loop have the following advantages compared to open loop PWM converters [8]:

- Excellent dynamic performance
- Peak current limitation
- Overload protection
- Compensation of machine parameter changes, semiconductor voltage drop, and variations of dc-link voltage

The current control loop in indirect RFOC comprises the stator current dynamics (3-66), the converter including PWM, and the current controller. Semiconductors are modeled as ideal switches (dead time = 0, $du/dt = \infty$) [2].

PWM [7], [13] :

The most straightforward modulation strategy is the natural sampled PWM. In the natural sampled modulation, low-frequency reference waveforms (e.g. three sinusoidal waveforms) are compared with a carrier waveform (e.g. triangle). This modulation is usually termed sinus-triangle modulation. If the reference signal is greater than the carrier signal, the phase leg is connected to the positive bus of the dc-link and to the negative bus of the dc-link if the carrier waveform is greater than the reference signal. The natural sinus-triangle modulation and converter output voltage (e.g. v_{aMCNP} in Fig. 3-1) are shown in Fig. 3-9 (a) and (b), respectively. The dc-link midpoint in Fig. 3-1 is considered to be the reference point.

Due to the limitations in the implementation of the natural sampled PWM in a digital control

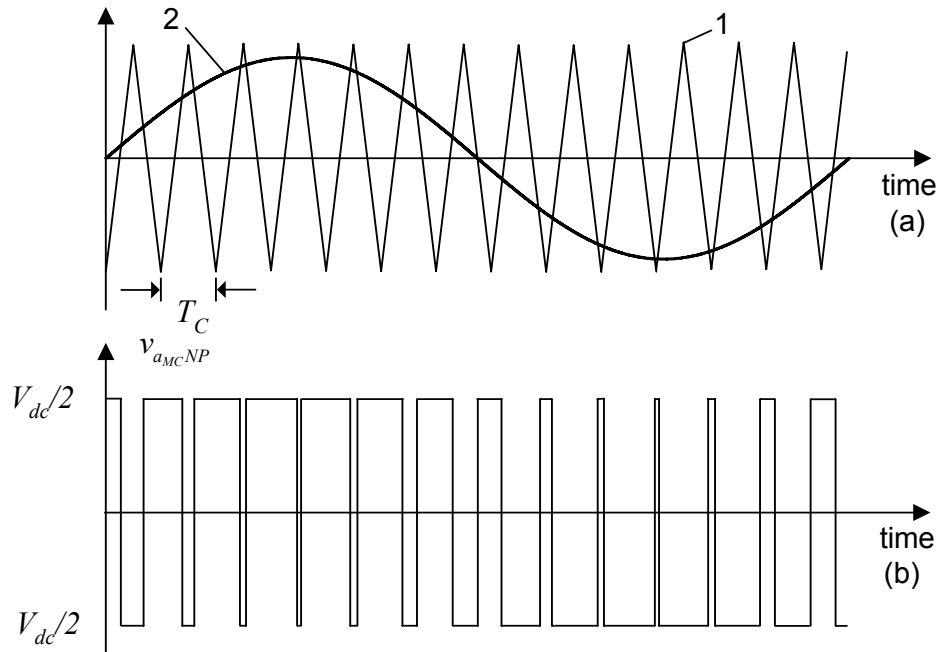


Fig. 3-9 (a) Natural sinus-triangle PWM (1: carrier waveform, 2: reference waveform), (b) converter output voltage (reference point is the dc-link midpoint)

system, regular sampled PWM as a state-of-the-art alternative is usually used [7]. In regular sampled PWM, the reference waveforms are sampled and held constant during the carrier period. Then these sampled references are compared with the carrier signal (Fig. 3-10). Depending on the sampling strategy, the sampling process must take place at either the positive Fig. 3-10 (a) or at both positive and negative peaks of the carrier waveform Fig. 3-10 (b). If the sampling occurs at the positive peak of the carrier signal, the sampling strategy is termed symmetrical sampling. If the reference signals are sampled at both positive and negative peaks of the carrier signal, the sampling strategy is called asymmetrical sampling [7]. The time interval $T_{s,cc}$ between two successive sampling is called sampling time. A PWM block is located in the current control loop (Fig. 3-7); therefore, the PWM and the current control loop have the same sampling time of $T_{s,cc}$.

The sampled reference signal can be approximated by an average signal. Obviously, the average signal lags the original signal by $T_{s,cc} / 2$ (Fig. 3-10). In the symmetrical sampling strategy, the phase delay of the sampled signal is one-half the carrier interval, while for the asymmetrical sampling this phase delay is reduced to one-quarter of the carrier period. The sampling time $T_{s,cc}$ and the phase delay of sampled signal $T_{d,PWM}$ for a symmetrical sampling strategy in proportion to the carrier period are as follows:

$$T_{s,cc} = T_C, T_{d,PWM} = \frac{T_C}{2}. \quad (3-72)$$

In the case of asymmetrical sampled strategy, the sampling time and the phase delay are related to the carrier interval as given below:

$$T_{s,cc} = \frac{T_C}{2}, T_{d,PWM} = \frac{T_C}{4}. \quad (3-73)$$

The phase delay due to the regular sampling can be approximated by a first order delay in the

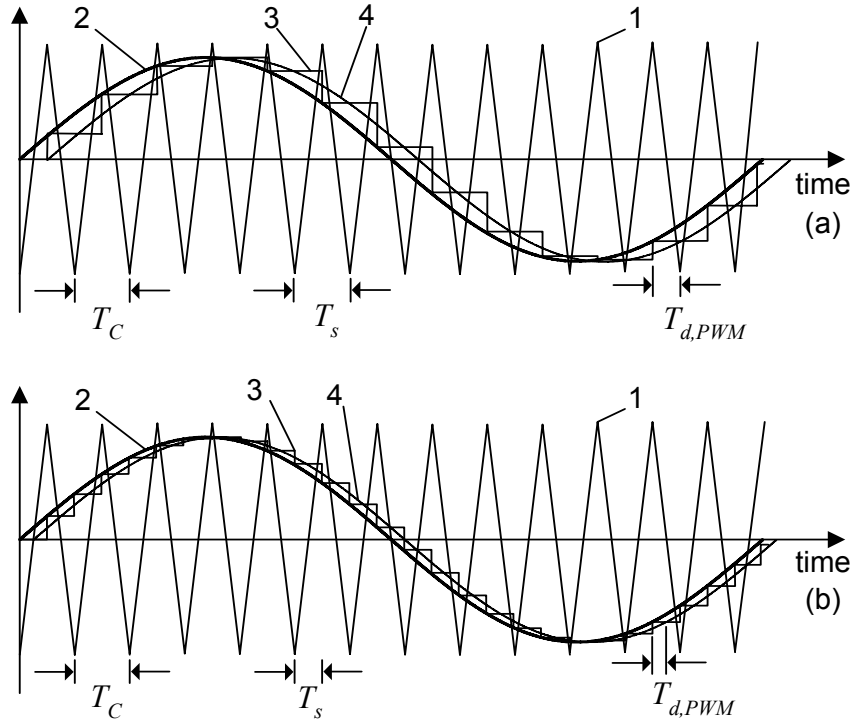


Fig. 3-10 (a) Symmetrical regular sampled PWM, (b) Asymmetrical regular sampled PWM (1: carrier waveform, 2: original reference signal, 3: sampled reference signal, 4: average signal of the sampled waveform)

current control loop. Therefore, the power converter can be modelled as a first order transfer function

$$G_{d,pwm} = K_{PWM} e^{-sT_{d,PWM}} \approx \frac{K_{PWM}}{1+sT_{d,PWM}} = \frac{K_{PWM}}{1+0.5sT_{s,cc}}, \quad (3-74)$$

where K_{PWM} is the gain of the power converter [8].

The processing time $T_{\mu p}$ which is required for the execution of the control algorithm should be considered in the current control loop, too. The maximum processing time equals one sampling time [8] and is approximated by

$$G_{\mu p} = e^{-sT_{\mu p}} \approx \frac{1}{1+sT_{\mu p}} = \frac{1}{1+sT_{s,cc}}. \quad (3-75)$$

Current control loop [8], [54], [60], [63], [67], [76],

In a simple classification, converter current controllers can be categorized into hysteresis controllers and modulator based current controllers. Hysteresis current controllers have simple structures but cause varying switching frequency [63]. In contrast to the hysteresis current controllers, modulator based current controllers (e.g. PWM current controllers) generate constant switching frequency with a definite harmonic spectrum [13].

Modulator based current controllers are classified into linear controllers (e.g. PI controllers) and nonlinear controllers (e.g. artificial neural network based controllers [18]). PI current

controllers are the most common controllers because they have simple structure and are easy to design. Transfer function of a PI controller is

$$G_{PI}(s) = K_p \frac{1 + sT_i}{sT_i} = K_p + \frac{K_i}{s}, \quad K_i = \frac{K_p}{T_i}, \quad (3-76)$$

where, K_p and T_i are the proportional gain and integral time constant of the controller.

The structure of a current control loop in the rotor-flux-oriented coordinate system with PI controller consisting of the converter model, processing delay and the load (stator voltage equations in (3-66)) is shown in Fig. 3-11.

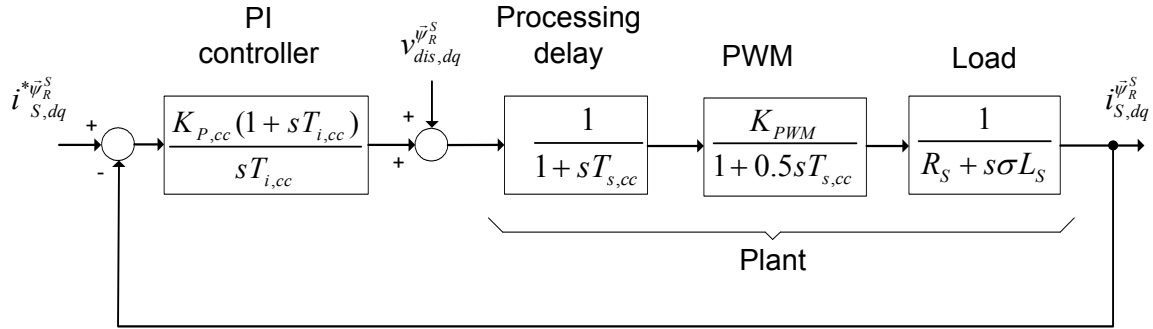


Fig. 3-11 Block scheme of the current control loop in indirect RFOC

$K_{p,cc}$ and $T_{i,cc}$ are the parameters of the PI current controller. Distortion in the current control loop (e.g. changes in dc-link voltage) is termed $v_{dis,dq}^s$ in the rotating reference frame. In the design of the current controller parameters ($K_{p,cc}$ and $T_{i,cc}$), reference tracking and disturbance rejection abilities as the main tasks should be considered. The processing time delay and the delay of the PWM can be approximated with a total current control loop delay of $1.5T_{s,cc}$ to simplify the design procedure of the PI controller

$$G_{d,cc}(s) = e^{-s(T_{\mu p} + T_{PWM})} \approx \frac{K_{PWM}}{1 + s(T_{\mu p} + T_{PWM})} = \frac{K_{PWM}}{1 + 1.5sT_{s,cc}}. \quad (3-77)$$

The open loop transfer function comprising the PI controller, total time delay, and the plant is

$$G_{ol,cc}(s) = K_{p,cc} \frac{1 + sT_{i,cc}}{sT_{i,cc}} \cdot \frac{K_{PWM}}{1 + 1.5sT_{s,cc}} \cdot \frac{1/R_s}{1 + s \frac{\sigma L_s}{R_s}}. \quad (3-78)$$

Optimal criteria such as technical optimum (TO) or symmetrical optimum (SO) are usually applied to tune the parameters of the PI controller [85]. In the case of current control, TO is preferred due to the good tracking ability with low overshoot in step response [85].

In the TO, the time constant of the integrator $T_{i,cc}$ equals the plant time constant to cancel the dominant pole ($s = -R_s/\sigma L_s$)

$$T_{i,cc} = \frac{\sigma L_s}{R_s}. \quad (3-79)$$

Substituting (3-79) in (3-78) leads to the following open loop transfer function

$$G_{ol,cc} = \frac{K_{p,cc}}{s\sigma L_s} \cdot \frac{K_{PWM}}{1 + 1.5sT_{s,cc}}. \quad (3-80)$$

Proportional gain of the PI controller $K_{p,cc}$ can be selected according to (3-81) in order to avoid undesirable current overshoot. Damping factor of the current control loop is shown by a_{cc} . If the damping factor a_{cc} is chosen to be greater than 2 ($a_{cc} \geq 2$), the current overshoot for a step change remains under 4% [85]

$$K_{p,cc} = \frac{\sigma L_s}{1.5 a_{cc} K_{PWM} T_{s,cc}}, \quad a_{cc} \geq 2. \quad (3-81)$$

The PI controller with TO and a proper damping factor (e.g. $a_{cc} = 2$) features an acceptable overshoot. However, the integral time constant is large (e.g. 10 ms according to Table 3.1) which leads to a poor disturbance rejection.

Table 3.4 summarizes the PI controller design results according to TO for plants with different transfer functions [11].

Table 3.4
Adjustment of controller parameters according to TO [11]

Plant	Controller	
	Type	Transfer function
$G_{plant}(s) = \frac{K_{plant}}{1 + sT_{plant}}$	I	$G_{controller}(s) = \frac{1}{sT_i}$ $T_i = a \cdot K_{plant} \cdot T_{plant}, \quad a \geq 2$
$G_{plant}(s) = \frac{K_{plant}}{(1 + sT_{plant,1})(1 + sT_{plant,2})}$ $T_{plant,1} \gg T_{plant,2}, \quad T_{plant,2} = \sum_{i=1}^n T_{plant,i}$	PI	$G_{controller}(s) = K_p \frac{1 + sT_i}{sT_i}$ $T_i = T_{plant,1},$ $K_p = \frac{T_{plant,1}}{a \cdot K_{plant} \cdot T_{plant,2}}, \quad a \geq 2$
$G_{plant}(s) = \frac{K_{plant}}{(1 + sT_{plant,1})(1 + sT_{plant,2})(1 + sT_{plant,3})}$ $T_{plant,1} > T_{plant,2} \gg T_{plant,3}, \quad T_{plant,3} = \sum_{i=1}^n T_{plant,i}$	PID	$G_{controller}(s) = K_p \frac{(1 + sT_i)(1 + sT_d)}{sT_i}$ $T_i = T_{plant,1}, \quad T_d = T_{plant,2},$ $K_p = \frac{T_{plant,1}}{a \cdot K_{plant} \cdot T_{plant,3}}, \quad a \geq 2$

The current control loop of the indirect RFOC (Fig. 3-11) for the exemplary HSIM with parameters given in Table 3.1 is simulated to investigate the dynamic performance of the current control loop. Basic parameters of the power converter (2L VSC) are according to Table 3.2. An asynchronous PWM with triangle carrier waveform is applied as modulator. Amplitude of the carrier signal equals $V_{dc}/2$ ($K_{PWM} = 1$).

In the case of asynchronous PWM, large m_f ($m_f > 21$) is recommended in order to reduce the amplitudes of subharmonics [13]. On the other hand, the converter switching frequency is limited to achieve reasonable converter efficiency. Therefore, the carrier frequency of 11.5 kHz ($m_f = 23$) has been selected. In the 2L VSC, the switching frequency is equal to the carrier frequency. Therefore, commercially available 2L VSC with IGBTs and maximum switching frequency of 10–15 kHz can be applied as power converters for the high-speed drive. Both symmetrical and asymmetrical regular samplings are simulated and results for the

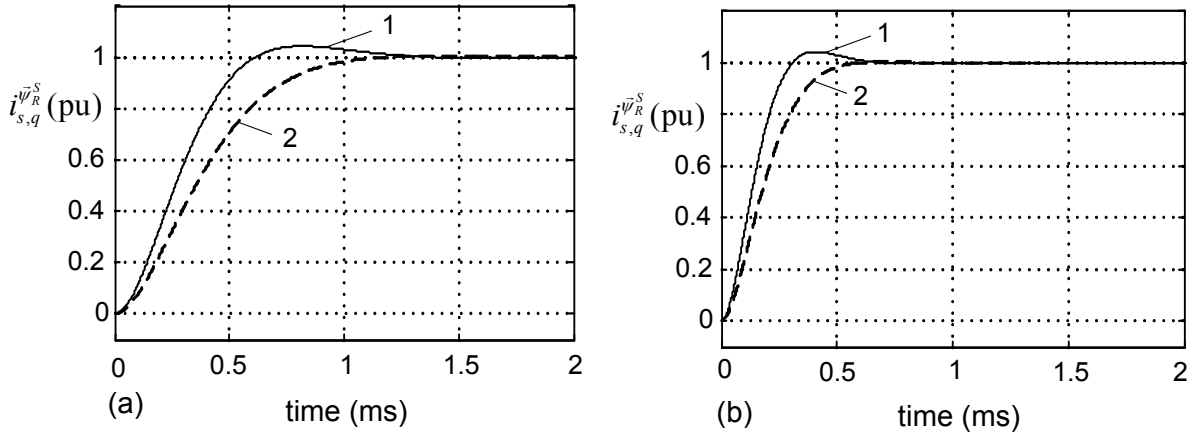


Fig. 3-12 Continuous step response of the current control loop of indirect RFOC with (a) regular symmetrical sampling and (b) regular asymmetrical sampling. 1: step response with $a_{cc} = 2$, and 2: step response with $a_{cc} = 3$

continuous step response are presented in Fig. 3-12. Simulation results for the symmetrical regular sampling for two different damping factor of the current control loop ($a_{cc} = 2$ and $a_{cc} = 3$) are shown in Fig. 3-12 (a). Furthermore, Fig. 3-12 (b) depicts the simulation results for the asymmetrical regular sampling for different values of current controller damping factor. Equations (3-79) and (3-81) are used to tune the PI parameters.

Obviously, the asymmetrical regular sampling ($T_{s,cc} = 22$ kHz) features faster response compared to the symmetrical regular sampling ($T_{s,cc} = 11.5$ kHz). However, a powerful processor is required to implement the asymmetrical regular sampling. Moreover, a proper damping factor can be chosen (e.g. $a_{cc} = 3$) to obtain a step response without substantial current overshoot.

Speed control loop

The speed controller is one of the outer control loops of the indirect RFOC. The speed control loop conations the current control loop and the mechanical dynamics of the HSIM. Transfer function of the closed loop current control system with the designed PI controller ((3-79) and (3-81)) and the corresponding approximated transfer function is given in (3-82). The carried out approximation to a first order transfer function simplifies the controller design procedure for the speed control loop

$$G_{ol,cc} = \frac{1}{1 + 1.5a_{cc}sT_{s,cc} + 1.5^2a_{cc}^2s^2T_{s,cc}^2} \approx \frac{1}{1 + 1.5a_{cc}sT_{s,cc}}. \quad (3-82)$$

Continuous step response of the original transfer function of the current control loop and the step response of the approximated one for $T_{s,cc} = 22$ kHz and different values of the damping factor $a_{cc} = 2$ and $a_{cc} = 3$ are shown in Fig. 3-13.

Applying the expression of electromechanical torque in (3-36) for the IM controlled by RFOC, the electromechanical equation is derived to:

$$J \frac{d\omega_M}{dt} = T_{em} - T_L = \frac{3}{2} Z_P \frac{L_M}{L_R} \psi_R i_{s,q}^S - T_L. \quad (3-83)$$

where, T_L denotes the mechanical load. Applying the approximated transfer function of current control loop (3-82) and the mechanical equation in (3-83), the speed control loop of the RFOC is depicted in Fig. 3-14.

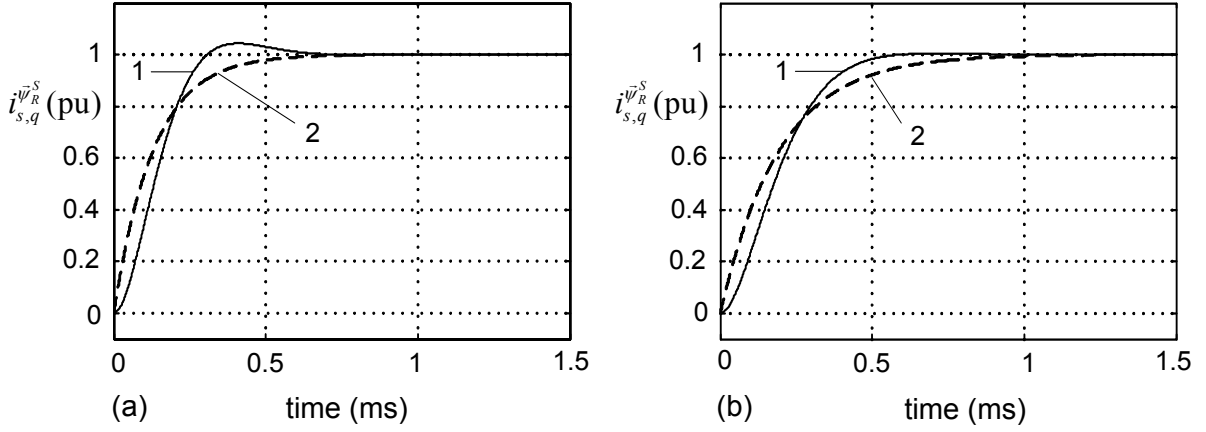


Fig. 3-13 Continuous step response of the current control loop with $T_{s,cc} = 22$ kHz. (a) $a_{cc} = 2$, (b) $a_{cc} = 3$. 1: Step response of original transfer function, 2: Step response of approximated transfer function

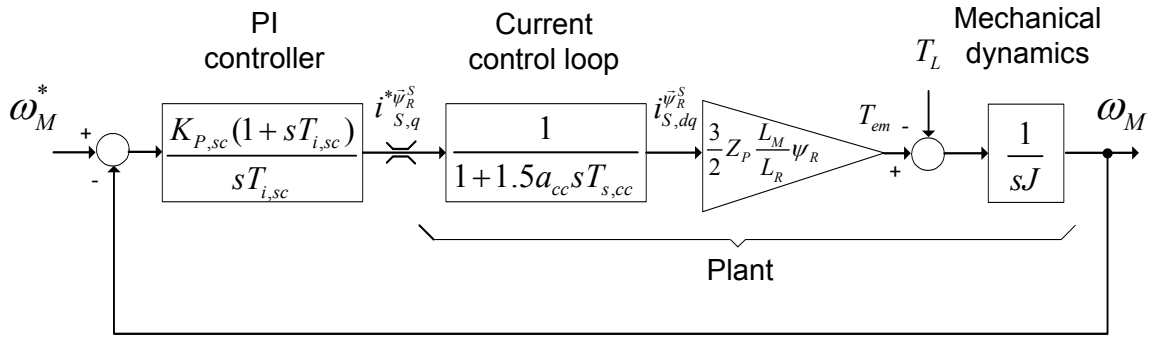


Fig. 3-14 A block scheme of the speed control loop in indirect RFOC

According to Fig. 3-14, the open loop transfer function of the speed control loop is calculated as:

$$G_{ol,sc} = \frac{K_{p,sc} k_{plant,sc} (1 + sT_{i,sc})}{sT_{i,sc} (1 + sT_{plant,sc}) sJ}, \quad (3-84)$$

where

$$k_{plant,sc} = \frac{3}{2} Z_P \frac{L_M}{L_R} \psi_R, \quad T_{plant,sc} = 1.5 a_{cc} T_{s,cc}. \quad (3-85)$$

In order to design the parameters of the PI controller ($K_{p,sc}$, $T_{i,sc}$), the symmetrical optimum (SO) is usually applied due to the excellent disturbance rejection of the PI controller design according to SO [85].

Bode diagrams of the open loop transfer function of (3-84) are symmetric around the frequency [9]

$$\omega = \frac{1}{\sqrt{T_{i,sc} T_{plant,sc}}}. \quad (3-86)$$

According to symmetrical optimization, the parameters of the PI controller are designed to achieve a unity gain of the open loop transfer function of (3-84) at the frequency given by (3-86). With a unity gain at the frequency ω in (3-86), the open loop system has the

maximum phase margin [85]. To achieve the maximum gain margin, the parameters of the PI controller should be [85]

$$T_{i,sc} = a_{sc}^2 T_{plant,sc} = 1.5 a_{sc}^2 a_{cc} T_{s,cc}, \tag{3-87}$$

$$K_{p,sc} = \frac{J}{a_{sc} K_{plant,sc} T_{plant,sc}} = \frac{J}{2.25 Z_p \psi_R \frac{L_M}{L_R} a_{cc} a_{sc} T_{s,cc}}, \quad a_{sc} \geq 2, \tag{3-88}$$

where, a_{sc} denotes the damping factor of the speed control loop.

The damping factor a_{sc} has a relation to the phase margin φ_{pm} of the open loop transfer function (3-84) as [9]

$$a_{sc} = \frac{1 + \cos(\varphi_{pm})}{\sin(\varphi_{pm})}. \tag{3-89}$$

The Bode diagram of the open loop transfer function in (3-84) for different damping factors of the PI parameters in (3-87) and (3-88) is depicted in Fig. 3-15 (a) for the exemplary HSIM. Furthermore, continuous step response of the speed control loop for various damping factors is shown in Fig. 3-15 (b). Obviously, for a phase margin of $\varphi_{pm} = 45^\circ$ a damping factor of $a_{sc} = 2.41$ is required. This damping factor leads to a moderate overshoot of about 30 %.

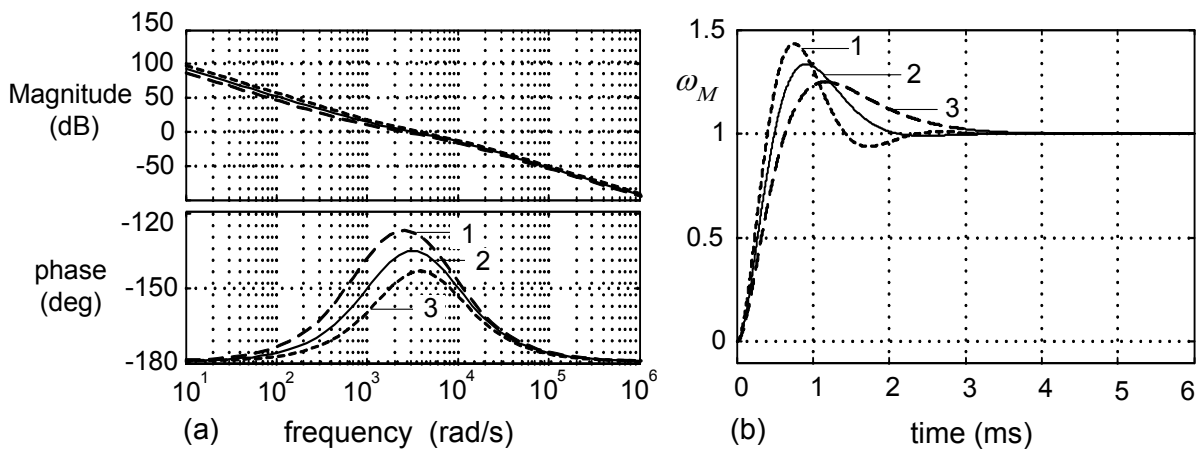


Fig. 3-15 (a) Bode diagram of the open loop transfer function of speed control loop, (b) continuous step response of the closed loop speed control; $a_{cc} = 2$, 1: $a_{sc} = 2$; 2: $a_{sc} = 2.41$; 3: $a_{sc} = 3$

Table 3.5 summarizes the PI controller design results according to SO for plants with different transfer functions [11].

Rotor flux control loop

Rotor flux control loop is another outer control loop in the RFOC. Similar to the speed control loop, the rotor flux control loop includes the current control loop. Moreover, the flux control loop comprises the dynamic of the rotor flux presented in (3-55). Fig. 3-16 presents a block diagram of the rotor flux control loop. Similar to the design procedure of the speed control loop, SO has been used to design the parameters of the PI controller ($K_{p,fc}$, $T_{i,fc}$). Considering the control plant shown in Fig. 3-16 and using Table 3.5, parameters of the PI controller are as follows:

Table 3.5
Adjustment of controller parameters according to SO [11]

Plant	Controller	
	Type	Transfer function
$G_{plant}(s) = \frac{K_{plant}}{T_{plant,0}s(1+sT_{plant,1})}$ $T_{plant,1} = \sum_{i=1}^n T_{plant,i}$	PI	$G_{controller}(s) = K_p \frac{1+sT_i}{sT_i}$ $T_i = a^2 \cdot T_{plant,1},$ $K_p = \frac{T_{plant,0}}{a \cdot K_{plant} \cdot T_{plant,1}}, \quad a \geq 2$
$G_{plant}(s) = \frac{K_{plant}}{T_{plant,0}s(1+sT_{plant,1})(1+sT_{plant,2})}$ $T_{plant,1} \gg T_{plant,2}, \quad T_{plant,2} = \sum_{i=1}^n T_{plant,i}$	PID	$G_{controller}(s) = K_p \frac{(1+sT_i)(1+sT_d)}{sT_i}$ $T_i = a^2 T_{plant,2}, \quad T_d = T_{plant,1},$ $K_p = \frac{T_{plant,0}}{a \cdot K_{plant} \cdot T_{plant,2}}, \quad a \geq 2$
$G_{plant}(s) = \frac{K_{plant}}{(1+sT_{plant,1})(1+sT_{plant,2})}$ $T_{plant,1} \gg a^2 T_{plant,2}, \quad T_{plant,2} = \sum_{i=1}^n T_{plant,i}$	PI	$G_{controller}(s) = K_p \frac{1+sT_i}{sT_i}$ $T_i = a^2 \cdot T_{plant,2},$ $K_p = \frac{T_{plant,1}}{a \cdot K_{plant} \cdot T_{plant,2}}, \quad a \geq 2$
$G_{plant}(s) = \frac{K_{plant}}{(1+sT_{plant,1})(1+sT_{plant,2})(1+sT_{plant,3})}$ $T_{plant,1} > T_{plant,2} \gg T_{plant,3},$ $T_{plant,1} \gg a^2 T_{plant,3}, \quad T_{plant,3} = \sum_{i=1}^n T_{plant,i}$	PID	$G_{controller}(s) = K_p \frac{(1+sT_i)(1+sT_d)}{sT_i}$ $T_i = a^2 T_{plant,3}, \quad T_d = T_{plant,2},$ $K_p = \frac{T_{plant,1}}{a \cdot K_{plant} \cdot T_{plant,3}}, \quad a \geq 2$

$$T_{i,fc} = 1.5a_{fc}^2 a_{cc} T_{s,cc}, \quad (3-90)$$

$$K_{p,sc} = \frac{\tau_R}{1.5a_{fc} a_{cc} T_{s,cc}}, \quad a_{fc} \geq 2. \quad (3-91)$$

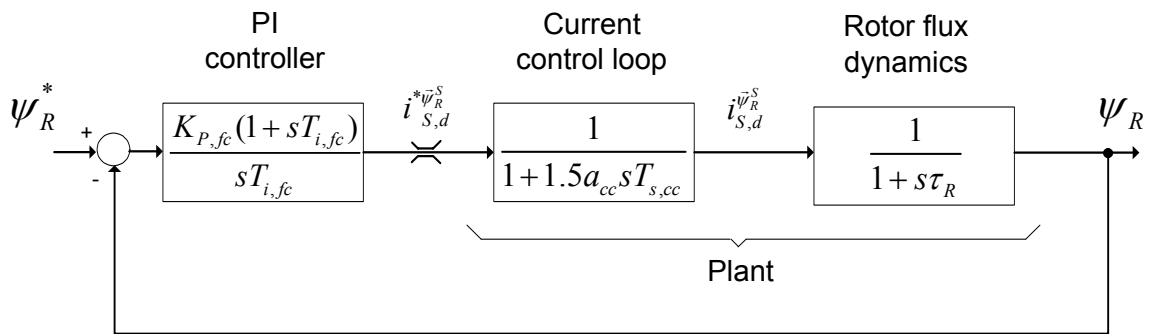


Fig. 3-16 A block scheme of the flux control loop in RFOC

3.5 Direct torque control of induction machines

DTC is a powerful method for control of IMs because of features like fast dynamics, simple structure (lack of current loops), and robustness (only the stator resistance is used in the control algorithm) [42], [44], [48], [49], [59], [61].

The main feature of the DTC for IMs is the direct control of the electromechanical torque and flux (e.g. stator flux). Hysteresis controllers are usually applied to control the torque and flux and no modulator is required. A power converter (e.g. 2L VSC with IGBTs) is used to feed the IM.

Electromechanical torque of an IM is proportional to the amplitude of the stator and rotor flux and the torque angle [47]

$$T_{em} = \frac{3}{2} Z_p \frac{L_M}{\sigma L_S L_R} \psi_S \psi_R \sin(\delta), \tag{3-92}$$

where, ψ_S and ψ_R are the magnitude of the stator and rotor flux vectors and δ denotes the machine torque angle (phase difference between the stator and rotor flux vectors) as shown in Fig. 3-5. Obviously, at a constant stator and rotor flux, the electromechanical torque can be controlled directly by the control of the torque angle.

According to (3-38) and (3-39), the stator flux vector is controlled with the stator voltage vector

$$\widehat{\psi}_S^S(t) = \int_0^t (\vec{v}_S^S(\tau) - R_S \vec{i}_S^S(\tau)) d\tau \tag{3-93}$$

where, $\widehat{\psi}_S^S$, \vec{v}_S^S , and \vec{i}_S^S are the estimated stator flux, the stator voltage, and the stator current vectors in the stator fixed stationary coordinate reference frame.

As depicted in Fig. 3-17, six active vectors ($\vec{v}_1, \dots, \vec{v}_6$) and two zero vectors (\vec{v}_0, \vec{v}_7) can be defined for output voltage of a 2L VSC, considering various states of the converter switches.

Therefore, in an IM fed by a 2L VSC, the stator voltage vector is related to the dc-link voltage as described in the following [12]:

$$\vec{v}_S^S = \begin{cases} \vec{v}_n = \frac{2}{3} V_{dc} \angle (n-1) \frac{\pi}{3} & n = 1, \dots, 6 \\ \vec{v}_n = 0 & n = 0, 7 \end{cases} \tag{3-94}$$

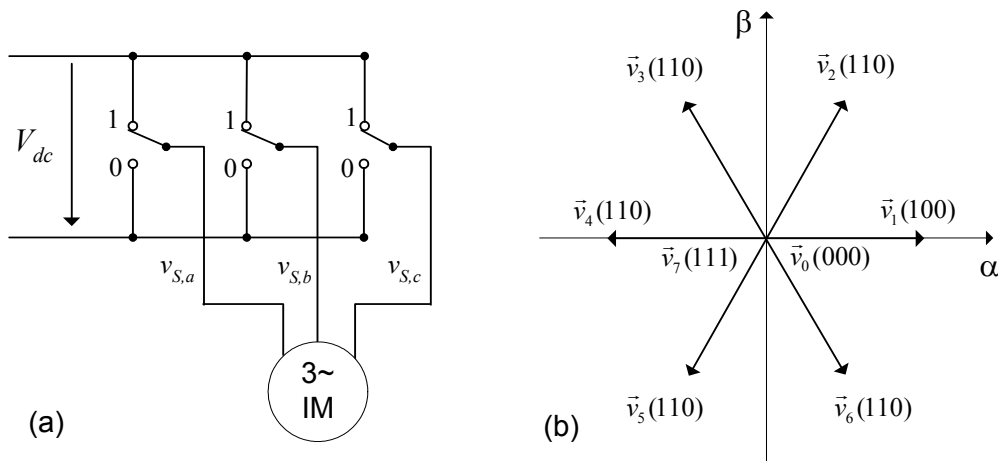


Fig. 3-17 (a) A 2L VSC feeding an induction machine, (b) representation of the converter output voltage vectors in the stator fixed stationary reference frame

If the stator resistance voltage drop is neglected, the stator flux vector can be expressed as

$$\hat{\psi}_s^s(t) = \int_0^t \bar{v}_s^s(\tau) d\tau. \tag{3-95}$$

Equation (3-95) clarifies that when using one of the active vectors of the converter output voltage, the stator flux moves in the direction of the corresponding voltage. Moreover, the stator flux vector stops if one of the zero vectors of the converter output voltage is applied.

In IMs, the stator flux vector can be changed rapidly using an appropriate active vector of converter output voltage but the rotor flux vector responds more slowly due to the rotor time constant [47]. Therefore, for a counterclockwise rotation of the stator flux vector, applying a forward switching vector of the converter output voltage accelerates the stator flux vector while the rotor flux vector does not change considerably for a short time period. Hence, the torque angle is increased and a positive electromechanical torque is generated. On the other hand, if a zero vector or a backward switching vector of the converter output voltage is used, the torque angle is reduced and consequently the electromechanical torque is reduced. Obviously, for a negative torque angle $\delta < 0$, the IM produces a negative torque.

To summarize, the amplitude and the phase angle (electromechanical torque) of the stator flux vector of an IM can be controlled using an appropriate converter switching sequence. This principle is the base of the direct torque control strategy.

A block scheme of classical DTC with speed control loop for the exemplary HSIM is presented in Fig. 3-18. In the classical DTC, the stator flux is controlled and the stator flux vector has a circular trajectory [21], [47], [73]. A 2L VSC with voltage dc-link feeds the HSIM. In order to estimate the stator flux vector and the electromechanical torque, the stator currents and the stator voltages are required to be measured or estimated.

Equations (3-38)–(3-40) are used to calculate the stator flux. A block scheme of the stator flux estimator using the stator voltage and the stator currents is shown in Fig. 3-3 (a). As mentioned in Section 3.3.1, the stator flux observer has a more simple structure, compared to the air gap or the rotor flux estimator if stator voltages and stator currents are measured.

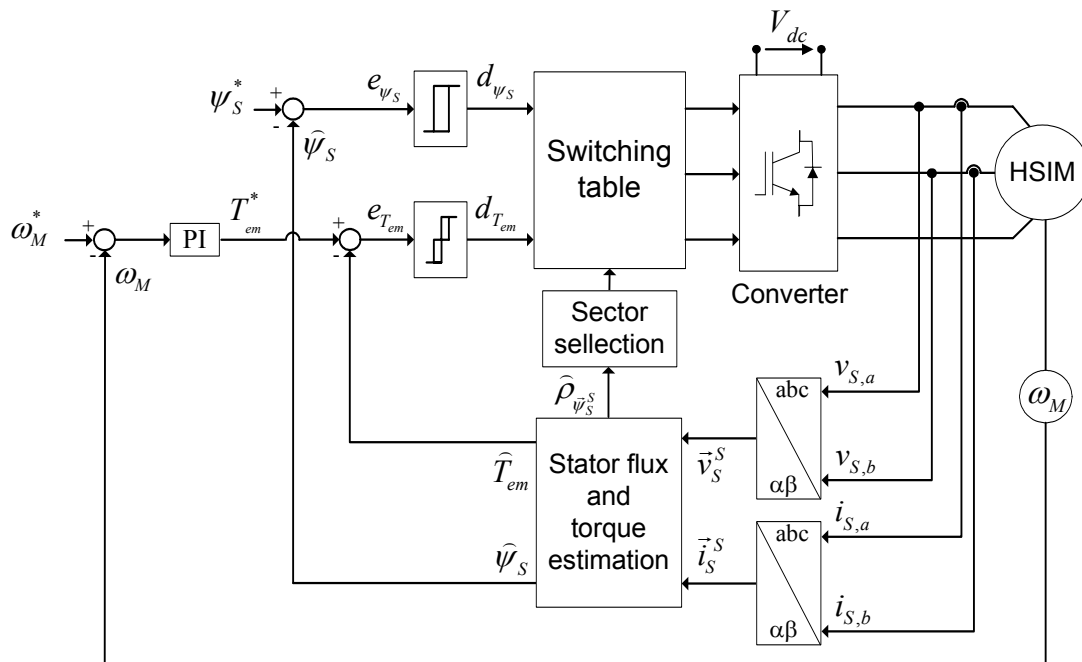


Fig. 3-18 A block diagram of the DTC with speed control loop

According to (3-21) and (3-23), real and imaginary parts of the stator current and the stator flux in the stator fixed stationary reference frame can be applied to estimate the electromechanical torque

$$\hat{T}_{em} = \frac{3}{2} Z_P (\hat{\psi}_{S,\alpha}^S i_{S,\beta}^S - \hat{\psi}_{S,\beta}^S i_{S,\alpha}^S). \tag{3-96}$$

The stator flux estimator in Fig. 3-3 (a) and electromechanical torque representation in (3-96) structure the stator flux and torque estimation block of Fig. 3-18.

3.5.1 Control of stator flux and electromechanical torque

As shown in Fig. 3-18, hysteresis controllers are applied to control the stator flux and the electromechanical torque. The stator flux amplitude and the torque reference (e.g. output of the speed controller) are compared with the estimated values. Corresponding to the flux and torque errors, $e_{\psi_s} = \psi_s^* - \hat{\psi}_s$ and $e_{T_{em}} = T_{em}^* - \hat{T}_{em}$, the hysteresis controllers produce appropriate values for the output variables d_{ψ_s} and $d_{T_{em}}$, respectively. In the classic DTC, a two-level hysteresis controller is applied for the flux control loop and for the torque control loop a three level hysteresis is used as shown in Fig. 3-19 [21], [47].

An appropriate vector of the converter output voltage should be chosen for each hysteresis output set ($d_{\psi_s}, d_{T_{em}}$) to reduce the absolute values of the flux and torque error. In this connection, the plane of the stator fixed coordinate system is divided for the six sectors as shown in Fig. 3-20. Regarding the stator flux angle, the sectors definition is presented in Table 3.6. The stator flux estimator in Fig. 3-18 estimates the angle of the flux vector and the sector selection block determines the corresponding sector according to Table 3.6.

Let us suppose that the location of the stator flux vector is estimated in sector 2 as shown in Fig. 3-21. In order to increase the amplitude of the stator flux vector (if $e_{\psi_s} > H_{\psi_s}$), the converter output vectors \vec{v}_1, \vec{v}_2 , and \vec{v}_3 can be selected. On the other hand, the converter output vectors \vec{v}_4, \vec{v}_5 , and \vec{v}_6 can be selected to reduce the amplitude of the stator flux vector (if $e_{\psi_s} < -H_{\psi_s}$). If the zero vectors \vec{v}_0 and \vec{v}_7 are selected, amplitude of the stator flux vector remains unchanged.

In order to decrease the electromechanical torque (if $e_{T_{em}} < 0$), the output voltage vectors \vec{v}_6, \vec{v}_1 , and \vec{v}_2 can be chosen. Conversely, output voltage vectors \vec{v}_3, \vec{v}_4 , and \vec{v}_5 can be selected to increase the electromechanical torque (if $e_{T_{em}} > 2H_{T_{em}}$).

Regarding the outputs of the hysteresis controllers ($d_{\psi_s}, d_{T_{em}}$) and the location of the stator flux vector (sector number), an optimum voltage vector can be selected for each sector.

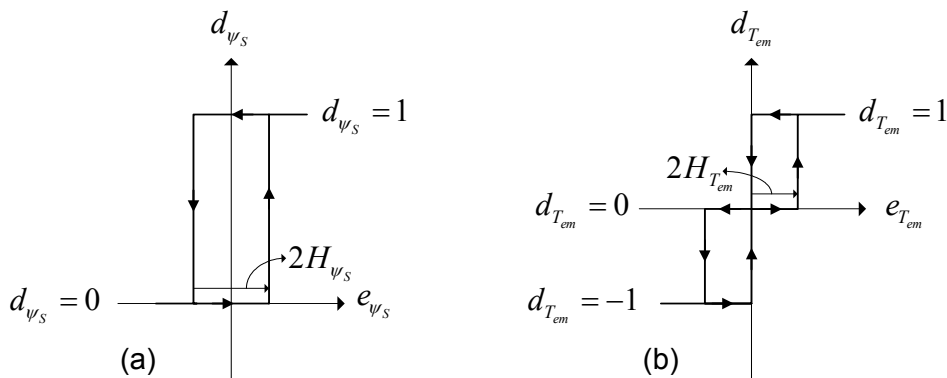


Fig. 3-19 (a) Two level hysteresis flux controller, (b) three level hysteresis torque controller

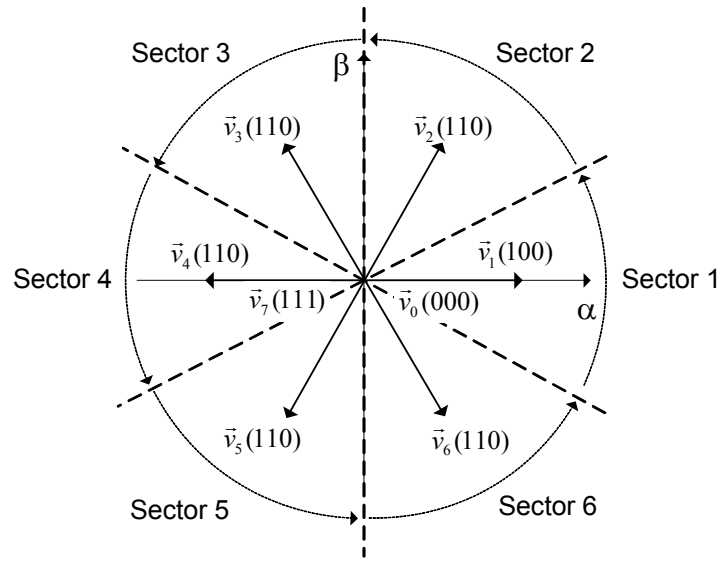


Fig. 3-20 Sector definition in DTC

Table 3.6
Sector intervals in DTC

Sector number	1	2	3	4	5	6
$\rho_{\vec{\psi}_s}$	$\left[-\frac{\pi}{6}, \frac{\pi}{6}\right)$	$\left[\frac{\pi}{6}, \frac{\pi}{2}\right)$	$\left[\frac{\pi}{2}, \frac{5\pi}{6}\right)$	$\left[\frac{5\pi}{6}, -\frac{5\pi}{6}\right)$	$\left[-\frac{5\pi}{6}, -\frac{\pi}{2}\right)$	$\left[-\frac{\pi}{2}, -\frac{\pi}{6}\right)$

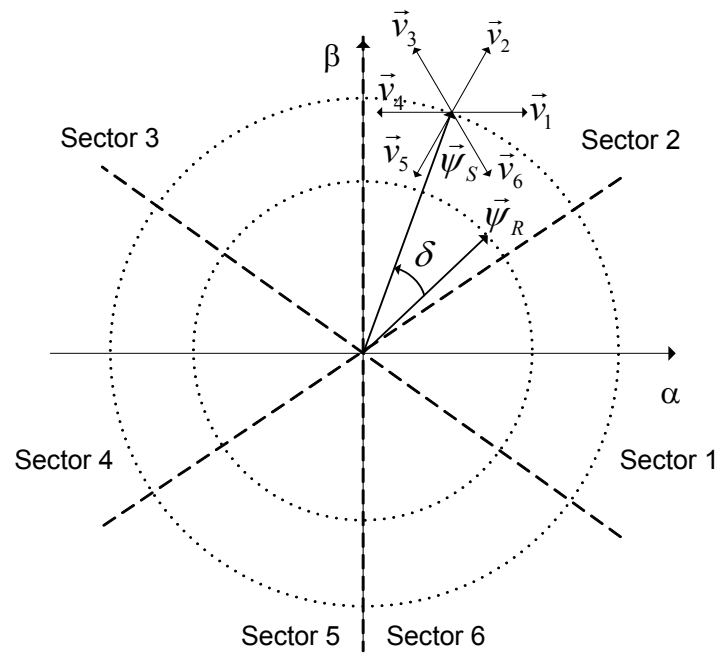


Fig. 3-21 Optimum voltage vector selection in DTC

Table 3.7
Switching table of DTC

d_{ψ_s}	$d_{T_{em}}$	Sector1	Sector2	Sector3	Sector4	Sector5	Sector6
1	1	$\vec{v}_2(110)$	$\vec{v}_3(010)$	$\vec{v}_4(011)$	$\vec{v}_5(001)$	$\vec{v}_6(101)$	$\vec{v}_1(100)$
	0	$\vec{v}_7(111)$	$\vec{v}_0(000)$	$\vec{v}_7(111)$	$\vec{v}_0(000)$	$\vec{v}_7(111)$	$\vec{v}_0(000)$
	-1	$\vec{v}_6(101)$	$\vec{v}_1(100)$	$\vec{v}_2(110)$	$\vec{v}_3(010)$	$\vec{v}_4(011)$	$\vec{v}_5(001)$
0	1	$\vec{v}_3(010)$	$\vec{v}_4(011)$	$\vec{v}_5(001)$	$\vec{v}_6(101)$	$\vec{v}_1(100)$	$\vec{v}_2(110)$
	0	$\vec{v}_0(000)$	$\vec{v}_7(111)$	$\vec{v}_0(000)$	$\vec{v}_7(111)$	$\vec{v}_0(000)$	$\vec{v}_7(111)$
	-1	$\vec{v}_5(001)$	$\vec{v}_6(101)$	$\vec{v}_1(100)$	$\vec{v}_2(110)$	$\vec{v}_3(010)$	$\vec{v}_4(011)$

Table 3.7 summarizes the optimum switching strategy for different output values of the hysteresis controllers and different sectors [19], [47].

Hysteresis controllers operate properly in a continuous control system. Obviously, for a proper operation in a discrete control, high sampling frequency is required [21]. In the classic DTC with discrete hysteresis controllers, amplitude of the electromechanical torque ripple strongly depends on the sampling period $T_{s,DTC}$ [42], [44], [49], [59]. The discrete hysteresis torque controller will operate like the analog one if the maximum value of the electromechanical torque variation in a sampling time is smaller than the width of the torque hysteresis controller [47]

$$\Delta T_{em,max} \ll 2H_{T_{em}}. \quad (3-97)$$

It should be noted that the width of the hysteresis controllers strongly affects the harmonic currents, average converter switching frequency, and the converter losses [48].

3.5.2 Speed control loop

Speed control loop is the outer control loop in the DTC. Due to the slower mechanical time constant compared to the time constant of the torque control loop, a longer sampling period (e.g. $T_{s,sc} = 10T_{s,DTC} - 20T_{s,DTC}$) is applicable. A PI controller can be used as controller in the speed control loop. In order to design the parameters of the speed PI controller, the torque control loop can be modelled as a first order system. A typical waveform of the torque step response in DTC and the approximated waveform are shown in Fig. 3-22.

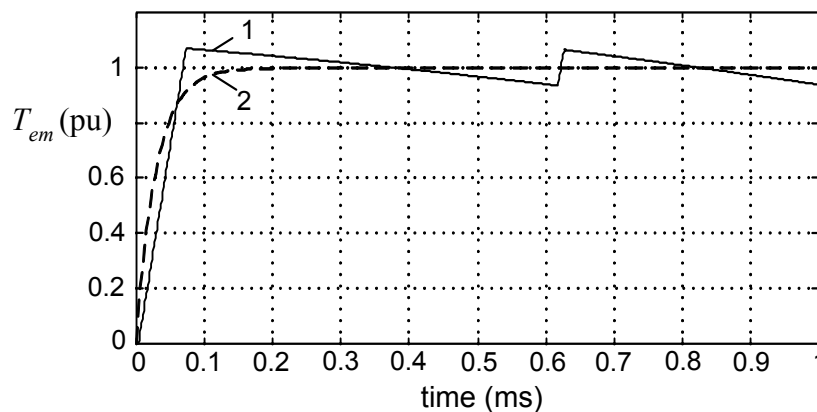


Fig. 3-22 Typical step response of the torque control loop in DTC; 1: original waveform; 2: approximated waveform

The torque response can be approximated by a first order system as:

$$G_{DTC}(s) = \frac{1}{1 + s\tau_{DTC}} \quad (3-98)$$

where, τ_{DTC} denotes the time constant of the approximated torque response.

The speed control loop with a PI controller is shown in Fig. 3-23. Similar to the speed control in RFOC, SO is applied to tune the parameters of the speed controller ($K_{p,sc}$, $T_{i,sc}$).

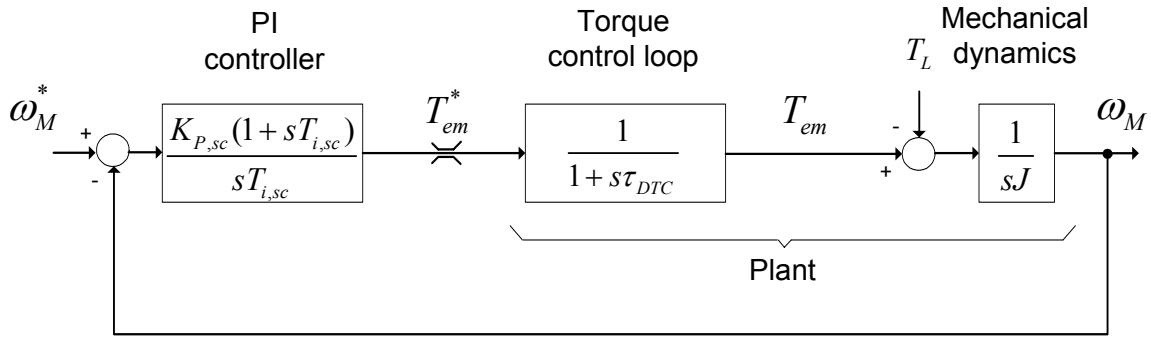


Fig. 3-23 Speed control loop in DTC

According to Table 3.5 and Fig. 3-23, the parameters of the PI controller are calculated as:

$$T_{i,sc} = a_{sc}^2 \tau_{DTC} \quad (3-99)$$

$$K_{p,sc} = \frac{J}{a_{sc} \tau_{DTC}}, \quad a_{sc} \geq 2. \quad (3-100)$$

3.6 Comparison of indirect RFOC and DTC for the exemplary high-speed induction machine

3.6.1 Simulation results

In order to compare the transient and steady-state performance of the indirect RFOC and DTC for the exemplary HSIM, both control strategies are simulated using MATLAB / SIMULINK. Parameters of the HSIM are as described in Table 3.1. A 2L VSC with ideal semiconductor behavior is applied as the power converter. Basic parameters of the converter are as given in Table 3.2. Simulated structure for the indirect RFOC and the DTC are shown in Fig. 3-24 (a), and (b), respectively.

Carrier frequency of the RFOC is $f_C = 11.5$. Current control loop of the RFOC is realized with both symmetrical regular sampled PWM (SRS-PWM) and asymmetrical regular sampled PWM (ARS-PWM). Sampling frequency of the RFOC with SRS-PWM and ARS-PWM equals $f_{s,cc} = 11.5$ kHz and $f_{s,cc} = 23$ kHz, respectively. In both cases, the sampling frequency of the speed control loop is $f_{s,sc} = 11.5$ kHz. The stator current is limited to 2 pu and an anti windup algorithm is applied for the speed and flux controllers [1].

Step response of the discrete current control loop of SRS-PWM ($f_C = 11.5$ kHz) and ARS-PWM ($f_C = 23$ kHz) are shown in Fig. 3-25. Obviously, waveforms in Fig. 3-25 are comparable to the step response of the continuous current control loop presented in Fig. 3-12.

In RFOC with ARS-PWM, the rise time of the current step response is 0.5 ms and 1.5 ms for $a_{cc}=2$ and $a_{cc}=3$, respectively. The rise time decreases to 0.25 ms and 0.75 ms for $a_{cc}=2$ and $a_{cc}=3$ with ARS-PWM.

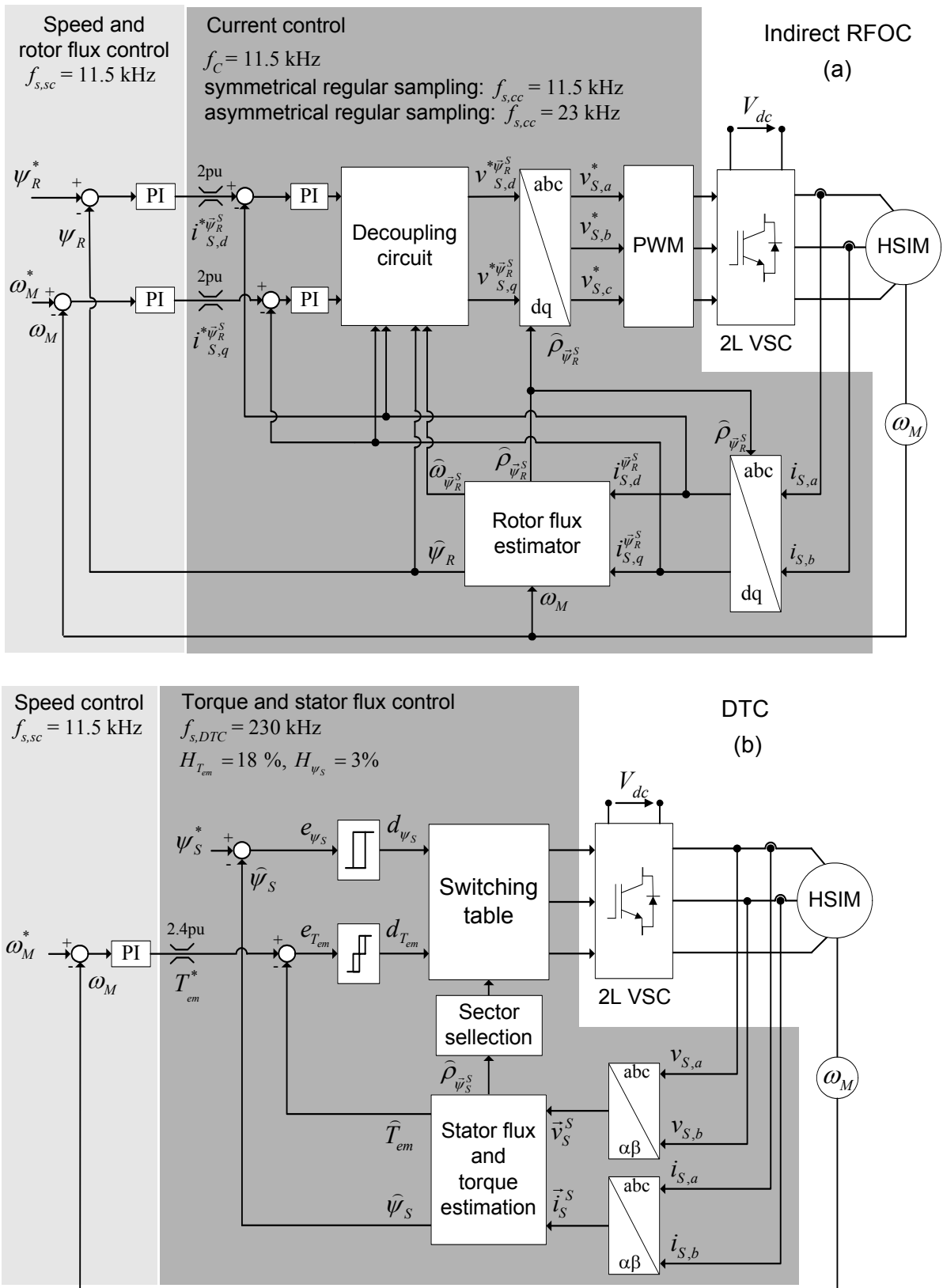


Fig. 3-24 Block diagram and the control parameters of the indirect RFOC and the DTC used in the simulation of the exemplary high-speed induction machine drive

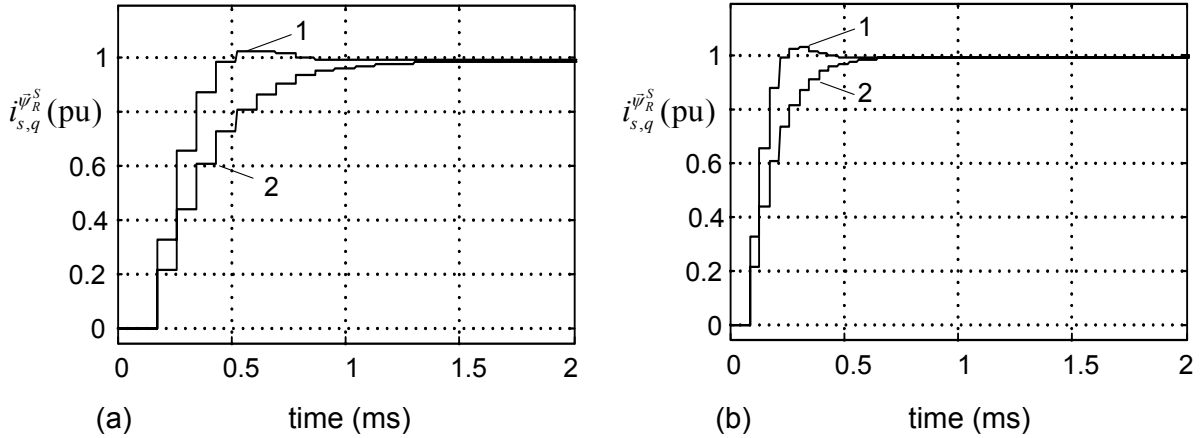


Fig. 3-25 Discrete step response of the current control loop of indirect RFOC with (a): SRS-PWM and (b): ARS-PWM; 1: step response with $a_{cc} = 2$ and 2: step response with $a_{cc} = 3$

The same sampling frequency of the speed control loop of RFOC is selected for the speed control loop of DTC $f_{s,sc} = 11.5$ kHz. The sampling frequency and the hysteresis width of the torque and flux controllers are chosen so that the RFOC and DTC produce comparable torque THD at the nominal load and the rated speed.

Electromechanical torque THD is determined using the first 500 torque harmonics obtained from the torque harmonic spectrum

$$THD_{T_{em}} = \frac{\sqrt{\sum_{h=2}^{500} \hat{T}_{em,h}^2}}{T_{em,av}}, \quad (3-101)$$

where, $\hat{T}_{em,h}$ is the amplitude of the h^{th} order harmonic of the electromechanical torque and $T_{em,av}$ denotes the average value of the electromechanical torque.

In order to achieve a comparable electromechanical torque THD for the RFOC and DTC ($THD_{T_{em}} \approx 20\%$), the sampling time of the torque and flux control loop in DTC is determined to 230 kHz according to the simulations carried out. The steady-state electromechanical torque at the rated load and nominal speed and the corresponding spectrum is shown in Fig. 3-26 (a), (b), and (c) for RFOC with SRS-PWM, RFOC with ARS-PWM, and DTC, respectively. Obviously, the harmonics of the electromechanical torque in RFOC occur around the carrier frequency and times of the carrier frequency. The low order torque harmonics ($h = 3$) in Fig. 3-26 (a) and (b) are related to the low order harmonics ($h = 2$ and $h = 4$) of the converter output voltages due to the PWM with a regular sampling [7]. In the case of DTC, the spectrum of the electromechanical torque is broad and comprises all even harmonics. The major harmonics occur around $h = 26$.

Control parameters of the RFOC with SRS-PWM, RFOC with ARS-PWM, and DTC are summarized in Table 3.8. Set point values of the stator current components on d and q axes in RFOC are limited to 2 pu. Consequently, the amplitude of the stator current in transient will be limited to 2 pu. Fig. 3-27 (a) depicts the simulation results for a speed variation from 0 to 1 pu for RFOC with ARS-PWM. Stator current is limited to 2 pu which leads to a linear speed variation from zero to nominal speed in 0.15 s. The electromechanical torque is limited indirectly to 2.4 pu. Considering the limit of the electromechanical torque in RFOC, the set point of the electromechanical torque in DTC is limited to 2.4 pu for a comparison between the load disturbance rejection of RFOC and DTC.

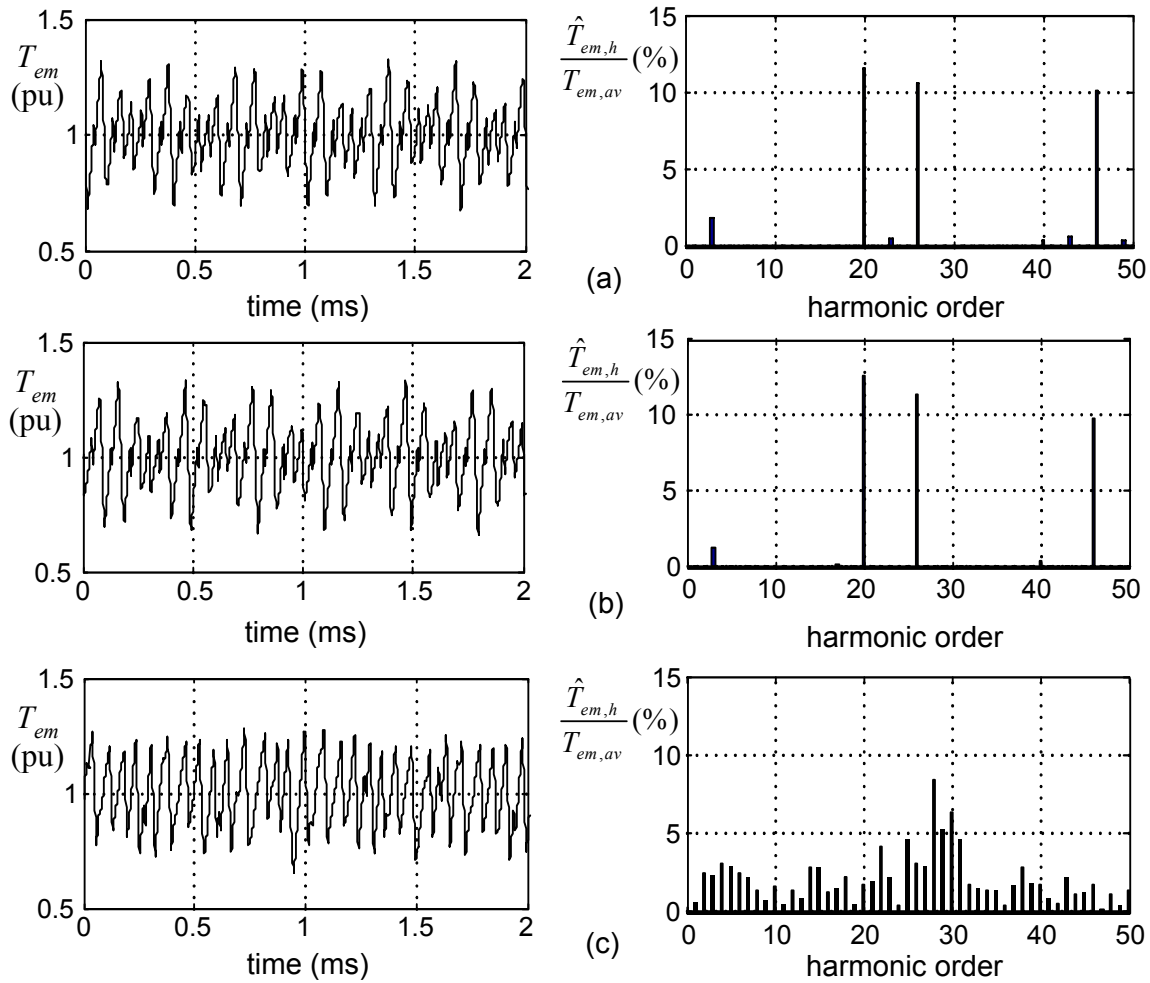


Fig. 3-26 Steady-state electromechanical torque and the corresponding spectrum at rated load and nominal speed: (a) RFOC with SRS-PWM; (b) RFOC with ARS-PWM; (c) DTC

Table 3.8
Parameters of the RFOC with SRS-PWM, RFOC with ARS-PWM, and DTC

	RFOC with SRS-PWM	RFOC with ARS-PWM	DTC
f_{sw} (kHz)	11.5	11.5	11.53 (average)
$f_{s,cc}$ (kHz)	11.5	23	11.5
$f_{s,DTC}$ (kHz)	-	-	230
$f_{s,sc}$ (kHz)	11.5	11.5	11.5
a_{cc}	2	2	-
a_{sc}	2.41	2.41	2.41
$H_{T_{em}}/T_{em,n}$ (%)	-	-	18
$H_{\psi_s}/\psi_{s,n}$ (%)	-	-	3
Torque THD (%)	19.4	20	20
Phase current THD (%)	16	16.3	16.4
Line-to-line voltage THD (%)	76	74	76

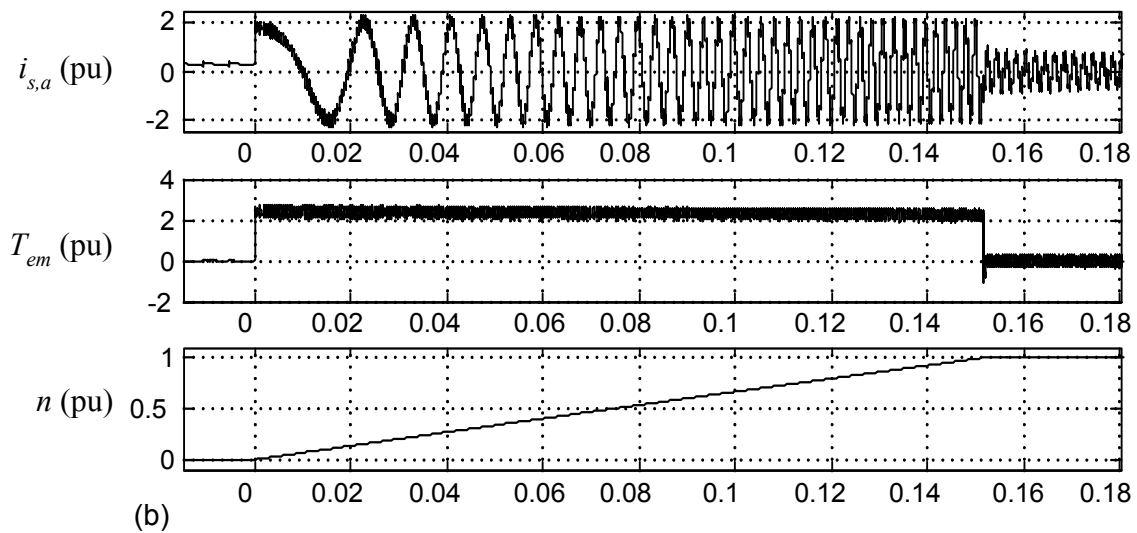
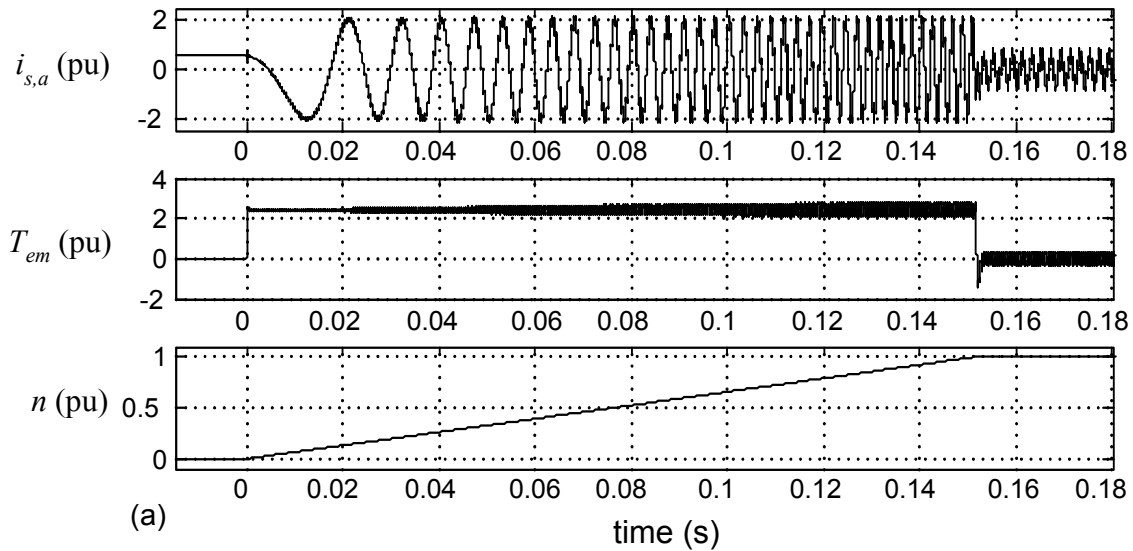


Fig. 3-27 Stator current, electromechanical torque and mechanical speed of the high-speed induction machine for speed step response: (a) Indirect RFOC with ARS-PWM; (b) DTC

For a speed set point variation from 0 to 1 pu, Fig. 3-27 (b) shows the stator current, the electromechanical torque, and the mechanical speed of the exemplary HSIM controlled with DTC. Electromechanical set point has been limited to 2.4 pu, which leads indirectly to the stator current limitation of 2 pu.

Load disturbance rejection of the high-speed drive with RFOC (SRS-PWM and ARS-PWM) and DTC are presented in Fig. 3-28. Waveforms of the electromechanical torque are filtered to acquire the average values which are required in investigations of transient performance. Load disturbance rejection for the rated load $T_L = 1$ pu at the nominal mechanical speed $n = 0.9969$ pu is shown in Fig. 3-28 (a). Fig. 3-28 (b) presents the load disturbance rejection for the rated load $T_L = 1$ pu at half of the nominal mechanical speed $n = 0.4985$ pu. Base values for the torque and the mechanical speed are $T_b = 6.39$ Nm and $N_b = 30,000$ rpm, respectively. As evident from Fig. 3-28, load disturbance rejection at the rated speed and half of the rated speed can be compared well, due to the adequate dc-link voltage reserve.

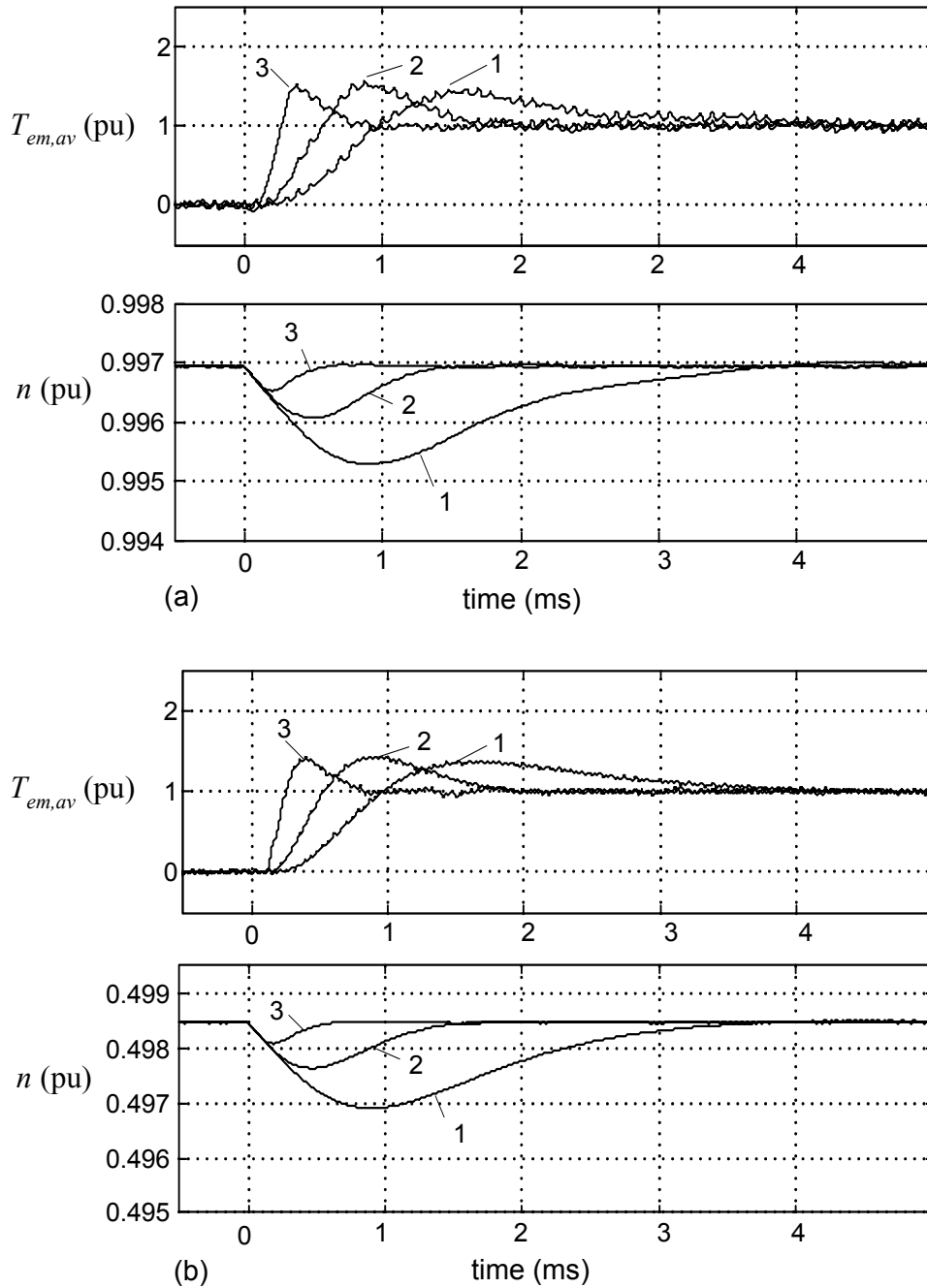


Fig. 3-28 Load disturbance rejection at rated mechanical speed (a) and half of the nominal mechanical speed (b); The average electromechanical torque and the mechanical speed for 1: RFOC with SRS-PWM; 2: RFOC with ARS-PWM; 3: DTC; $T_b = 6.39$ Nm, $n_b = 30000$ rpm

Considering the nominal stator rms phase voltage ($V_s = 230$ V) and the selected dc-link voltage ($V_{dc} = 700$ V), modulation depth at the rated load for RFOC is $M_n = 0.929$ which realizes enough control reserve in linear range of modulation.

Obviously, DTC realizes the best load disturbance rejection due to the very high sampling frequency of the torque control loop $f_{s,DTC} = 230$ kHz. The nominal load disturbance has been rejected in about 0.5 ms if DTC is applied.

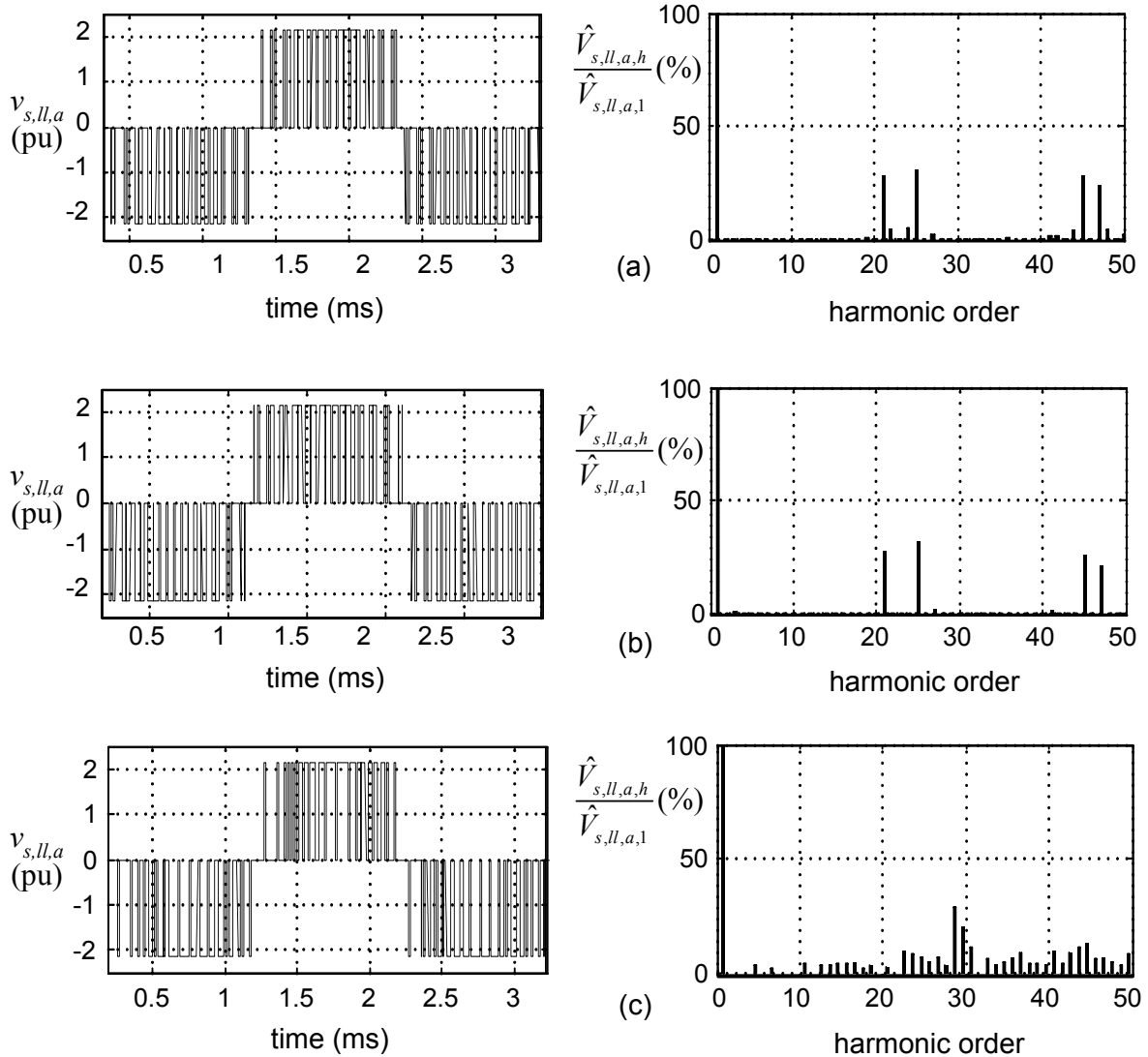


Fig. 3-29 Stator line to line voltage of the high-speed machine at rated load, nominal mechanical speed, and steady-state: (a) RFOC with SRS-PWM; (b) RFOC with ARS-PWM; (c) DTC

RFOC with ARS-PWM features a better load disturbance rejection compared to RFOC with SRS-PWM as shown in Fig. 3-28. The nominal load disturbance has been rejected in about 1.5 ms and 3.5 ms in rotor-flux-oriented high-speed drive with ARS-PWM and SRS-PWM, respectively. However, twice the sampling frequency of the current control loop of RFOC with SRS-PWM is required in the case of RFOC with ARS-PWM.

Steady-state performance of RFOC with SRS-PWM and ARS-PWM as well as the steady-state performance of DTC for the HSIMD are shown in Fig. 3-29 (stator line to line voltage) and Fig. 3-30 (stator phase current). Obviously, RFOC causes well defined voltage and current spectra in contrast to the broad spectra of DTC. THD of the line to line stator voltage and stator current for all three control methods are given in Table 3.8. As depicted in Table 3.8, the investigated HSIMD produces considerable torque ripple ($THD_{T_{em}} = 20\%$) due to the low frequency ratio and lower stray inductance ($L_{IS} + L_{IR}$) than standard induction machines [4].

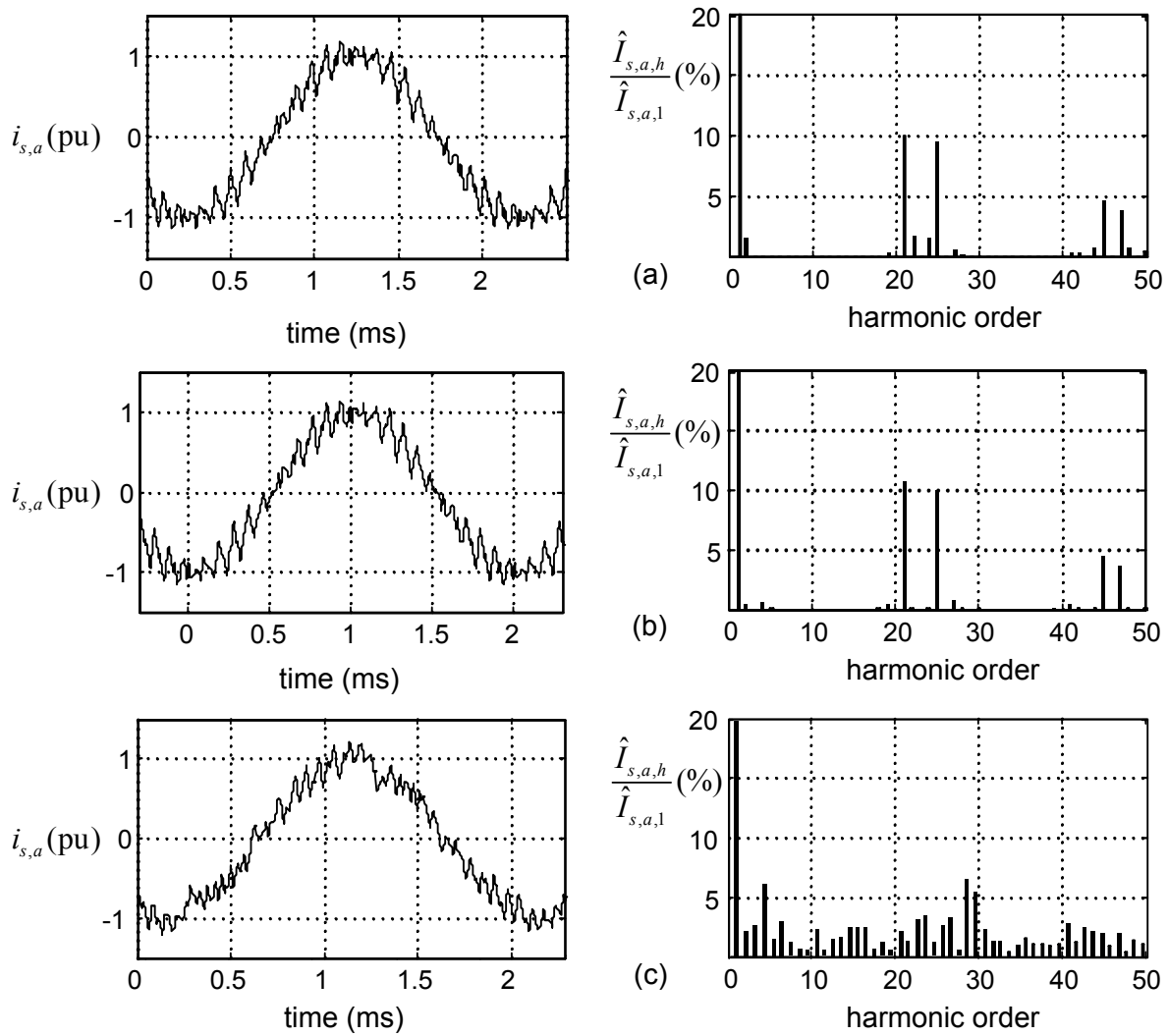


Fig. 3-30 Stator phase current of the high-speed machine at rated load, nominal mechanical speed, and steady-state: (a) RFOC with SRS-PWM; (b) RFOC with ARS-PWM; (c) DTC

According to the simulation results, the corresponding value for a standard induction machine drive ($V_{S,ll,n} = 400$ V, $I_{S,n} = 104$ A, $P_{mech,n} = 44$ kW, $f_{0M} = 50$ Hz) fed by a 2L VSC with $V_{dc} = 700$ V and SRS-PWM with $f_C = 4$ kHz ($m_f = 80$) is about $THD_{T_{em}} = 5\%$.

Application of a sine LC-filter between the converter and the HSIM is an attractive solution to reduce the current and torque ripple [57]. The LC-sine filter features further advantages like reduced stress on the stator windings isolation. In the case of RFOC, the LC-filter can be designed to achieve a significant damping at harmonics around the first carrier band while the LC-filter of drive with DTC should damp the lower order harmonics (Fig. 3-30 (c)) which leads to the need for a bigger filter.

To summarize, HSIMD controlled by DTC features a better load disturbance rejection as compared to the drive controlled by RFOC. However, a higher sampling frequency and fast current sensors are required if the DTC is applied as the control strategy of the HSIMD. Moreover, considering the harmonic spectra of the electromechanical torque and the stator current and voltage, a bigger LC-filter is required in the case of DTC as compared to RFOC (e.g. to reduce $THD_{T_{em}}$ at the given switching frequency). If an LC-filter is applied to reduce the torque THD to a desired value for both RFOC and DTC with a comparable dc-link

voltage, a bigger filter inductance in case of DTC increases in the electromechanical torque rise time compared to the HSIMD with RFOC.

Table 3.9 presents features, advantages, and disadvantages of RFOC with SRS-PWM, RFOC with ARS-PWM, and DTC for the control of the exemplary HSIMD. As shown in Fig. 3-28, RFOC with ARS-PWM features a better torque response as compared to RFOC with SRS-PWM. Consequently, the disturbance rejection is improved in the case of RFOC with ARS-PWM.

Table 3.9

Features of RFOC and DTC for the exemplary high-speed drive fed by a 2L VSC ($V_{S,ll,n} = 400$ V, $I_{S,n} = 38,25$ A, $P_{mech,n} = 20$ kW, $f_{0M} = 500$ Hz, $n_{syn,n} = 30,000$ rpm, $V_{dc} = 700$ V)

Control strategy	RFOC		DTC
Switching frequency,	constant ($f_{sw} = 11.5$ kHz)		variable ($f_{sw,average} = 11.53$ kHz)
Sampling frequency of the inner control loop	SRS-PWM	ARS-PWM	very high ($f_{s,DTC} = 230$ kHz)
	low ($f_{s,cc} = 11.5$ kHz)	moderate ($f_{s,cc} = 23$ kHz)	
LC-sine filter	small		big (or increased $f_{sw,average}$)
Control algorithm	complex abc \rightarrow dq projections, linear controllers, and decoupling circuit		Simple abc \rightarrow $\alpha\beta$ projections and hysteresis controllers
Parameter sensitivity	High sensitivity to rotor parameters and sensitive to stator parameters		sensitive to stator resistance
Direct controlled variables	stator currents		torque
Required time for Load disturbance rejection	SRS-PWM	ARS-PWM	excellent (0.5 ms)
	good (3.5 ms)	very good (1.5 ms)	
Coordinate system	Rotating coordinate synchronous to rotor flux		Stator fixed stationary coordinate
Estimated variables	Rotor flux vector		Torque and stator flux vector
Measured variables for speed control	Stator currents and rotor speed		Stator currents, stator voltages, and rotor speed

The main advantage of DTC for HSDs is the excellent dynamic performance which is not very essential in high-speed drive applications. A significantly high sampling frequency and consequently the requirement of an expensive control platform are the disadvantages of DTC for HSDs. Furthermore, a big LC-filter is required to damp the low order harmonics of the electromechanical torque.

RFOC features a satisfactory dynamic performance with a lower sampling frequency compared to DTC. Therefore, simpler control platforms can be applied. Due to the well defined behavior of PWM in RFOC, smaller LC-filter is required to reduce the THD of the electromechanical torque. Hence, RFOC is more desirable in high-speed induction machine drive applications like microturbines and spindles.

Sensorless control

RFOC and DTC with speed sensor have been investigated for the exemplary HSIM. However, application of control strategies without speed sensor is more desirable especially for very high-speed drives. The electrical drives without mechanical sensors (speed and

position sensors) are referred to as sensorless drives. Sensorless drives are attractive due to features like [19]:

- Reduced hardware expense,
- Increased mechanical robustness,
- Higher reliability and decreased maintenance requirements,

However, sensorless drives can not operate appropriately at very low frequencies [19].

Several RFOC and DTC methods without speed measurement have been proposed for standard induction machine drives in recent literature (e.g. [10], [19]). For example, the following techniques have been applied for sensorless control strategies:

- Open loop estimator using stator voltages and currents [10],
- Model reference adaptive system [50],
- Observers (Kalman, Luenberger) [69],
- Estimators using artificial intelligence [68].

All the above mentioned techniques can be applied in case of HSIMDs to omit the speed sensor [32]. As mentioned, application of sensorless techniques becomes more significant in case of very high- speed drives [71].

3.6.2 Experimental investigations of the RFOC

As concluded in the previous section, RFOC with ARS-PWM is a suitable control strategy for HSIMs. Since the simulated HSIM was completed after the completion of this work [4], a standard IM has been applied to verify the operation of simulated RFOC with SRS-PWM and ARS-PWM.

A schematic of the applied test bench is shown in Fig. 3-31. A 400 kVA line transformer provides the grid voltage. The dc motor (DCM) fed by a 4Q-B6C is used to load the IM. The IM is connected to a 2L VSC which realizes torque and speed control on the basis of a rotor-flux-oriented control with SRS-PWM and ARS-PWM. Photographs of the low speed drive test bench are shown in Fig. 3-32.

The control system is realized by an ABB OPCoDe control platform [133]. The control system is based on a power PC board linked to a host PC. Control tasks with higher priorities (e.g. protection) are realized by means of local programmable devices. The control structure depicted in Fig. 3-24 (a) is applied in order to control of the standard IM.

Converter switching frequency is 4 kHz ($m_f = 80$) and the sampling frequency of the current control loop is 4 kHz and 8 kHz for RFOC with SRS-PWM and ARS-PWM, respectively. Sampling frequency of speed control loop for RFOC with both SRS-PWM and ARS-PWM is 4 kHz. Stator currents on the direct and quadrature axis are limited to 1.5 pu. Basic parameters of the converter and the control system are summarized in Table 3.10. The induction machine has two pole pares and a synchronous speed of 1500 rpm. The nominal mechanical power equals 44 kW.

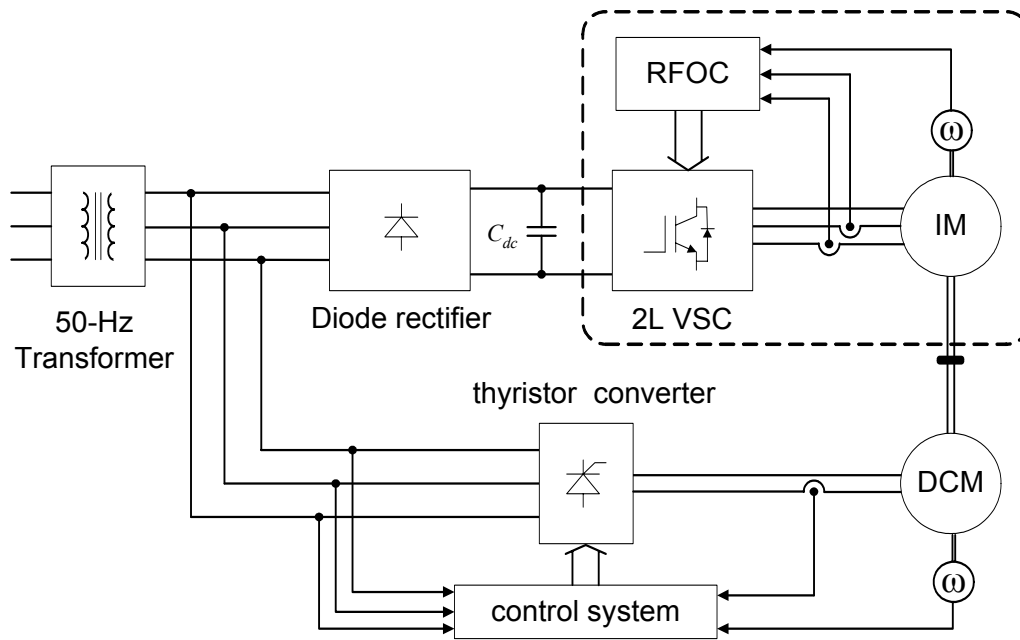


Fig. 3-31 A block diagram of the test bench of induction machine drive

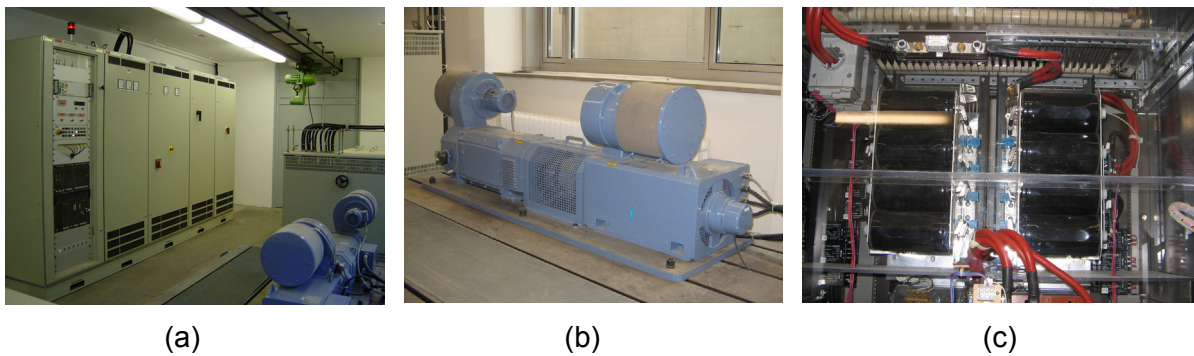


Fig. 3-32 Photographs of the standard drive test bench (a), induction machine and dc-machine (b), 2L VSC of the induction machine (c)

Table 3.10

Basic data of the converter and control system for the standard induction machine drive

Parameter	Value	
IGBTs	SKiiP 642GH120-2*208CTV	
Carrier frequency, f_c	4 kHz	
DC-link voltage, V_{dc}	560 V	
Sampling frequency of current control loop, $f_{s,cc}$	SRS-PWM	ARS-PWM
	4 kHz	8 kHz
Sampling frequency of speed control loop, $f_{s,sc}$	4 kHz	
Current control loop damping factor, a_{cc}	3	
Speed control loop damping factor, a_{sc}	4	

Table 3.11
Data and parameters of the standard induction machine

Parameter	Value
Nominal rms stator line-to-line voltage, $V_{s,ll,n}$	320 V
Base voltage of machine side per unit system, $V_{b,M}$	$V_{b,M} = \sqrt{2}v_{s,ll,n}/\sqrt{3}$
Nominal rms stator current, $I_{s,n}$	104.5 A
Base current of machine side per unit system, $I_{b,M}$	$I_{b,M} = \sqrt{2} I_{s,n}$
Rated load power factor, $\cos(\varphi_M)$	0.85
Nominal stator frequency, f_{0M}	50 Hz
Number of pole pairs, Z_p	2
Nominal synchronous speed, $n_{syn,n}$, $N_b = n_{syn,n}$	1500 rpm
Nominal mechanical power, $P_{mech,n}$	44 kW
Moment of inertia, J	0.483 Kgm ²
Nominal electromechanical torque, $T_{em,n}$, $T_{em,b} = T_{em,n}$	280 Nm
Nominal stator flux, $\psi_{S,n}$	0.8165 Wb
Nominal rotor flux, $\psi_{R,n}$	0.7798 Wb
Stator resistance, R_S	0.038 Ω
Rotor resistance, R_R	0.032 Ω
Stator leakage inductance L_{lS}	0.5 mH
Rotor leakage inductance L_{lR}	0.5 mH
Mutual inductance, L_M	12.46 mH

Speed step response and load disturbance rejection are investigated to analyze the dynamic performance of the rotor-flux-oriented controlled IM with SRS-PWM and ARS-PWM. Both simulation and experimental results are presented. MATLAB/SIMULINK is used in the simulation. All parameters of the controllers are the same in the simulation and experiment.

Simulation and experimental results for speed step response of RFOC with SRS-PWM are shown in Fig. 3-33 (a) and (b), respectively. The speed set point is changed stepwise from 0.5 pu (750 rpm) to 0.967 pu (1450 rpm). The mechanical speed show a linear rise with a constant mechanical torque and the stator current is amplitude limited to 1.5 pu. Simulation and experimental results for the same speed step change for RFOC with ARS-PWM are shown Fig. 3-33 (c) and (d), respectively. The electromechanical torque is filtered in both simulation and experimental results to obtain the average torque.

The main difference between simulation and experimental results is the maximum amplitude of the electromechanical torque and consequently the rotor speed rise time. In the simulation results, the maximum amplitude of the electromechanical torque is 1.7 pu and the rotor speed varies from 0.5 pu to 0.967 pu in about 75 ms. In the experimental results the electromechanical torque is limited to 1.2 pu and the required time to change the rotor speed from 0.5 pu to 0.967 pu is about 120 ms. The main reasons for the difference between simulation and experimental results are summarized in the following:

- All speed and current sensors are considered to be ideal sensors in simulation,
- An ideal IM is used in simulation and the parameters deviation as well as the saturation is ignored,
- Ideal semiconductor device behavior is considered in simulation.

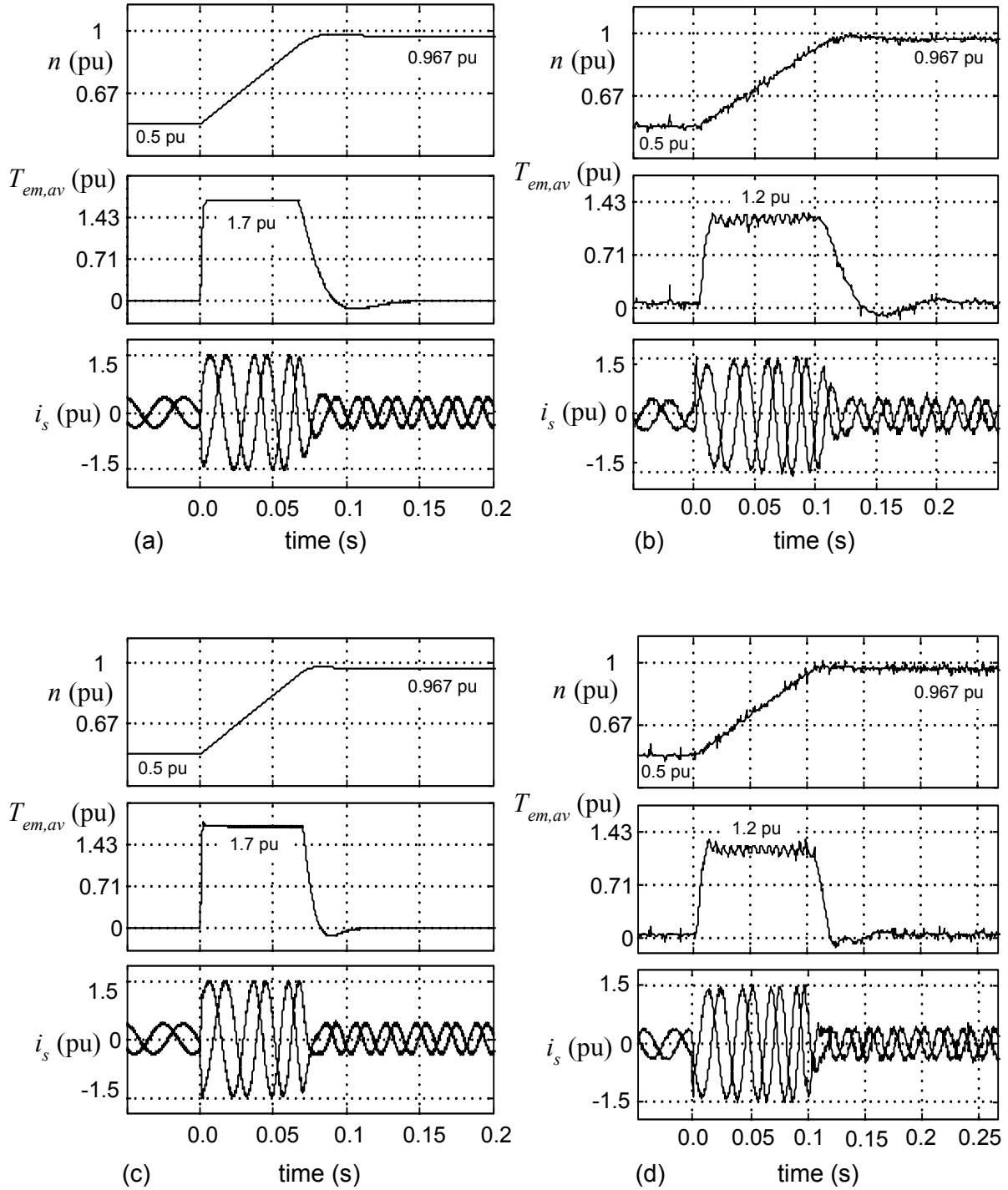


Fig. 3-33 Speed step response of the standard induction machine: (a) and (b) simulation and experimental results for RFOC with SRS-PWM; (c) and (d) simulation and experimental results for RFOC with ARS-PWM; $N_b = 1500$ rpm, $T_{em,b} = 280$ Nm, $I_{b,M} = 147.8$ A

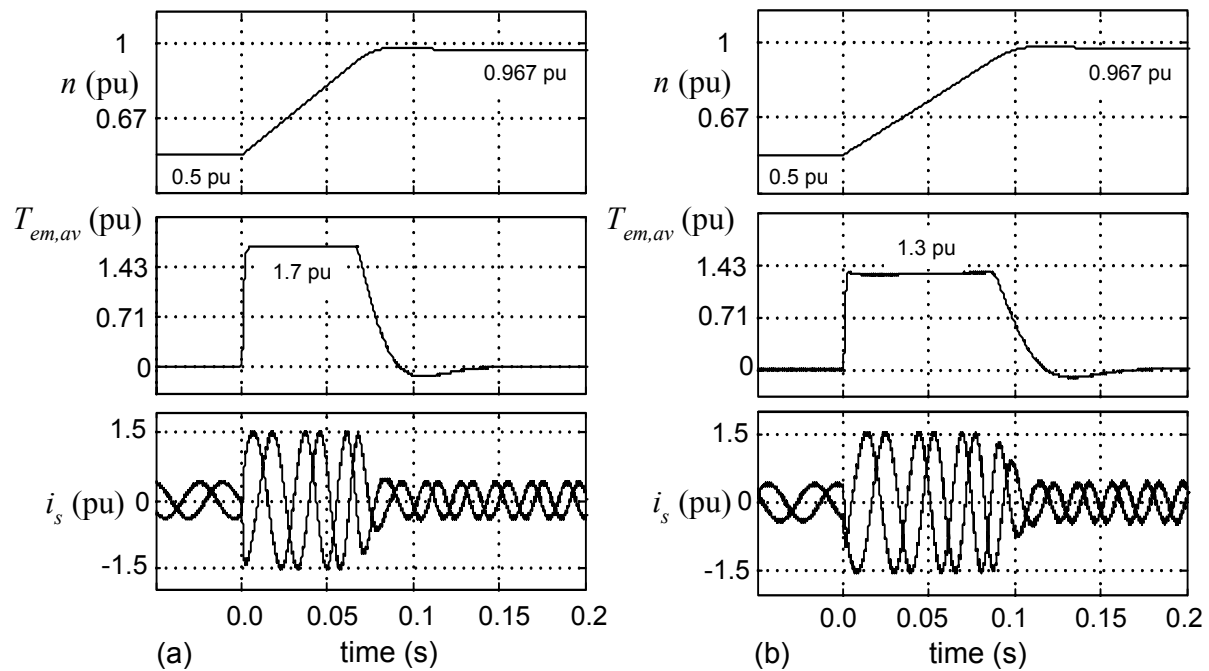


Fig. 3-34 Influence of the main inductance saturation on the transient performance (speed step response): (a) speed step response with the same parameters in control system and the machine; (b) speed step response with 20 % saturation of the main inductance of the machine; $N_b = 1500$ rpm, $T_{em,b} = 280$ Nm, $I_{b,M} = 147.8$ A

Simulation results for the influence of the IM main inductance saturation on the speed step response of the standard induction machine drive are shown in Fig. 3-34. Stator currents are limited to 1.5 pu and the speed set point has a step change from 0.5 pu to 0.967 pu. Fig. 3-34 (a) depicts the simulation results for the speed step response with no deviation between the real machine parameters and the parameters of IM as applied in the control system. In Fig. 3-34 (b), 20 % saturation of the main inductance is considered for the induction machine. Because of the saturation and the consequent flux amplitude reduction, the maximum amplitude of the electromechanical torque is reduced to 1.3 pu. Obviously, maximum amplitude of the stator current is limited to 1.5 pu in both cases.

Simulation and experimental results for disturbance rejection of the-rotor-flux oriented controlled IM with SRS-PWM and ARS-PWM are shown in Fig. 3-35. The dc machine shown in Fig. 3-31 is used to load the induction machine drive. In the simulation, a step load disturbance with amplitude of 90 % is applied. The same amplitude of the load disturbance is applied in the experiment. However, generating an ideal step mechanical load with the dc machine is not realizable. As shown in Fig. 3-35, RFOC with ARS-PWM features a better load disturbance rejection as compared to RFOC with SRS-PWM. The load disturbance rejection time is reduced by about 50 % if ARS-PWM is applied. Moreover, the speed drop in the transient is reduced significantly in the case of RFOC with ARS-PWM.

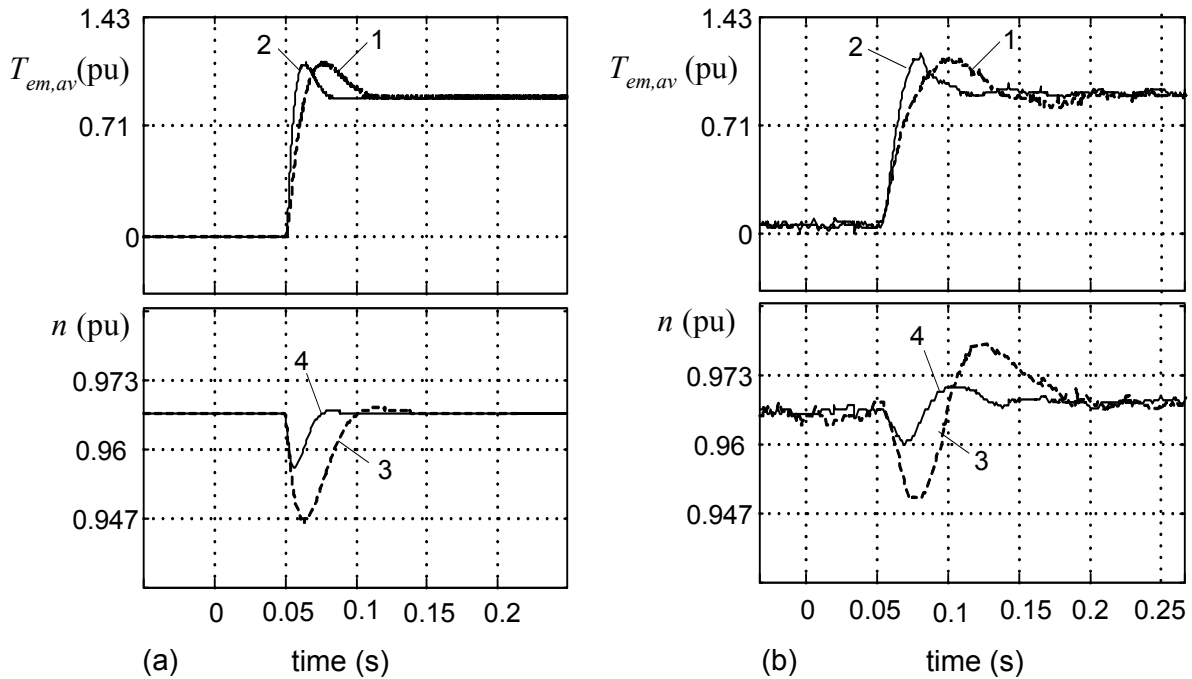


Fig. 3-35 Disturbance rejection of rotor-flux-oriented controlled induction machine with SRS-PWM and ARS-PWM: (a) simulation results; (b) experimental results; 1 and 3: electromechanical torque and rotor speed for RFOC with SRS-PWM; 2 and 4: electromechanical torque and rotor speed for RFOC with ARS-PWM; $N_b = 1500$ rpm, $T_{em,b} = 280$ Nm

3.7 Comparison of 2L VSC and 3L-NPC VSC for the high-speed induction machine drive with RFOC

Comparison of 2L VSC and 3L-NPC VSC for a HSIMD has been described in [58]. A comprehensive comparison with more details will be carried out in this subchapter.

The type of the converter which feeds the HSIM does not substantially affect the drive dynamic performance [58]. However, the effect of the topology on the machine and converter losses, voltage stress of the stator windings, and the torque ripple is undeniable. Converters which are connected to high-speed machines differ from standard converters due to the drastically increased fundamental frequency. Obviously, a lower value of the machine harmonic losses in the case of high-speed machines, considering the high power density of the high-speed machine, is very important.

In this subchapter the effect of the converter topology (2L VSC and 3L-NPC VSC) on the machine torque ripple is investigated for two different operating conditions. In a first step both converters operate at an identical carrier frequency of $f_c = 11.5$ kHz. In a second step the carrier frequency of the 2L VSC is varied so that the harmonic distortion of the machine torque is comparable to that of the 3L-NPC VSC applying a carrier frequency of $f_c = 11.5$ kHz. Then the installed switch power, converter losses, and converter efficiency for both cases are investigated and compared.

Fig. 3-36 show the waveform and the spectrum of the electromechanical torque of the exemplary HSIM which is fed by a 2L VSC (Fig. 3-36 (a)) and a 3L-NPC VSC (Fig. 3-36 (b)). The carrier frequency of both converters is $f_c = 11.5$ kHz ($m_f = 23$). It can be seen that, with an identical carrier frequency, the torque THD and the maximum torque ripple of the

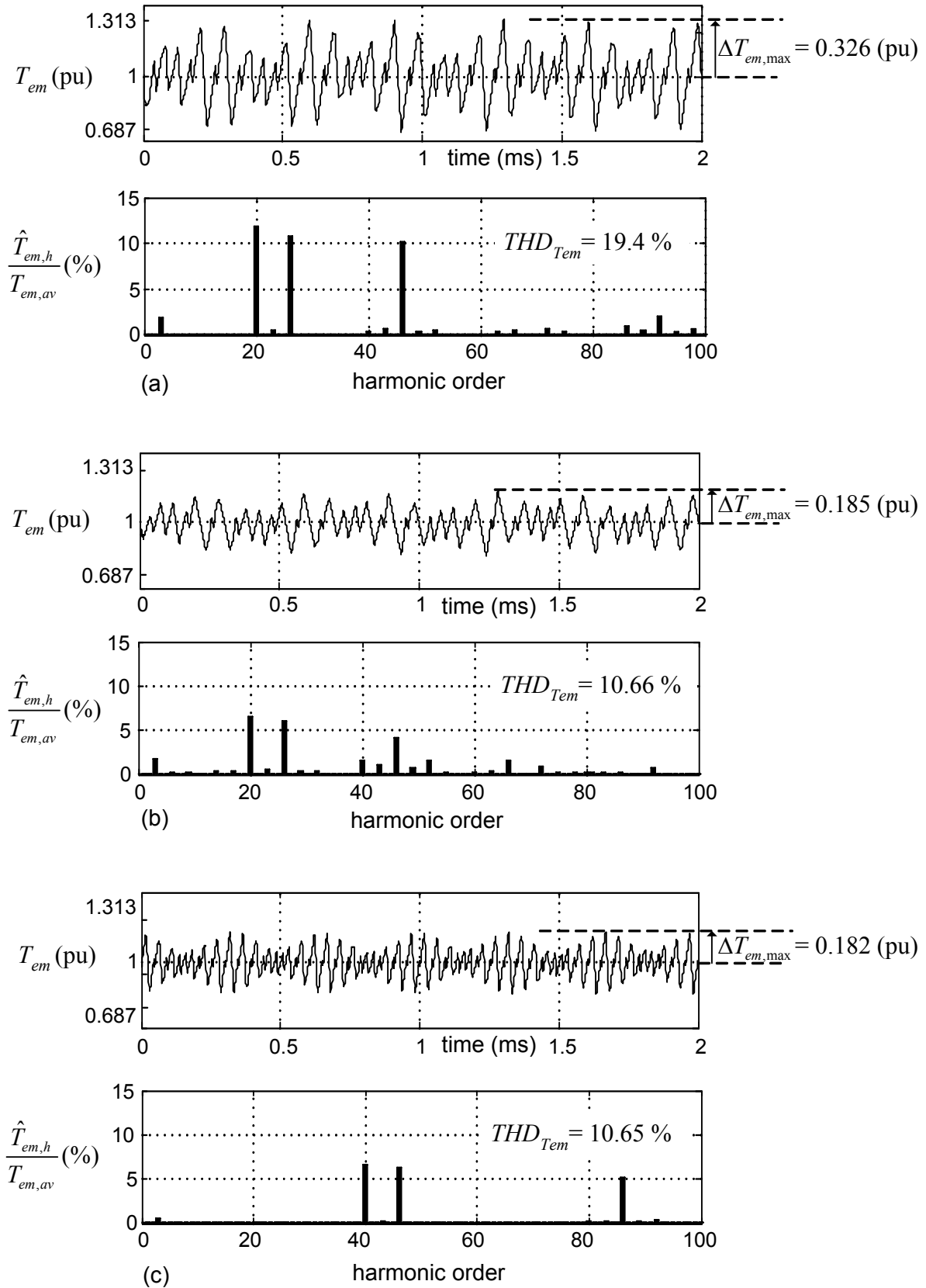


Fig. 3-36 Electromechanical torque and corresponding spectra of the exemplary high-speed induction machine fed by: (a) 2L VSC; $f_c = 11.5$ kHz; (b) 3L -NPC VSC; $f_c = 11.5$ kHz; (c) 2L VSC; $f_c = 21.5$ kHz

HSIM being fed by the 2L VSC is about 87 % and 76 % larger as compared to the values if a 3L-NPC VSC had been connected to the HSIM.

To reduce the torque THD of the HSIM fed by the 2L VSC, the carrier frequency f_c has to be increased, since the harmonic values of the inverter voltage and current of a 2L VSC are substantially higher than those of a 3L-NPC VSC at a constant carrier frequency [75]. An increase of the carrier frequency will shift the carrier bands occurring at $n f_c$ to higher frequencies of the harmonic voltages, causing a better damping of the harmonic currents. The carrier frequency of the 2L VSC was determined at 21.5 kHz to achieve the same torque THD ($\text{THD}_{\text{Tem}} = 10.66\%$) as in the HSIM applying 3L-NPC VSC at a carrier frequency of $f_c = 11.5$ kHz. The electromechanical torque of the HSIM fed by the 2L-VSC with a carrier frequency of $f_c = 21.5$ kHz ($m_f = 43$) and corresponding spectrum are shown in Fig. 3-36 (c). Obviously, the torque ripple of the HSIM fed by 2L VSC ($f_c = 21.5$ kHz) is comparable to the torque ripple if a 3L-NPC VSC ($f_c = 11.5$ kHz) feeds the HSIM.

It should be noted that the simulation results of Fig. 3-36 are for converters with ideal behavior of the semiconductor devices. However, a typical dead time of 2-3 μs is required in the implementation of the converters with IGBTs. The dead time influences the converter output voltage [13] which is especially considerable in case of HSDs, due to high switching frequencies. The effects of the dead time on the converter output voltage can be reduced using a dead time compensation algorithm (e.g. [77]).

3.7.1 Converter design

Table 3.12 summarizes the design of the power semiconductors for 2L VSC and 3L-NPC VSC for the exemplary HSIM. Parameters of the HSIM and the basic converter parameters are listed in Table 3.1 and Table 3.2. $V_{CE,n}$ and $I_{C,n}$ denote the rated collector emitter voltage and the nominal current of the IGBTs. The voltage V_{com} describes the commutation voltage of the corresponding commutation cells. The current rating $I_{C,n}$ of each power semiconductor is determined by the occurring device losses in a worst case operating point, the maximum junction temperature $T_{j,max} = 125^\circ\text{C}$, and the thermal resistances of IGBTs and diodes. The simulations are based on the losses given in the IGBT datasheets by applying a natural sampled PWM with added third harmonics.

The losses were determined by converter simulations using an earlier developed accurate semiconductor loss model [3], [5], [43], [52], [65]. In order to calculate the converter power

Table 3.12

Semiconductor specifications for 2L VSC and 3L-NPC VSC for the high-speed induction machine drive ($V_{s,ll,n} = 400\text{V}$; $I_{s,n} = 38.25\text{A}$; $T_{j,max} = 125^\circ\text{C}$)

Converter topology	2L-VSC	3L-NPC VSC	2L-VSC
	$f_c = 11.5$ kHz	$f_c = 11.5$ kHz	$f_c = 21.5$ kHz
Nominal dc-link voltage, V_{dc}	700 V	700 V	700 V
Commutation voltage, V_{com}	700 V	350 V	700 V
Rated device voltage/current, $V_{CE,n} / I_{C,n}$	1.2 kV / 50 A	600 V / 50 A	1.2 kV / 100 A
	IGBT	IGBT	IGBT
Installed switch power, S_s (3-111)	360 kVA	360 kVA + 90 kVA (NPC-diodes)	720 kVA

losses, the conduction and switching power losses of IGBTs and diodes of each half-bridge are taken into consideration. Then the total converter power loss, device thermal resistances, and the heat-sink temperature are applied to estimate the junction temperature. It is assumed that all IGBT modules have been mounted on a single heat-sink. Information about output characteristics of IGBTs and diodes as well as the switching loss energy presented in product datasheets [141] are applied to determine the power losses. In order to realize an accurate power loss estimation, output characteristic and switching loss energy are modelled as nonlinear first order functions of IGBT or diode current [52], [65], [143].

The output characteristics of IGBTs and diodes can be approximated by

$$v_{CE,T}(t) = v_{0,T} + A_{cond,T} \cdot i(t)^{B_{cond,T}}, \quad (3-102)$$

$$v_{F,D}(t) = v_{0,D} + A_{cond,D} \cdot i(t)^{B_{cond,D}}, \quad (3-103)$$

where

$v_{CE,T}$ is IGBT on-state collector-emitter voltage,

$v_{F,D}$ is diode on-state anode-cathode voltage,

$v_{0,T}$ and $v_{0,D}$ are threshold voltage,

$A_{con,T}$, $B_{con,T}$, $A_{con,D}$, and $B_{con,D}$ are the curve-fitted constants,

$i(t)$ is the instantaneous value of the device current.

IGBTs and diodes are shown with T and D , respectively.

According to (3-102) and (3-103), the conduction power losses of IGBTs and diodes are as follows:

$$P_{loss,cond,x} = \frac{1}{T_1} \int_0^{T_1} (v_{0,x} + A_{cond,x} \cdot i(t)^{B_{cond,x}}) \cdot i(t) \cdot dt, \quad x = D, T, \quad (3-104)$$

where, T_1 is the fundamental period.

Commutation processes which create switching losses are classified into inductive and capacitive commutation. The inductive commutations are characterized by the turn-on losses of the active switches and the recovery losses of diodes. Capacitive commutation is characterized by turn-off losses of the active switches [5].

Similar to the approximation applied for the output characteristics, the switching loss energy offered in datasheets can be approximated by a first order nonlinear function of the device current. Applied function for the IGBTs turn-on and turn-off loss energy ($E_{sw,on,T}$, $E_{sw,off,T}$) and the diode recovery loss energy ($E_{sw,rec,D}$) are as follows

$$E_{loss,sw,on,T}(t) = A_{sw,on,T} \cdot i(t)^{B_{sw,on,T}}, \quad (3-105)$$

$$E_{loss,sw,off,T}(t) = A_{sw,off,T} \cdot i(t)^{B_{sw,off,T}}, \quad (3-106)$$

$$E_{loss,sw,rec,D}(t) = A_{sw,rec,D} \cdot i(t)^{B_{sw,rec,D}}, \quad (3-107)$$

where

$E_{loss,sw,on,T}$ and $E_{loss,sw,off,T}$ are IGBT turn-on and turn-off loss energy,

$E_{loss,sw,rec,D}$ is diode recovery loss energy,

$A_{sw,on,T}$, $B_{sw,on,T}$, $A_{sw,off,T}$, $B_{sw,off,T}$, $A_{sw,rec,D}$, and $B_{sw,rec,D}$ are the curve-fitted constants.

If the commutation voltage v_{com} of the IGBTs as well as the diodes differ from the commutation voltage $v_{com,ref}$ at which the measurement of the loss energy has been carried out, the following modification is required to estimate the actual loss energy [3], [45]:

$$E_{loss,sw,T}(i(t)) = \left(A_{sw,on,T} \cdot i(t)^{B_{sw,on,T}} + A_{sw,off,T} \cdot i(t)^{B_{sw,off,T}} \right) \frac{v_{comm}(t)}{v_{com,ref}}, \quad (3-108)$$

$$E_{loss,sw,D}(i(t)) = \left(A_{sw,rec,D} \cdot i(t)^{B_{sw,rec,D}} \right) \frac{v_{com}(t)}{v_{com,ref}}. \quad (3-109)$$

The sum of IGBT and diode switching loss energy ($E_{loss,sw,T}$, $E_{loss,sw,D}$) in a fundamental time period T_1 can be used to determine the switching power loss $P_{loss,sw}$.

$$P_{loss,sw} = \frac{1}{T_1} \sum_{j=1}^{j=T_1 \cdot f_{sw}} (E_{loss,sw,T}(j) + E_{loss,sw,D}(j)) \quad (3-110)$$

The total power losses for each device (IGBTs and diodes) is then the sum of the conduction and the switching losses in (3-104) and (3-110). The total module losses can be calculated considering the number of IGBTs and diodes per module. Furthermore, the total converter losses are the sum of all module losses.

Fitting parameters of the IGBT modules which are used in the 2L VSC and 3L-NPC VSC are presented in Table 3.13.

In order to estimate the junction temperatures for an operating point at steady-state, the device total power loss, and the thermal resistance is applied. According to the information for the thermal resistance in data sheet, one of the equivalent thermal circuit diagrams for a module which is shown in Fig. 3-37 is applied. In case that a common case to heat-sink thermal resistance ($R_{th,ch}$) is proposed for all devices of the module (e.g. BSM 50 GB120 DLC and BSM 50 GB 60 DLC), the circuit diagram of Fig. 3-37(b) is used. For the modules with separate case to heat-sink thermal resistance for every device (e.g. BSM 100 GB 120 DLC), the circuit diagram in Fig. 3-37(c) was applied [142].

The accuracy of the given method to determine the converter losses and to estimate the junction temperature is investigated in [3], providing experimental measurements. According to [3], the relative error of the estimated junction temperatures can equal maximally $\pm 30\%$ of the measured values.

3.7.2 Investigation of simulation results

According to the simulation results presented in Table 3.12, the required current rating to achieve a nominal output current is different due to different semiconductor losses in the different converter topologies, while the voltage utilization of the semiconductors is the same for the 2L-VSC and 3L-NPC VSC. The installed switch power of the 2L VSC operating at a carrier frequency of 11.5 kHz is only half, compared to that of the 2L VSC operating at a carrier frequency of 21.5 kHz. The 3L-NPC VSC requires about the same installed switch power as the 2L VSC operating at a carrier frequency of 11.5 kHz. The installed switch power is a measure of the semiconductor expense and is defined as:

$$S_S = V_{CE,n} \cdot I_{C,n} \cdot n_T + 0.5 \cdot V_{RRM} \cdot I_{F,n} \cdot n_D, \quad (3-111)$$

where, V_{RRM} is the repetitive peak reverse voltage of diodes,

Table 3.13
Fitting parameters and thermal resistances of IGBTs / diodes

	BSM 50 GB 120 DLC EUPEC	BSM 100 GB 120 DLC EUPEC	BSM 50 GB 60 DLC EUPEC
$V_{CE,n}$	1200 V	1200 V	600 V
$I_{C,n}$	50 A	100 A	50 A
$V_{o,T}$	0.4 V	0.4 V	0.25 V
$V_{o,D}$	0.25 V	0.4 V	0.5 V
$A_{sw,on,T}$	0.00017171	0.00038093	0.000011710
$B_{sw,on,T}$	0.9284	0.6738	0.9308
$A_{sw,off,T}$	0.00055698	0.00021665	0.000040426
$B_{sw,off,T}$	0.6162	0.8666	0.8069
$A_{sw,rec,D}$	0.00056091	0.0014	0.00024812
$B_{sw,rec,D}$	0.5062	0.4154	0.4621
$A_{cond,T}$	0.2900	0.1524	0.3032
$B_{cond,T}$	0.4895	0.5707	0.4736
$A_{cond,D}$	0.2487	0.1233	0.0762
$B_{cond,D}$	0.4507	0.5127	0.5622
$R_{th-jc,T}$	0.27 K/W	0.16 K/W	0.44 K/W
$R_{th-jc,D}$	0.6 K/W	0.3 K/W	0.8 K/W
$R_{th-ch,T}$	-	0.03 K/W	-
$R_{th-ch,D}$	-	0.06 K/W	-
R_{th-ch}	0.05 K/W	-	0.03 K/W

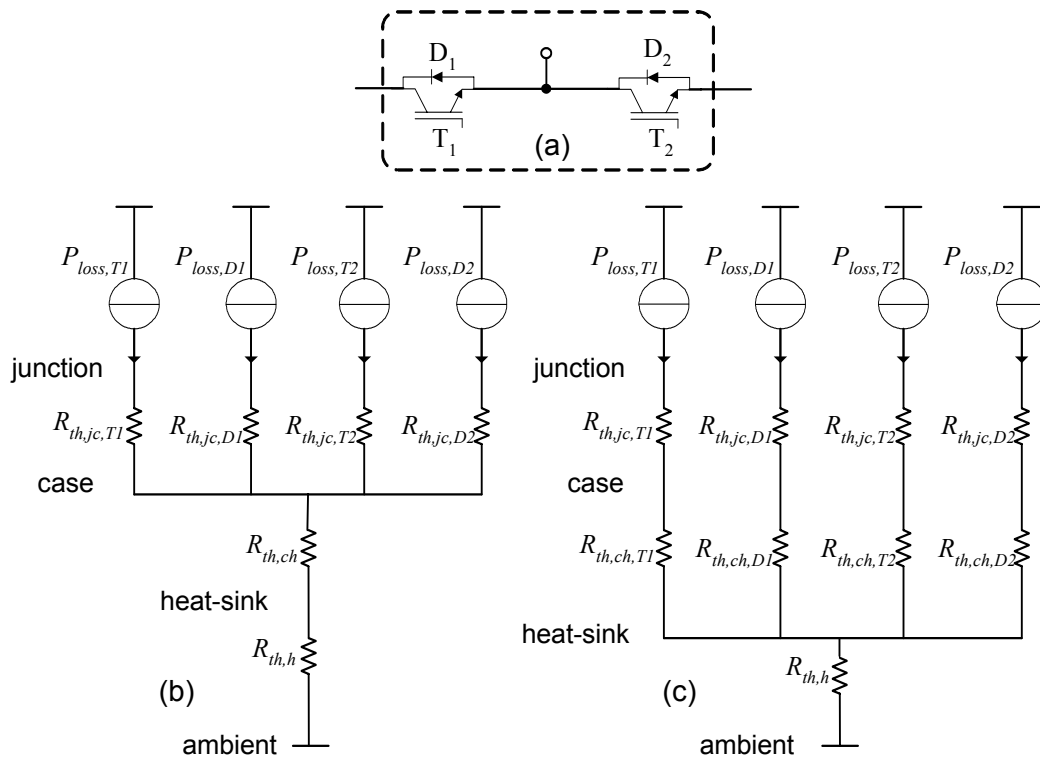


Fig. 3-37 Steady-state equivalent thermal circuit diagram of a half bridge IGBT module (a) with common $R_{th,ch}$ for all IGBTs and diodes (BSM 50 GB120 DLC and BSM 50 GB 60 DLC) (b); with separate $R_{th,ch}$ for IGBTs and diodes (BSM 100 GB 120 DLC) (c)

$I_{F,n}$ denotes the nominal diode current,
 n_T/n_D is the number of IGBTs/diodes in the converter.

Characteristic values for the operation at rated speed and rated load are summarized in Table 3.14. The semiconductor loss distribution of the considered converter topologies is depicted in Fig. 3-38.

Table 3.14
 Comparison of 2L VSC and 3L-NPC VSC for the high-speed induction machine drive

Converter topology	2L-VSC	3L-NPC VSC	2L-VSC
	$f_c = 11.5 \text{ kHz}$	$f_c = 11.5 \text{ kHz}$	$f_c = 21.5 \text{ kHz}$
Torque THD (%)	19.4	10.66	10.65
Torque ripple (%)	32.6	18.5	18.2
Total converter losses (kW)	0.710	0.463	1.231
Total converter losses (%)	3.48	2.27	6.03
Converter efficiency (%)	96.64	97.8	94.3

Obviously, the semiconductor losses of the 2L-VSC are 53% larger than those of the 3L-NPC VSC, if a comparable converter switching frequency $f_c = 11.5 \text{ kHz}$ is assumed (Fig. 3-38). In this case both converters have a comparable installed switch power.

If both 2L-VSC and 3L-NPC VSC realize a constant torque THD ($THD_{Tem} = 10.7 \%$) the semiconductor losses of the 2L-VSC are 166% larger than those of the 3L-NPC VSC with the carrier frequency of $f_c = 11.5 \text{ kHz}$ (Fig. 3-38). Furthermore, the 2L-VSC requires about twice the installed switch power as compared to the 3L-NPC VSC.

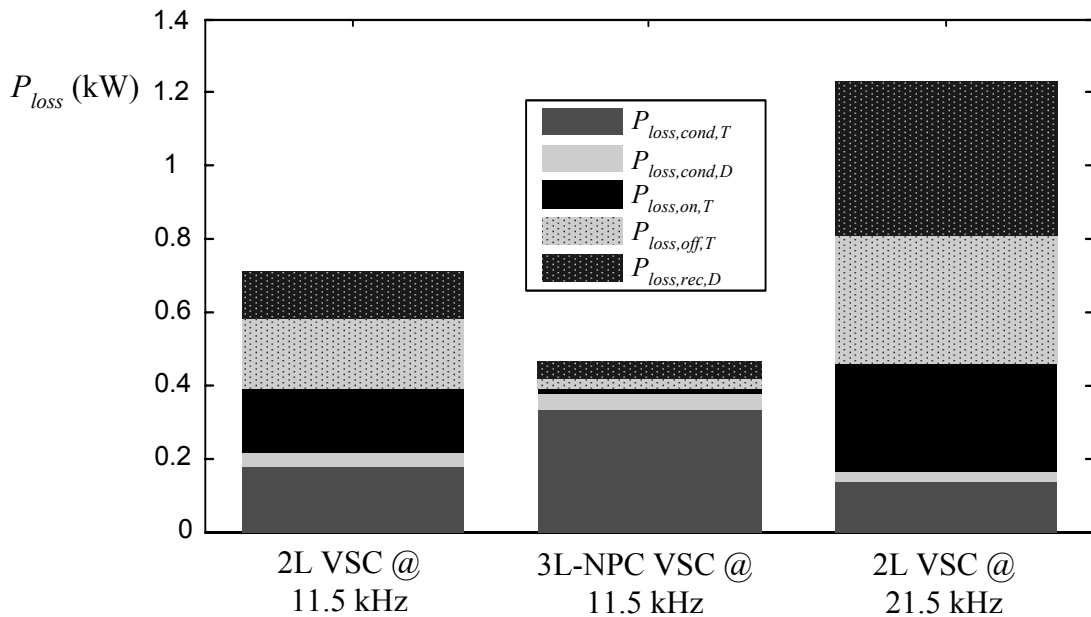


Fig. 3-38 Semiconductor loss distribution at nominal load ($V_{dc} = 700 \text{ V}$; $I_S = 38.25 \text{ A}$); $P_{loss,con,T/D}$: conduction losses of IGBTs/diodes; $P_{loss,on,T/D}$: Turn-on losses of IGBTs; $P_{loss,off,T}$: Turn-off losses of IGBTs; $P_{loss,rec,D}$: Turn-off losses of diodes

The investigated results of Table 3.12, Table 3.14, and Fig. 3-38 depict clearly that 3L-NPC VSCs are substantially more attractive than 2L VSCs in high-speed drives. A detailed comparison of further characteristics of 2L VSC and 3L-NPC VSC for low voltage drives can be taken from [74].

3.8 Summary

RFOC and DTC are compared for an exemplary HSIMD fed by a 2L VSC. A switching frequency of 11.5 kHz ($m_f = 23$) is applied for the RFOC. The electromechanical torque THD with the given frequency ratio is equal to $THD_{Tem} \approx 20\%$ for RFOC with both SRS-PWM ($f_{s,cc} = 11.5$ kHz) and ARS-PWM ($f_{s,cc} = 23$ kHz).

The sampling frequency of the torque and flux control loop for DTC is determined to 230 kHz to realize a comparable torque THD of $THD_{Tem} \approx 20\%$. In this case, the average switching frequency of DTC is 11.53 kHz.

For the applied sampling frequencies for RFOC ($f_{s,cc} = 11.5$ kHz for SRS-PWM and $f_{s,cc} = 23$ kHz for ARS-PWM) and DTC ($f_{s,DTC} = 230$ kHz), the DTC features the best load disturbance rejection capability with a disturbance rejection time of 0.5 ms. RFOC with ARS-PWM and SRS-PWM realize a disturbance rejection time of 1.5 ms and 3.5 ms, respectively.

Spectrum analysis of the electromechanical torque for the DTC shows low order harmonics while the RFOC cause a well defined torque spectrum with harmonics at switching frequency and times of the switching frequency. Consequently, DTC requires a larger LC-filter to reduce the torque THD at the given switching frequency.

The main advantage of the DTC for HSIMDs is the excellent dynamic performance which is not very essential in high-speed drive applications. A significantly higher sampling frequency and consequently the requirement of an expensive control platform are the disadvantages of DTC for HSDs. Furthermore, a large LC-filter is required to damp the low order harmonics of the electromechanical torque.

RFOC features a satisfactory dynamic performance for HSIMDs with a lower sampling frequency as compared to DTC. Therefore, simpler control platforms can be applied. Due to the well defined behavior of PWM in RFOC, a smaller LC-filter is required to reduce the THD of the electromechanical torque. Hence, the RFOC is more desirable for the control of HSIMDs.

Application of a 3L-NPC VSC instead of a 2L VSC in high-speed drives is an attractive solution to reduce the voltage stress of the stator windings, electromechanical torque ripple, and converter power losses. The investigations which are carried out in this thesis show that at a constant carrier frequency of 11.5 kHz for the exemplary HSIM ($V_{S,ll,n} = 400$ V, $I_{S,n} = 38.25$ A, $P_{mech,n} = 20$ kW, $f_{0M} = 500$ Hz), power losses of the 3L-NPC VSC are about 50 % lower than the power loss of the 2L VSC. Both converters have a comparable installed switch power in this case.

If the switching frequency of the 2L VSC is increased so that both converters generate a comparable torque THD (e.g. $THD_{Tem} = 10.7\%$), the semiconductor power losses of the 2L VSC are about 166% higher than that of the 3L-NPC VSC. Furthermore, the 2L VSC requires twice the installed switch power as compared to the 3L-NPC VSC.

Chapter 4

PWM Active Front End Converters

Subject of this chapter is the investigation of a PWM active front end converter with L- or LCL-filter between converter and grid. Voltage-oriented control is applied as the control strategy of PWM active front end converter. At first, transient and steady-state performance of active front end converter with L-filter connected to an ideal as well as distorted grid is investigated, using simulation and experimental results.

Secondly, an iterative procedure to design L- and LCL-filter parameters is proposed. The main goal of the filter design procedure is to meet the IEEE-519 limits for the grid current harmonics. The procedure uses the analytical expression of converter voltage harmonics by Bessel functions. The stored energy of the filter passive components as a measure for expense of the components is considered exemplarily to compare different LCL-filter designs.

Finally, an active damping scheme of current control loop is applied to avoid LCL-filter resonances. Simulation and experimental results are applied to investigate the transient and steady-state performance of active front end converter with LCL-filter.

4.1 Advantages and disadvantages of PWM active front end converters

PWM voltage source converters are increasingly applied as active front end converters in low-voltage drives for reasons such as strict international grid standards and emerging applications like regenerative energy sources (e.g. microturbines) [84], [89], [90], [91], [95], [116], [122].

The main **advantages** of PWM active front end converters with voltage dc-link are [12]:

- **Bidirectional power flow:** Due to this feature, PWM active front end converters are very attractive for distributed power generation systems (e.g. microturbines and wind turbines) and applications with a high share of regenerative energy such as cranes, elevators, and high-speed drives with a high inertia.
- **Sinusoidal input current:** Input current of PWM active front end converters connected to a grid has a sinusoidal waveform with current harmonics occurring in carrier frequency and times of carrier frequency in principle. Current harmonics can be damped by an input filter (e.g. L- or LCL-filter). This feature of PWM active front end converters is very beneficial as compared to passive front ends (e.g. diode front ends) in the case that grid current harmonics are restricted by grid standards like IEEE-519 [97]. Diode and thyristor rectifiers cause low-order current harmonics (e.g. $h = 6n \pm 1$; $n = 1, 2, 3, \dots$) and voltage notches which require a substantially higher filter expense to be damped [12].
- **Adjustable power factor:** Diode rectifiers have an unchangeable displacement power factor ($DPF = P/S_1$, P is input active power, and S_1 denotes the fundamental component of input apparent power [13]). In thyristor active rectifiers DPF varies with variation of

dc-link voltage [13]. In PWM active front end converters DPF at point of common coupling can be adjusted separately thanks to decoupling control of the active and reactive power [111].

- **Adjustment of dc-link voltage:** PWM active front end converters with voltage dc-link operate as boost converter with a fixed dc-link voltage polarity. Amplitude of dc-link voltage is theoretically adjustable for all voltages greater than amplitude of the grid line-to-line voltage. Amplitude of the dc-link is practically limited according to blocking capability of the applied semiconductor devices (e.g. IGBTs).

However, PWM active front end converters have also some **disadvantages**. These converters require a relative complex control structure. Active semiconductor devices (e.g. IGBTs) are needed, which cause extra switching losses compared to diode rectifiers. Moreover, a high switching frequency in PWM active front end converters can lead to electromagnetic interferences (EMI) which have to be limited by corresponding filters.

4.2 Mathematical description of PWM active front end converters

A block diagram of the power part of a PWM active front end converter with L-filter is shown in Fig. 4-1. The grid side converter (GC) is a 2L VSC which is connected by an L-filter to the grid at the point of common coupling (PCC).

The grid is modeled as an ideal voltage source in series with the grid stray inductance L_G and the grid resistance R_G . The grid phase voltage and the grid phase current are expressed by $v_{G,x}$ and $i_{G,x}$ where $x = a, b, c$. Grid and PCC line-to-line voltages are denoted by $v_{G,ll,x}$ and $v_{PCC,ll,x}$, respectively.

The output phase voltage of the converter is shown by $v_{GC,x}$ and $i_{GC,x}$ denotes the phase current of the grid side converter. Star point of the grid N_G is considered as the reference point for the definition of the converter output phase voltages. The inductance and resistance of the L-filter are shown by L_F and R_F .

The dc-link voltage and the dc-link capacitance are expressed by V_{dc} and C_{dc} . Variables $i_{dc,GC}$ and $i_{dc,MC}$ denote the dc-link current of the grid side converter and the machine side converter, respectively. Current of the dc-link capacitor is shown by $i_{C_{dc}}$.

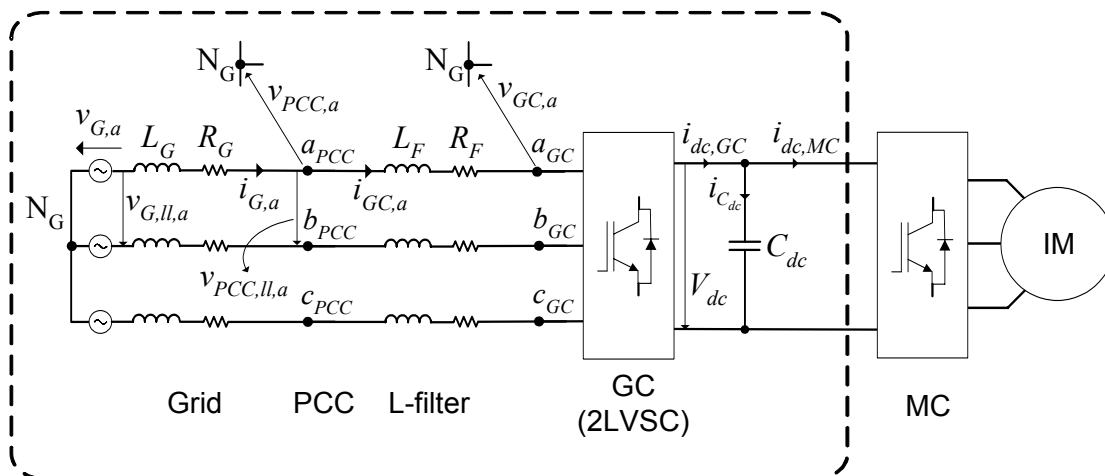


Fig. 4-1 Block diagram of the power part of a PWM active front end

For simplicity, the grid is assumed to form a symmetric three-phase system. Regarding this assumption the grid phase voltages in Fig. 4-1 are defined as follows:

$$\begin{cases} v_{G,a}(t) = \sqrt{\frac{2}{3}}V_{G,ll} \sin(\omega_G t) \\ v_{G,b}(t) = \sqrt{\frac{2}{3}}V_{G,ll} \sin(\omega_G t - \frac{2\pi}{3}), \\ v_{G,c}(t) = \sqrt{\frac{2}{3}}V_{G,ll} \sin(\omega_G t + \frac{2\pi}{3}) \end{cases} \quad (4-1)$$

where, $V_{G,ll}$ denotes the rms value of the grid line-to-line voltage and $\omega_G = 2\pi f_G$. The parameter f_G is the grid frequency.

The converter currents and the dc-link voltage are the system's state variables and should be taken into consideration in the mathematical description of the PWM active front end converters.

Description of the converter currents and the dc-link voltage

The converter currents can be described by using the filter voltage drop, the converter output voltage, and the voltage of the PCC. For a balanced three-phase system without neutral point connection, the filter voltage drop has been described as:

$$v_{PCC,x} - v_{GC,x} = R_F i_{GC,x} + L_F \frac{di_{GC,x}}{dt}; \quad x = a, b, c, \quad (4-2)$$

where

$$v_{PCC,a} + v_{PCC,b} + v_{PCC,c} = 0, \quad (4-3)$$

$$i_{GC,a} + i_{GC,b} + i_{GC,c} = 0. \quad (4-4)$$

In order to describe the converter output voltage $v_{GC,x}$, a basic representation of the grid side converter with 2L VSC is depicted in Fig. 4-2 (a). Switching states of the converter legs are denoted by $S_{GC,x}$; $x = a, b, c$. These switching states can be determined by applying a modulation strategy (e.g. PWM for voltage-oriented control [111]) or by hysteresis controllers (e.g. in direct power control [112]).

Sinus-triangle modulation and resulting switching state for phase leg a in a 2L VSC are shown in Fig. 4-2 (b) and (c). The switching state is 1 if the reference signal is greater than the carrier signal. If the carrier signal is greater than the reference signal, the switching state is considered to be 0.

Considering Fig. 4-2 (c), if the dc-link midpoint (shown in Fig. 4-2 (a) as NP) is assumed as the reference point, the grid side converter output voltages can be described as follows, based on the switching states and the dc-link voltage

$$v_{GC,xNP} = (2S_{GC,x} - 1) \cdot \frac{V_{dc}}{2}, \quad x = a, b, c. \quad (4-5)$$

Due to the system symmetry, voltage difference between the grid neutral point N_G and the midpoint of dc-link NP can be expressed as follows:

$$V_{N_GNP} = \frac{1}{3}(v_{a_{GCNP}} + v_{b_{GCNP}} + v_{c_{GCNP}}), \quad (4-6)$$

where $v_{GC,xNP}$, $x = a, b, c$ is the converter output phase voltage if the dc-link midpoint is considered as reference point.

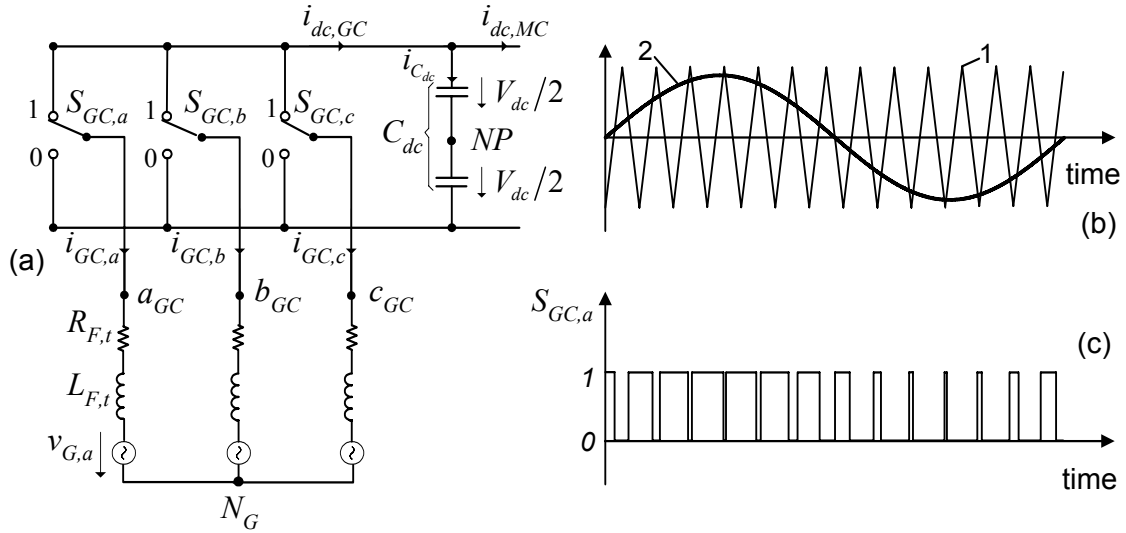


Fig. 4-2 (a) Block diagram of a grid side converter with 2L VSC; (b) natural sampled sinus-triangle modulation (e.g. phase a, 1: triangle carrier signal, 2: reference signal); (c) switching state of converter leg *a*

Hence, the output voltages of the converter with N_G as reference point can be described as

$$\begin{cases} v_{GC,a} = (2S_{GC,a} - S_{GC,b} - S_{GC,c})V_{dc}/3 \\ v_{GC,b} = (2S_{GC,b} - S_{GC,a} - S_{GC,c})V_{dc}/3 \\ v_{GC,c} = (2S_{GC,c} - S_{GC,a} - S_{GC,b})V_{dc}/3 \end{cases} \quad (4-7)$$

The dc-link currents of the grid side and the machine side converters are required to describe the dc-link voltage. According to the applied definition for the switching states, the dc-link current of the grid side converter can be calculated as follows:

$$i_{dc,GC} = S_{GC,a} \cdot i_{GC,a} + S_{GC,b} \cdot i_{GC,b} + S_{GC,c} \cdot i_{GC,c} \quad (4-8)$$

Using (4-8) and the dc-link current of the machine side converter $i_{dc,MC}$, the voltage equation of the dc-link is derived as

$$C_{dc} \frac{dV_{dc}}{dt} = i_{dc,GC} - i_{dc,MC} = S_{GC,a} \cdot i_{GC,a} + S_{GC,b} \cdot i_{GC,b} + S_{GC,c} \cdot i_{GC,c} - i_{dc,MC} \quad (4-9)$$

Description of the converter currents and the dc-link voltage in α - β coordinates

A space vector representation of the three-phase variables of the PWM active front end converter can be applied to reduce the number of equations in the mathematical model. Similar to the definition used to calculate the space vector of machine variables in the previous chapter, the projection in (3-4) has been used to determine the space vectors of the grid side converter three-phase variables. Using this space vector projection, the voltage drop equation in (4-2) is projected into the following equation

$$\vec{v}_{PCC} - \vec{v}_{GC} = R_F \vec{i}_{GC} + L_F \frac{d\vec{i}_{GC}}{dt}, \quad (4-10)$$

where

\vec{v}_{PCC} is the PCC voltage vector,

\vec{v}_{GC} and \vec{i}_{GC} denote the converter output voltage vector and the converter current vector.

Equation (4-10) can be expressed in s-domain in form of real and imaginary components (α - β) as below:

$$\begin{bmatrix} i_{GC,\alpha} \\ i_{GC,\beta} \end{bmatrix} = \frac{1}{R_F + sL_F} \begin{bmatrix} -v_{GC,\alpha} + v_{PCC,\alpha} \\ -v_{GC,\beta} + v_{PCC,\beta} \end{bmatrix}, \quad (4-11)$$

where

$i_{GC,\alpha}$ and $i_{GC,\beta}$ are real and imaginary components of the grid side converter current vector, $v_{PCC,\alpha}$ and $v_{PCC,\beta}$ denote real and imaginary components of the grid voltage vector at the PCC, $v_{GC,\alpha}$ and $v_{GC,\beta}$ being real and imaginary components of the converter voltage vector.

Space vector of the grid side converter output voltage can be determined by using (4-7) and the projection presented in (3-4). The real and imaginary components of the converter output voltage vector are related to the real and imaginary parts of the converter switching states as presented in the following equation

$$\begin{bmatrix} v_{GC,\alpha} \\ v_{GC,\beta} \end{bmatrix} = V_{dc} \begin{bmatrix} S_{GC,\alpha} \\ S_{GC,\beta} \end{bmatrix}, \quad (4-12)$$

$$\begin{cases} S_{GC,\alpha} = \frac{1}{3}(2S_{GC,a} - S_{GC,b} - S_{GC,c}) \\ S_{GC,\beta} = \frac{1}{\sqrt{3}}(S_{GC,b} - S_{GC,c}) \end{cases}. \quad (4-13)$$

In the same way, projection (3-4) is applied to project the dc-link voltage equation (4-9) into the α - β coordinate system. Following equation is derived as the expression of the dc-link voltage in terms of the real and imaginary parts of the converter current and the switching states vector

$$C_{dc} \frac{dV_{dc}}{dt} = \frac{3}{2} (S_{GC,\alpha} \cdot i_{GC,\alpha} + S_{GC,\beta} \cdot i_{GC,\beta}) - i_{dc,MC}. \quad (4-14)$$

A block diagram of the grid side converter model in stationary coordinate system (α - β) based on (4-11), (4-12), and (4-14) is shown in Fig. 4-3.

Instantaneous input active and reactive power in the α - β coordinates

Real and imaginary components of the converter current vector and the PCC voltage vector can be used to determine the instantaneous input active and reactive power of the grid side converter at the PCC. A definition of the grid side converter active and reactive power at PCC is presented in the following equation [12]

$$\begin{cases} p_{GC,PCC} = \vec{v}_{PCC} \cdot \vec{i}_{GC} \\ q_{GC,PCC} = \vec{v}'_{PCC} \cdot \vec{i}_{GC} \end{cases}, \quad (4-15)$$

where “ \cdot ” denotes the scalar product of the vectors. Furthermore, \vec{v}'_{PCC} lags the voltage vector \vec{v}_{PCC} by 90° .

Using the definition in (4-15) and the real and imaginary components of the PCC voltage vector and the converter current vector, the input active and reactive power of the grid side converter are expressed as following:

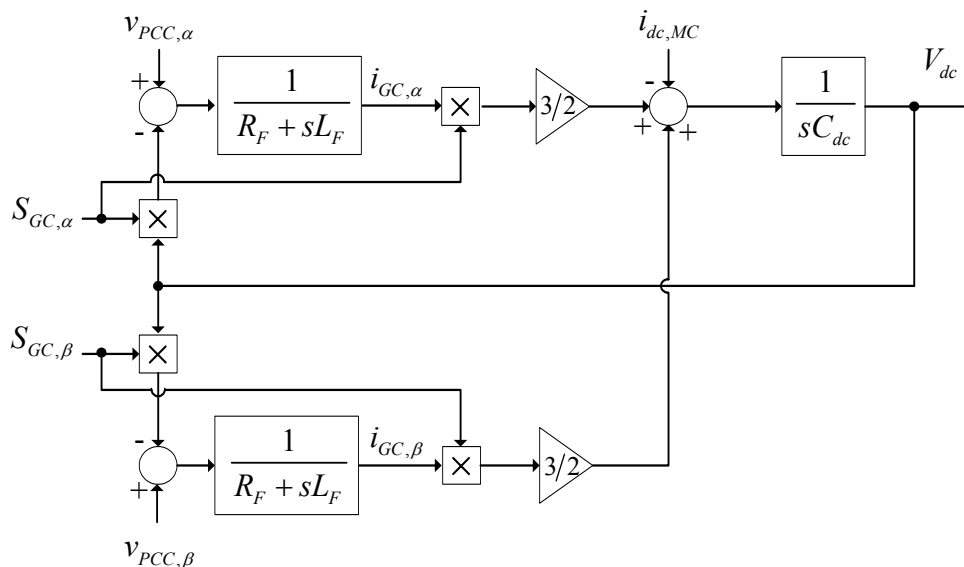


Fig. 4-3 Block diagram of the grid side converter model in stationary coordinate system

$$\begin{cases} p_{GC,PCC} = \frac{3}{2}(v_{PCC,\alpha} \cdot i_{GC,\alpha} + v_{PCC,\beta} \cdot i_{GC,\beta}) \\ q_{GC,PCC} = \frac{3}{2}(v_{PCC,\beta} \cdot i_{GC,\alpha} - v_{PCC,\alpha} \cdot i_{GC,\beta}) \end{cases} \quad (4-16)$$

Instantaneous active and reactive powers are required in the direct power control strategy, which will be introduced briefly in the next subchapter.

4.3 Selection of the control strategy

An overview of the control strategies of PWM active front end converters has been presented in the Chapter 1. As mentioned there, these control techniques can be categorized into voltage-based and virtual-flux-based methods.

Voltage-based control techniques

Voltage-oriented control (VOC) and voltage-based direct power control (V-DPC) are the two types of the voltage-based control strategies of PWM active front end converters [111]. A basic block diagram of VOC is presented in Fig. 4-4 (a). VOC is similar to the well-known field-oriented control of induction machines. The grid side converter currents and the line voltage at the PCC are the measured variables. In VOC a rotating reference frame synchronous to the line voltage vector at PCC (\vec{v}_{PCC}) is applied to realize the control strategy. Therefore, the angle of the line voltage vector $\rho_{\vec{v}_{PCC}}$ is used to project the converter current vector into the rotating reference frame. Then, the direct and quadrature components of the converter current vector in the rotating reference frame ($i_{GC,d}^{\vec{v}_{PCC}}$, $i_{GC,q}^{\vec{v}_{PCC}}$ in Fig. 4-4 (a)) can be used to control the dc-link voltage V_{dc} and the DPF at the PCC, respectively. VOC comprises inner current control loops, and the outputs of the current controllers are the reference voltages required in the modulation unit. Due to the application of a modulator (sinus-triangle PWM or SVM), the output voltage of converter has a well-defined harmonic spectrum.

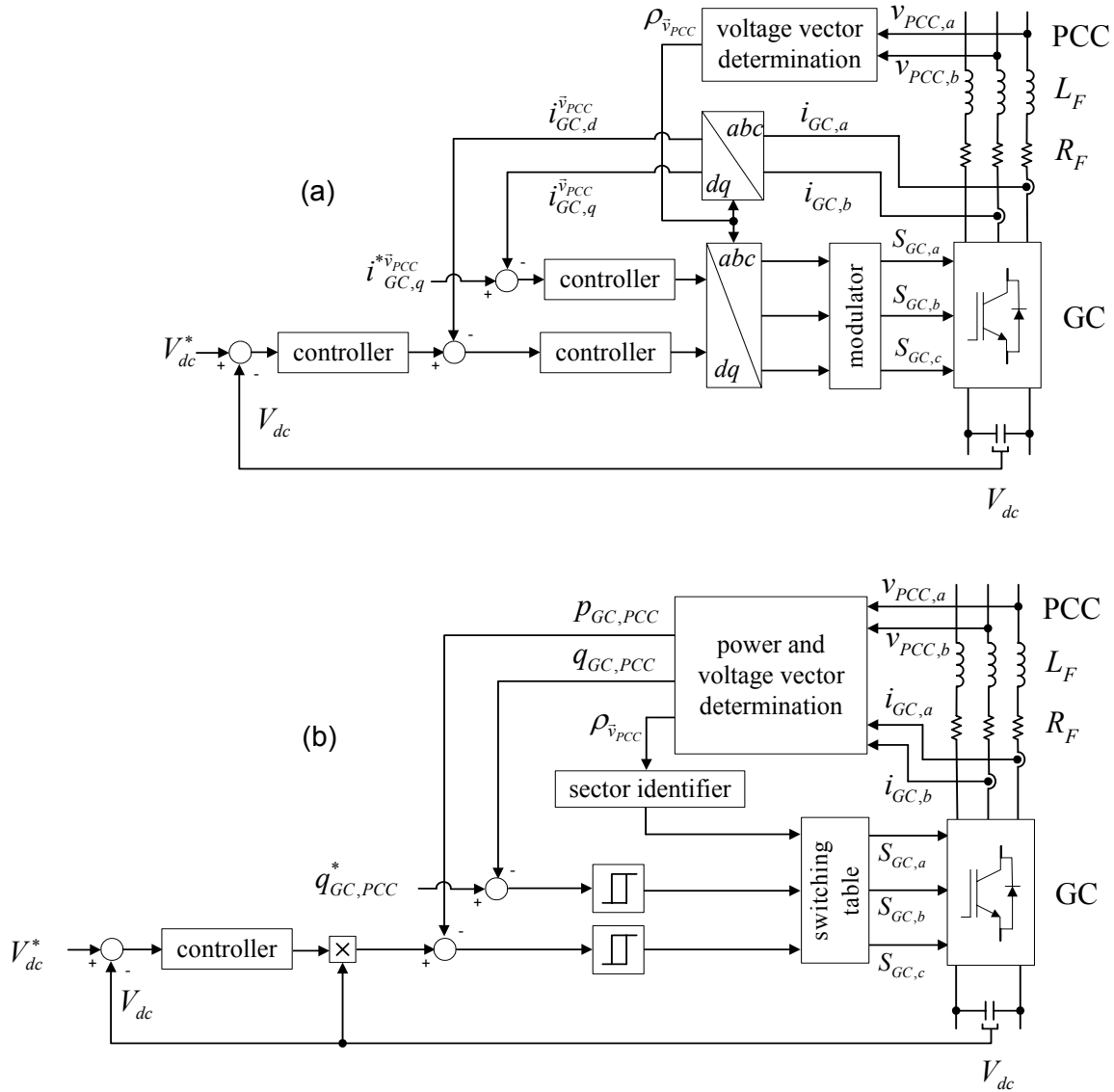


Fig. 4-4 Block diagram of the voltage-oriented control (a) and the voltage-based direct power control (b)

Another control strategy called V-DPC (Fig. 4-4 (b)) is based on instantaneous active and reactive power control. Instantaneous active and reactive power at PCC can be determined by using measured converter currents and grid voltages at PCC. Equation (4-16) can be applied to calculate the active and reactive power. Input real and imaginary power at PCC can also be estimated based on the converter currents, the dc-link voltage, and the converter switching states [111]. In this case there is no requirement to measure the line voltages at the PCC.

In V-DPC, there are no internal current control loops. Modulation unit is not required since the converter switching states are appropriately selected by a switching table based on the instantaneous errors between the commanded and estimated values of the active and reactive power [12], [111], [112], [115]. Due to the application of hysteresis controllers in V-DPC, converter output voltage has a variable switching frequency. Furthermore, because of the lack of current control loop, direct limitation of converter current is not possible.

Virtual-flux-based control techniques

Virtual-flux-based control techniques can be divided into virtual-flux-oriented control (VFOC) and virtual-flux-based direct power control (VF-DPC). Structure of VFOC is very

similar to the structure of VOC presented in Fig. 4-4 (a). Instead of a voltage vector, virtual flux vector, which is defined as time integral of the line voltage, is used to define the rotating coordinate system [12]. Application of the line voltage time integral instead of the line voltage is advantageous for supplies with distorted voltage [111].

In virtual-flux-based direct power control (VF-DPC) active and reactive powers are estimated based on converter current and real and imaginary components of the virtual flux [110]. Structure of VF-DPC is similar to the block diagram shown in Fig. 4-4 (b). In VF-DPC virtual flux vector of PCC is determined by using the line voltage at PCC, and the angle of the flux vector is used to identify the sector number.

Like sensorless control strategies for induction motors, PWM active front end converters can be controlled by only using grid currents as feedback eliminating grid voltage sensors [12], [94], [102], [103], [104], [115]. In some sensorless techniques the grid voltage angle is estimated by considering the converter output voltage and voltage drop across the line inductor [12]. It should be noted, however, that if the line inductance is used to estimate the projection angle, the steady-state performance (e.g. DPF) of the sensorless techniques will be sensitive to the accuracy of the inductance value used in the estimation.

To summarize, in VOC and VFOC the rotating reference frame is aligned with grid voltage vector and grid virtual flux vector, respectively. Inner current control loops are applied to control the active and reactive power indirectly. A separate modulator (e.g. sinus-triangle PWM) is required. Similar to the FOC of IMs, the sampling frequency of current control loop is equal to the carrier frequency for SRS-PWM and twice the carrier frequency for ARS-PWM if a sinus-triangle PWM is applied.

V-DPC and VF-DPC are very similar to the DTC of IMs. Active and reactive powers are controlled directly with hysteresis controllers, and no additional modulator is required. For a proper operation of the discrete hysteresis controllers a high sampling frequency

Table 4.1
Advantages and disadvantages of PWM active front end control strategies [111]

Technique	Advantages	Disadvantages
VOC VFOC	<ul style="list-style-type: none"> • Constant switching frequency • Low sampling frequency • Low cost A/D converters • Application of optimized PWM strategies possible • Inherent current control and current limitation 	<ul style="list-style-type: none"> • Requirement of coordinate projection and decoupling of active and reactive components • Dependence of current controller parameters to filter parameters
V-DPC VF-DPC	<ul style="list-style-type: none"> • No current regulation loop • Avoidance of coordinate projection • Decoupled control of active and reactive power 	<ul style="list-style-type: none"> • Requirement of high sampling frequency • Larger input filters than VOC at constant average switching frequency due to limitations of IEEE 519 compliance.

(e.g. $10 \cdot f_{sw} - 20 \cdot f_{sw}$) is required. Hence, V-DPC and VF-DPC require more powerful processors [111].

Advantages and disadvantages of VOC, VFOC, V-DPC, and VF-DPC strategies are summarized in Table 4.1. Because of some advantages like lower sampling frequency and a constant switching frequency, VOC is a widely distributed control strategy for the PWM active front end converters. Distinct similarities between VOC and rotor flux-oriented control of induction machines especially concerning the parameter tuning of current PI controllers make it possible that the current controllers of induction machines can be applied directly in VOC. A constant switching frequency leads to a smaller input LCL-filter to meet the IEEE-519 limits for the grid current harmonics. Regarding these features and advantages, VOC is investigated as control strategy for the grid side converter in this thesis.

4.4 Voltage-oriented control of PWM active front end converters

As mentioned in the previous subchapter, VOC is structured based on current control in a rotating reference frame. In order to design the current controllers, a model of the converter in the rotating reference frame is required. Furthermore, for projecting the converter currents into the rotating reference frame, precise information about the angle of the reference vector is required. In this thesis, the rotating reference frame is considered to be synchronous to the PCC voltage vector. A phase-locked loop (PLL) is applied to determine the angle of the PCC voltage vector, which is required for the projection.

In the following sections, mathematical model of a PWM active front end converter with L-filter in a rotating reference frame synchronous to the PCC voltage vector is illustrated. Then, the structure of the applied PLL and PI-based current and voltage control loops are illustrated. Corresponding simulation and experimental results are also presented.

4.4.1 d-q Model of PWM active front end converters with L-filter

An α - β model of PWM active front end converters has been presented in Subchapter 4.2. Equations (4-10) and (4-14) present the mathematical model of a PWM active front end converter with L-filter. These two equations are required to be projected into a rotating reference frame to obtain the d-q model. In the case that grid voltages at PCC are measured, a rotating frame fixed on PCC voltage vector can be defined as shown in Fig. 4-5. Then, converter current vector, converter output voltage vector as well as equations (4-10) and

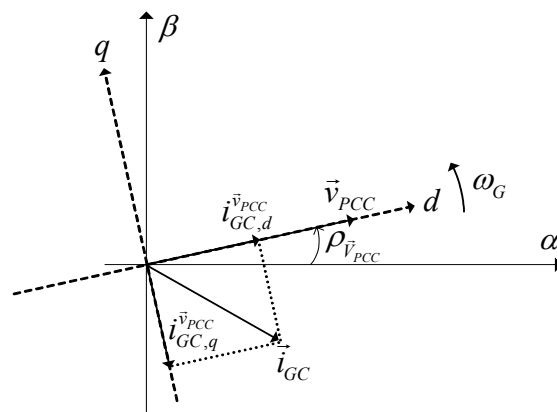


Fig. 4-5 Rotating reference frame fixed on the voltage vector of PCC

(4-14) should be projected into this rotating reference frame to describe a mathematical model of a PWM active front end converter in PCC voltage-oriented coordinate system.

It is assumed that the switching frequency of converter is adequately high so that the converter current ripple at switching frequency is ignorable compared to amplitude of the fundamental component. Moreover, the PCC voltage is considered to have a sinusoidal waveform.

From projecting (4-10) into rotating reference frame (multiplying by $e^{-j\rho_{\bar{v}_{PCC}}}$), the following voltage equation is derived:

$$e^{-j\rho_{\bar{v}_{PCC}}} \bar{\mathbf{v}}_{PCC} - e^{-j\rho_{\bar{v}_{PCC}}} \bar{\mathbf{v}}_{GC} = R_F e^{-j\rho_{\bar{v}_{PCC}}} \bar{\mathbf{i}}_G + L_F \frac{d(e^{-j\rho_{\bar{v}_{PCC}}} \bar{\mathbf{i}}_G)}{dt} + j\omega_G e^{-j\rho_{\bar{v}_{PCC}}} \bar{\mathbf{i}}_G, \quad (4-17)$$

where ω_G denotes the grid angular frequency ($\omega_G = d\rho_{\bar{v}_{PCC}}/dt$).

Direct and quadrature components of (4-17) are

$$\begin{cases} -v_{GC,d}^{\bar{v}_{PCC}} = L_F \frac{di_{GC,d}^{\bar{v}_{PCC}}}{dt} + R_F i_{GC,d}^{\bar{v}_{PCC}} - \omega_G L_F i_{GC,q}^{\bar{v}_{PCC}} - v_{PCC,d}^{\bar{v}_{PCC}} \\ -v_{GC,q}^{\bar{v}_{PCC}} = L_F \frac{di_{GC,q}^{\bar{v}_{PCC}}}{dt} + R_F i_{GC,q}^{\bar{v}_{PCC}} + \omega_G L_F i_{GC,d}^{\bar{v}_{PCC}} \end{cases}, \quad (4-18)$$

where

$i_{GC,d}^{\bar{v}_{PCC}}$ and $i_{GC,q}^{\bar{v}_{PCC}}$ are direct and quadrature components of grid side converter current vector in the rotating reference frame synchronous to the voltage vector of PCC $\bar{\mathbf{v}}_{PCC}$,

$v_{GC,d}^{\bar{v}_{PCC}}$ and $v_{GC,q}^{\bar{v}_{PCC}}$ denote direct and quadrature components of grid side converter output voltage in the rotating reference frame synchronous to the voltage vector of PCC,

$v_{PCC,d}^{\bar{v}_{PCC}}$ is direct component of the PCC voltage vector in the rotating reference frame synchronous to the voltage vector of PCC which equals the amplitude of $\bar{\mathbf{v}}_{PCC}$.

Obviously, using proper decoupling terms, the direct and quadrature current components can be controlled independently by direct and quadrature components of the converter output voltage, respectively.

In VOC with a limited sampling frequency (e.g. $f_s = 2f_{sw}$) average values of converter currents and dc-link voltage are going to be controlled. Hence, voltage ripple of the dc-link has been ignored, and average values of the converter switching states are applied to determine the dc-link voltage. From projecting (4-14) into the rotating frame, the following equation for the dc-link voltage (ignoring the voltage ripple) is derived:

$$C_{dc} \frac{dV_{dc}}{dt} = \frac{3}{2} \left(\bar{S}_{GC,d}^{\bar{v}_{PCC}} \cdot i_{GC,d}^{\bar{v}_{PCC}} + \bar{S}_{GC,q}^{\bar{v}_{PCC}} \cdot i_{GC,q}^{\bar{v}_{PCC}} \right) - \bar{i}_{dc,MC}. \quad (4-19)$$

Parameters $\bar{S}_{GC,d}^{\bar{v}_{PCC}}$ and $\bar{S}_{GC,q}^{\bar{v}_{PCC}}$ denote the average values of the direct and quadrature components of the converter switching states in the rotating reference frame synchronous to $\bar{\mathbf{v}}_{PCC}$. $\bar{i}_{dc,MC}$ is the average value of the machine side dc-link current. Following equation has been applied to determine the average values

$$\bar{x}(t) = \frac{1}{T_s} \int_{t-T_s}^t x(\tau) d\tau, \quad (4-20)$$

where, T_s in (4-20) denotes the sampling time in discrete control.

For a 2L VSC with dc-link voltage of V_{dc} , (4-12) and the definition in (4-20) are used in order to relate the average values of the switching states to the converter output voltage as follows:

$$\begin{bmatrix} \bar{S}_{GC,d}^{\bar{v}_{PCC}}(t) \\ \bar{S}_{GC,q}^{\bar{v}_{PCC}}(t) \end{bmatrix} = \frac{1}{V_{dc}} \begin{bmatrix} \bar{v}_{GC,d}^{\bar{v}_{PCC}}(t) \\ \bar{v}_{GC,q}^{\bar{v}_{PCC}}(t) \end{bmatrix}. \quad (4-21)$$

Therefore, equation of the dc-link voltage can be represented as:

$$C_{dc} \frac{dV_{dc}}{dt} = \frac{3}{2V_{dc}} \left(\bar{v}_{GC,d}^{\bar{v}_{PCC}} \cdot \bar{i}_{GC,d}^{\bar{v}_{PCC}} + \bar{v}_{GC,q}^{\bar{v}_{PCC}} \cdot \bar{i}_{GC,q}^{\bar{v}_{PCC}} \right) - \bar{i}_{dc,MC}. \quad (4-22)$$

A block diagram of the grid side converter with L-filter based on (4-18) and (4-22) in a rotating reference frame fixed on the grid voltage vector at the PCC is depicted in Fig. 4-6.

By projecting (4-16) into the rotating reference frame, following expression for the input active and reactive power of the converter is obtained:

$$\begin{cases} p_{GC,PCC} = \frac{3}{2} v_{PCC,d}^{\bar{v}_{PCC}} \cdot i_{GC,d}^{\bar{v}_{PCC}} \\ q_{GC,PCC} = -\frac{3}{2} v_{PCC,d}^{\bar{v}_{PCC}} \cdot i_{GC,q}^{\bar{v}_{PCC}} \end{cases}. \quad (4-23)$$

Equation (4-23) and the d-q model of the grid side converter presented in Fig. 4-6 show that the dc-link voltage (active power) and the DPF at PCC (reactive power) can be controlled indirectly by using the components of the grid side converter current on the d- and q-axis, respectively. In order to determine the direct and quadrature components of the converter current vector, the angle of the PCC voltage vector is required. Similar to the projection (3-37) in the previous chapter, the following projection can be applied to project the converter current vector into the rotating reference frame.

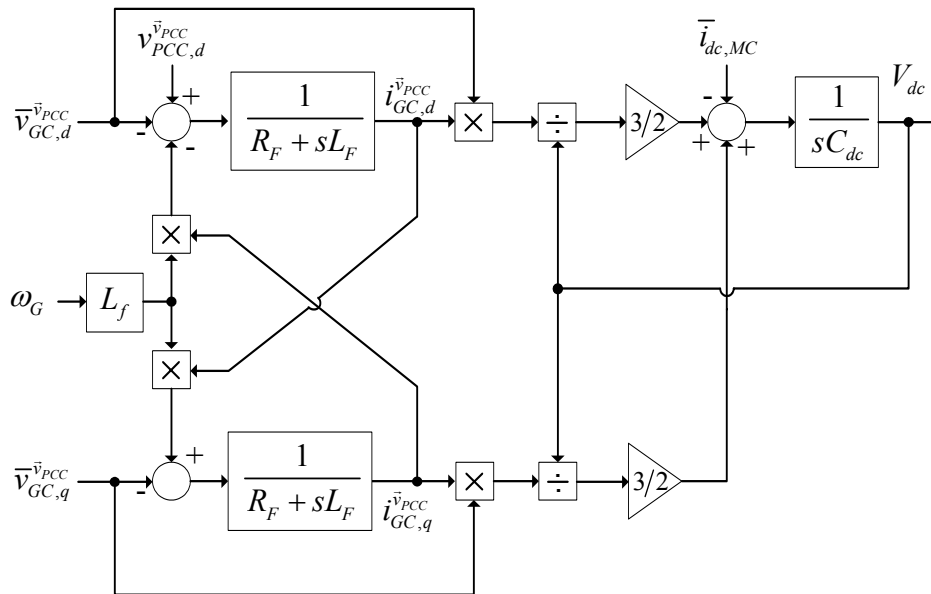


Fig. 4-6 Block diagram of PWM active front end converter with L-filter in the d-q coordinate system synchronous to the PCC voltage vector

$$\begin{bmatrix} \bar{i}_{GC,d}^{v_{PCC}} \\ \bar{i}_{GC,q}^{v_{PCC}} \end{bmatrix} = \begin{bmatrix} \cos(\rho_{v_{PCC}}) & \sin(\rho_{v_{PCC}}) \\ -\sin(\rho_{v_{PCC}}) & \cos(\rho_{v_{PCC}}) \end{bmatrix} \begin{bmatrix} i_{GC,\alpha} \\ i_{GC,\beta} \end{bmatrix} \quad (4-24)$$

Structure of the applied PLL to measure the angle of the PCC voltage vector $\rho_{v_{PCC}}$, which is required for the projection is illustrated in the following section.

4.4.2 Structure of the applied PLL

For a proper operation of VOC, a fast, stable, and distortion-free phase and frequency detection of PCC voltage vector is required. The three-phase PLL structure shown in Fig. 4-7 is used to detect the required phase and frequency [82], [83], [101]. The phase voltages measured at the PCC are the inputs of the PLL. Considering the grid voltage definition in (4-1), three-phase voltage of the PCC can be described as (4-25), where $V_{PCC,ll}$ is

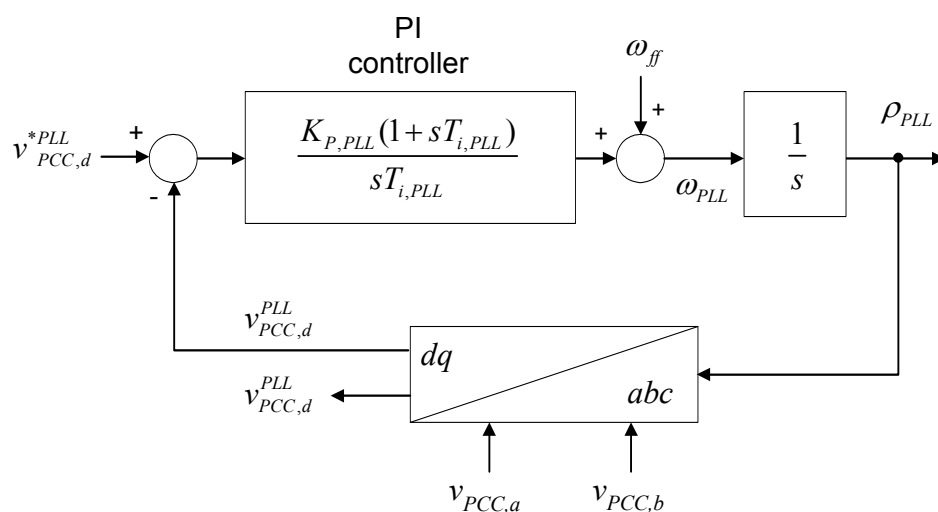


Fig. 4-7 Structure of a three-phase PLL

the rms value of the line-to-line voltage at PCC and $\theta_{v_{PCC}}$ denotes the phase of $v_{PCC,a}$ at $t = 0$

$$\begin{cases} v_{PCC,a}(t) = \sqrt{\frac{2}{3}}V_{PCC,ll} \sin(\omega_G t + \theta_{v_{PCC}}) \\ v_{PCC,b}(t) = \sqrt{\frac{2}{3}}V_{PCC,ll} \sin(\omega_G t + \theta_{v_{PCC}} - \frac{2\pi}{3}) \\ v_{PCC,c}(t) = \sqrt{\frac{2}{3}}V_{PCC,ll} \sin(\omega_G t + \theta_{v_{PCC}} + \frac{2\pi}{3}) \end{cases} \quad (4-25)$$

These voltages are then projected into the PLL rotating reference frame using the angle of the PLL rotating frame $\rho_{PLL}(t)$. If the angular frequency of the PLL ω_{PLL} equals the grid angular frequency ω_G , the components of the PCC voltage vector in the PLL rotating frame ($v_{PCC,d}^{PLL}, v_{PCC,q}^{PLL}$) are dc signals.

In the structure of the PLL in Fig. 4-7 a PI controller is applied to determine the PLL angular frequency based on the difference between the reference value for the direct component of the PCC voltage vector $v_{PCC,d}^{*PLL}$ and the corresponding measure on $v_{PCC,d}^{PLL}$. A feed-forward signal ω_{ff} equal to the nominal grid angular frequency can be used to improve the PLL tracking performance [83]. Magnitude of the reference signal $v_{PCC,d}^{*PLL}$ determines the phase difference between the PLL rotating frame and the phase a of the PCC voltage ($v_{PCC,a}$).

If the reference signal is adjusted as $v_{PCC,d}^{*PLL} = 0$, then ρ_{PLL} approaches the phase of $v_{PCC,a}$ ($\rho_{PLL}(t) = \omega_G t + \theta_{v_{PCC}}$) [101]. Using the phase of $v_{PCC,a}$, the voltage vector angle at PCC can be derived as follows for a symmetric three phase system:

$$\rho_{\bar{v}_{PCC}} = \rho_{PLL} - \pi/2, \quad \rho_{PLL} = \int_0^t \omega_{PLL}(\tau) d\tau. \quad (4-26)$$

Considering the phase difference between the PCC voltage vector and the PLL rotating frame, the direct component of the PCC voltage vector in the rotating reference frame synchronous to \bar{v}_{PCC} is determined as follows:

$$v_{PCC,d}^{\bar{v}_{PCC}} = v_{PCC,q}^{PLL}. \quad (4-27)$$

In order to design the parameters of the PI controller of the PLL, a simplified linear model of PLL proposed by [101] is applied. Using (4-25) and the projection defined in (3-37), direct component of the PCC voltage vector in the PLL rotating reference frame is:

$$v_{PCC,d}^{PLL} = \sqrt{\frac{2}{3}} V_{PCC,\Pi} \sin((\omega_G t + \theta_{V_{PCC}}) - \rho_{PLL}). \quad (4-28)$$

For small values of $(\omega_G t + \theta_{V_{PCC}}) - \rho_{PLL}$, equation (4-28) can be approximated by the following linear equation:

$$v_{PCC,d}^{PLL} = \sqrt{\frac{2}{3}} V_{PCC,\Pi} ((\omega_G t + \theta_{V_{PCC}}) - \rho_{PLL}). \quad (4-29)$$

For a reference value equal to zero $v_{PCC,d}^{*PLL} = 0$ in Fig. 4-7, the PLL control loop for small signals is presented in Fig. 4-8. $T_{s,PLL}$ is the PLL sampling time and a processing delay of one sampling time is considered in the PLL control loop. This control loop is a standard control

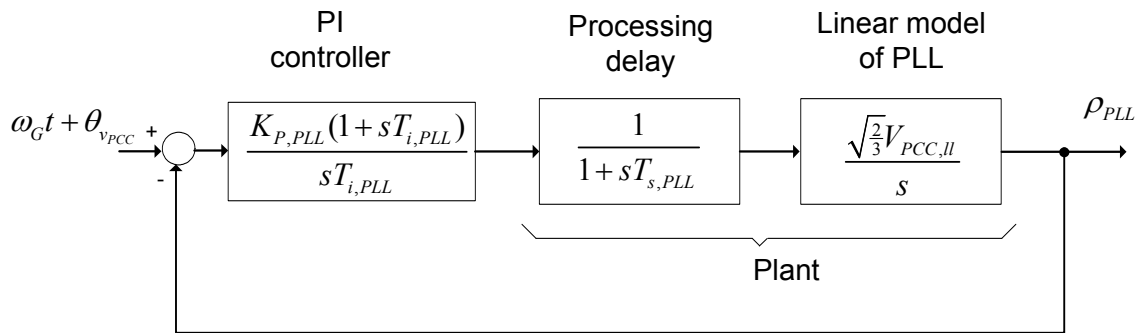


Fig. 4-8 Simplified small signal model of the control loop of PLL

loop similar to the speed control loop of induction machine drives. Similar to the design procedure of the speed control loop, symmetrical optimum was used to tune the parameters of the PLL PI controller. According to Table 3.5, the PI parameters in Fig. 4-8 are:

$$T_{i,PLL} = a_{PLL}^2 T_{s,PLL}, \quad (4-30)$$

$$K_{P,PLL} = \frac{1}{a_{PLL} \sqrt{\frac{2}{3}} V_{PCC,\Pi} T_{s,PLL}}, \quad a_{PLL} \geq 2. \quad (4-31)$$

where, a_{PLL} is the PLL damping factor.

By changing a_{PLL} , PLL bandwidth can be controlled [101]. For grids with distorted voltage (e.g. notched grids) pollutions normally do not affect the locking capability although they cause harmonics in the the PLL output. Selection of a high value of a_{PLL} leads to a clean output of PLL despite the line distortions but reduces the bandwidth of the PLL. For utility

interface applications where the frequency does not change substantially a low value of a_{PLL} could be used to obtain a quick lock at startup and later a suitable value to obtain a smooth PLL output [101]. It should be mentioned that the bandwidth reduction leads to a poor PLL dynamics and is not an acceptable solution in the presence of an unbalanced grid voltage [123]. The decoupled double synchronous reference frame PLL introduced in [124] is recommended in the case of unbalanced notched grids.

Structure of the VOC in this thesis is established according to Fig. 4-4 (a). Obviously, the current control and the dc-link voltage control are the main two parts of the applied control strategy. PI controllers are used for both control loops. The design procedure of the applied PI controller is illustrated in the following sections.

4.4.3 PI-based current control

As shown in Fig. 4-4 (a), current control loop is the inner control loop of VOC; therefore, the performance of the entire system strongly depends on the performance of the current control loop. The current control can be realized by different methods. A review of the recently used current control techniques for the three-phase voltage source PWM converters is presented in [63]. Current controllers can be categorized into two main groups: current control in stationary frame (working with AC current components) and current control in rotating frame (working with DC current components). For each group, linear controllers (such as PI, state feedback, predictive control, etc.) or nonlinear controllers (such as hysteresis, fuzzy controller, etc.) can be applied. Using hysteresis controllers, the converter switching frequency depends on load parameters and varies with the ac voltage. Among linear controllers, PI controllers have a simple structure and are easy to implement with low cost microcontrollers. According to [125], it is concluded that the rotating frame current controller has no steady-state error and therefore very good steady-state accuracy. Hence, PI controllers in a rotating frame are chosen as the current controllers in this thesis. A sinus-triangle PWM with asymmetrical regular sampling ARS-PWM (Fig. 3-10 (b)) is applied as modulator in the block diagram shown in Fig. 4-4 (a). Peak-to-peak amplitude of the triangle signal is considered to be constant and equal to the nominal voltage of the dc-link $V_{dc,n}$. The current control loop comprises the converter model presented in Fig. 4-6, model of ARS-PWM, and the processing delay. For simplicity, it is assumed that the semiconductor devices with ideal behavior have been used in the converter. Considering the dynamic model of the ARS-PWM presented in Section 3.4.2, output voltage of the grid side converter ($v_{GC,x}$, $x = a, b, c$) are related to reference signals $v_{GC,x}^*$, $x = a, b, c$ of the PWM as follows:

$$\bar{v}_{GC,x} = \frac{V_{dc}}{V_{dc,n}} \frac{1}{1 + 0.5sT_s} v_{GC,x}^*, \quad x: a, b, c, \quad (4-32)$$

where, V_{dc} is the actual dc-link voltage.

It is assumed that the PWM reference signals do not change significantly over a sampling period (sampling frequency is very much higher than the grid frequency, e.g. $m_f = 80$). As mentioned above, the peak-to-peak amplitude of the carrier signal is kept constant and equal to the nominal value of the dc-link voltage $V_{dc,n}$. By projecting (4-32) into the rotating reference frame synchronous to the PCC voltage vector \bar{v}_{PCC} , following equation as the PWM model can be obtained

$$\begin{bmatrix} \bar{v}_{GC,d}^{\bar{v}_{PCC}} \\ \bar{v}_{GC,q}^{\bar{v}_{PCC}} \end{bmatrix} = \frac{V_{dc}}{V_{dc,n}} \frac{1}{1+0.5sT_s} \begin{bmatrix} v_{GC,d}^{*\bar{v}_{PCC}} \\ v_{GC,q}^{*\bar{v}_{PCC}} \end{bmatrix} \quad (4-33)$$

Using (4-33) and the model of the converter shown in Fig. 4-6, a block diagram of the d - q model of the grid side converter comprising simple models of the ARS-PWM and processing delay is presented in Fig. 4-9.

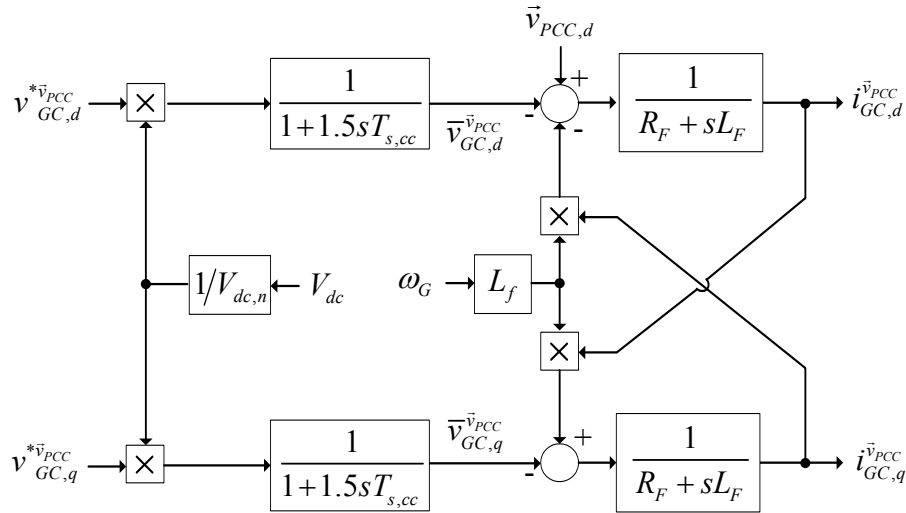


Fig. 4-9 d - q model of PWM active front end converter with L-filter comprising models of the modulator and processing delay (input: PWM reference signals, output: converter currents)

Similar to the current control of IMs, the processing delay (equal to one sampling period of the current control loop) and the delay of ARS-PWM are approximated with a total delay of $1.5T_{s,cc}$ where $T_{s,cc}$ denotes the sampling period of the current control loop. Obviously, the current model in Fig. 4-9 is nonlinear (due to the multiplication of the input signal by V_{dc}) and there are coupling terms between current models on the d - and q -axis. The structure in Fig. 4-10 can be applied for linearization and decoupling the direct and quadrature components of the converter current vector.

When applying the linearization and decoupling structure shown in Fig. 4-10 and the current

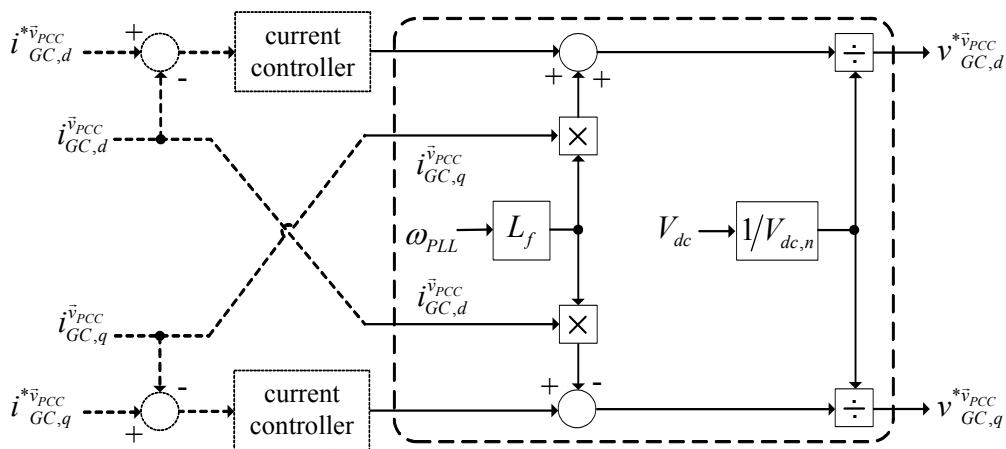


Fig. 4-10 Block diagram of linearization and decoupling circuits of current control loops on the d - and q -axis

model of the converter presented in Fig. 4-9, the current control loop of the grid side converter with ARS-PWM and L-filter is simplified to the control loop shown in Fig. 4-11.

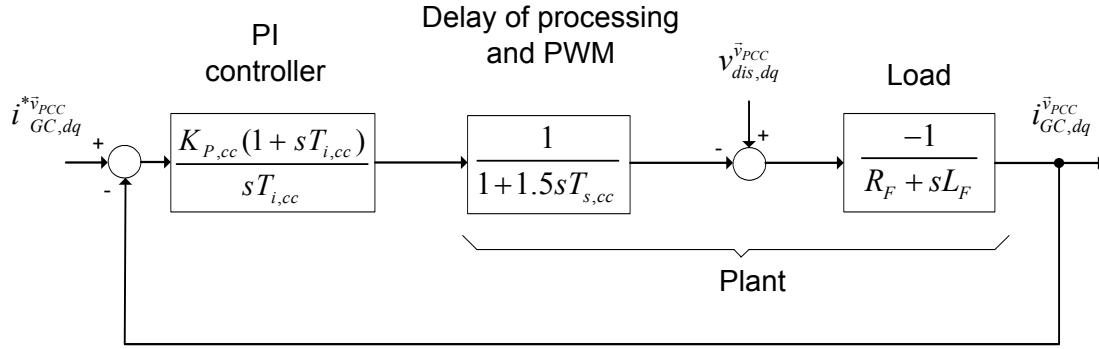


Fig. 4-11 Block scheme of current control loop in VOC

It should be noted that due to the processing and PWM delays, a complete decoupling between direct and quadrature current control loops is not possible if the decoupling circuit in Fig. 4-10 is applied. A full decoupling is possible if the delays are compensated by using derivative terms as proposed in [19]. However, application of derivative terms could lead to undesirable noise amplification.

Voltage distortions of PCC in the rotating coordinate system are modeled as $v_{dis,dq}^{v_{PLL}}$ at the converter output in Fig. 4-11.

The current control loop in VOC is very similar to the current control loop of RFOC of IMs presented in Fig. 3-11. Similar to the design procedure of the current controller of IMs, technical optimum was applied to tune the parameters of the PI controller for the current control loop. According to Fig. 4-11 and Table 3.4, parameters of the current PI controller are designed as follows:

$$T_{i,cc} = \frac{L_F}{R_F}, \quad (4-34)$$

$$K_{p,cc} = \frac{L_F}{1.5a_{cc}T_{s,cc}}, \quad a_{cc} \geq 2, \quad (4-35)$$

where, a_{cc} and $T_{s,cc}$ denote the damping factor and the sampling period of the current control loop, respectively.

4.4.4 PI-based dc-link voltage control

As shown in Fig. 4-4, the voltage control loop of VOC comprises the current control loop and the voltage dynamics of the dc-link capacitor. According to Fig. 4-6, the dc-link voltage of the PWM active front end converter has a nonlinear model. However, PWM active front end converters operate usually at a constant dc-link voltage. Therefore a linear model around the converter operating point at steady-state was applied to tune the controller parameters.

It is assumed that the converter operates at a desired dc-link voltage of v_{dc}^* at unity power factor condition ($i_{GC,q}^{v_{PCC}} = 0$). In steady-state, the dc-link voltage equals the desired value ($v_{dc} = v_{dc}^*$). Furthermore, if the filter voltage drop is ignored, the direct component of the converter output voltage is equal to the amplitude of the PCC voltage vector

$$v_{GC,q}^{v_{PLL}} = \sqrt{\frac{2}{3}} V_{PCC,ll}. \quad (4-36)$$

Therefore, the linear model in Fig. 4-12 can be considered as the dc-link voltage model for an operating point with the dc-link voltage reference of v_{dc}^* and unity power factor condition.

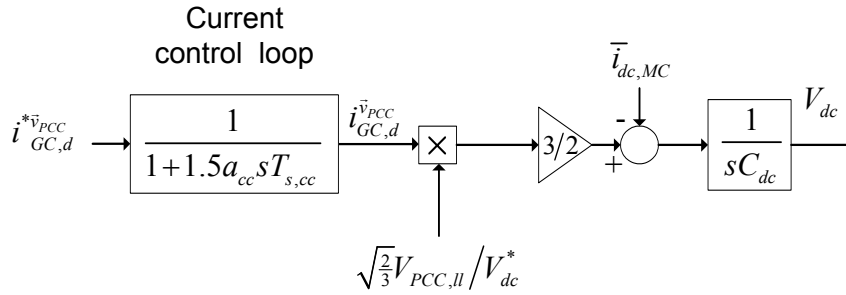


Fig. 4-12 Linear model of dc-link voltage at unity power factor and a dc-link voltage reference of v_{dc}^*

The current control loop of Fig. 4-11 is approximated by a first order transfer function of $i_{GC,dq}^{v_{PCC}}/i_{GC,dq}^{*v_{PCC}} = 1/(1 + 1.5a_{cc}sT_{s,cc})$ in Fig. 4-12. The parameters of the PI current controller have been selected according to (4-34) and (4-35).

A PI controller is also applied to control the dc-link voltage. A block diagram of the dc-link voltage control loop with PI controller based on the linear model in Fig. 4-12 is shown in Fig. 4-13. Obviously, the voltage control loop in VOC is very similar to the speed control loop in RFOC presented in Fig. 3-13.

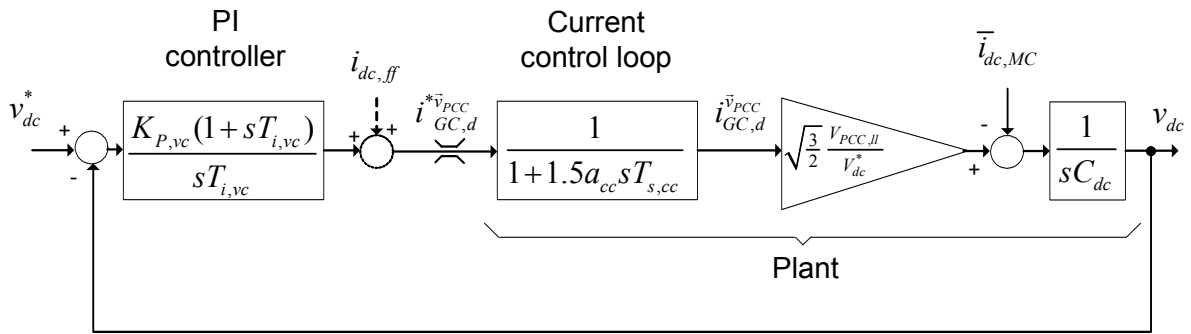


Fig. 4-13 Voltage control loop of VOC with a PI controller

Similar to the design procedure of the controller parameters for the speed control loop of RFOC, symmetrical optimum is used to tune the parameters of the voltage PI controller. According to Fig. 4-13 and using Table 3.5, following values for the PI parameters are derived:

$$T_{i,vc} = 1.5a_{vc}^2 a_{cc} T_{s,cc}, \quad (4-37)$$

$$K_{p,vc} = \frac{C_{dc}}{1.84 \frac{V_{PCC,II}}{V_{dc}^*} a_{cc} a_{vc} T_{s,cc}}, \quad a_{vc} \geq 2, \quad (4-38)$$

where, a_{vc} denotes the damping factor of the dc-link voltage control loop.

A detailed block diagram of the applied VOC comprising PLL, decoupling and linearization grids, and the PI controllers is shown in Fig. 4-14. In case of load disturbance, the PI controller of the voltage control loop responds to the dc-link voltage drop. If a big damping factor a_{vc} is applied to avoid oscillation of the voltage control loop, the voltage control loop will be slow and a large transient dc-link voltage drop will occur.

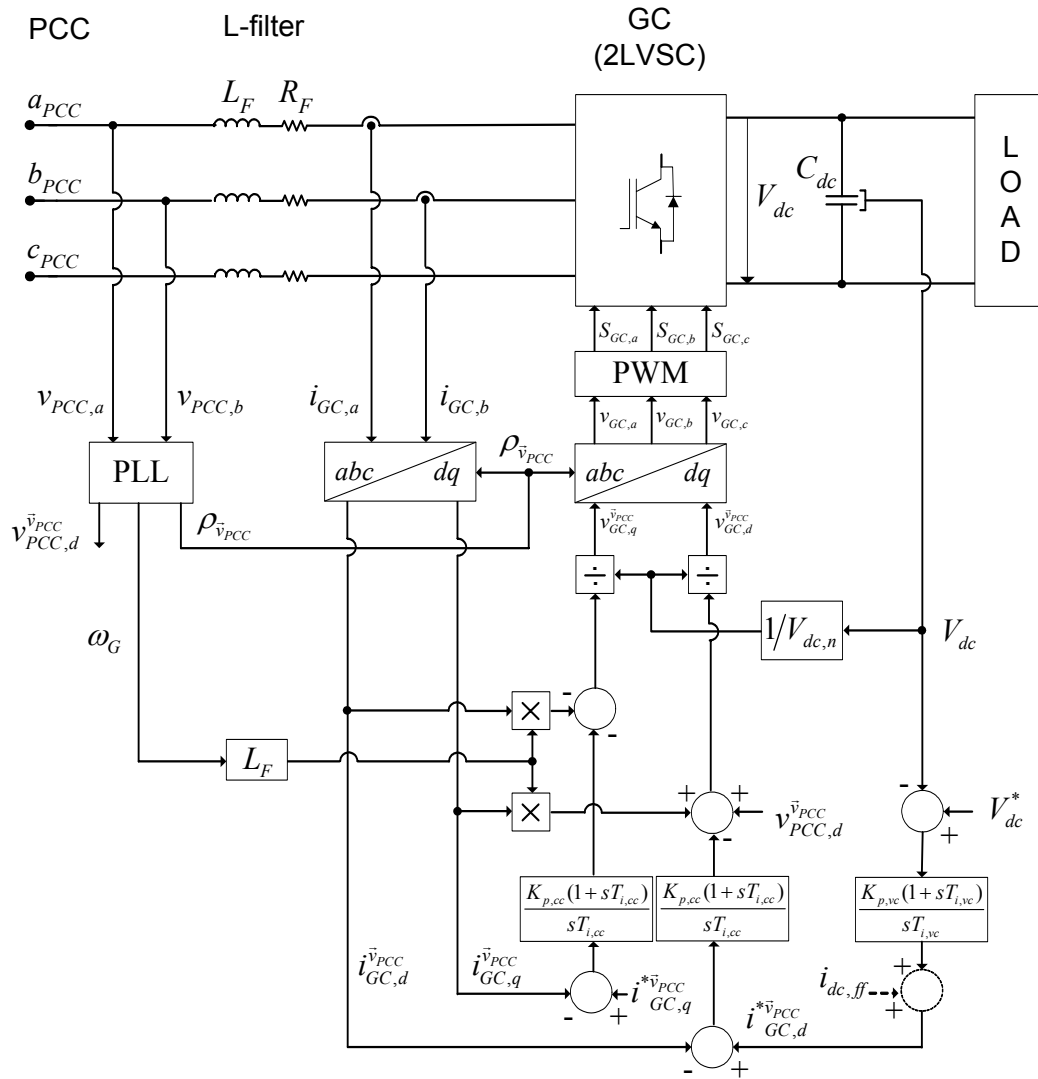


Fig. 4-14 Detailed block diagram of VOC

The dc-link current of the machine side converter $\bar{i}_{dc,MC}$ can be estimated and a feed-forward signal $i_{dc,ff}$ corresponding to the estimated value can be added to the current set point on the d -axes in order to reduce the dc-link voltage drop in case of a load disturbance [20]. If an induction motor drive with RFOC is connected to the dc-link, set point values of the stator voltages and currents (see Fig. 3-7) in the rotating reference frame can be applied to estimate the active and reactive output power of the machine side converter in a method similar to the procedure carried out to obtain equation (4-23). If the power loss of the machine side converter is ignored, the machine side dc-link current can be estimated using the dc-link voltage and the machine side converter output active power as follows:

$$\bar{i}_{dc,MC} = \frac{3}{2} \frac{(v_{S,d}^* \bar{\psi}_{R,d}^S i_{S,d}^* + v_{S,q}^* \bar{\psi}_{R,q}^S i_{S,q}^*)}{V_{dc}^*} \quad (4-39)$$

Considering the gain of the voltage control loop, the following feed-forward signal can be applied in Fig. 4-14 as the feed-forward signal

$$i_{dc,ff} = \sqrt{\frac{3}{2}} \frac{(i_{S,d}^* v_{S,d}^* + i_{S,q}^* v_{S,q}^*)}{V_{PCC,II}} \quad (4-40)$$

4.4.5 Performance investigation of the voltage-oriented controlled PWM active front end converter at symmetrical sinusoidal grid voltage

The performance of VOC for PWM active front end converters is investigated using simulation and experimental results. Simulations are carried out in the SIMULINK. A block diagram of the applied PWM active front end converter test bench is shown in Fig. 4-15. The

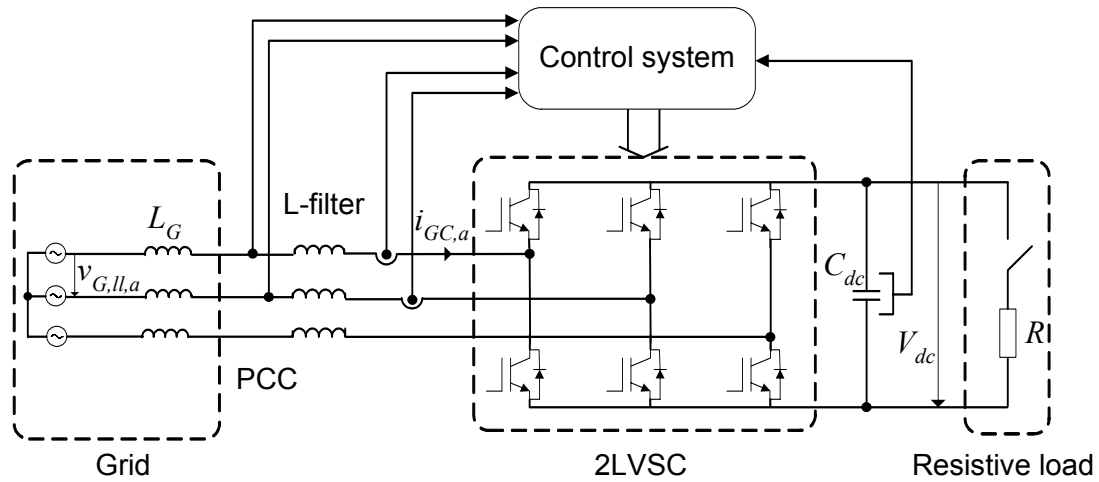


Fig. 4-15 Block diagram of the PWM active front end converter test bench with a resistive load

Table 4.2
Basic parameters of the grid and the PWM active front end

Parameter	Value
Grid	
Nominal grid effective line-to-line voltage, $V_{G,ll,n}$	400 V
Base voltage of grid per-unit system, $V_{b,G}$	$V_{b,G} = \sqrt{\frac{2}{3}} V_{G,ll,n,1}$
Nominal grid frequency, f_G	50 Hz
Base angular frequency, $\omega_{b,G}$	$\omega_{b,G} = 2\pi f_G$ rad/s
Grid stray inductance, L_G	$L_G = 51 \mu\text{H}$
Input L-filter	
L-filter inductance, L_F	1.5 mH
Resistance of the L-filter inductor, R_F	6.4 m Ω
Grid side converter	
IGBTs	SKM400GB128 ($V_{CE} = 1200$ V, $I_C = 400$ A)
Nominal effective converter phase current, $I_{GC,n}$	70 A
Base current of grid per-unit system, $I_{b,G}$	$I_{b,G} = \sqrt{2} I_{GC,n,1}$
Modulation	Asymmetrical regular sampled sinus-triangle PWM
Carrier frequency, f_C	4.05 kHz
Switching frequency, f_{sw}	4.05 kHz
dc-link capacitance, C_{dc}	9 mF
Nominal dc-link voltage, $V_{dc,n}$	700 V

test bench comprises a 2L VSC with a resistive load. The converter is connected to the grid at the PCC through an L-filter. A 400 kVA line transformer (stray inductance $L_G = 51 \mu\text{H}$) provides the grid voltage at the PCC. The basic parameters of the grid and the converter are depicted in Table 4.2.

The block diagram of the control system in Fig. 4-14 is used in simulation and experimental investigation. An ARS-PWM with a carrier frequency of $f_c = 4.05 \text{ kHz}$ ($m_f = 81$) is used as the modulator. The sampling frequencies of the PLL, the current control loop, and the voltage control loop are $f_s = 8.1 \text{ kHz}$ (twice the carrier frequency).

The damping factor of the PLL is considered to be $a_{PLL} = 30$. This damping factor leads to a PLL cut-off frequency of $\omega_{cut-off} = 55 \text{ Hz}$. With this bandwidth, the PLL output will be synchronized to the phase a of the PCC voltage within one cycle, and the PLL output remains clean in spite of line distortions [101].

The damping factors of the current control loop and the dc-link voltage control loop are $a_{cc} = 3$ and $a_{vc} = 4$, respectively. A large damping factor of the voltage control loop is selected to obtain a damped control loop and to reduce noise amplification in the implementation.

The simulation and experimental results for the step response of the current control loop of the VOC are presented in Fig. 4-16(a) and Fig. 4-16(b), respectively. A step reference of 1 pu (99 A) is applied in the current control loop of the q -axis. All parameters are considered to be

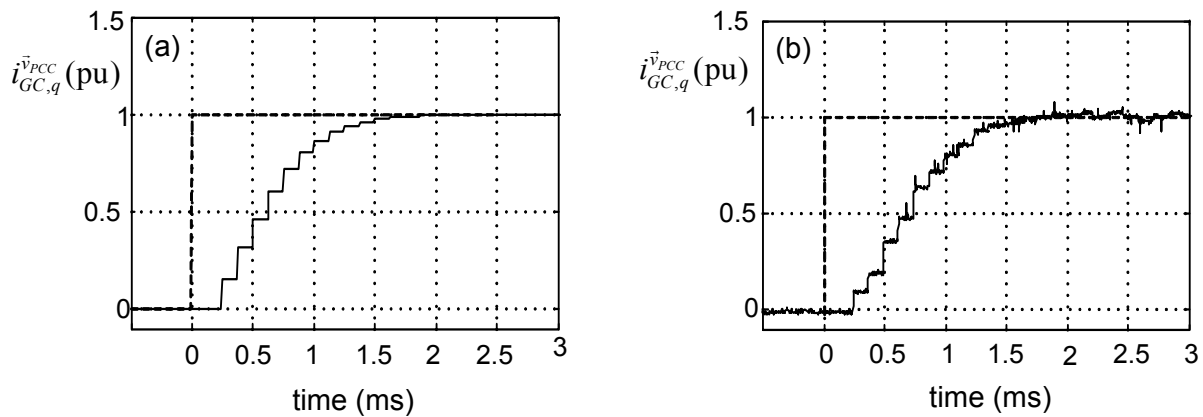


Fig. 4-16 Step response of the current control loop of VOC: (a) Simulation results; (b) Experimental results; $I_{b,G} = 99 \text{ A}$

the same in simulation and experiment. Obviously, simulation and experimental results are well comparable. It can be seen that the current step response has no overshoot ($a_{cc} = 3$) and the settling time of the step response is about 2 ms. By using the control structure in Fig. 4-14 and the PI parameters in (4-34) and (4-35), the current control loop becomes independent of filter parameters (L_f, R_f), and the time constant of the current control loop becomes $1.5a_{cc}T_{s,cc} = 0.56 \text{ ms}$.

The dc-link voltage variation and the converter phase current for nominal load disturbance are presented in Fig. 4-17. The dc-link voltage reference value is 700 V, and a rated load disturbance of 48.5 kW is applied in both simulation and experiment. The results are shown in Fig. 4-17 (a) and Fig. 4-17 (b), respectively. Obviously, simulation and experimental results are comparable. The set point of the converter current on the direct axis is limited to 1.5 pu in both simulation and experiment. The dc-link voltage drop is about 6% of the nominal dc-link voltage $V_{dc,n} = 700 \text{ V}$. The load disturbance is rejected in less than 30 ms in both simulation and experiment results.

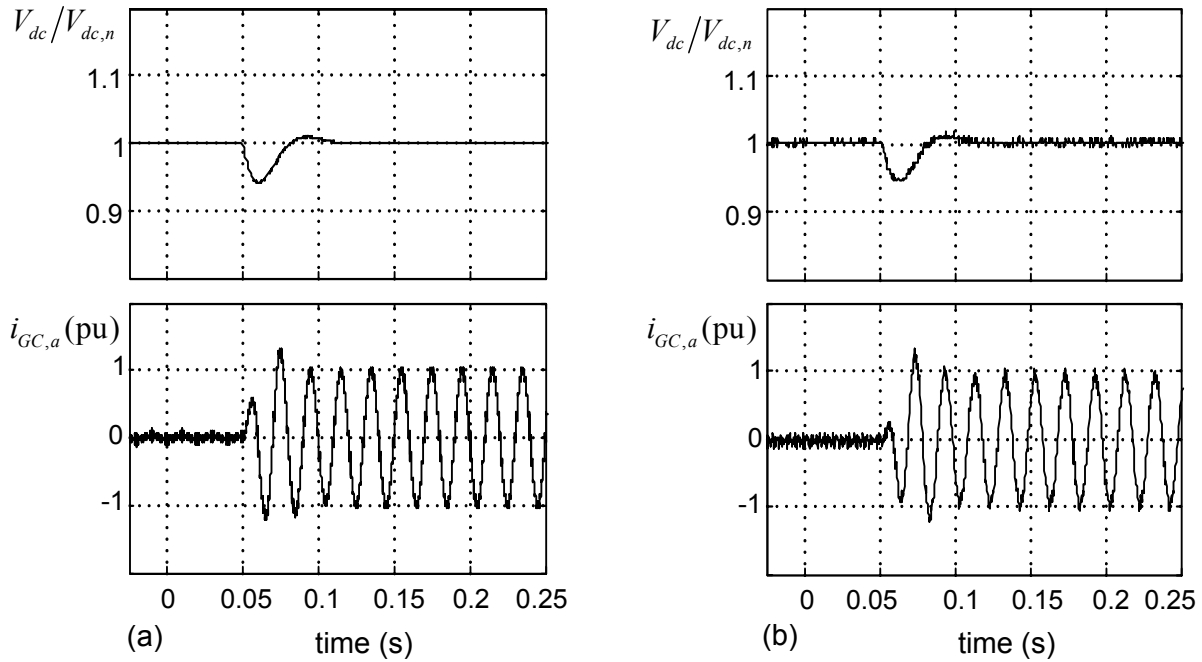


Fig. 4-17 The dc-link voltage and the converter phase current for nominal load disturbance of 48.5 kW: (a) Simulation results; (b) Experimental results; $V_{dc,n} = 700$ V, $I_{b,G} = 99$ A

As mentioned, one of the interesting features of the PWM active front end converters is the sinusoidal input current with the current ripple occurring at switching frequency. However, this statement is valid only if the PWM active front end converter is connected to an ideal distortion-free grid. The line-to-line voltage of the PCC and the grid side converter current at steady-state and nominal load are shown in Fig. 4-18. A distortion-free voltage at the PCC is applied in the simulation (Fig. 4-18 (a)), and the converter current has a sinusoidal waveform with the current ripple at the switching frequency. In the experimental results presented in

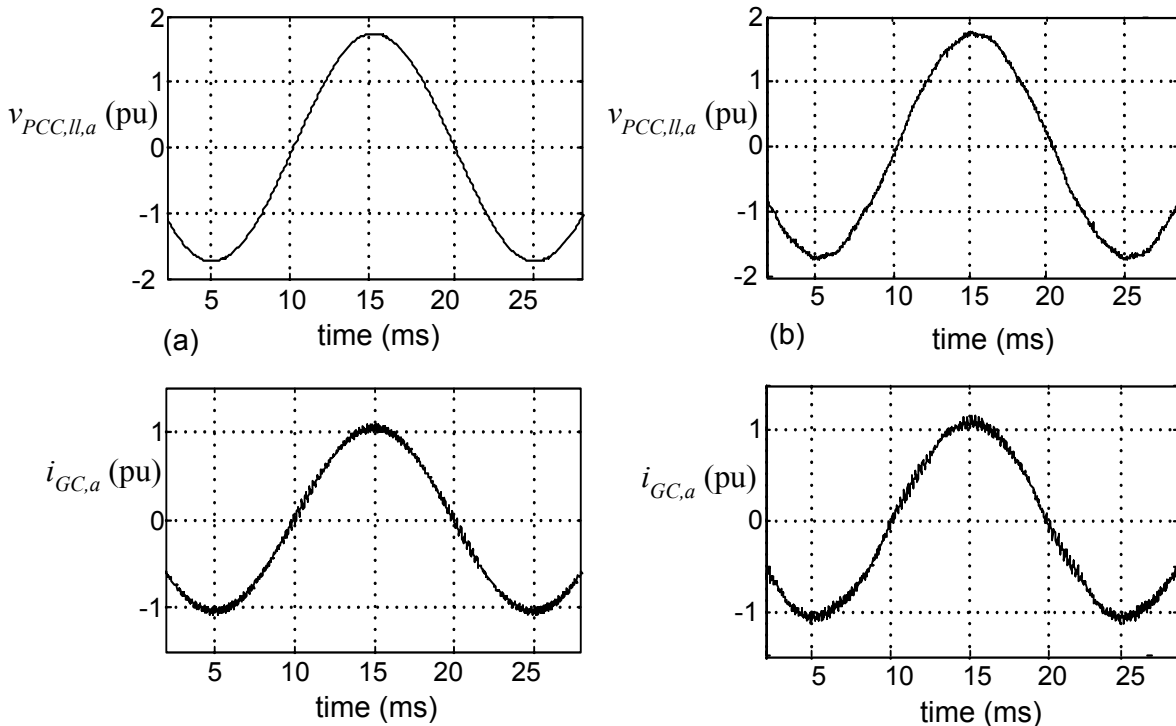


Fig. 4-18 PCC line-to-line voltage and the PWM active front end converter phase current at nominal load and steady-state: (a) Simulation results; (b) Experimental results; $V_{b,G} = 327$ V, $I_{b,G} = 99$ A

Fig. 4-18 (b), the grid voltage at the PCC contains slight low-order harmonics, which are related to the saturation of the mains transformer and other parallel nonlinear loads connected to the grid at the PCC such as diode and thyristor rectifiers. Apparently, the converter current is slightly affected by these distortions of the PCC voltage.

PWM active front end converters operate in parallel with nonlinear loads like diode and thyristor converters in many industrial applications. Nonlinear loads cause voltage distortions (e.g. voltage notches) which can affect the performance of the PWM active rectifiers [98]. The steady-state behavior of the PWM active front end converters in the presence of parallel thyristor converters is depicted in the following section.

4.4.6 Influences of the grid voltage distortions on the steady-state performance of voltage-oriented control

Effects of grid voltage distortions caused by thyristor converters on the steady-state performance of a PWM rectifier with dc-voltage link for low-voltage applications are presented in this section. Disturbance transfer function of the current control loop is used to analyze the effects of the grid distortions. Furthermore, influences of the current controller damping factor, PLL parameters and the filter inductance on the generated current harmonics are presented. For existing grid voltage harmonics, amplitude of the corresponding current harmonics are determined and compared to current harmonics measured by using a 400 V 44 kW test bench consisting of a PWM active front end converter with voltage dc-link in parallel to a thyristor converter. Results of the investigations carried out in this section have been presented in [98].

Nonlinear loads such as diode and thyristor rectifiers cause substantial current and voltage harmonics which decrease the power quality of grids at PCC. Additional problems caused by an input line voltage distortion include a significant distortion of the input current waveforms and an increase of the dc capacitor current and voltage ripple. Performance of PWM active front end converters applying different control schemes to eliminate the dominant line current harmonics under different line voltage conditions has been investigated in recent publications (e.g. [87], [114], [120], [121], [128]). Although PWM three-phase ac/dc/ac converters are increasingly applied in parallel to existing thyristor converters (e.g. dc drives), the influences of a thyristor converter operation on the performance and the current control loop of a PWM

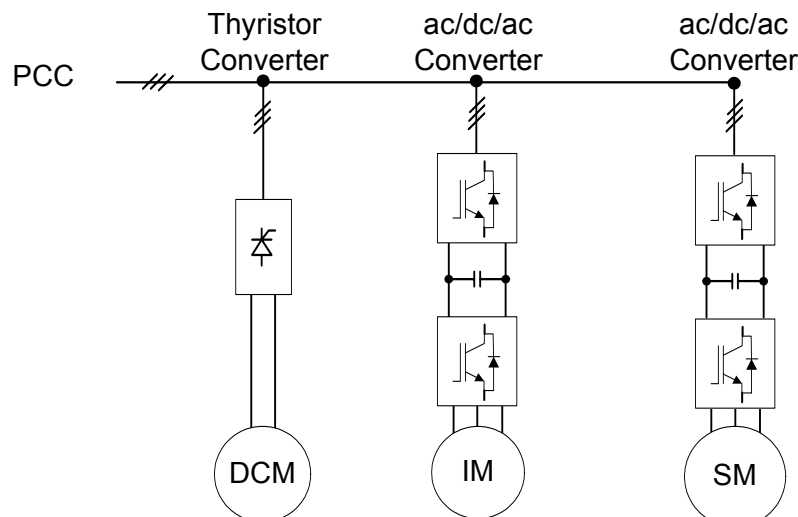


Fig. 4-19 Low-voltage PWM active front ends and thyristor converters connected to PCC

active front end converter with voltage-oriented control has not been investigated in the literature in detail so far.

A typical configuration of PWM ac/dc/ac converters and ac/dc thyristor converter fed drives for low-voltage applications is presented in Fig. 4-19. PWM active front end converters and thyristor converters are connected in parallel to the grid at the PCC. In several industrial applications like in the paper and chemical industry, PWM active front end converters commonly operate at low voltages in parallel to thyristor converter fed dc drives. Corresponding conditions can be found in a large variety of currently existing industrial

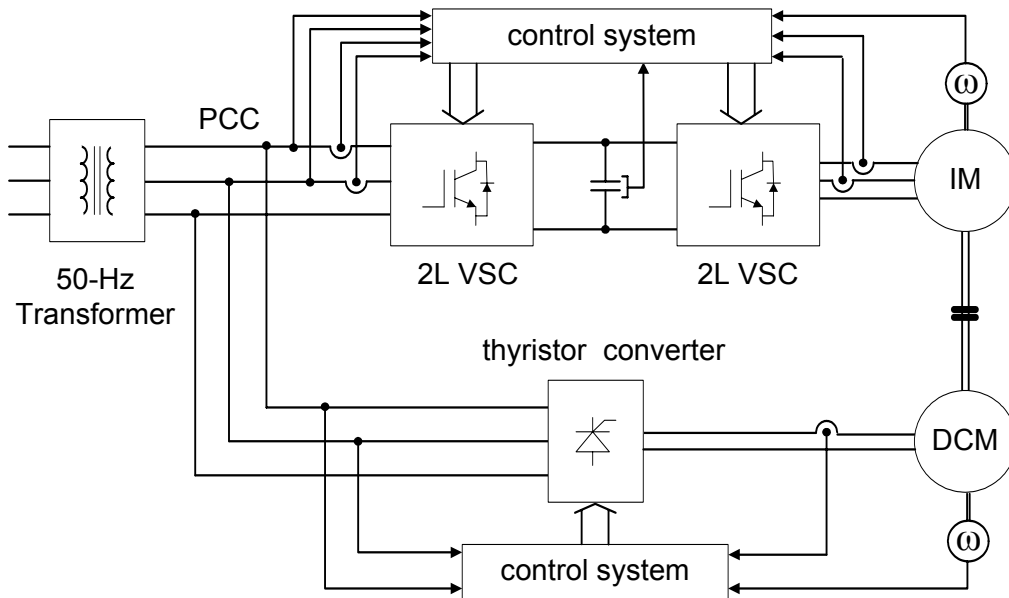


Fig. 4-20 A block diagram of the test bench

applications. For example, such configurations have been recently applied to the newest hot and cold rolling mills.

A block diagram of the applied test bench to investigate the steady-state performance of a PWM active front end converter with VOC connected to a distorted grid is depicted in Fig. 4-20. The power part of the test bench is illustrated in Fig. 4-21 in more detail.

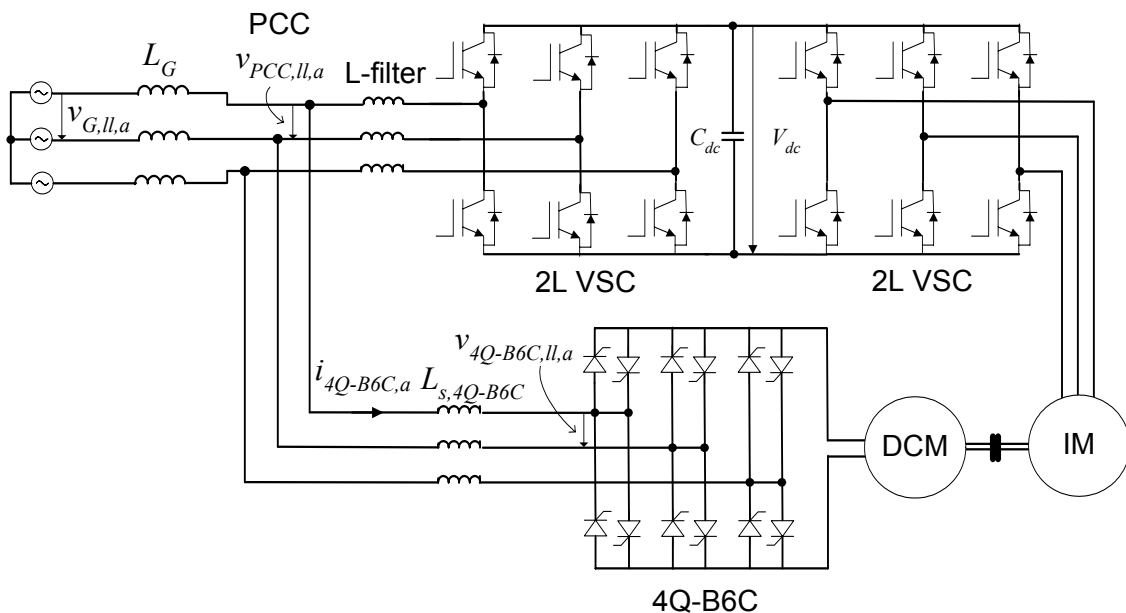


Fig. 4-21 A detailed block diagram of the test bench power part

The basic parameters of the IM and the machine side 2L VSC are presented in Table 3.10 and Table 3.11 of the previous chapter. Specification of the grid, input filter of the PWM active front end converter, and the grid side converter are presented in Table 4.2. The IM and the DCM are coupled to configure a motor-generator system. The DCM is fed by a four-quadrant thyristor converter (4Q-B6C) which allows speed, torque, and armature current control. The parameters of the DCM and the thyristor converter are listed in Table 4.3.

Table 4.3
Basic parameters of the dc machine and the thyristor converter

Parameter	Value
DC Machine	
Nominal mechanical power	84.6 kW
Nominal speed	2710 1/min
Nominal torque	298 Nm
Nominal armature voltage	400 V
Nominal armature current	229 A
Thyristor converter (4Q-B6C)	
Type	PAD 664A V5
Nominal voltage	400 V/50 Hz
Nominal current	350 A
Nominal power	147 kW
Filter inductance, $L_{s,4Q-B6C}$	82 μ H

The induction machine is connected to an inverter which realizes torque and speed control on the basis of a rotor-flux-oriented control. A large dc-link capacitor (46 Ws / kVA) is applied to reduce the dc-link voltage ripple to less than 1% of the dc-link voltage ($V_{dc} = 700$ V) and to decrease the effects of the induction motor current harmonics on the active rectifier line current harmonics. The maximum value of the dc-link voltage ripple is 2.8% if a typical designed dc-link capacitance of 13 Ws/kVA is used. Fig. 4-22 (a) shows the thyristor converter and its grid side inductor (L_s) connected to the PCC. The PWM active front end converter and its grid side L-filter are shown in Fig. 4-22 (b) and Fig. 4-22 (c).

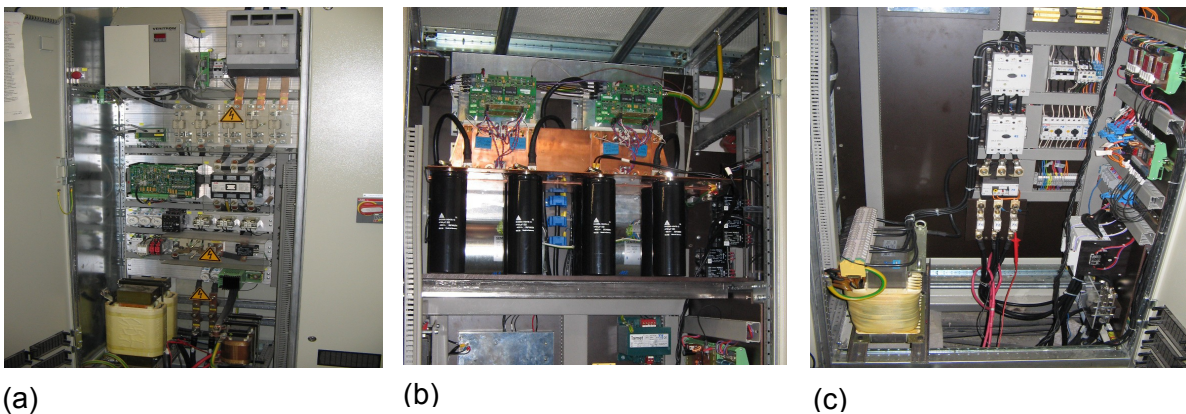


Fig. 4-22 (a) Thyristor converter and the line inductor; (b) grid side converter; (c) input L-filter of the PWM active front end

4.4.6.1. Performance of the current control loop of VOC for a polluted grid

Distortions of the grid voltage as a result of nonlinear loads such as diode and thyristor rectifiers and also saturation of transformers can be modeled as a distortion in the current control loop added to the PWM converter output as shown in Fig. 4-11. In order to model the voltage harmonics in the rotating frame synchronous to the fundamental positive sequence of the PCC voltage, a voltage harmonic with h^{th} order is assumed. Considering the converter model in the stationary reference frame described in (4-10), the model of the grid side converter with input L-filter for voltage and current harmonic vectors with h^{th} order is as follows:

$$\hat{V}_{PCC,h} e^{j\theta_{\bar{v}_{PCC,h}}} = L_F \frac{d}{dt} \left(\hat{I}_{GC,h} e^{j\theta_{\bar{i}_{GC,h}}} \right) + R_F \hat{I}_{GC,h} e^{j\theta_{\bar{i}_{GC,h}}} + \hat{V}_{GC,h} e^{j\theta_{\bar{v}_{GC,h}}}, \quad (4-41)$$

where

$\hat{V}_{PCC,h}$ and $\theta_{\bar{v}_{PCC,h}}$ are amplitude and phase angle of the PCC voltage harmonic vector $\bar{v}_{PCC,h} = \hat{V}_{PCC,h} \angle \theta_{\bar{v}_{PCC,h}}$,
 $\hat{I}_{GC,h}$ and $\theta_{\bar{i}_{GC,h}}$ denote amplitude and phase angle of the grid side converter current harmonic vector $\bar{i}_{GC,h} = \hat{I}_{GC,h} \angle \theta_{\bar{i}_{GC,h}}$,
 $\hat{V}_{GC,h}$ and $\theta_{\bar{v}_{GC,h}}$ being amplitude and phase angle of the grid side converter output voltage harmonic vector $\bar{v}_{GC,h} = \hat{V}_{GC,h} \angle \theta_{\bar{v}_{GC,h}}$.

The projection presented in (3-4) has been applied to determine the voltage and current harmonic vectors.

The vector arguments ($\theta_{\bar{v}_{PCC,h}}, \theta_{\bar{i}_{GC,h}}, \theta_{\bar{v}_{GC,h}}$) can be represented as a function of the fundamental positive sequence of the PCC voltage vector argument at steady state as below:

$$\begin{cases} \theta_{\bar{v}_{PCC,h}} = n\rho_{\bar{v}_{PCC}} + \theta_{0,\bar{v}_{PCC,h}} \\ \theta_{\bar{v}_{GC,h}} = n\rho_{\bar{v}_{PCC}} + \theta_{0,\bar{v}_{GC,h}} \\ \theta_{\bar{i}_{GC,h}} = n\rho_{\bar{v}_{PCC}} + \theta_{0,\bar{i}_{GC,h}} \end{cases}, \quad (4-42)$$

where

$\rho_{\bar{v}_{PCC}}$ denotes the phase angle of the fundamental positive sequence of the PCC voltage vector, $\theta_{0,\bar{v}_{PCC,h}}$, $\theta_{0,\bar{v}_{conv,n}}$, and $\theta_{0,\bar{v}_{conv,n}}$ are the phase angles of the corresponding vectors at $t = 0$. Furthermore, n is a positive or a negative integer for harmonics with positive sequences ($n = h$) or negative sequences ($n = -h$), respectively.

Projecting (4-42) into the rotating reference frame synchronous to the fundamental positive sequence of the PCC voltage vector results in:

$$L_F \frac{d\bar{i}_{GC,dq,h}}{dt} + R_F \bar{i}_{GC,dq,h} = (\bar{v}_{PCC,dq,h} - \bar{v}_{GC,dq,h}) + j\omega_G \bar{i}_{GC,dq,h}, \quad (4-43)$$

where

$\bar{v}_{PCC,dq,h}$ denotes the voltage harmonic vector of the PCC in the rotating reference frame,
 $\bar{i}_{GC,dq,h}$ is the grid side converter current harmonic vector in the rotating reference frame,
 $\bar{v}_{GC,dq,h}$ being the grid side converter output voltage harmonic vector in the rotating reference frame.

It is noticeable that all voltage and current harmonics in the rotating frame are ac signals of frequencies different from those of the corresponding line voltage and current harmonics as presented in the following equation:

$$\begin{cases} \vec{v}_{PCC,dq,h} = \hat{V}_{PCC,h} e^{j((n-1)\rho_{\vec{v}_{PCC}} + \theta_{0,\vec{v}_{PCC,h}})} \\ \vec{v}_{GC,dq,h} = \hat{V}_{GC,h} e^{j((n-1)\rho_{\vec{v}_{PCC}} + \theta_{0,\vec{v}_{GC,h}})} \\ \vec{i}_{GC,dq,h} = \hat{I}_{GC,h} e^{j((n-1)\rho_{\vec{v}_{PCC}} + \theta_{0,\vec{i}_{GC,h}})} \end{cases} \quad (4-44)$$

Applying the real and imaginary parts of $-j\omega_g \vec{i}_{dq,g,n}$ as the decoupling terms, the last term in (4-43) is compensated for and, similar to the converter model for the fundamental positive sequence, a first order system is obtained as the converter model for the h^{th} order harmonic. Consequently, the current control loop in Fig. 4-11 can be used to investigate the influences of the grid distortions on the converter currents.

Considering the current control loop in Fig. 4-11, the transfer function corresponding to the h^{th} order harmonic is:

$$\frac{\hat{I}_{GC,dq,h}}{\hat{V}_{PCC,dq,h}} = \frac{1}{(R_F + L_F s)} \cdot \frac{(1 + sT_{s,cc})(1 + 0.5sT_{s,cc})}{(1 + sT_{s,cc})(1 + 0.5sT_{s,cc}) + R_F / (1.5a_{cc}T_{s,cc}s)} \quad (4-45)$$

For a distorted symmetrical grid, the voltage harmonics and their positive (+) or negative (-) natural phase sequence in stationary ($\alpha\text{-}\beta$) and rotating ($d\text{-}q$) coordinate systems are listed in Table 4.4. Assuming a balanced system, the phase sequence indicates the harmonic space phasor rotational direction. By projecting (4-41) into the fundamental reference frame, the harmonic order is increased (positive sequence) or decreased (negative sequence) as described in Table 4.4.

Consequently, in order to calculate the current harmonic amplitude caused by an h^{th} order PCC voltage harmonic in steady-state, the frequency in (4-45) should be set as follows:

$$\begin{cases} s = j(n-1)\omega_g; \text{ for harmonics with positive sequence} \\ s = j(1-n)\omega_g; \text{ for harmonics with negative sequence} \end{cases} \quad (4-46)$$

For harmonics with positive sequence, n is a positive integer ($n = h$) and for harmonics with negative sequence, n is a negative integer ($n = -h$).

Bode diagram of the current harmonics transfer function in (4-45) and the bode diagram of the input L-filter are shown in Fig. 4-23 using the parameters presented in Table 4.2. The Bode diagram of the current control loop for the line distortions has two cut-off frequencies. The cut-off frequency at low frequencies is related to the ability of the current control loop to reject the low-order current harmonics. Obviously, the current control loop is fast enough to reject the low-order grid voltage harmonics (lower than 0.5 Hz). The second cut-off frequency is related to the grid side filter. Harmonics with a higher order (higher than 800 Hz) are attenuated because of the high value of the inductor impedance for higher frequencies.

Table 4.4
Harmonics order in stationary ($\alpha\text{-}\beta$) and rotating ($d\text{-}q$) reference frame

Harmonic order in stationary reference frame	Harmonic order in rotating reference frame
$1^+, 4^+, 7^+, 10^+, 13^+, 16^+ \dots k^+$	$0, 3^+, 6^+, 9^+, 12^+, 15^+ \dots (k-1)^+$
$2^-, 5^-, 8^-, 11^-, 14^-, 17^- \dots (k+1)^-$	$3^-, 6^-, 9^-, 12^-, 15^-, 18^- \dots (k+2)^-$

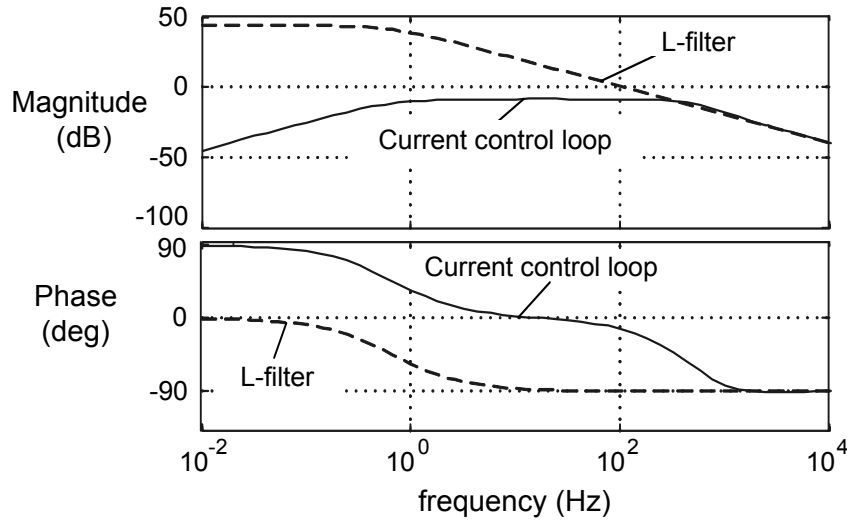


Fig. 4-23 Bode diagram of the disturbance transfer function of VOC

Varying the current controller’s damping factor ($a_{cc} \geq 2$) and the line side inductance changes the behavior of the current control loop against a distorted grid. A lower damping factor ($a_{cc} = 2$) leads to an increase in the current control loop bandwidth and reduces the gain of the current control loop for line voltage harmonics as shown in Fig. 4-24 (a). It is noticeable that a high current control loop bandwidth will cause problems like noise amplification.

A higher grid side inductance also leads to a better harmonics rejection. The Bode diagram of the current control loop for voltage distortion as input is shown in Fig. 4-24 (b) for two different line inductances.

Provided that the line voltage harmonics are located at the second corner of the closed loop Bode diagram, the current controller is not able to reject the effects of the line voltage distortions significantly, even with a low damping factor and a high value of the line inductance. Therefore, the grid voltage harmonics in this range will cause current harmonics with considerable amplitudes.

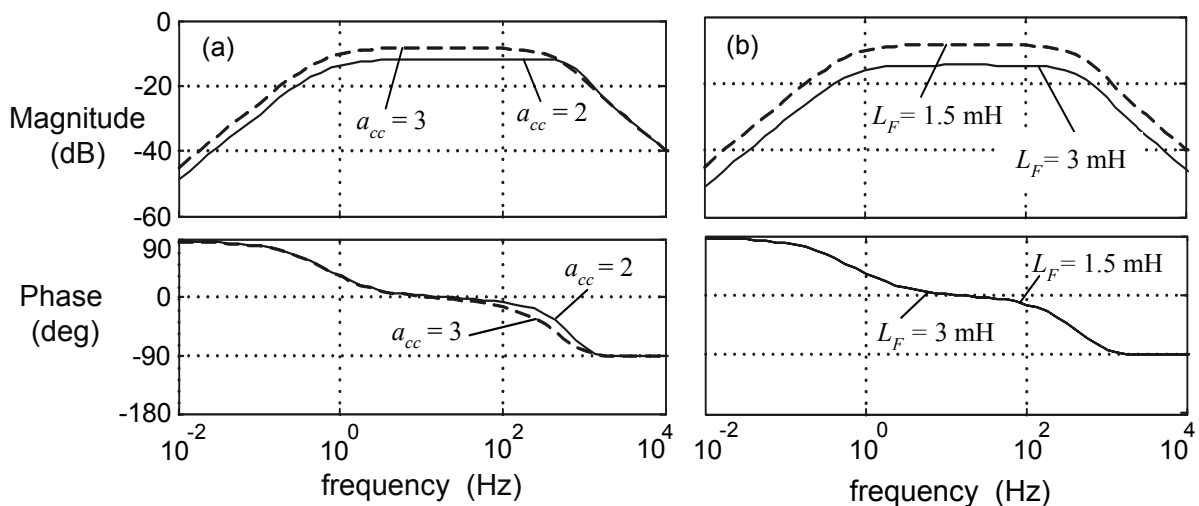


Fig. 4-24 Bode diagram of the disturbance transfer function of VOC for various damping factors of PI controller and the filter inductance: (a) with a constant line inductor ($L_F = 1.5$ mH); (b) with a constant damping factor of PI controller ($a_{cc} = 3$)

4.4.6.2. Simulation and experimental results

The measured line-to-line voltage of the thyristor converter ($v_{4Q-B6C,ll,a}$ in Fig. 4-21) and the PCC ($v_{PCC,ll,a}$ in Fig. 4-21) are shown in Fig. 4-25 where the thyristor converter operates at a load of 44 kW. Furthermore, Fig. 4-25 illustrates the line current of the thyristor converter ($i_{4Q-B6C,a}$ in Fig. 4-21) and shows that the voltage of the PCC is notched during the converter

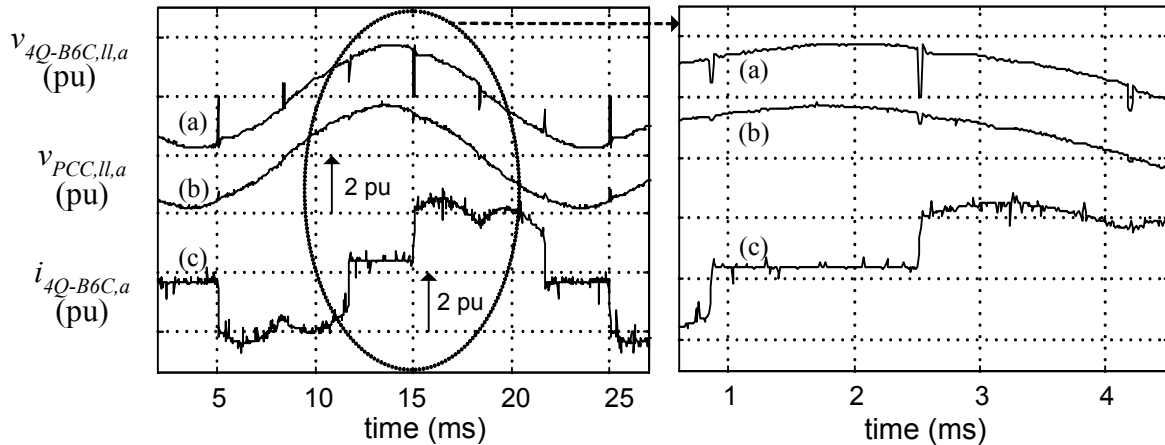


Fig. 4-25 (a) Line-to-line voltage of the thyristor converter ($v_{4Q-B6C,ll,a}$); (b) the PCC line-to-line voltage ($v_{PCC,ll,a}$); (c) phase current of the thyristor converter ($i_{4Q-B6C,a}$)

current commutation. Line voltage notching is periodic in nature and causes low-order odd voltage harmonics (5^{th} , 7^{th} , 9^{th} ...). The effects of this voltage harmonics on the phase current of the PWM active front end converter are investigated in this section using simulation and experimental results. MATLAB / SIMULINK are used in the simulations.

Table 4.5 summarizes the simulation results for the effects of the PLL parameter, current controller attenuation factor, and line filter inductance on the amplitude of the PWM active front end converter current harmonics. In part (a) of Table 4.5, the damping factor of the PLL (a_{PLL}) and the current control loop (a_{cc}) are 30 and 3, respectively. The inductance of the input L-filter equals 1.5 mH. Current harmonics obtained from simulation and determined by using (4-45), (4-46), and the voltage harmonics amplitude are presented. The current harmonics obtained from simulation and the calculated current harmonics are well comparable. Fig. 4-26 shows the simulation results for the grid voltage, the grid current and their harmonic spectra corresponding to part (a) of Table 4.5.

In part (b) of Table 4.5, the simulation results for the PLL with a smaller damping factor ($a_{PLL} = 3$) are presented. These results show that a smaller damping factor leads to increased amplitude of the 5^{th} harmonic in the grid current, but the higher harmonic orders are not changed significantly.

The current control loop damping factor is reduced to $a_{cc} = 2$, and the effect of the reduction of the current controller damping factor on the current harmonics is presented in part (c) of Table 4.5. This reduction by 33% in damping factor leads to a 19% decrease in the amplitude of the 5^{th} current harmonic while the amplitude of current harmonics with a higher order increased as expected according Fig. 4-24 (a).

According to Fig. 4-24 (b), using a higher value of the filter inductor will reduce the amplitude of the current harmonics significantly. The simulation results of using a line filter with $L_F = 3$ mH are shown in part (d) of Table 4.5.

Table 4.5

PCC voltage harmonics and current harmonics of the PWM active front end converter in percent of the base voltage and current (simulation results), $V_{b,G} = 327 \text{ V}$, $I_{b,G} = 99 \text{ A}$

Harmonic order (h)	5	7	11	13	17	19
(a) $a_{PLL} = 30$, $a_{cc} = 3$, $L_F = 1.5 \text{ mH}$						
Amplitude of the line-to-line voltage harmonics (%)	2.65	0.88	1.89	1.11	1.75	1.19
Calculated current harmonics (%)	1.60	0.52	0.70	0.41	0.46	0.31
Simulated current harmonics amplitude (%)	1.61	0.70	0.83	0.48	0.52	0.34
Calculated / Simulated (%)	99	74	84	85	88	91
(b) $a_{PLL} = 3$, $a_{cc} = 3$, $L_F = 1.5 \text{ mH}$						
Amplitude of line-to-line voltage harmonics (%)	2.65	0.87	1.91	1.11	1.75	1.18
Simulated current harmonics amplitude (%)	1.85	0.70	0.85	0.43	0.54	0.34
Variation in current harmonics compared to (a) (%)	15	0	2.4	-10	4	0
(c) $a_{PLL} = 30$, $a_{cc} = 2$, $L_F = 1.5 \text{ mH}$						
Amplitude of line-to-line voltage harmonics (%)	2.67	0.90	1.89	1.13	1.77	1.21
Simulated current harmonics amplitude (%)	1.30	0.67	0.87	0.57	0.63	0.42
Variation in current harmonics compared to (a) (%)	-19	-4.3	2	18	21	24
(d) $a_{PLL} = 30$, $a_{cc} = 3$, $L_F = 3 \text{ mH}$						
Amplitude of line-to-line voltage harmonics (%)	2.70	0.90	1.94	1.16	1.73	1.26
Simulated current harmonics amplitude (%)	0.78	0.43	0.41	0.27	0.29	0.18
Variation in current harmonics compared to (a) (%)	-52	-39	-50	-44	-44	-47

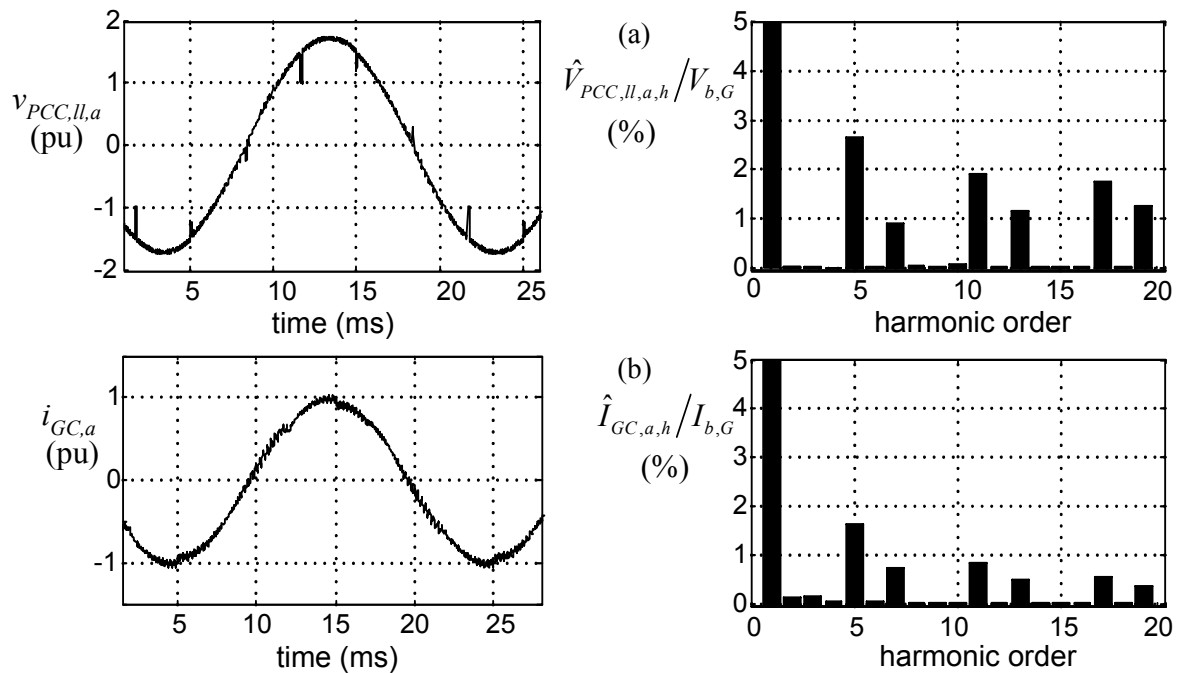


Fig. 4-26 Simulation results for the steady-state performance of the active front end converter connected to a notched grid: (a) grid line-to-line voltage at the PCC and the corresponding harmonic spectrum; (b) phase current of the active front end converter and the corresponding harmonic spectrum; $V_{b,G} = 327$, $I_{b,G} = 99 \text{ A}$

Obviously, an increase in the filter inductance by 50 % reduces the amplitude of the 5th order current harmonic by about 50% and the higher order harmonics are reduced by 39% - 50%. The steady-state performance of the active front end converter is also evaluated practically under notched grid conditions. The measured PCC line-to-line voltage and its harmonic spectrum are depicted in Fig. 4-27(a). The parameters of the PWM converter and the PLL are chosen according to the part (a) of Table 4.5. The measured grid phase current of the active front end converter and the related harmonic spectrum are shown in Fig. 4-27(b). It can be seen that the 5th and 7th harmonics of the grid current cannot be damped satisfactorily. The measured and calculated results are also summarized in Table 4.6 part (a). The amplitude of the line voltage harmonics and equations (4-45) and (4-46) are used to calculate the amplitude of the current harmonics. The fundamental amplitude of the line-to-line voltage and

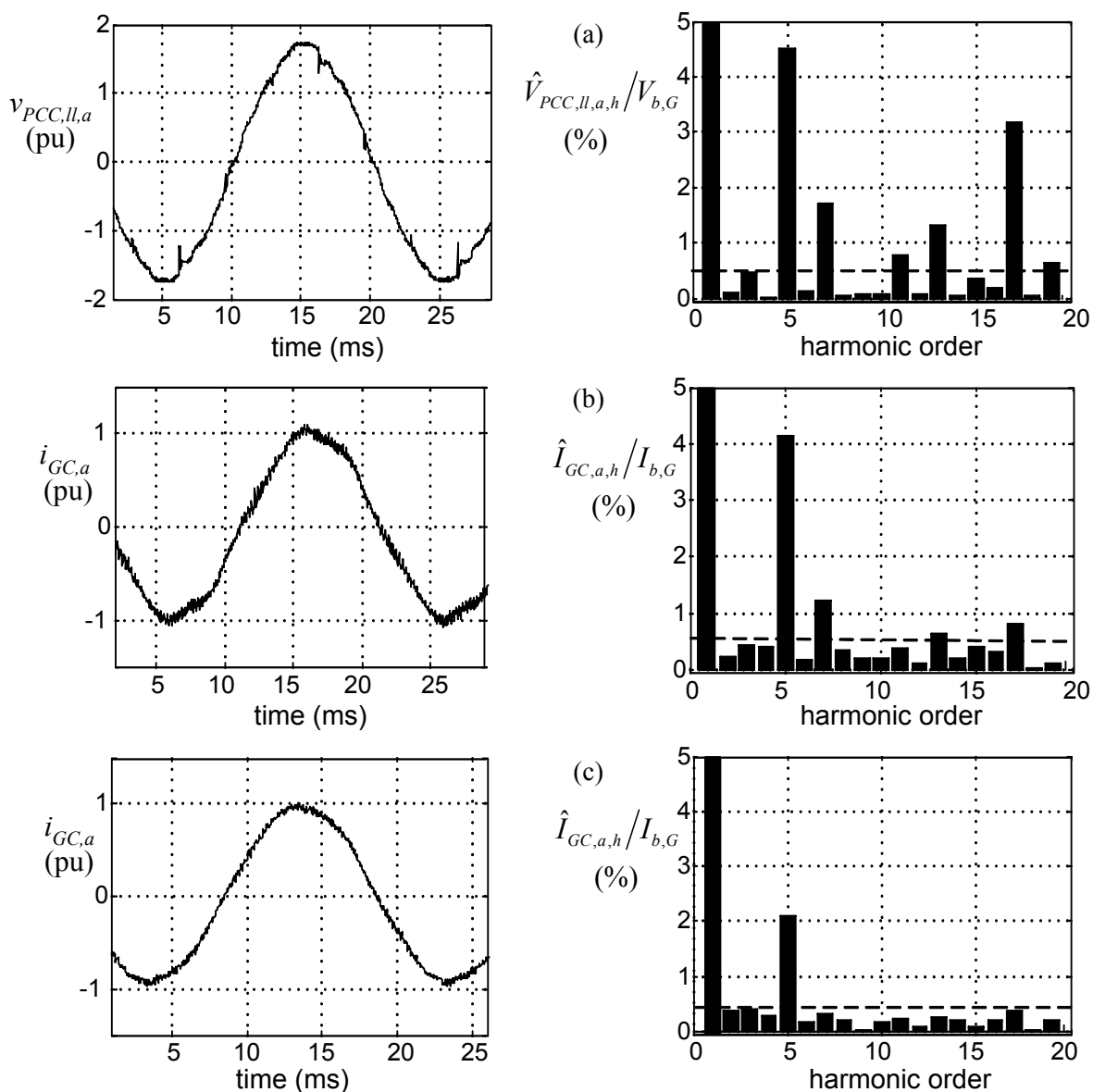


Fig. 4-27 Experimental results for the steady-state performance of the active front end converter connected to a notched grid: (a) the PCC line-to-line voltage and the corresponding harmonic spectrum; (b) phase current of the active front end converter and the corresponding harmonic spectrum, $L_F = 1.5$ mH (0.143 pu); (c) phase current of the active front end converter and the corresponding harmonic spectrum, $L_F = 3$ mH (0.286 pu); $V_{b,G} = 327$, $I_{b,G} = 99$ A

Table 4.6

Measured voltage and current harmonics of the active front end converter for a notched grid in percent of the base voltage and current, $V_{b,G} = 327$, $I_{b,G} = 99$ A

Harmonic order (h)	5	7	13	17
(a) $a_{PLL} = 30$, $a_{cc} = 3$, $L_F = 1.5$ mH				
Amplitude of PCC line-to-line voltage harmonics (%)	4.49	1.7	1.33	3.19
Calculated amplitude of current harmonics (%)	2.7	1.00	0.53	0.86
Measured current harmonics amplitude (%)	4.14	1.24	0.65	0.82
Calculated / Measured (%)	66	81	82	105
(b) $a_{PLL} = 30$, $a_{cc} = 3$, $L_F = 3$ mH				
Amplitude of PCC line-to-line voltage harmonics (%)	4.2	1.07	1.05	2.84
Measured current harmonics amplitude (%)	2.1	-	-	-
Variation in current harmonics compared to (a) (%)	-49	-	-	-

the grid side converter current are 550 V and 101 A, respectively. Current and voltage harmonics with amplitudes below 5% are considered as measurement error.

The main reasons for the difference between measured and calculated values in Table 4.6 are:

- Dead time effects are not considered in the simulations and in the transfer function (4-45). The converter's dead time is considered to be $2\mu\text{s}$ and produces harmonics of $6n \pm 1$ ($n = 1, 2, 3, \dots$) in the converter output voltages which affects the grid current,
- The applied approximation in the modeling of the PWM and processing delays (both of them are modeled as simple first-order delay),
- Distortions in the measured voltage cause the PLL to produce a distorted grid voltage angle because of its incomplete attenuation of the angle distortion.

As shown in Table 4.5, solely a larger line inductor leads to a reduction in the amplitude of all current harmonics. The experimental results for the steady-state performance of the PWM active front end converter with a greater value of the filter inductance ($L_F = 3$ mH) are presented in Fig. 4-27 (c). The damping factors of the PLL and the current controllers are 30 and 3, respectively. The measurement results are given in Table 4.6 part (b). The experimental results confirm the simulation results presented in Table 4.5 part (d).

To summarize; assuming symmetrical sinusoidal grid voltages and a constant dc-link voltage, the widely spread voltage-oriented controlled PWM active front end converters generate grid current harmonics in carrier bands of n times the switching frequency, which are usually sufficiently damped by moderate inductive filters in industrial grids. However, grid voltage at the PCC is substantially distorted by the commutation of thyristors if PWM active front end converters and thyristor converters are operated in parallel. In this case, voltage-oriented controlled PWM active front end converters are not able to suppress low-order current harmonics (e.g. 5th and 7th) if conventional state-of-the-art PI current controllers are applied. The use of faster PI current controllers decreases the lower current harmonics (e.g. 5th and 7th) but increases the higher current harmonics (e.g. >11th). An increase in the filter inductor leads to a significant damping of all current harmonics between grid and switching frequency. However, additional costs, size and weight of an increased inductor as well as the limitation of the maximum dc-link voltage and the dynamic performance prevent the use of large filter

inductors. Obviously, the application of control schemes like individual harmonic control overriding current controller [117], [118] and Multi-Resonant current controllers [96], [108], [109], which are able to suppress harmonic currents at distorted grids, are the most attractive solution if sinusoidal grid currents are required in industrial applications where thyristor converters operate in parallel to self-commutated PWM active front end converters.

4.5 Input filter design for PWM active front end converters

An inductance is the most simple filter configuration between a PWM voltage source converter and the grid. However, the limited maximum dc-link voltage and dynamic performance of a converter with common switching frequencies as well as the substantial costs and size of the inductance prevent the use of a pure inductive filter for medium- and high-power converters if grid standards have to be guaranteed (e.g. IEEE-519).

The existing application of an LCL-filter is an attractive solution to overcome these problems. The higher harmonic attenuation of the LCL-filter permits the use of lower switching frequencies to meet the harmonic limits presented in the standards (e.g. IEEE-519-1992 [97]).

The design of the LCL-filter components according to the given maximum current harmonics (e.g. IEEE-519-1992) is a complex task. The reference [107] presents a design procedure using the trial-and-error method. The selection of the initial values for the converter current ripple and the filter capacitance absorbed reactive power, especially, complicates the design procedure. Furthermore, the design of the converter side inductance for a selected converter current ripple is not addressed in this reference. Basic analytical expressions to calculate the upper limits of the filter inductance, the filter capacitance, and the converter current ripple are presented in [12], [43], [75], [119]. Reference [100] describes a design procedure where the maximum converter current ripple determines the design of the filter inductance and the filter capacitance is chosen based on the reactive power. Basic criteria for an LCL-filter design on the basis of the filter attenuation factor for the grid current harmonics at switching frequency are presented in [129]. However, so far a precise and clear design procedure considering the control reserve limitation and the amplitudes of the grid current harmonics has not been presented.

In this thesis, an iterative procedure to design the L- and LCL-filter parameters considering the most significant grid current harmonics is proposed based on the guidelines presented in [107]. The procedure uses the analytical expression of the converter voltage harmonics by Bessel functions. As an example, the stored energy of the filter components as a measure for the expense of the passive components is considered to compare different filter designs. The structure of the active front end converter used to investigate the filter design procedure and the system performance is presented in Fig. 4-28. The interface between grid and converter is an L-filter or an LCL-filter to damp the current harmonics injected into the grid. The filter components are considered to be variable to study the filter performance for various filter designs. A 2L VSC with a carrier frequency of 4.05 kHz is used as power converter. An asymmetrical regular sampled PWM (ARS-PWM) is applied as modulator. The basic parameters of grid and the grid side converter are presented in Table 4.2.

The input L- and LCL-filters are designed to meet the harmonic distortion limits according to IEEE-519-1992. Table 4.7 shows the IEEE-519-1992 definitions for the current harmonic

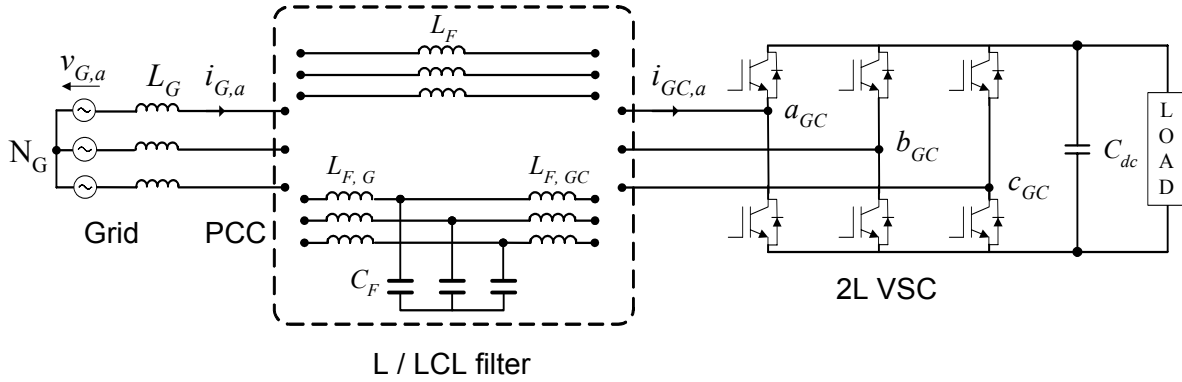


Fig. 4-28 Three-phase active front end converter with L- and LCL-filter

limits at PCC [97]. Considering the capability of the PWM converter to operate at power generation mode, the spectra content of the grid currents around the switching frequency and multiples of the switching frequency should be attenuated to be lower than 0.3%. It should be noted that in the design procedure of both L- and LCL-filters, the resistance of the filter inductors is assumed negligible in comparison to the inductive reactance at the switching frequency. Results of the investigations carried out in this section are presented in [99].

Table 4.7

Current harmonic limits in percentage of rated current amplitude according to IEEE-519

Maximum odd harmonic current distortion (in percent) of I_G for general distribution systems (120V–69kV)					
I_{SC} / I_G	$h < 11$	$11 \leq h < 17$	$17 \leq h < 23$	$23 \leq h < 35$	$35 \leq h$
$< 20^*$	4.0	2.0	1.5	0.6	0.3
$20 < 50$	7.0	3.5	2.5	1.0	0.5
$50 < 100$	10.0	4.5	4.0	1.5	0.7
$100 < 1000$	12.0	5.5	5.0	2.0	1.0
> 1000	15.0	7.0	6.0	2.5	1.4

I_{SC} : grid short circuit current.

I_G : maximum demand grid current.

Even harmonics are limited to 25% of the odd harmonics.

*All power generation equipment is limited to this value of current distortion.

4.5.1 L-filter design procedure

A single-phase representation of the PWM active front end converter with L-filter is shown in Fig. 4-29 (a). There are upper and lower limits for the total filter inductance $L_{F,t} = L_G + L_F$. The upper limit of the total inductance is related to the limited maximum filter voltage drop at a limited dc-link voltage for a given power semiconductor voltage class. The lower limit of the total inductance is caused by the limitations of the grid current harmonics (e.g. IEEE-519).

Upper limit of the L-filter inductance

The converter is considered to operate with its maximum output voltage (maximum modulation depth in the linear range) at rated current in order to determine the upper limit

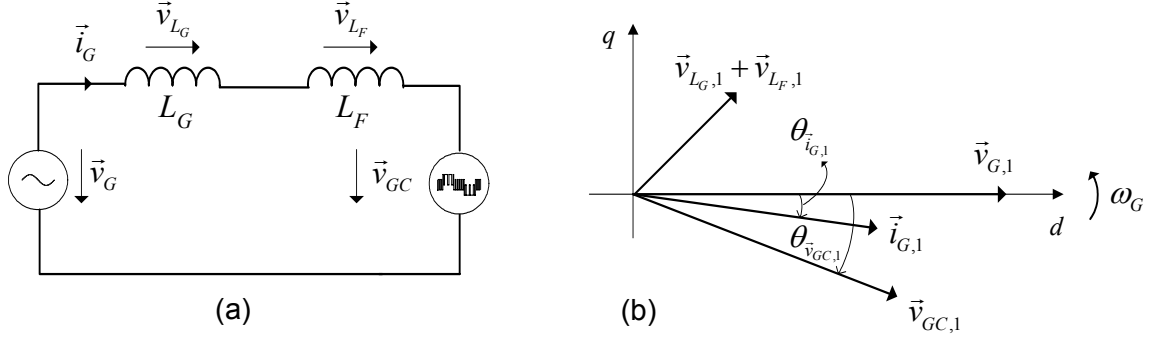


Fig. 4-29 (a) A single-phase representation of PWM active front end with L-filter; (b) fundamental components of line voltage vector, grid current vector, and converter output phase voltage vector in a rotating coordinate system synchronous to the grid voltage vector $\vec{v}_{G,1}$

inductance corresponding to the maximum filter voltage drop. If the fundamental component $\vec{v}_{G,1}$ of the grid voltage vector \vec{v}_G is considered as the reference vector (Fig. 4-29 (b)), the fundamental component of the filter inductance voltage drop at steady state is:

$$\vec{v}_{G,1} - \vec{v}_{GC,1} = j\omega_G(L_G + L_F)\vec{i}_{G,1}, \quad (4-47)$$

where

$$\vec{v}_{G,1} = \sqrt{2}V_{G,n,1}\angle 0, \quad \vec{v}_{GC,1} = \sqrt{2}V_{GC,1}\angle \theta_{v_{GC,1}}, \quad \vec{i}_{G,1} = \sqrt{2}I_{G,n,1}\angle \theta_{i_{G,1}}, \quad \omega_G = 2\pi f_G,$$

$V_{G,n,1}$ is the fundamental component of the grid rms rated phase voltage,
 $V_{GC,1}$ denotes the fundamental component of the grid side converter rms phase voltage,
 $I_{G,n,1}$ being the fundamental component of the grid rated rms phase current.

The upper limit filter inductance at the rated grid current can be calculated by substituting the maximum amplitude of the converter phase voltage for $\vec{v}_{GC,1}$ in (4-47). For a sinus-triangle PWM, the maximum value of the converter rms phase voltage in the linear range of modulation is $V_{GC,1} = V_{dc} / 2\sqrt{2}$.

The real and imaginary parts of (4-47) for the maximum rms value of $V_{GC,1}$ are:

$$\begin{cases} V_{G,n,1} - \frac{\sqrt{2}}{4}V_{dc} \cos(\theta_{v_{GC,1}}) = -\omega_G(L_G + L_{F,\max})I_{G,n,1} \sin(\theta_{i_{G,1}}) \\ -\frac{\sqrt{2}}{4}V_{dc} \sin(\theta_{v_{GC,1}}) = \omega_G(L_G + L_{F,\max})I_{G,n,1} \cos(\theta_{i_{G,1}}) \end{cases} \quad (4-48)$$

From (4-48), the upper limit of the filter inductance $L_{F,\max}$ corresponding to the maximum amplitude of the converter output voltage at the rated grid current can be derived as:

$$L_{F,\max} = \frac{-V_{G,n,1} \sin(\theta_{i_{G,1}}) \pm \sqrt{\frac{V_{dc}^2}{8} - V_{G,n,1}^2 \cos^2(\theta_{i_{G,1}})}}{\omega_G I_{G,n,1}} - L_G. \quad (4-49)$$

For the grid unity power factor condition $\text{DPF} = \pm 1$ (rectifying mode: $\text{DPF} = 1$, $\sin(\theta_{i_{G,1}}) = 0$, $\cos(\theta_{i_{G,1}}) = 1$, regenerating mode: $\text{DPF} = -1$, $\sin(\theta_{i_{G,1}}) = 0$, $\cos(\theta_{i_{G,1}}) = -1$), the upper limit of the filter inductance in (4-49) has been simplified to

$$L_{F,max} = \frac{\sqrt{\frac{V_{dc}^2}{8} - V_{G,n,1}^2}}{\omega_G I_{G,n,1}} - L_G \tag{4-50}$$

Grid current vector and converter output voltage vector in a rotating reference frame synchronous to the grid voltage vector are shown in Fig. 4-30 (a) and (b) for the rectifying and regenerating mode, respectively.

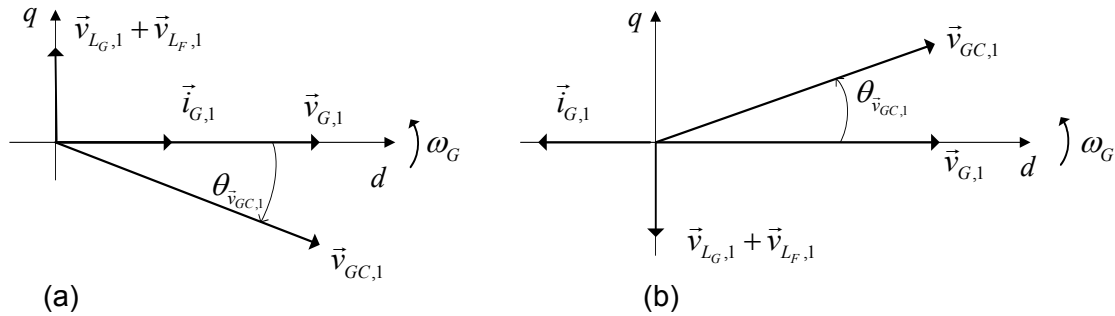


Fig. 4-30 Fundamental components of grid current vector and active front end converter output voltage vector in a rotating reference frame synchronous to the grid voltage vector: (a) rectifying operation; (b) regenerating operation

In the case of asymmetrical regular sampled sinus-triangle modulation with added third harmonic zero sequence signal to the modulator reference signals (ARS-ZSS-PWM) [12], the maximum rms value of the converter output voltage in the linear range of the modulation increases to $V_{GC,1} = V_{dc}/\sqrt{6}$ [7]. From substituting this maximum value in (4-47) and (4-48), the upper limit of the filter inductance for ARS-ZSS-PWM at the grid unity power factor $DPF = \pm 1$ is derived to (4-51) in the same manner as that for ARS-PWM presented in (4-47) to (4-50).

$$L_{F,max} = \frac{\sqrt{\frac{V_{dc}^2}{6} - V_{G,n,1}^2}}{\omega_G I_{G,n,1}} - L_G \tag{4-51}$$

$L_{F,max}$ in (4-50) and (4-51) causes the upper limit filter voltage drop at the rated current and the unity power factor conditions for a dc-link voltage of V_{dc} .

Lower limit of the L-filter inductance

The lower limit of the filter inductance is caused by the required limitation of the current harmonics around the first carrier band according to IEEE-519. Below, the analytical representation of the converter phase voltage harmonics is applied in order to determine the lower limit of the filter inductance.

The harmonic voltage amplitude per harmonic frequency is a measure for the potential of the voltage harmonic to produce a corresponding current harmonic. The filter inductance is designed based on the most significant converter phase voltage harmonic with the highest ratio of the voltage and frequency. For an ARS-PWM, the amplitude of the converter phase voltage harmonics based on the Bessel functions is as follows [7]:

$$\hat{V}_{n,\mu} = \frac{2V_{dc}}{\pi q_{n,\mu}} \sin[(n + \mu)\frac{\pi}{2}] J_{\mu}(q_{n,\mu} \frac{\pi}{2} M), \tag{4-52}$$

where

$\hat{V}_{n,\mu}$ is the amplitude of the converter output phase voltage harmonic,

n denotes the carrier band number $[1, \infty)$,

μ being the side band number $(-\infty, \infty)$,

J_μ is Bessel function,

$q_{n\mu} = n + \mu f_G / f_C$ (f_G : grid frequency, f_C : carrier frequency).

The first carrier band of the converter output phase voltage is shown in Fig. 4-31 (a). The harmonic voltage of $(m_f - 2)^{\text{th}}$ order ($n = 1, \mu = -2$) is the most significant harmonic voltage in the harmonic spectrum of the grid side converter output phase voltage because of its higher Volt-per-Hertz ratio compared to the other significant harmonics. The Volt-per-Hertz ratio of the harmonic voltage of $(m_f + 2)^{\text{th}}$ order is smaller than that of the harmonic voltage of $(m_f - 2)^{\text{th}}$ order for an ARS-PWM despite of its higher amplitude. The ratio of the Volt-per-Hertz value of the harmonic voltage of the $(m_f - 2)^{\text{th}}$ order to the Volt-per-Hertz value of the harmonic voltage of $(m_f + 2)^{\text{th}}$ order depending on the modulation depth M and the carrier frequency f_C is shown in Fig. 4-31 (b) if an ARS-PWM is applied.

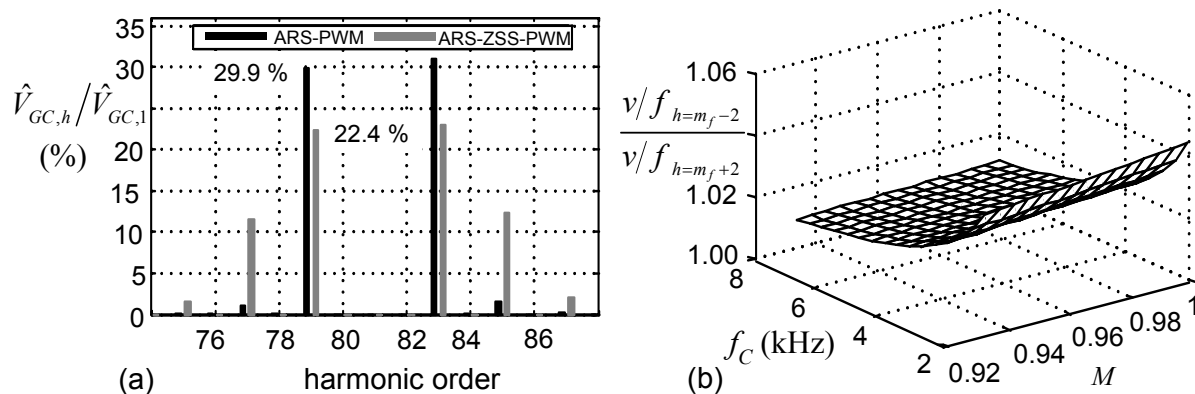


Fig. 4-31 (a) First carrier band of a 2L VSC output phase voltage harmonic spectra for ARS-PWM ($V_{GC,LL} = 400$ V, $V_{dc} = 700$ V, $m_f = 81$) and ARS-ZSS-PWM ($V_{GC,LL} = 400$ V, $V_{dc} = 609$ V, $m_f = 81$); (b) Volt-per-Hertz value of the $(m_f - 2)^{\text{th}}$ order harmonic to the Volt-per-Hertz value of the $(m_f + 2)^{\text{th}}$ order harmonic of the converter phase voltage for various values of M and f_C

Fig. 4-31(a) shows the first carrier band spectrum of the converter output phase voltage for a frequency ratio of $m_f = 81$ and the dc-link voltage of 700 V and 609 V for ARS-PWM and ARS-ZSS-PWM, respectively. Different dc-link voltage is chosen for both modulations to enable a comparable dc-link voltage reserve. Obviously, the application of the ARS-ZSS-PWM reduces the amplitude of the harmonic voltages and results in a wider sideband than the ARS-PWM does [7]. The complex analytical depiction of the harmonic voltages for the ARS-ZSS-PWM is presented in [7]. In order to simplify the filter design procedure, the filter inductance is determined based on the harmonic voltage amplitude for ARS-PWM. According to the afore-mentioned comparison between the first carrier band spectrum of the ARS-PWM and the ARS-ZSS-PWM, the filter inductance determined based on (4-52) will guarantee that the IEEE-519 limits will not be exceeded if a ARS-ZSS-PWM is applied instead of the ARS-PWM.

The amplitude of the $(m_f - 2)^{\text{th}}$ converter phase voltage harmonic at nominal load can be used to design the filter inductance for a desired grid current harmonic. The nominal load

modulation depth M_n is required in the design according to (4-52). M_n depends on the filter voltage drop in a closed loop control system. Thus, the filter inductance is required for determining M_n . Obviously, an iterative procedure is essential to calculate the filter inductance. Therefore, the no load modulation depth M_0 which is independent of the filter inductance is used in the proposed design procedure to calculate the amplitude of the $(m_f-2)^{th}$ converter phase voltage harmonic in the first step. In the next step, the required filter inductance is determined by considering the grid current harmonic limitations $\hat{I}_{G,(m_f-2),0,\%} \leq \hat{I}_{G,(m_f-2),desired,\%}$. $\hat{I}_{G,(m_f-2),0,\%}$ denotes the amplitude of the $(m_f-2)^{th}$ grid harmonic current at no load conditions in percent of the rated fundamental component. The desired amplitude of the $(m_f-2)^{th}$ grid harmonic current in percent of the fundamental component at rated load conditions (e.g. according to IEEE-519) is denoted as $\hat{I}_{G,(m_f-2),desired,\%}$.

Finally, the amplitude of the $(m_f-2)^{th}$ grid current harmonic at nominal load $\hat{I}_{G,(m_f-2),n,\%}$ is calculated by applying the filter inductance and M_n . The initial value of $\hat{I}_{G,(m_f-2),0,\%}$ should be changed in an iterative manner based on the calculated $\hat{I}_{G,(m_f-2),n,\%}$ to obtain a grid harmonic current of $(m_f-2)^{th}$ order which is below the IEEE-519 limitations.

Using (4-52), the converter phase harmonic voltage of $(m_f-2)^{th}$ order at no load condition is given as:

$$\hat{V}_{1,-2} = \frac{2V_{dc}}{q_{1,-2}\pi} J_2(\pi\sqrt{2}q_{1,-2} \frac{V_{G,n,1}}{V_{dc}}), \quad q_{1,-2} = 1 - 2 \frac{f_G}{f_c} \quad (4-53)$$

Therefore, the per-unit value of the required inductance to limit the amplitude of the $(m_f-2)^{th}$ grid current harmonic to $\hat{I}_{G,(m_f-2),0,\%}$ at no load is:

$$L_{F,t,pu} = 100\sqrt{2} \frac{J_2(\pi\sqrt{2}q_{1,-2} \frac{V_{G,n,1}}{V_{dc}})}{\pi q_{1,-2}(m_f-2) \hat{I}_{G,(m_f-2),0,\%} \frac{V_{G,n,1}}{V_{dc}}} \quad (4-54)$$

where, $L_{F,t} = L_F + L_G$, $L_{F,t,pu} = L_{F,t} / L_b$, $L_b = V_{b,G} / \omega_{b,G} I_{b,G} = V_{G,n,1} / \omega_G I_{G,n,1}$.

Variations of the modulation depth at nominal load condition should be taken into account in order to calculate the value of the current harmonic $\hat{I}_{G,(m_f-2),n,\%}$ at rated load. Using the filter inductance voltage drop (4-47), the fundamental component of the converter phase voltage for the rated grid current and unity power factor is

$$V_{GC,1} = \sqrt{V_{G,n,1}^2 + I_{G,n,1}^2 \omega_G^2 L_{F,t}^2} = V_{G,n,1} \sqrt{1 + L_{F,t,pu}^2} \quad (4-55)$$

Therefore, the modulation depth at nominal load for the designed filter inductance with a carrier peak-to-peak amplitude of $V_{dc,n}$ is

$$M_n = \frac{2\sqrt{2}V_{G,n,1}}{V_{dc}} \sqrt{1 + L_{F,t,pu}^2} \quad (4-56)$$

Applying M_n and the amplitude of the $(m_f-2)^{th}$ converter voltage harmonic in (4-53), the amplitude of the grid current harmonic of $(m_f-2)^{th}$ order at nominal load is

$$\hat{I}_{G, (m_f-2), n, \%} = 100\sqrt{2} \frac{J_2(q_{1,-2} \frac{\pi}{2} M_n)}{\pi q_{1,-2} (m_f - 2) L_{F,t,pu} \frac{V_{G,n,1}}{V_{dc}}} \quad (4-57)$$

As mentioned above, if $\hat{I}_{G, (m_f-2), n, \%}$ in (4-57) exceeds the IEEE-519 limitation, the chosen initial value for no load grid current harmonic $\hat{I}_{G, (m_f-2), 0, \%}$ in (4-54) should be reduced and the filter inductance should be designed in an iterative manner applying equations (4-54) - (4-57).

Converter current ripple and dc-link voltage reserve

For a designed L-filter, the maximum amplitude of the inductor current ripple can be approximated by the following equation, neglecting the inductor resistance and assuming a closed loop control [43]

$$\hat{I}_{ripple, max, pu} \approx \frac{V_{G,n,1}}{2\sqrt{6} f_C L_{F,t}} \quad (4-58)$$

Furthermore, the dc-link voltage reserve for the control system can be defined as

$$V_{dc, reserve, \%} = 100 \frac{V_{dc} - V_{dc, min}}{V_{dc}} \quad (4-59)$$

$V_{dc, min}$ is the minimum required dc-link voltage for the designed filter inductance ($M = 1$ at nominal load). According to the filter voltage drop (4-47) and the fundamental component of the converter phase voltage in (4-55), the minimum required dc-link voltage for a total filter inductance of $L_{F,t} = L_G + L_F$ is

$$V_{dc, min} = V_{G,n,1} \sqrt{m(1 + L_{F,t, pu}^2)} \quad (4-60)$$

Parameter m is 8 for ARS-PWM and 6 for ARS-ZSS-PWM. Consequently, the dc-link voltage reserve (in percent) of the rated dc-link voltage for a designed filter inductance is

$$V_{dc, reserve, \%} = 100 \left(1 - \frac{V_{G,n,1}}{V_{dc,n}} \sqrt{m(1 + L_{F,t, pu}^2)} \right) \quad (4-61)$$

Flowchart of the proposed L-filter design procedure

A flowchart of the proposed L-filter design procedure is shown in Fig. 4-32. The design can be started with useful initial values of the dc-link voltage and the modulation index (e.g. $V_{dc} = 700$ V, $m_f = 81$). The dc-link voltage or the switching frequency can be increased to achieve an increased upper limit of the inductance if the calculated inductance is larger than the upper limit according to (4-50). In the flowchart of Fig. 4-32, the dc-link voltage is increased in the first step to get a higher upper limit filter inductance. In the second step, the carrier frequency f_C and subsequently the frequency index should be increased if the limits of the IEEE-519 can not be achieved for the given maximum dc-link voltage. The maximum possible dc-link voltage $V_{dc, max}$ is determined by the blocking characteristics of the applied power semiconductors, gate units, cooling conditions, and the stray inductance of the converter configuration [14]. The upper limit of the filter inductance is $L_{f, max} = 4.2$ mH according to (4-50), assuming the grid parameters presented in Table 4.2, and applying ARS-PWM. The grid current harmonic of $(m_f - 2)^{th}$ order is limited to about 1% of the rated grid

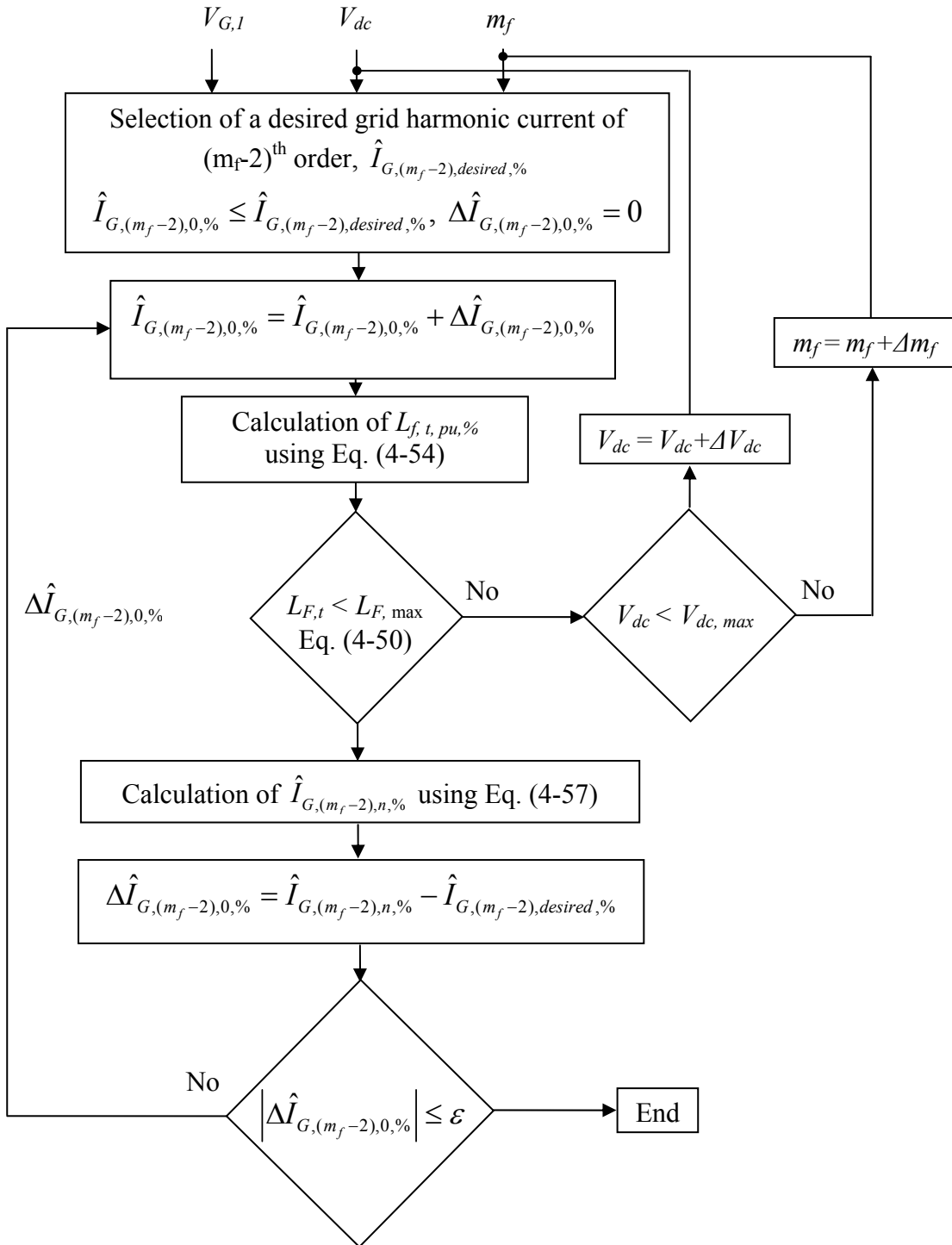


Fig. 4-32 A flowchart of the proposed L-filter design procedure to limit the amplitude of grid harmonic current to a desired value

current amplitude in this case. Using a proper gate resistance and a suitable mechanical design to reduce the turn-off over voltage, the dc-link voltage can be increased to 800 V considering the applied IGBT modules.

The upper limit of the filter inductance is calculated to $L_{f,max} = 7.5$ mH for $V_{dc} = 800$ V. If the new upper limit is used, the grid current harmonic of $(m_f - 2)^{th}$ order is limited to about 0.7 %

of the rated grid current amplitude, which is again above the IEEE-519 limitation of 0.2%. Thus, the carrier frequency has to be increased to reach the IEEE-519 compliance.

Finally, an inductance value of $L_f = 6.3$ mH was calculated during the iterative design procedure according to the flowchart of Fig. 4-32 for $f_c = 15$ kHz ($m_f = 300$) and $V_{dc} = 800$ V. The dc-link voltage reserve is about 5 % in this case according to (4-61). The required switching frequency and filter inductance in order to fulfill the IEEE-519 conditions ($\hat{I}_{G,(m_f-2),n,\%} = 0.2$) for different dc-link voltages are presented in Table 4.8. The dc-link voltage reserve $V_{dc,reserve,\%}$ is considered to be about 5 %.

Table 4.8

Required switching frequency and corresponding L-filter inductance to fulfill the conditions of IEEE-519 ($I_{G,(m_f-2),n,\%} = 0.2$) for different dc-link voltages, $V_{dc,reserve,\%} \approx 5$

V_{dc} (V)	f_c (kHz)	m_f	L_F (mH)	L_F (pu)
700	33.5	670	2.4	0.227
750	18.5	370	4.7	0.450
800	15	300	6.3	0.599

4.5.2 LCL-filter design procedure

As shown in the previous section, the L-filter is only a useful solution at very high switching frequencies. An LCL-filter enables a distinctly cheaper and smaller filter solution at low switching frequencies (e.g. $f_c = 2$ kHz – 8 kHz), which are usually applied in industrial low-voltage drives [85], [107].

An iterative design procedure of an LCL-filter is proposed in this section. The main goal is to limit the most significant grid current harmonic at nominal load to the values defined in IEEE-519. A single-phase representation of the PWM active front end converter with LCL-filter is given in Fig. 4-33.

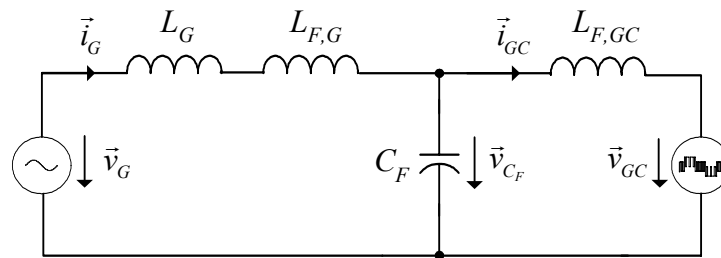


Fig. 4-33 A single-phase representation of PWM active front end with LCL-filter

Filter split factor r and filter resonance frequency f_{res} as the LCL-filter parameters are given by:

$$r = \frac{L_{F,G,t}}{L_{F,GC}}, \quad L_{F,G,t} = L_G + L_{F,G}, \quad (4-62)$$

$$f_{res} = \frac{1}{2\pi} \sqrt{\frac{L_{F,GC} + L_{F,G,t}}{L_{F,GC} L_{F,G,t} C_F}}. \quad (4-63)$$

The filter resonance frequency (4-63) is considered to be in a range between ten times of the grid frequency and one-half of the carrier frequency in order to avoid a filter excitation by the converter voltage harmonics [107].

In the proposed LCL-filter design procedure, the converter side filter inductance $L_{F,GC}$ is determined at no load condition $M = M_0$ in the first step. The required inputs of the design procedure are the filter parameters (r and f_{res}), the IEEE-519 defined $(m_f - 2)^{th}$ grid current harmonic amplitude $\hat{I}_{G,(m_f-2),desired, \%}$, and the basic parameters of the PWM active front end converter (e.g. Table 4.2). The other passive filter components $L_{F,G}$ and C_F are calculated then based on $L_{F,GC}$ and the filter parameters defined in (4-62) and (4-63). The thevenin equivalent circuit of the converter side LC-grid is used in the next step to model the LCL-filter as an L-filter. The $(m_f - 2)^{th}$ grid current harmonic amplitude $\hat{I}_{G,(m_f-2),n,\%}$ for the rated grid current is determined by applying this model and the calculated passive filter components in order to verify the filter effectiveness at nominal load. Finally, the required passive filter components for nominal load conditions are calculated in an iterative manner applying the deviation $\Delta \hat{I}_{G,(m_f-2),0,\%} = \hat{I}_{G,(m_f-2),n,\%} - \hat{I}_{G,(m_f-2),desired, \%}$.

Design of the converter side filter inductance

The converter side filter inductance $L_{F,GC}$ is determined on the basis of (4-54) to limit the $(m_f - 2)^{th}$ converter current harmonic at no load condition as described for the design of the L-filter. The filter capacitors are assumed to have zero impedance at the switching frequency. The amplitude of the $(m_f - 2)^{th}$ converter side current harmonic is required to determine $L_{F,GC}$, which is calculated applying the IEEE-519 defined grid current harmonic amplitude and the filter attenuation factor $i_G(s) / i_{GC}(s)$.

According to Fig. 4-33, the grid current harmonics are related to the converter current harmonics by:

$$\frac{i_G(s)}{i_{GC}(s)} = \frac{1}{1 + s^2 L_{F,G,t} C_F} \quad (4-64)$$

$$L_{F,G,t} = L_G + L_{F,G}, \quad s \neq j\omega_G$$

Substituting the filter inductance values and the resonance frequency for the filter capacitance, the attenuation factor (4-64) becomes

$$\frac{\hat{I}_{G,(m_f-2)}}{\hat{I}_{GC,(m_f-2)}} = \left| \frac{k_F^2}{k_F^2 - r - 1} \right| \quad (4-65)$$

for the $(m_f - 2)^{th}$ current harmonic, with

$$k_F = \frac{f_{res}}{(m_f - 2) f_G} \quad (4-66)$$

Applying (4-65), the converter side filter inductance is derived for the given filter parameters r and f_{res} on the basis of (4-54) as:

$$L_{F,GC,pu} = a_1 \left| \frac{k_F^2}{k_F^2 - r - 1} \right|, \quad (4-67)$$

where

$$a_1 = 100\sqrt{2} \frac{J_2(\pi\sqrt{2}q_{1,-2} \frac{V_{G,n,1}}{V_{dc}})}{\pi q_{1,-2} (m_f - 2) \hat{I}_{G,(m_f-2),0,\%} \frac{V_{G,n,1}}{V_{dc}}}, L_{F,GC,pu} = \frac{L_{F,GC}}{L_b}, L_b = \frac{V_{G,n,1}}{\omega_G I_{G,n,1}}.$$

$\hat{I}_{G,(m_f-2),0,\%}$ is the amplitude of the grid harmonic current of $(m_f-2)^{\text{th}}$ order at no load conditions in percent of the rated grid current amplitude.

Design of the grid side filter inductance and the filter capacitance

Applying the determined converter side filter inductance in (4-67) and the filter split factor (4-62), the grid side filter inductance is:

$$L_{F,G,t,pu} = a_1 r \left| \frac{k_F^2}{k_F^2 - r - 1} \right|, L_{F,G,pu} = L_{F,G,t,pu} - L_{G,pu}. \quad (4-68)$$

Using (4-63), the filter capacitance is

$$C_{F,pu} = a_2 \frac{r^2 + r(2 - k_F^2) + (1 - k_F^2)}{r k_F^4}, a_2 = \frac{1}{(m_f - 2)^2 a_1} \quad (4-69)$$

for a chosen filter resonance frequency and split factor with

$$C_{F,pu} = \frac{C_F}{C_{F,b}}, C_{F,b} = \frac{I_{G,n,1}}{\omega_G V_{G,n,1}}.$$

Effectiveness verification of the designed LCL-filter at rated load

The modulation depth at nominal load condition M_n can be specified by using the calculated passive component values $L_{F,GC}$, $L_{F,G}$, and C_F . M_n is used to verify the amplitude of the $(m_f-2)^{\text{th}}$ grid current harmonic while the PWM active front end converter operates at nominal load and unity power factor. In order to calculate M_n , the single-phase representation of the LCL-filter in Fig. 4-33 is simplified to the single-phase representation shown in Fig. 4-34,

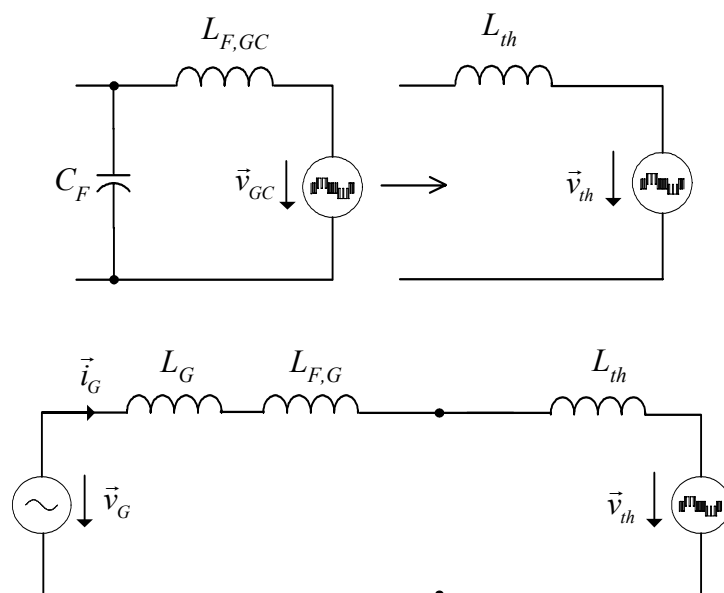


Fig. 4-34 A single-phase representation of PWM active front end converter with LCL-filter applying the thevenin equivalent circuit for the converter side LC-grid

applying the thevenin equivalent circuit of the converter side LC-grid. The parameters and variables presented in Fig. 4-34 for an angular frequency ω are:

$$L_{th} = \frac{L_{F,GC}}{X_{LC}}, \bar{v}_{th} = \frac{\bar{v}_{GC}}{X_{LC}} \quad (4-70)$$

$$X_{LC} = 1 - L_{F,GC} C_F \omega^2 = 1 - L_{F,GC,pu} C_{F,pu} \left(\frac{\omega}{\omega_G}\right)^2$$

Using the fundamental component of the filter voltage drop in Fig. 4-34, the modulation depth for an ARS-PWM at rated load can be calculated in the same manner as presented in (4-56) for the L-filter design

$$M_n = 2\sqrt{2} \frac{V_{G,n,1}}{V_{dc}} \sqrt{X_{LC,f_G}^2 + (L_{F,G,t,pu} X_{LC,f_G} + L_{F,GC,pu})^2}, \quad (4-71)$$

$$X_{LC,f_G} = 1 - L_{F,GC,pu} C_{F,pu}$$

When substituting the nominal modulation depth in equation (4-52), the amplitude of the most significant converter voltage harmonic can be determined. By using the converter voltage harmonic and the LCL-filter total inductance $L_{F,G,t} + L_{th}$ in Fig. 4-34, the amplitude of the most significant grid current harmonic at rated load $\hat{I}_{G,(m_f-2),n,\%}$ is:

$$\hat{I}_{G,m_f-2,n,\%} = \frac{100\sqrt{2}V_{dc,n}}{\pi q_{1,-2}(m_f-2)V_{G,n,1}} \times \frac{J_2\left(\frac{\pi}{2}q_{1,-2}M_n\right)}{(X_{LC,(m_f-2)f_G} L_{F,G,t,pu} + L_{F,GC,pu})}, \quad (4-72)$$

$$X_{LC,(m_f-2)f_G} = 1 - (m_f - 2)^2 L_{F,GC,pu} C_{F,pu}$$

The dc-link voltage reserve and the converter current ripple

Applying the definition of the dc-link voltage reserve in (4-59) and the LCL-filter voltage drop in Fig. 4-34, the dc-link voltage reserve for the PWM active front end converter at unity power factor is calculated as before for the L-filter design

$$V_{dc,reserve,\%} = 100 \left(1 - \frac{V_{G,n,1}}{V_{dc}} \sqrt{m(X_{LC,f_G}^2 + (L_{F,G,t,pu} X_{LC,f_G} + L_{F,GC,pu})^2)}\right). \quad (4-73)$$

Parameter m is 8 for ARS-PWM and 6 for ARS-ZSS-PWM.

If the influence of the filter capacitance on the converter side current ripple is neglected, the following equation can be used to approximate the maximum converter current ripple [43]:

$$\hat{I}_{ripple,max} \approx \frac{V_{G,n,1}}{2\sqrt{6} f_{sw} L_{F,GC}}. \quad (4-74)$$

Flowchart of the LCL-filter design procedure with a constant dc-link voltage

The grid current harmonics at rated load condition in (4-72) should not exceed the IEEE-519 limits. The chosen amplitude of the grid current harmonic $\hat{I}_{G,(m_f-2),0,\%}$ should be reduced in (4-67), and the passive filter components should be designed in an iterative manner applying equations (4-67) - (4-73) if the grid current harmonic in (4-72) is higher than the limits. A flowchart of the proposed LCL-filter design procedure is presented in Fig. 4-35. The design procedure can be started with the initial values of the dc-link voltage V_{dc} , modulation index m_f ,

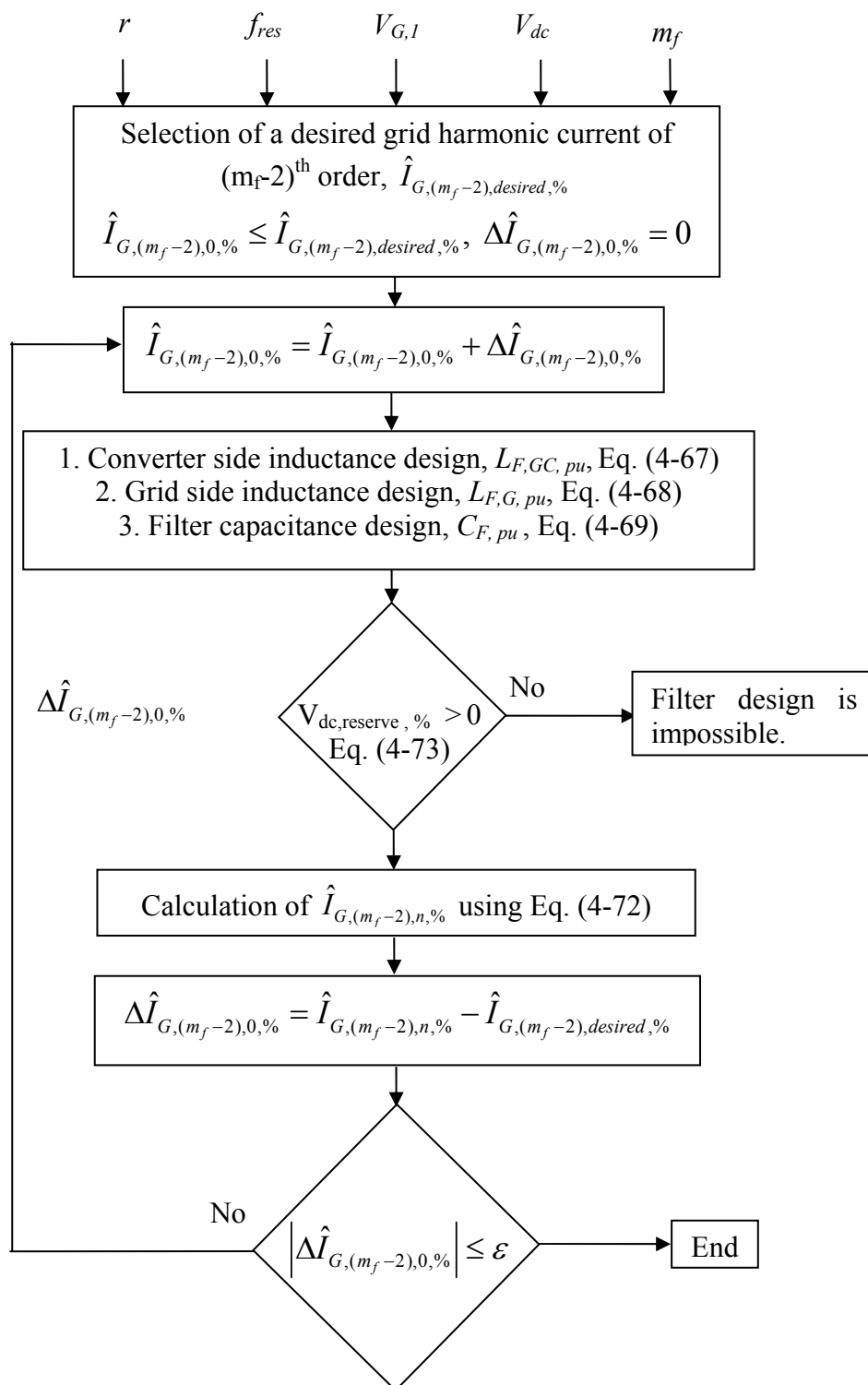


Fig. 4-35 A flowchart of the proposed LCL-filter design procedure to limit the amplitude of the grid current harmonics to a desired value with constant dc-link voltage and carrier frequency

chosen filter parameters r , f_{res} , and the desired amplitude of the $(m_f-2)^{th}$ grid current harmonic $\hat{I}_{G,(m_f-2),desired,\%}$. In the first iteration, $\hat{I}_{G,(m_f-2),0,\%}$ is considered to be equal to $\hat{I}_{G,(m_f-2),desired,\%}$. Applying equations (4-67) - (4-69), the LCL-filter reactive component values $L_{F,GC}$, $L_{F,G}$, and C_F are determined at no load condition. The rated load modulation depth M_n is calculated by using (4-71) to determine the dc-link voltage reserve and the $(m_f-2)^{th}$ grid current harmonic $\hat{I}_{G,(m_f-2),n,\%}$ at nominal load. Obviously, the dc-link voltage reserve must be positive and

correspond to the required converter dynamic. Furthermore, $\hat{I}_{G,(m_f-2),n,\%}$ should be in the vicinity of $\hat{I}_{G,(m_f-2),desired,\%}$ with an acceptable tolerance ε . The difference between $\hat{I}_{G,(m_f-2),n,\%}$ and $\hat{I}_{G,(m_f-2),desired,\%}$ is applied to change the initial value of $\hat{I}_{G,(m_f-2),0,\%}$ and to design the filter components in an iterative procedure as shown in Fig. 4-35.

The grid current harmonics will be limited to the required values (e.g. IEEE-519) for every combination of the filter parameters r and f_{res} , while considering the limitation of the resonance frequency and the dc-link voltage reserve, if the filter components are designed according to the procedure presented in Fig. 4-35. Fig. 4-36 shows the LCL-Filter

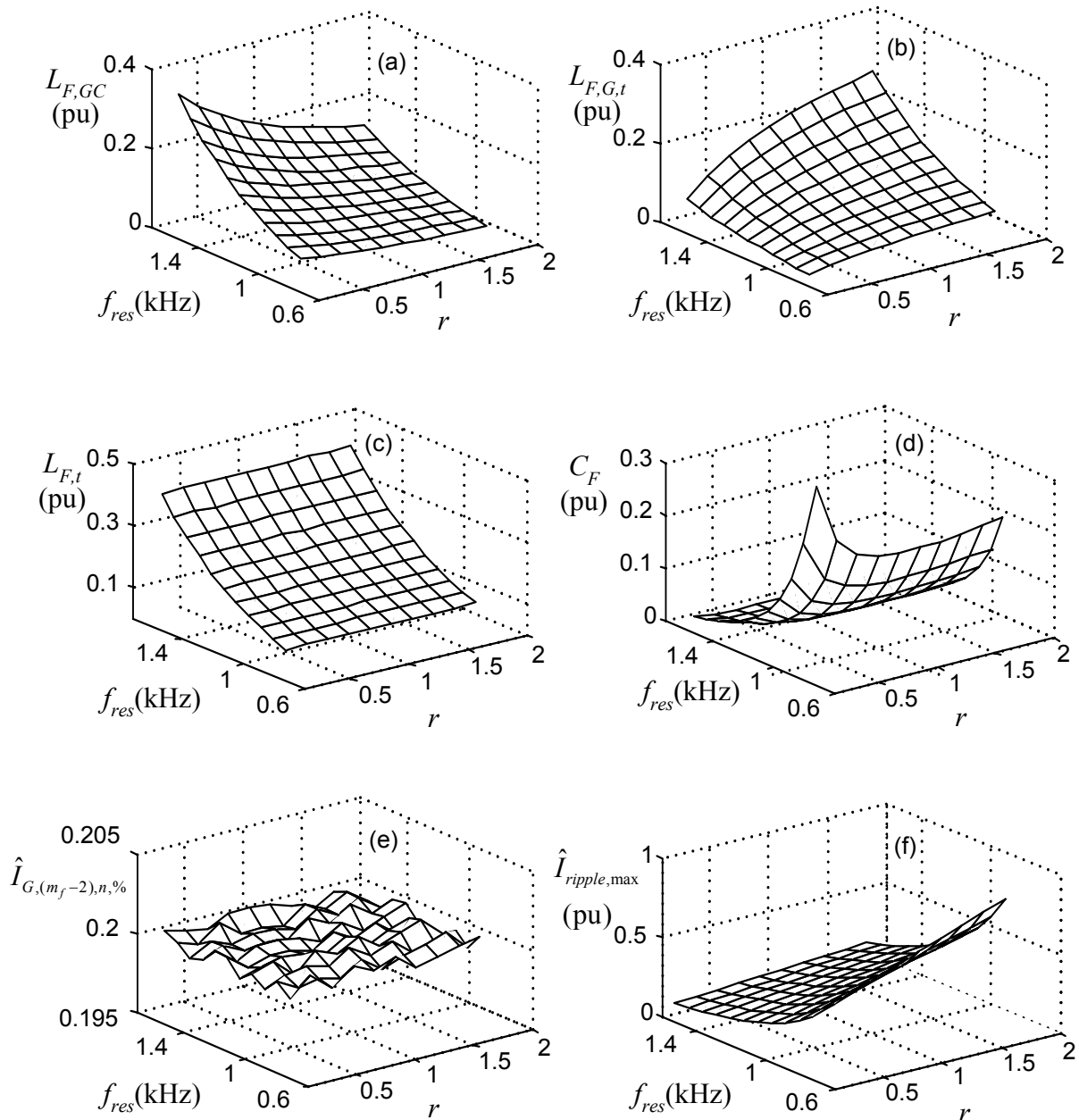


Fig. 4-36 Filter components for various values of r and f_{res} to fulfil the IEEE-519 condition: $V_{G,LL1} = 400$ V, $V_{dc} = 700$ V, $m_f = 81$; (a) converter side inductance; (b) total grid side inductance; (c) filter total inductance; (d) filter capacitance; (e) amplitude of the grid harmonic current; (f) the converter current ripple

components for different values of r and f_{res} . The filter design is achieved by applying the iterative procedure to obtain a grid harmonic current $\hat{I}_{G,(m_f-2),n,\%}$ of e.g. 0.2% according to IEEE-519. The error tolerance ε in Fig. 4-36 is considered to be 0.001% of the fundamental component of the grid current. The parameters of the grid and the converter are taken from Table 4.2.

It is demonstrated in Fig. 4-36 that for high resonance frequencies the value of the filter total inductance $L_{F,t} = L_{F,G,t} + L_{F,GC}$ increases. Moreover, the total inductance remains almost constant for every resonance frequency while r changes. By contrast, the filter capacitor increases if the resonance frequency is decreased. Furthermore, the grid current harmonic with $(m_f - 2)^{\text{th}}$ order at nominal load condition is presented in Fig. 4-36(e), which remains almost constant for filters with different component values. The maximum converter current ripple (4-74) is presented in Fig. 4-36(f). The converter side filter inductance increases for high resonance frequencies; consequently, the maximum amplitude of the converter current ripple decreases. As mentioned above, the total inductance $L_{F,t}$ remains almost constant while r changes. Therefore, the converter side inductance decreases while the converter current ripple increases for rising values of r .

Optimized LCL-filter with minimum stored energy

There are several LCL-filter optimization criteria like minimum volume, weight, and minimum filter stored energy. In order to select a useful LCL-filter design, the stored energy, as a measure for the size and expense of the passive components, is considered in this thesis. Thus, the filter parameters r and f_{res} are derived corresponding to the minimum filter energy. The total filter energy can be approximated by:

$$W_t = 3/2(I_{G,n,1}^2(L_{F,GC} + L_{F,G,t}) + C_f V_{G,n,1}^2) . \quad (4-75)$$

The stored energy in the total filter inductance $L_{F,t}$ and the filter capacitance C_f , as well as the total stored energy (4-75) corresponding to the filter reactive component values in Fig. 4-36 are depicted in Fig. 4-37. The amplitude of the grid current harmonic $\hat{I}_{G,(m_f-2),desired,\%}$ is limited to 0.2% with a tolerance of 0.001%. Obviously, the total stored filter energy reaches a minimum for a specific filter resonance frequency. By contrast, ratio $r = L_{F,G} / L_{F,GC}$ only slightly influences the stored energy of the filter. The filter parameters as well as the filter component values corresponding to the minimum energy are presented in Table 4.9 for grids with different rated currents, different dc-link voltages, and industrial line-to-line voltages of 400 V and 690 V. As shown in Table 4.9, the per-unit values for the reactive filter components and the filter parameters (r , k_f) corresponding to the minimum stored energy remains constant for grids with different rated currents. Furthermore, the parameters and the component values do not change for the 690 V grid if the dc-link voltage increases proportionally to the line voltage ($V_{dc} = 1212$ V). The design results are independent of the rated grid voltage and the dc-link voltage according to (4-67) - (4-69) if the ratio of $V_{G,1}/V_{dc}$ is considered to be constant. An increased dc-link voltage to 800 V leads to smaller filter components because of a lower modulation depth at nominal load condition. The amplitude of the $(m_f - 2)^{\text{th}}$ converter voltage harmonic decreases according to (4-52) if the index of modulation M_n is reduced. Obviously, a smaller inductance is required for a reduced converter voltage harmonic and constant desired grid current harmonics. The converter current ripple for the PWM active front end converter with 800 V dc-link voltage increases and the resonance frequency causing the minimum filter energy varies from 1.016 kHz to 1.046 kHz.

The converter side inductance and the grid side inductance are almost equal for all converter data of Table 4.9.

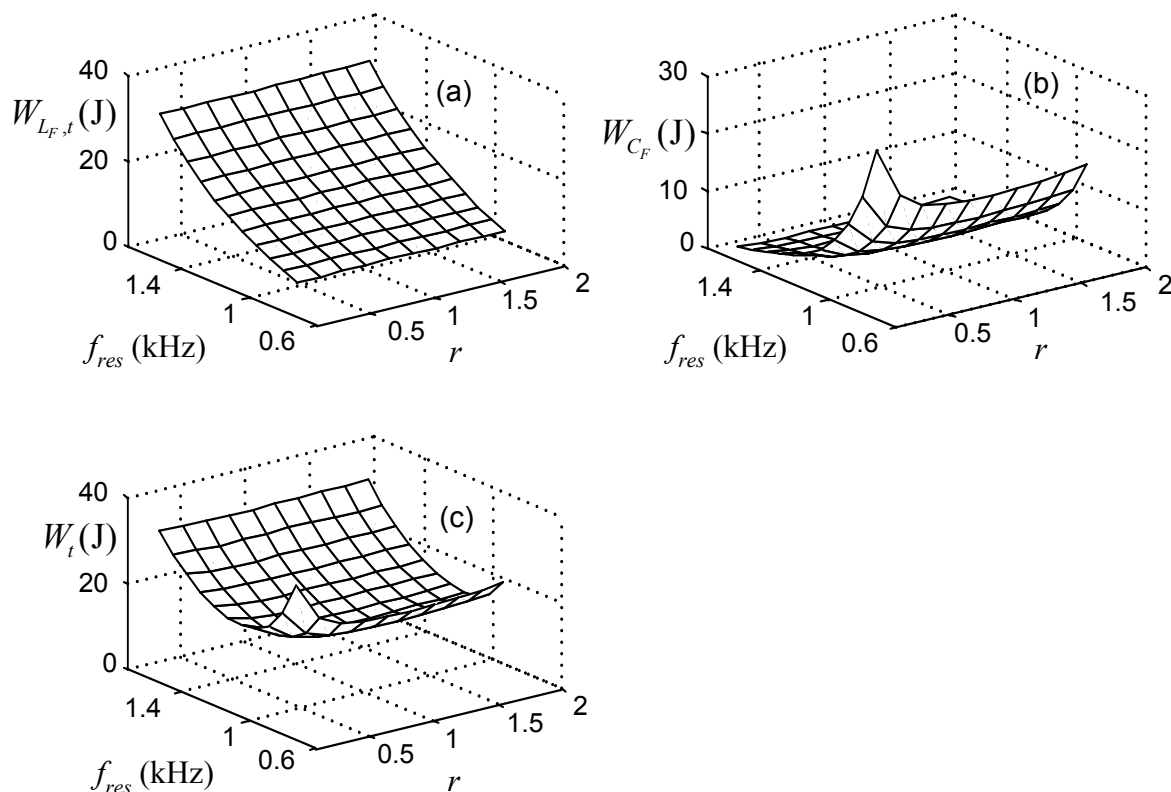


Fig. 4-37 Stored energy of the reactive components of the LCL-filters presented in Fig. 4-36: $V_{G,1,1} = 400$ V, $I_{G,1} = 70$ A, $V_{dc} = 700$ V, $m_f = 81$, (a) energy of the total inductance; (b) energy of the filter capacitance; (c) the filter total energy

Influences of the ARS-ZSS-PWM on the effectiveness of the LCL-filter

The ARS-ZSS-PWM is usually applied in industry applications due to the reduced dc-link voltage (15%) compared to the ARS-PWM for the same maximum output voltage. The filter components depicted in Table 4.9 are used for a PWM active front end converter with LCL-filter and ZSS-ARS-PWM, and the simulation results for the $(m_f - 2)^{th}$ order grid current harmonic are shown in Table 4.10. The dc-link voltage is reduced to achieve a dc-link voltage reserve like that of the ARS-PWM. The amplitude of the $(m_f - 2)^{th}$ grid current harmonic is given in Table 4.10 which is reduced to 0.15%. However, a certain reserve is useful in the simulative design of LCL-filters because of parasitic effects and the component variation in a real configuration (see Section 4.6.2).

Flowchart of the LCL-filter design procedure with a constant control reserve

The dc-link voltage is considered to be constant for filters with different component values in the LCL-filter design procedure of Fig. 4-35, which induces different control reserves. The total filter inductance increases, as shown in Fig. 4-36, for filters with increasing resonance frequencies; consequently, the control reserve decreases, leading to a decreasing dynamic performance.

Table 4.9

LCL-filter parameters and reactive component values corresponding to the minimum filter energy for different rated grid currents, dc-link voltage, and line voltage (Modulation: ARS-PWM, $\hat{I}_{G,(m_f-2),desired,\%} = 0.2$)

V_{dc} (V)	$V_{ll,G,1}$ (V)	$I_{G,1}$ (A)	$L_{F,GC}$		$\hat{I}_{ripple,max}$ (%)	r	C_F		k_F	f_{res} (Hz)	$V_{dc, reserve}$ (%)	$\hat{I}_{G,(m_f-2),n}$ (%)
			(mH)	(pu)			(μ F)	(pu)				
700	400	7	7.109	0.068	23.29	0.989	6.942	0.072	0.257	1016	7	0.2
700	400	70	0.711	0.068	23.29	0.989	69.418	0.072	0.257	1016	7	0.2
700	400	700	0.071	0.068	23.29	0.989	694.18	0.072	0.257	1016	7	0.2
1212	690	70	1.231	0.068	23.29	0.989	40.079	0.072	0.257	1016	7	0.2
800	400	70	0.7	0.066	24	0.989	67.489	0.070	0.257	1046	18.5	0.2

Table 4.10

LCL-filter parameters and reactive component values corresponding to the minimum filter energy for different rated grid currents, dc-link voltage, and line voltage (Modulation: ARS-ZSS-PWM, $\hat{I}_{G,(m_f-2),desired,\%} = 0.2$)

V_{dc} (V)	$V_{ll,G,1}$ (V)	$I_{G,1}$ (A)	$L_{F,GC}$		$\hat{I}_{ripple,max}$ (%)	r	C_F		k_F	f_{res} (Hz)	$V_{dc, reserve}$ (%)	$\hat{I}_{G,(m_f-2),n}$ (%)
			(mH)	(pu)			(μ F)	(pu)				
609	400	7	7.109	0.068	23.29	0.989	6.942	0.072	0.257	1016	7	0.15
609	400	70	0.711	0.068	23.29	0.989	69.418	0.072	0.257	1016	7	0.15
609	400	700	0.071	0.068	23.29	0.989	694.18	0.072	0.257	1016	7	0.15
1054	690	70	1.231	0.068	23.29	0.989	40.079	0.072	0.257	1016	7	0.15
696	400	70	0.7	0.066	24	0.989	67.489	0.070	0.257	1046	18.5	0.15

Considering the control reserve (4-73), the dc-link voltage can be changed in order to achieve a defined dc-link voltage reserve, as shown in the flowchart of Fig. 4-38. As mentioned in reference to the L-filter design, it should be noted that the maximum value of the dc-link voltage is limited by the blocking characteristics of the semiconductors and the converter design.

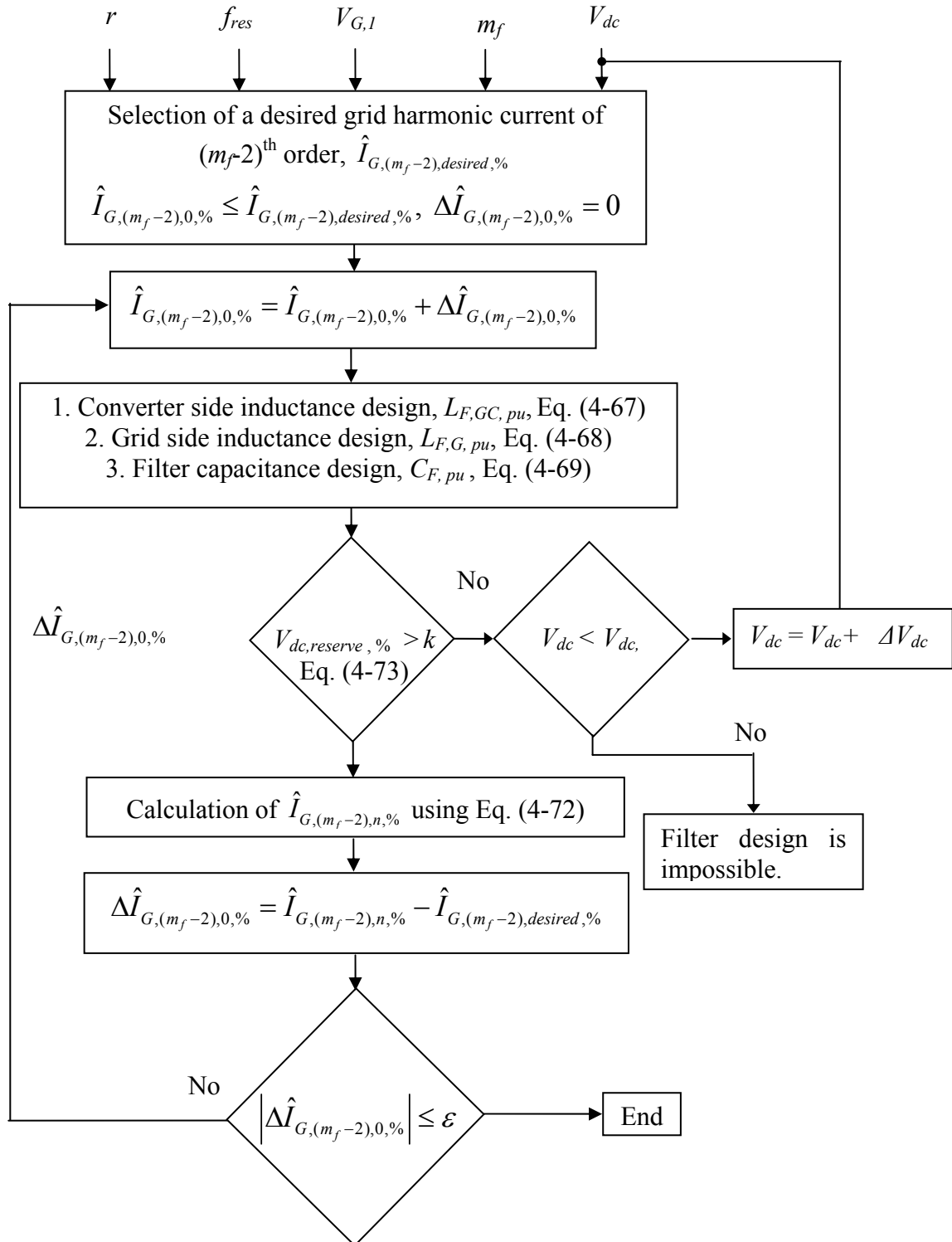


Fig. 4-38 A flowchart of the proposed LCL-filter design procedure to limit the amplitude of the grid current harmonics to a desired value for a defined control reserve of k %

4.6 Control of PWM active front end converters with LCL-filter

The voltage-oriented control strategy is also applied to control the PWM active front end converter with LCL-filter. Similar to the control of the PWM active front end converter with L-filter, all voltages and currents are projected into a rotating reference frame synchronous to the voltage vector of PCC \vec{v}_{PCC} . Using the single phase representation of the PWM active front end converter with LCL-filter shown in Fig. 4-39(a) and ignoring the resistance of the inductors, the transfer function of the converter and grid currents in the rotating reference frame synchronous to \vec{v}_{PCC} are as follows:

$$G_{i,GC}(s) = \frac{\vec{i}_{GC,dq}^{\vec{v}_{PCC}}}{\vec{v}_{GC,dq}^{\vec{v}_{PCC}}} = \frac{-1}{L_{F,GC}s} \frac{s^2 + \frac{1}{L_{F,G}C_F}}{s^2 + \frac{L_{F,G}+L_{F,GC}}{L_{F,G}L_{F,GC}}s + \frac{1}{L_{F,G}L_{F,GC}C_F}}, \quad (4-76)$$

$$G_{i,G}(s) = \frac{\vec{i}_{G,dq}^{\vec{v}_{PCC}}}{\vec{v}_{GC,dq}^{\vec{v}_{PCC}}} = \frac{-1}{L_{F,GC}s} \frac{\frac{1}{L_{F,G}C_F}}{s^2 + \frac{L_{F,G}+L_{F,GC}}{L_{F,G}L_{F,GC}}s + \frac{1}{L_{F,G}L_{F,GC}C_F}}. \quad (4-77)$$

Obviously, the current control plant of the PWM active front end converter with LCL-filter comprises the dynamics of the LCL-filter; consequently, the characteristic polynomial of the current control plant has two more poles than the current control plant of the PWM active front end converter with L-filter in Fig. 4-11.

Passive damping of the LCL-filter resonance

Equations (4-76) and (4-77) demonstrate that the current transfer functions have two imaginary poles at LCL-filter resonance frequency. Selecting the resonance frequency in a range between ten times of the grid frequency and one-half of the carrier frequency will prevent filter excitation by the converter voltage harmonics. However, converter output voltage in transients could excite the filter.

Using a resistance series to the filter capacitor as shown in Fig. 4-39(b) is a simple solution to damp the LCL-filter oscillations [107]. Transfer functions of the converter and grid currents for a PWM active front end converter with passively damped LCL-filter are derived as follows:

$$G_{i,GC}(s) = \frac{\vec{i}_{GC,dq}^{\vec{v}_{PCC}}}{\vec{v}_{GC,dq}^{\vec{v}_{PCC}}} = \frac{-1}{L_{F,GC}s} \frac{s^2 + \frac{R_d}{L_{F,G}}s + \frac{1}{L_{F,G}C_F}}{s^2 + R_d \frac{L_{F,G}+L_{F,GC}}{L_{F,G}L_{F,GC}}s + \frac{L_{F,G}+L_{F,GC}}{L_{F,G}L_{F,GC}C_F}}, \quad (4-78)$$

$$G_{i,G}(s) = \frac{\vec{i}_{G,dq}^{\vec{v}_{PCC}}}{\vec{v}_{GC,dq}^{\vec{v}_{PCC}}} = \frac{-1}{L_{F,GC}s} \frac{\frac{R_d}{L_{F,G}}s + \frac{1}{L_{F,G}C_F}}{s^2 + R_d \frac{L_{F,G}+L_{F,GC}}{L_{F,G}L_{F,GC}}s + \frac{L_{F,G}+L_{F,GC}}{L_{F,G}L_{F,GC}C_F}}. \quad (4-79)$$

The transfer functions in (4-78) and (4-79) have real stable poles if the damping resistance is

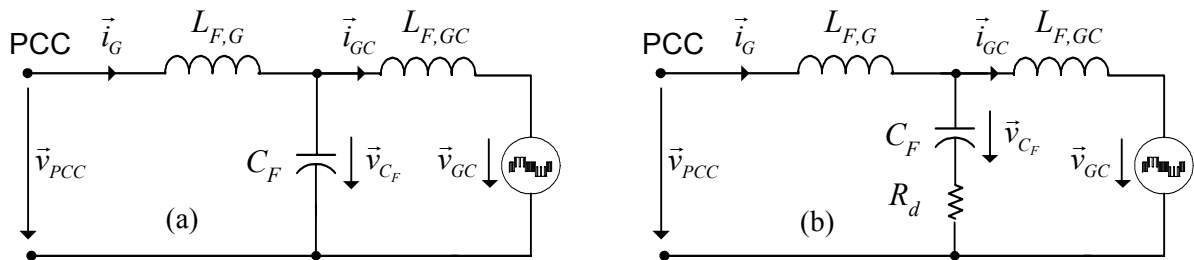


Fig. 4-39 (a) A single-phase representation of LCL-filter; (b) LCL-filter with passive damping

designed as:

$$R_d \geq \frac{2\sqrt{L_{F,G}L_{F,GC}}}{\sqrt{C_F(L_{F,G} + L_{F,GC})}}. \quad (4-80)$$

The application of a passive damping is a simple and robust solution to damp the resonance of the LCL-filter. However, the damping resistor will cause further power loss and reduce the effectiveness of the LCL-filter to damp the grid current harmonics.

Active damping of the LCL-filter resonance

In order to overcome the drawbacks of the passive damping, an active damping scheme of the current control loop can be applied. In recent publications, the active damping function has been achieved based on the feedback of filter state variables [85], [92], [95], [105], [131] or sensorless methods [106], [113]. In this thesis, the filter capacitor voltages are applied to control the grid side converter currents and avoid the LCL-filter resonance. The main advantage of such a control is the robustness of the current controller against the grid inductance variation [85]. A description of the principles of the applied current control based on the voltage feedback of the filter capacitor is presented below.

Considering the single-phase representation of the active rectifier with LCL-filter in Fig. 4-39(a), the current of the converter side inductor can be described as:

$$L_{F,GC} \frac{d}{dt} \vec{i}_{GC} + R_{F,GC} \vec{i}_{GC} = \vec{v}_{C_F} - \vec{v}_{GC}. \quad (4-81)$$

Equation (4-81) is projected into the rotating frame synchronous to the PCC voltage vector. The corresponding d-q components are:

$$\begin{cases} -v_{GC,d}^{\bar{v}_{PCC}} = L_{F,GC} \frac{d}{dt} i_{GC,d}^{\bar{v}_{PCC}} + R_{F,GC} i_{GC,d}^{\bar{v}_{PCC}} - v_{C_F,d}^{\bar{v}_{PCC}} - L_{F,GC} \omega_G i_{GC,q}^{\bar{v}_{PCC}}, \\ -v_{GC,q}^{\bar{v}_{PCC}} = L_{F,GC} \frac{d}{dt} i_{GC,q}^{\bar{v}_{PCC}} + R_{F,GC} i_{GC,q}^{\bar{v}_{PCC}} - v_{C_F,q}^{\bar{v}_{PCC}} + L_{F,GC} \omega_G i_{GC,d}^{\bar{v}_{PCC}}. \end{cases} \quad (4-82)$$

Equation (4-82) is similar to the current dynamics of the PWM active front end converter with L-filter presented in (4-18). Both equations are presented in the rotating reference frame synchronous to the PCC voltage vector \vec{v}_{PCC} . The current model of the PWM active front end converter with L-filter contains the components of the PCC voltage vector while the direct and quadrature components of the filter capacitor voltages appear in the current model of the PWM active front end converter with LCL-filter. The following decoupling terms should be added to the output of the current controllers in the current control loop of the PWM active front end converter with LCL-filter to compensate for the influence of the filter capacitor voltage and the cross-coupling of direct and quadrature currents:

$$\begin{cases} \Delta v_d = v_{C_F,d}^{\bar{v}_{PCC}} + L_{F,GC} \omega_G i_{GC,q}^{\bar{v}_{PCC}}, \\ \Delta v_q = v_{C_F,q}^{\bar{v}_{PCC}} - L_{F,GC} \omega_G i_{GC,d}^{\bar{v}_{PCC}}. \end{cases} \quad (4-83)$$

Using the decoupling terms in (4-83), the current model is reduced to a first-order system which comprises only the parameters of the converter side filter inductor ($L_{F,GC}$, $R_{F,GC}$). Consequently, the control structure of the PWM active front end converter with LCL-filter

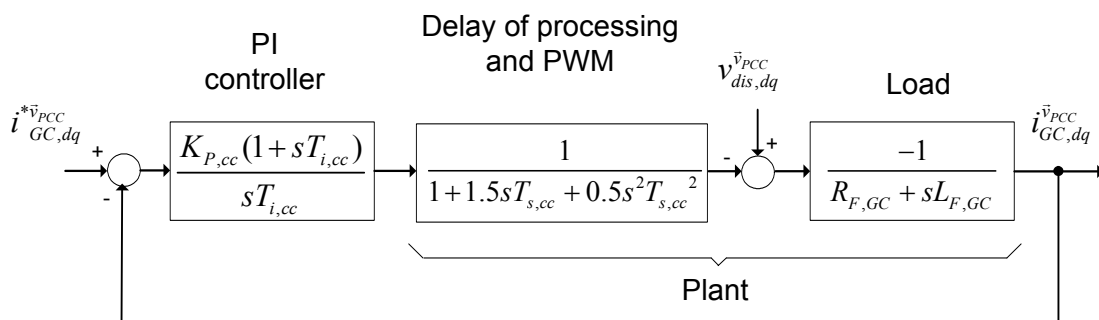


Fig. 4-40 Current control loop of PWM active front end with LCL-filter

becomes similar to the control structure of the PWM active front end converter with L-filter. A current control loop with the corresponding processing and PWM delays is shown in Fig. 4-40. The PI parameters of the current control loop according to the technical optimum (Table 3.4) are:

$$T_{i,cc} = \frac{L_{F,GC}}{R_{F,GC}}, \quad K_{p,cc} = \frac{L_{F,GC}}{1.5a_{cc}T_{s,cc}}, \quad a_{cc} \geq 2, \quad (4-84)$$

where, $T_{s,cc}$ denotes the sampling time of the current control loop.

Due to the delay of the current control loop (shown as processing and PWM delay in Fig. 4-40), a completely decoupled system is not achievable. The total delay $G_{d,t}$ of the current control loop containing the PWM delay and the processing delay is presented by

$$G_{d,t} = \frac{1}{1 + 1.5sT_{s,cc} + 0.5s^2T_{s,cc}^2}. \quad (4-85)$$

The following compensator should be applied to achieve an ideal decoupled system:

$$G_{compensator} = 1 + 1.5sT_{s,cc} + 0.5s^2T_{s,cc}^2. \quad (4-86)$$

Applying this compensator leads to the amplification of noise and harmonics around the switching frequency. In order to avoid the noise amplification problem, a Lead-Lag compensator with limited amplification of high frequencies is applied:

$$G_{ll}(s) = k_{ll} \frac{1 + T_{d,ll}s}{1 + \alpha_{ll}T_{d,ll}s}, \quad \alpha_{ll} < 1. \quad (4-87)$$

A part of the delay can be compensated using the Lead-Lag compensator [85], [105]. In order to design the parameters of the Lead-Lag compensator, the total delay of the current control loop is approximated by

$$G_{d,t} \approx \frac{1}{1 + 1.5sT_{s,cc}}. \quad (4-88)$$

Considering (4-88), the following Lead-Lag compensator is added to compensate the delay partially:

$$G_{ll}(s) = \frac{1 + 1.5T_{s,cc}s}{1 + 1.5\alpha_{ll}T_{s,cc}s}. \quad (4-89)$$

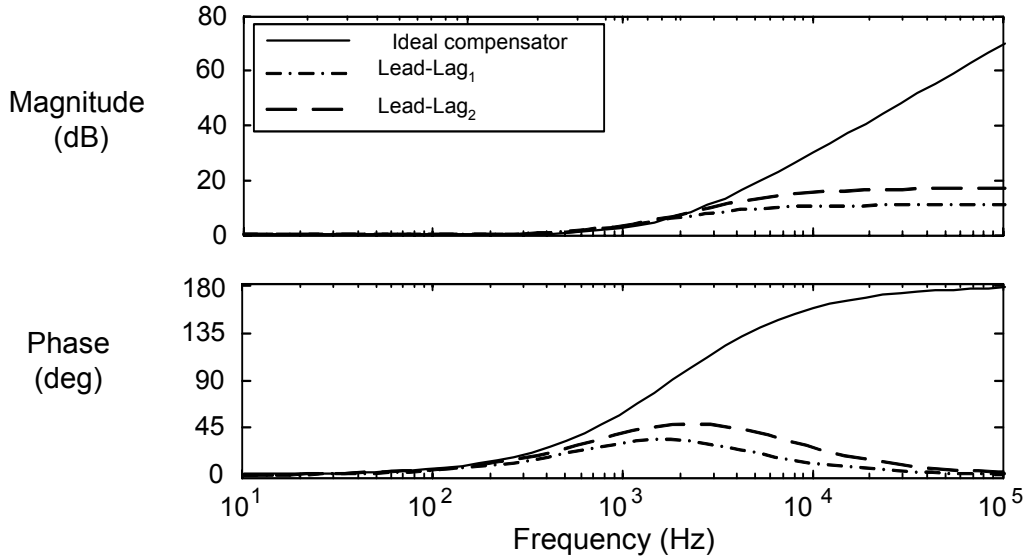


Fig. 4-41 Bode diagram of the compensators with various parameters: the approximated ideal compensator $1+1.5T_s s$; Lead-Lag₁ = $(1+1.5T_s s)/(1+1.5\alpha_{ll,1}T_s s)$ with $\alpha_{ll,1} = 4/3\pi$; Lead-Lag₂ = $(1+1.5T_s s)/(1+1.5\alpha_{ll,2}T_s s)$ with $\alpha_{ll,2} = 2/3\pi$

A compromise must be achieved between compensation and noise amplification to design the position of the Lead-Lag pole. Fig. 4-41 shows the Bode plots of an ideal compensator ($G_{compensator} = 1+1.5sT_{s,cc}$) to compensate the approximated delay in (4-88) as well as the Lead-Lag compensator with two different values of α_{ll} in (4-89). The Lead-Lag pole position is considered to be at switching and sampling frequencies in an ARS-PWM. α_{ll} should be $4/3\pi$ to assign the pole position in the switching frequency. If α_{ll} is equal to $2/3\pi$, then the Lead-Lag pole position is at the sampling frequency. It can be seen in Fig. 4-41 that the smaller α_{ll} , the greater the compensation but also noise amplification. The next sections will present the simulation and experimental results of the influence of different compensator designs on the dynamic behavior of the current control loop.

As mentioned above, the main effect of the filter capacitor voltages feedback in the current control loop is the active damping of the LCL-filter oscillations. In order to explain the

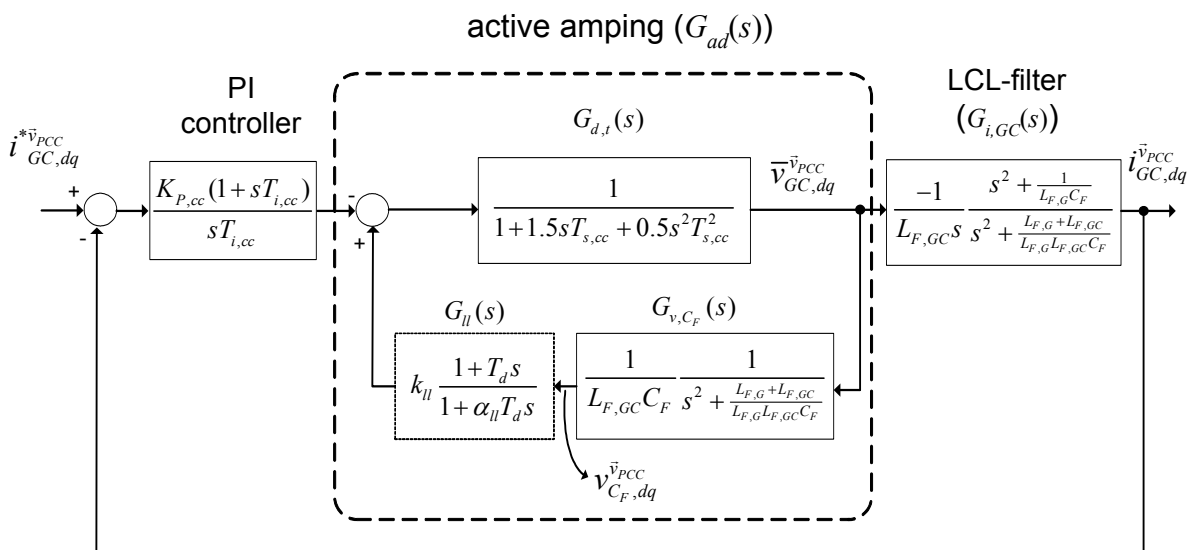


Fig. 4-42 Current control loop with active damping and a Lead-Lag compensator

performance of the active damping, the converter current control loop with filter capacitor voltages as feedbacks is shown in Fig. 4-42. The current control loop comprises the current transfer function in (4-76) as the model of an LCL-filter and a PI current controller with parameters presented in (4-84). Using the single-phase representation of the LCL-filter in Fig. 4-39 (a), the relation between the converter output voltage $\bar{v}_{GC,dq}^{\bar{v}_{PCC}}$ and the voltage of the filter capacitor $\bar{v}_{C_F,dq}^{\bar{v}_{PCC}}$ is expressed as follows:

$$G_{v,CF}(s) = \frac{\bar{v}_{C_F,dq}^{\bar{v}_{PCC}}}{\bar{v}_{GC,dq}^{\bar{v}_{PCC}}} = \frac{1}{L_{F,GC} C_F} \frac{1}{s^2 + \frac{L_{F,G} + L_{F,GC}}{L_{F,G} L_{F,GC} C_F}} \quad (4-90)$$

Considering the active damping block shown in Fig. 4-42, the transfer function of the active damping loop is derived as follows:

$$G_{ad}(s) = \frac{G_{d,t}(s)}{1 - G_{d,t}(s)G_{v,CF}(s)G_{ll}(s)} \quad (4-91)$$

The Bode diagram of the open loop transfer function of the current control loop without active damping ($G_{d,t}(s)G_{i,GC}(s)$), the Bode diagram of the active damping loop transfer function ($G_{ad}(s)$), and the Bode diagram of the open loop current transfer function with active damping are given in Fig. 4-43. The passive component values of the LCL-filter correspond to the LCL-filter with minimum stored energy addressed in Table 4.9 ($L_{F,G,t} = 0.703$ mH (0.067 pu), $L_{F,GC} = 0.711$ mH (0.068 pu), $C_F = 69.418$ μ F (0.072 pu),

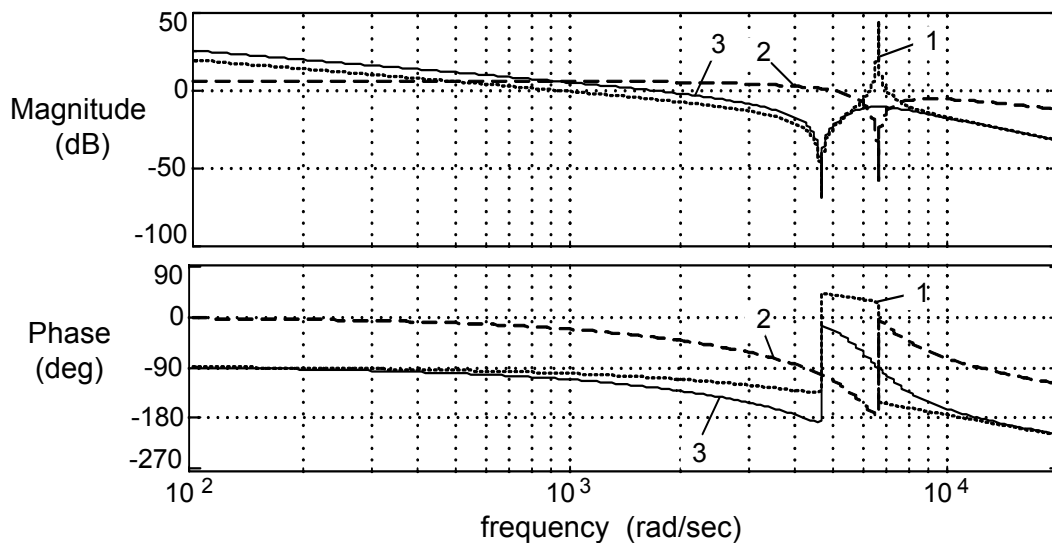


Fig. 4-43 1: Bode diagram of the current open loop transfer function without active damping ($G_{d,t}(s)G_{i,GC}(s)$); 2: bode diagram of the active damping loop transfer function ($G_{ad}(s)$); 3: bode diagram of the open loop current transfer function with active damping ($k_{ll} = 1$, $\alpha_{ll} = 1$)

$f_{res} = 1016$ Hz). The active damping loop is considered to not have a Lead-Lag compensator ($k_{ll} = 1$, $\alpha_{ll} = 1$). Obviously, the active damping loop acts as a notch filter which damps the peak value of the current open loop transfer function at the resonance frequency below 0 db.

The application of a Lead-Lag compensator in the active damping loop leads to a better damping at the resonance frequency and increases the bandwidth of the current control loop. The Bode diagram of the active damping loop transfer function with various Lead-Lag

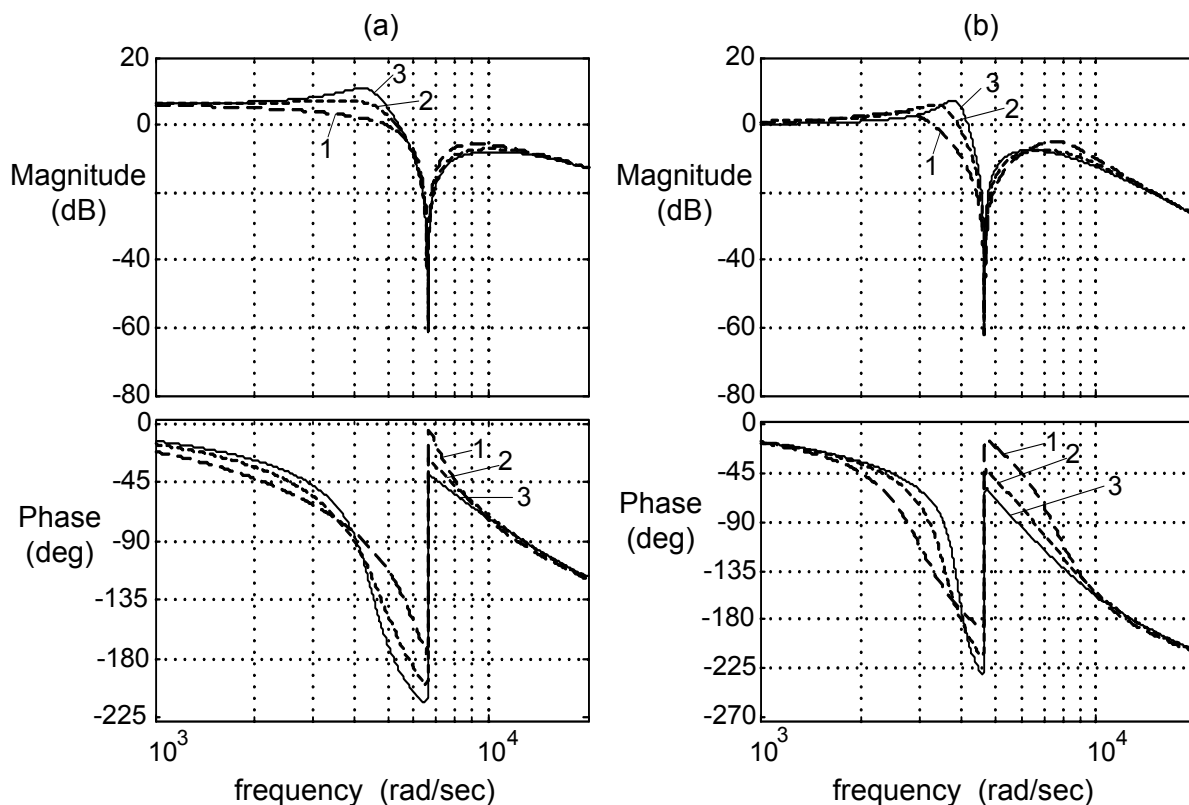


Fig. 4-44 (a) Bode diagram of the active damping control loop with various Lead-Lag compensators; (b) bode diagram of the converter current control loop with different Lead-Lag compensators in the active damping loop; $k_{ll} = 1$, $T_{d,ll}=1.5T_{s,cc}$, 1: $\alpha_{ll} = 1$; 2: $\alpha_{ll} = 4/3\pi$; 3: $\alpha_{ll} = 2/3\pi$

compensators is shown in Fig. 4-44(a). Moreover, the corresponding Bode diagrams of the closed loop transfer function of the converter current are presented in Fig. 4-44 (b). Obviously, the application of a Lead-Lag compensator (waveforms 2 and 3) results in a faster current control loop (increased bandwidth) and a better damping at the resonance frequency of the LCL filter (more reduction of the amplitude at the resonance frequency).

Detailed block diagram of the VOC for PWM active front end converter with LCL-filter

A detailed structure of the VOC for the PWM active front end converter with LCL-filter and active damping is depicted in Fig. 4-45. The line voltages at PCC are measured to determine the angle of the PCC voltage vector. The angle of the PCC voltage vector is required to project the converter currents and voltage of the filter capacitor into the rotating reference frame synchronous to the PCC voltage vector. The structure and parameters of the applied PLL are as described in Section 4.4.2. The filter capacitor voltages are measured and projected into the rotating coordinate. The direct and quadrature components of the capacitors voltages ($v_{C_{F,d}}^{\bar{v}_{pcc}}, v_{C_{F,q}}^{\bar{v}_{pcc}}$) should be added to the output of the current controllers. The Lead-Lag compensators in (4-89) can be applied to compensate for the effects of the PWM and processing delays. The parameters of the current controllers are according to (4-84). The dc-link voltage is measured, and a PI controller with anti-windup is applied in the dc-link voltage control loop. The parameters of the current controllers are according to (4-37) and (4-38). Similar to the VOC for the PWM active front end converter with L-filter, the feed-forward dc-current $i_{dc,ff}$ expressed in (4-40) can be used to achieve a faster load disturbance rejection. The

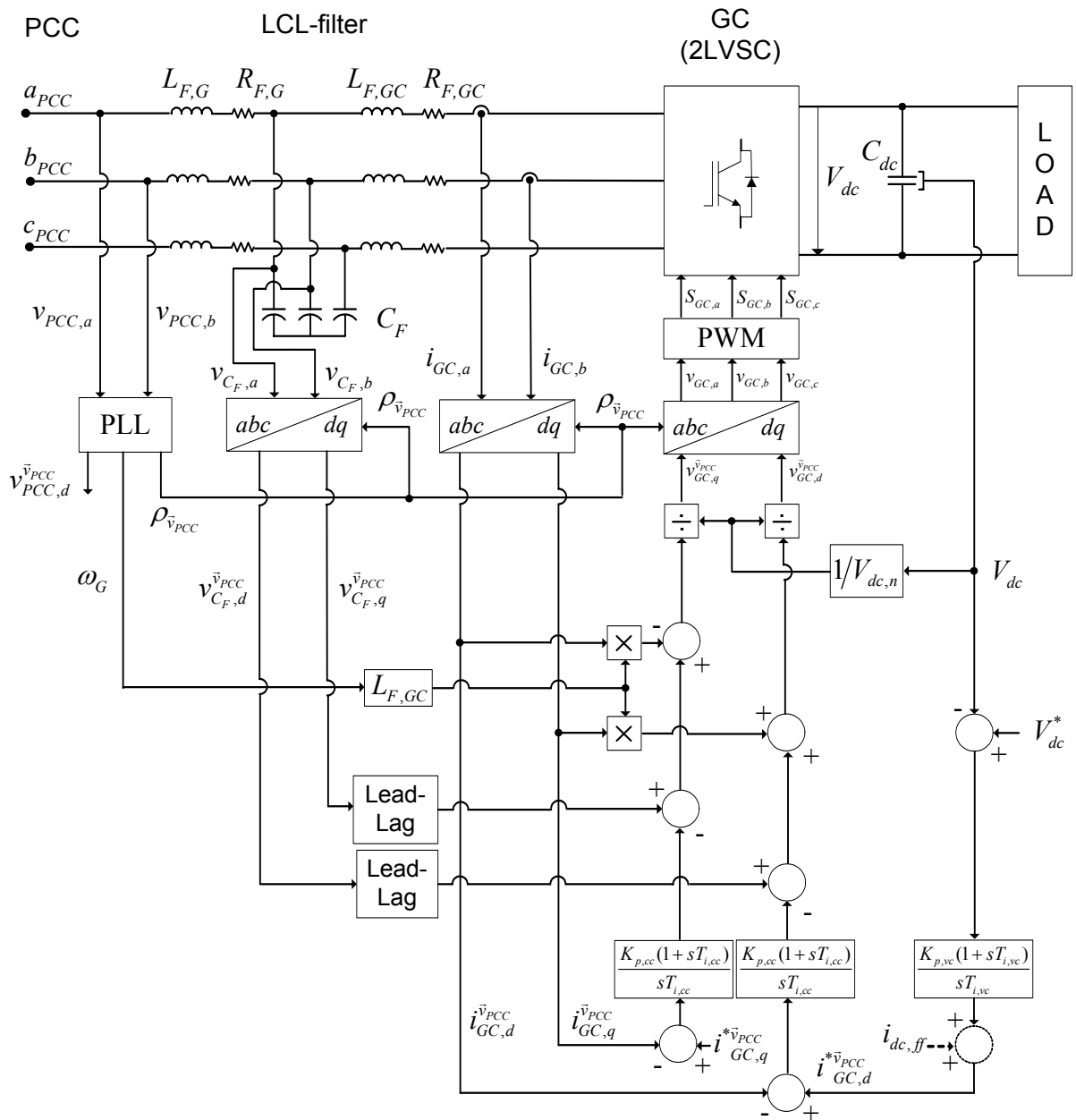


Fig. 4-45 Block diagram of voltage-oriented control system for PWM active front end converter with LCL filter

dc-link voltage V_{dc} and the amplitude of the carrier signal are applied for linearization in the current control loop as described in Section 4.4.3. The peak-to-peak amplitude of the carrier signal is considered to be constant and equal to the nominal value of the dc-link voltage $V_{dc,n}$. Asymmetrical regular sampled sinus-triangle modulation is used as modulator.

4.6.1 Simulative investigations

The entire system comprising grid, LCL-filter, an ideal 2L VSC, and the control system is simulated in MATLAB/SIMULINK in order to verify the performance of the controllers and the effectiveness of the designed LCL-filters. The control structure depicted in Fig. 4-45 is applied in the simulations. The parameters of the grid and the grid side converter were chosen according to Table 4.2. The structure of the applied PLL is as described in Section 4.4.2. The

PLL sampling frequency is 8.1 kHz and a damping factor of $a_{PLL} = 30$ is used for the PI controller of the PLL.

As described in Table 4.2, the converter switching frequency is 4.05 kHz ($m_f = 81$) and a PWM with asymmetrical regular sampling is used as modulator. The sampling frequencies of the current and the dc-link voltage control loops are 8.1 kHz (twice the switching frequency). The damping factors of the current and voltage controllers are assigned to $a_{cc} = 3$ and $a_{vc} = 4$, respectively.

In order to investigate the effectiveness and performance of LCL-filters with different parameters and component values, two sets of filter components were designed, applying the flowchart in Fig. 4-35. The first design variant is the LCL-filter with minimum energy for $I_{G,1} = 70$ A, $V_{G,ll} = 400$ V, and $V_{dc} = 700$ V, as presented in Table 4.9. The second variant was determined for a unity split factor r and a resonance frequency $f_{res} = 1350$ Hz larger than the resonance frequency of the filter with minimum stored energy. The parameters and components values of the investigated filters are presented below

- 1) $L_{F,G,t} = 0.703$ mH (0.067 pu), $L_{F,GC} = 0.711$ mH (0.068 pu), $C_F = 69.418$ μ F (0.072 pu), $r = 0.989$, and $f_{res} = 1016$ Hz.
- 2) $L_{F,G,t} = 1.379$ mH (0.132 pu), $L_{F,GC} = 1.379$ mH (0.132 pu), $C_F = 20.153$ μ F (0.021 pu), $r = 1$, and $f_{res} = 1350$ Hz.

The amplitude of the $(m_f - 2)^{th}$ grid current harmonic is considered to be 0.2% of the amplitude of the fundamental component of the grid current for both filters. The simulation results for steady-state and transient performance of the PWM active front end converter with both filters are discussed in the following sections.

Steady-state performance

The simulation results for the amplitude of the main harmonics of the first carrier band in steady-state are depicted in Table 4.11 for the designed LCL-filters. Obviously, the amplitude of the most significant current harmonic for both filters is around the desired value of 0.2% with an acceptable error.

A voltage-oriented controlled active front end converter based on the control of the converter currents does not operate exactly at unity power factor, which was assumed in the filter design procedure. The reason for this is the difference between the grid and the converter currents caused by the filter capacitors. Furthermore, the grid voltage angle, which is required for the projections, cannot be measured exactly in a discrete control system. Therefore, using a proper set point of converter quadrature current $i_{GC,q}^{\bar{v}_{pcc}}$, the grid reactive power is adjusted to zero in the simulation results presented in Table 4.11. Grid and the converter currents as well

Table 4.11
Simulation results for the amplitude of the grid current harmonics

LCL-Filter parameters and reactive components value							Amplitude of grid current harmonics (%)			
$L_{F,G,t}$		$L_{F,GC}$		C_F		f_{res} (Hz)	Harmonic order			
(mH)	(pu)	(mH)	(pu)	(μ F)	(pu)		77	79	83	85
0.703	0.067	0.711	0.068	69.418	0.072	1016	-	0.202	0.177	-
1.379	0.132	1.379	0.132	20.153	0.021	1350	-	0.201	0.174	-

as the corresponding harmonic spectra are shown in Fig. 4-46. Obviously, the application of a higher filter resonance frequency leads to a lower amplitude of the converter current harmonics. However, the filter voltage drop increases because of the higher value of the total filter inductance. Consequently, the dc-link voltage reserve is reduced. The amplitudes of the converter current harmonics as well as the control reserve for both filters are presented in Table 4.12. According to (4-74), the maximum converter current ripple is 24.3% and 13.7% of the rated grid current for the filter with a resonance frequency of 1016 Hz and 1350 Hz.

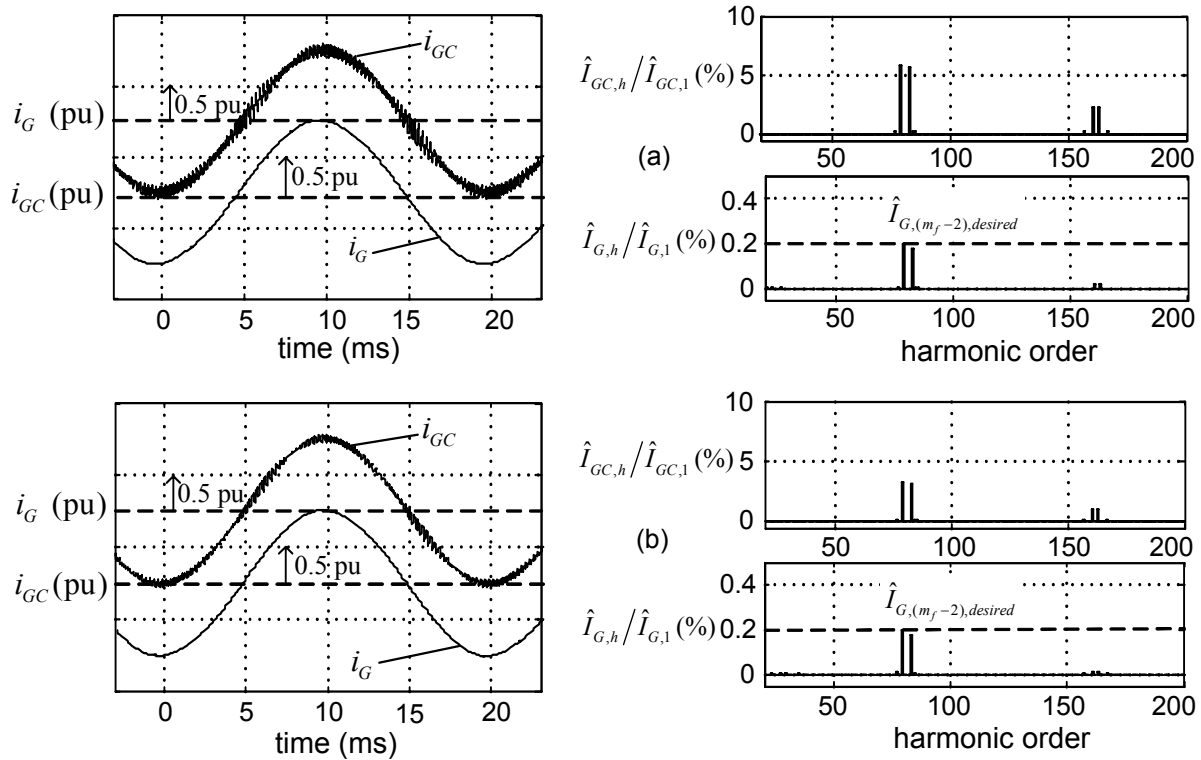


Fig. 4-46 Simulation results for the grid and the converter current waveforms and the corresponding harmonic spectra at steady state: (a) $L_{F,G,t} = 0.703$ mH (0.067 pu), $L_{F,GC} = 0.711$ mH (0.068 pu), and $C_F = 69.418$ μ F (0.072 pu); (b) $L_{F,G,t} = 1.379$ mH (0.132 pu), $L_{F,GC} = 1.379$ mH (0.132 pu), and $C_F = 20.153$ μ F (0.021 pu), $I_{b,G} = 99$ A

Table 4.12

Simulation results for the amplitude of the converter current harmonics and the control reserve

LCL-Filter parameters and reactive components value							Amplitude of converter current harmonics (%)		
$L_{F,G,t}$	$L_{F,GC}$	C_F	f_{resr}			Harmonic order			
(mH)	(pu)	(μ F)	(Hz)	79	83			$V_{dc, reserve}$	
								(%)	
0.703	0.067	69.418	1016	5.848	5.679			7	
1.379	0.132	20.153	1350	3.245	3.121			4	

Transient performance

As shown in Fig. 4-45, the converter current is measured and controlled by applying the capacitor voltages for decoupling and active damping. The transient performance of the

current control loop is investigated for the designed filters in this section. The parameters of the current controllers are designed according to (4-84).

The simulation results for a reference step of 1 pu (99 A) on the q-axis are presented in Fig. 4-47 (a) and (b) for LCL-filters with the resonance frequency of 1030 Hz and 1350 Hz, respectively. Waveform 1 shows the step response when there is no compensator in the active

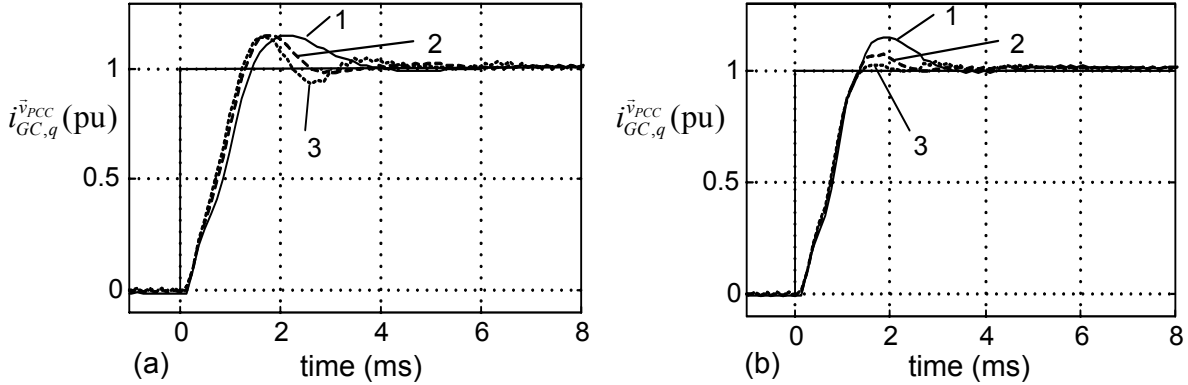


Fig. 4-47 Simulation results for the current controller performance: (a) $L_{F,G,t} = 0.703$ mH (0.067 pu), $L_{F,GC} = 0.711$ mH (0.068 pu), and $C_F = 69.418$ μ F (0.072 pu); (b) $L_{F,G,t} = 1.379$ mH (0.132 pu), $L_{F,GC} = 1.379$ mH (0.132 pu), and $C_F = 20.153$ μ F (0.021 pu), $I_{b,G} = 99$ A, 1: active damping without compensator, 2: active damping with Lead-Lag compensator and $\alpha = 4/3\pi$, 3: active damping with Lead-Lag compensator and $\alpha = 2/3\pi$

damping loop of Fig. 4-42. Furthermore, waveforms 2 and 3 show the step response of the current control loop with two different Lead-Lag designs of $\alpha = 4/3\pi$ and $\alpha = 2/3\pi$ respectively.

It is remarkable that the current control loop is stable even without compensation. The application of the Lead-Lag compensator leads to a faster step response and lower current

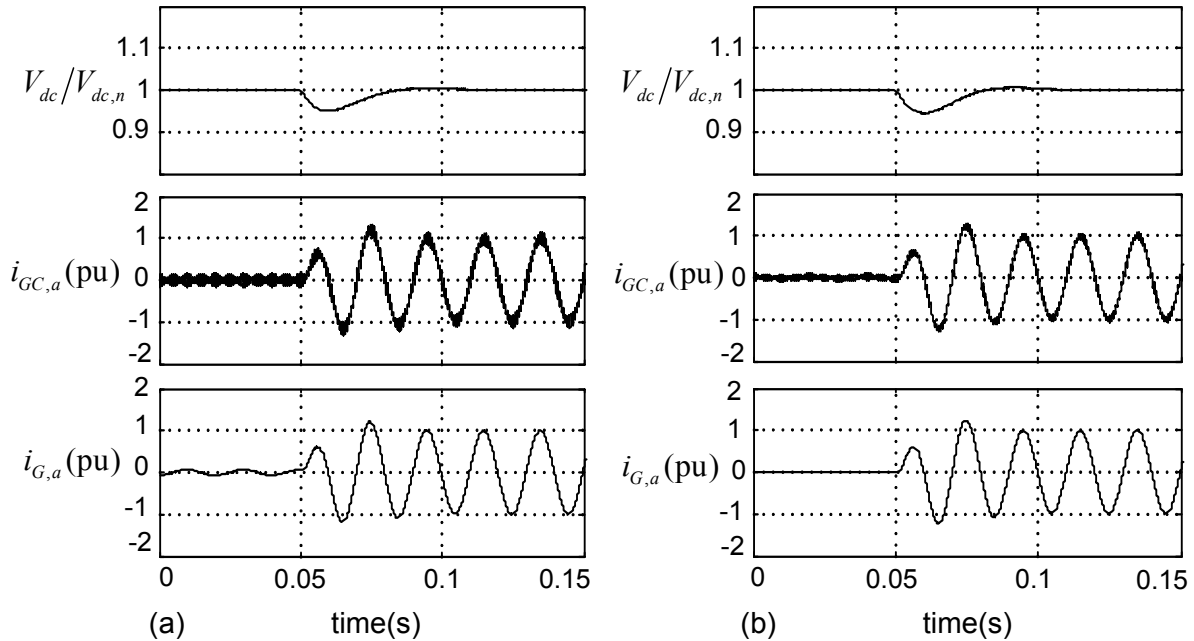


Fig. 4-48 Simulation results for the load disturbance rejection of the PWM active front end with LCL-filter: (a) $L_{F,G,t} = 0.703$ mH (0.067 pu), $L_{F,GC} = 0.711$ mH (0.068 pu), and $C_F = 69.418$ μ F (0.072 pu); (b) $L_{F,G,t} = 1.379$ mH (0.132 pu), $L_{F,GC} = 1.379$ mH (0.132 pu), and $C_F = 20.153$ μ F (0.021 pu), $V_{dc,n} = 700$ V, $I_{b,G} = 99$ A

overshoot especially for the filter with the higher resonance frequency. The resonance frequency is far from the corner frequency of the current control loop in that case. As shown in Fig. 4-47, applying the Lead-Lag with stronger compensation leads to a better current step response but can cause noise amplification in the implementation.

Fig. 4-48 shows the simulation results for the load disturbance rejection of the PWM active front end converter with the two LCL-filter designs. The nominal dc-link voltage is $V_{dc,n} = 700$ V. The converter is loaded with a rated load of about 49 kW, and the disturbance is rejected in about 30 ms. Direct and quadrature components of the converter current are limited to 1.5 pu in the control system.

4.6.2 Experimental investigations

The effectiveness of the designed LCL-Filters and the dynamic performance of the PWM active front end converter with LCL-filter are verified by experimental investigations in this section. The control structure shown in Fig. 4-45 is realized by using an ABB OPCoDe control platform [133]. A picture of the LCL-filter of the PWM active front end converter test bench is given in Fig. 4-49. Passive damping (R_d in series with C_F in Fig. 4-49) or active damping can be selected in the test bench to damp the LCL-filter resonance. The parameters of the grid and the grid side converter are given in Table 4.2. All parameters of the control



Fig. 4-49 A picture of the LCL-filter of the test bench; $L_{F,G}$: grid side inductor, $L_{F,GC}$: inductor of the grid side converter; C_F : filter capacitor; R_d : resistor for passive damping

system are similar to the corresponding values applied in the simulation in the previous section. The sampling frequencies of the PLL, current control loop, and the dc-link voltage control loop are 8.1 kHz (twice the switching frequency). A damping factor of $a_{PLL} = 30$ is used for the PI controller of PLL. The damping factors of the current and voltage control loops are assigned to $a_{cc} = 3$ and $a_{vc} = 4$, respectively. The converter switching frequency is

4.05 kHz ($m_f = 81$), and a PWM with asymmetrical regular sampling is used as modulator. The parameters and reactive components value of the LCL-filters are considered to be comparable to the parameters and reactive component values of the simulated LCL-filters. The following LCL-filters are used in the experimental investigations:

- 1) $L_{F,G} = 0.6$ mH (0.057 pu), $L_{F,GC} = 0.6$ mH (0.057 pu), $C_F = 88$ μ F (0.091 pu), $f_{res} = 980$ Hz,
- 2) $L_{F,G} = 1.2$ mH (0.114 pu), $L_{F,GC} = 1.2$ mH (0.114 pu), $C_F = 22$ μ F (0.023 pu), $f_{res} = 1385$ Hz.

The filter capacitance tolerances are within $\pm 5\%$. Furthermore, a tolerance of -10% to -15% is specified for the filter inductance at the switching frequency of 4 kHz according to achieved measurements.

Steady-state performance

The measured grid and converter currents and the corresponding spectra for both filters at rated load and unity power factor conditions are presented in Fig. 4-50. The amplitude of the fundamental component of the grid current is 100 A. The grid line-to-line voltage and the dc-link voltage are 400 V and 700 V, respectively. The filter capacitors voltages without Lead-Lag compensator are used in the VOC and the active damping. As described in Section 4.4.6, low-order harmonics of the grid voltage leads to a distorted grid current with low-order harmonics. The influences of the line voltage distortion on the grid current are stronger in the case of the filter with the lower resonance frequency because of the lower filter total

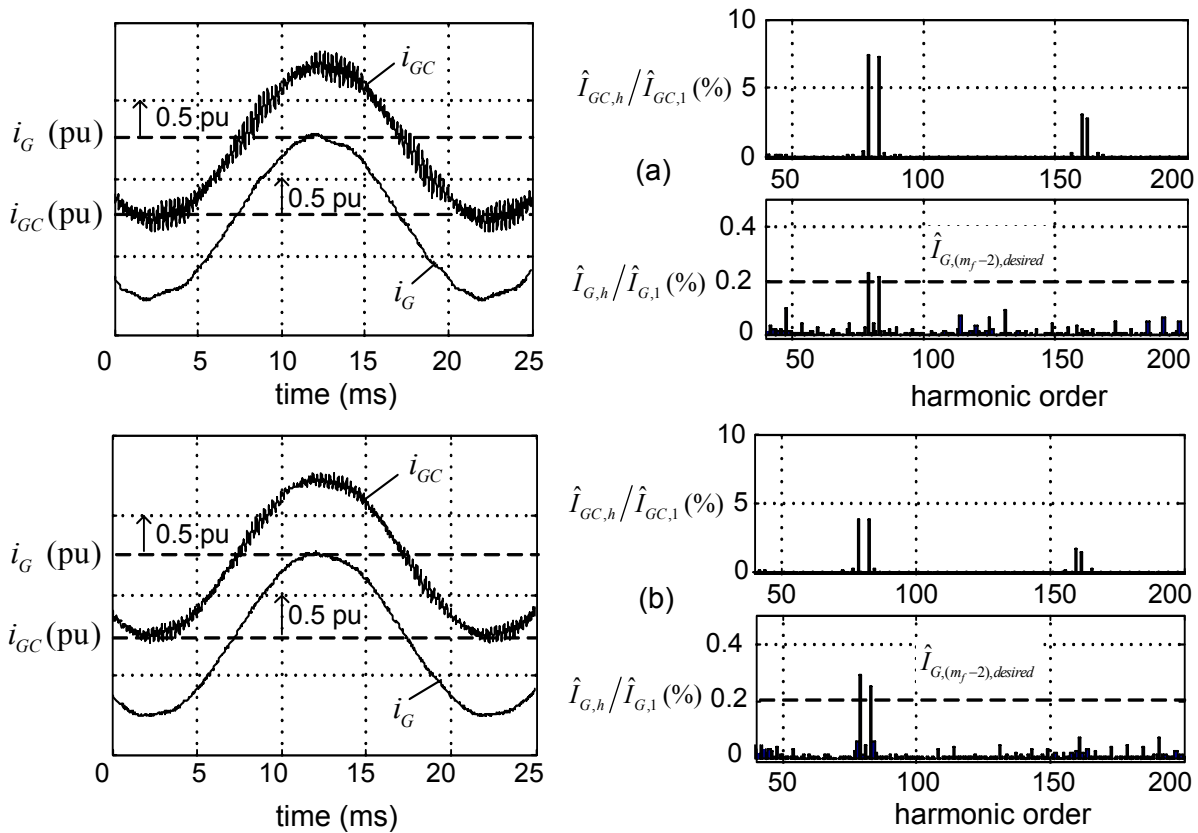


Fig. 4-50 Experimental results for the grid and the converter currents and the corresponding harmonic spectra at steady state: (a) $L_{F,G,t} = 0.6$ mH (0.057 pu), $L_{F,GC} = 0.6$ mH (0.057 pu), and $C_F = 88$ μ F (0.091 pu); (b) $L_{F,G,t} = 1.2$ mH (0.114pu), $L_{F,GC} = 1.2$ mH (0.114 pu), and $C_F = 22$ μ F (0.021 pu), $I_{b,G} = 99$ A

inductance. Experimental results for the amplitudes of the major grid current harmonics of the first carrier band and the corresponding simulation results are presented in Table 4.13. A current monitor with a sensitivity of 0.1 Volt/Ampere +1/-0% is used to measure the current harmonics. The fundamental grid current component is filtered by applying a 4th-order Butterworth high-pass filter to enable precise current harmonics measurement.

The main reason for the difference between the simulation and experimental results is the tolerance of the filter component values at the switching frequency.

Table 4.13

Simulation and experimental results for the amplitude of the grid current harmonics for two sets of LCL-Filters

LCL-Filter parameters and reactive components value							Amplitudes of grid current harmonic (%)			
							Harmonic order		Simulation Results	Experimental Results
$L_{F,G,t}$	$L_{F,GC}$	C_F	f_{resr}							
(mH)	(pu)	(mH)	(pu)	(μ F)	(pu)	(Hz)	79	83	79	83
0.6	0.057	0.6	0.057	88	0.091	980	0.2	0.175	0.25	0.205
1.2	0.114	1.2	0.114	22	0.023	1385	0.235	0.204	0.304	0.254

The PWM active front end converter with LCL-filter and a -10%-deviation of the component values given in Table 4.13 is simulated to investigate the effects of the component values variation. The simulation results are summarized in Table 4.14. Obviously, the simulation results are comparable to the experimental results given in Table 4.13. The drawbacks of the reactive component values deflection can be counterbalanced by choosing a properly desired amplitude of the $(m_f - 2)^{th}$ grid current harmonic $\hat{I}_{G,(m_f-2),desired, \%}$ or by applying filter components with appropriate values regarding the eventual variations.

Table 4.14

Simulation results for -10%-deviations of the filter component values for the LCL-Filters presented in Table 4.13

LCL-Filter parameters and reactive components value							Amplitudes of grid current harmonic (%)			
							Harmonic order		Simulation Results	Experimental Results
$L_{F,G,t}$	$L_{F,GC}$	C_F	f_{resr}							
(mH)	(pu)	(mH)	(pu)	(μ F)	(pu)	(Hz)	79	83	79	83
0.54	0.052	0.54	0.052	83.6	0.086	1059	0.258	0.227	0.258	0.227
1.08	0.103	1.08	0.103	20.9	0.021	1498	0.314	0.271	0.314	0.271

Transient performance

The experimental results for the step response of the current control loop of the PWM active front end converter with LCL-filter are presented in Fig. 4-51 for the above LCL-filters. The

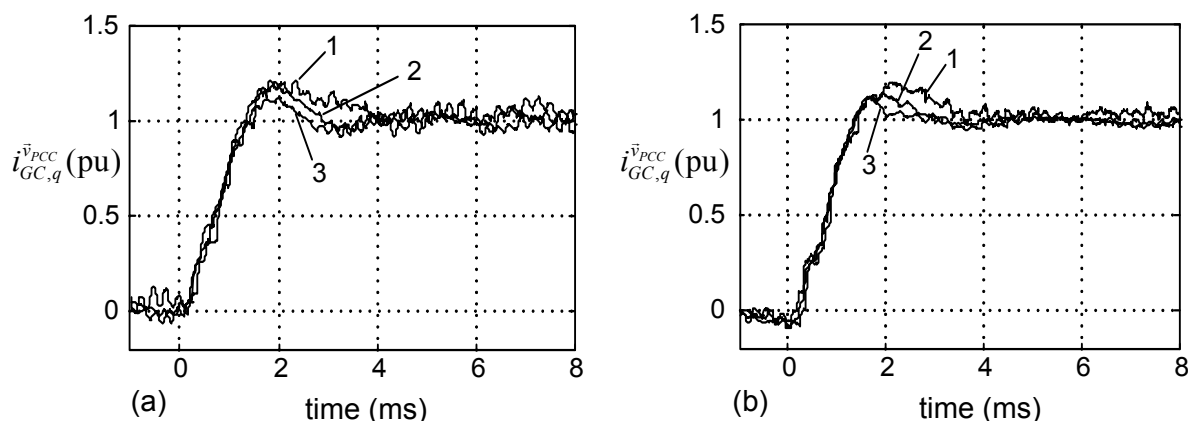


Fig. 4-51 Experimental results for the current controller performance of the PWM active front end with LCL/filter: (a) $L_{F,G,t} = 0.6$ mH (0.057 pu), $L_{F,GC} = 0.6$ mH (0.057 pu), and $C_F = 88$ μ F (0.091 pu); (b) $L_{F,G,t} = 1.2$ mH (0.114 pu), $L_{F,GC} = 1.2$ mH (0.114 pu), and $C_F = 22$ μ F (0.023 pu), $I_{b,G} = 99$ A; 1: active damping without compensator, 2: active damping with Lead-Lag compensator and $\alpha = 4/3\pi$, 3: active damping with Lead-Lag compensator and $\alpha = 2/3\pi$

performance of the current controller for a step of 99 A on the q-axis for the filters with 980 Hz and 1385 Hz as resonance frequencies is presented in Fig. 4-51(a) and (b), respectively. The capacitor voltage feedback is considered to be without compensator for waveform 1, with a Lead-Lag compensator and $\alpha = 4/3\pi$ for waveform 2, and with a Lead-Lag compensator and $\alpha = 2/3\pi$ for waveform 3. The control system is stable without a compensator. The Lead-Lag compensator leads to a faster step response with lower overshoot especially if the resonance frequency is far from the corner frequency of the current controller. The current control loop features a rise time of about 1.5 ms and an overshoot of 20% for both filters if there is no compensator in the active damping loop.

Fig. 4-52 shows the experimental results for the load disturbance rejection of the PWM active front end converter with the two LCL-filter designs. The nominal dc-link voltage is $V_{dc,n} = 700$ V. The converter is loaded with a rated load of about 49 kW, and the disturbance is rejected in about 30 ms. Direct and quadrature components of the converter current are limited to 1.5 pu in the control system.

4.6.3 Robustness of the current control loop

Variations in the grid structure and other parallel devices connected to PCC can lead to a deviation in the grid stray inductance L_G . Due to the deviation of the grid stray inductance; the LCL-filter resonance frequency will be changed. As mentioned above, the filter resonance frequency should be in a range between ten times of the grid frequency and one-half of the carrier frequency in order to prevent a filter excitation by the converter voltage harmonics. The control system stability cannot be guaranteed if the grid stray inductance variations move the filter resonance frequency beyond the mentioned frequency range.

As described in Subchapter 4.6, the parameters of the current controller depend only on the converter side inductor parameters. Therefore, in the case that the grid inductance variation does not lead to filter excitation by grid or converter harmonics, the performance of the current control loop will not be affected considerably by resonance frequency variations. However, due to the processing and PWM delays and consequently no ideal decoupling

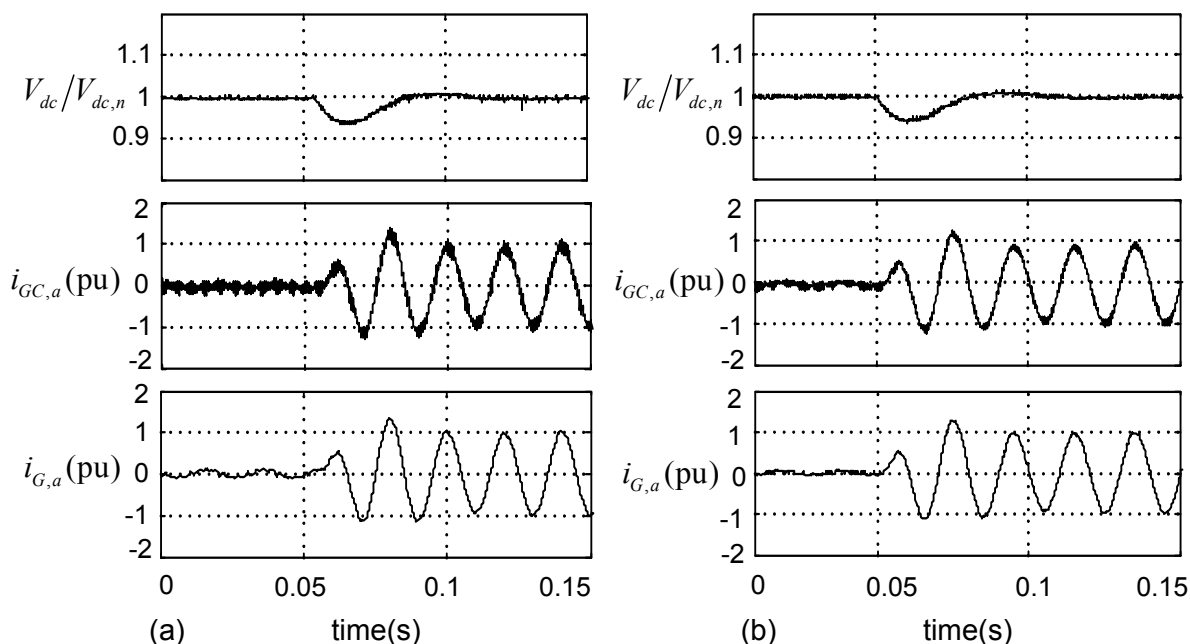


Fig. 4-52 Experimental results for load disturbance rejection of the PWM active front end with LCL filter: (a) $L_{F,G,l} = 0.6$ mH (0.057 pu), $L_{F,GC} = 0.6$ mH (0.057 pu), and $C_F = 88$ μ F (0.091 pu); (b) $L_{F,G,l} = 1.2$ mH (0.114 pu), $L_{F,GC} = 1.2$ mH (0.114 pu), and $C_F = 22$ μ F (0.023 pu), $V_{dc,n} = 700$ V, $I_{b,G} = 99$ A

system, variations of the grid inductance could slightly change the behavior of the current control loop.

The investigated PWM active front end converter with LCL-filter is applied to simulative and experimental investigations to examine the influence of the grid inductance variations on the current control loop performance. The parameters of the grid and the grid side converter are as presented in Table 4.2. The following LCL-filter is applied in the robustness evaluation of the control system:

$$L_{F,G} = 1.2 \text{ mH (0.114 pu)}, L_{F,GC} = 1.2 \text{ mH (0.114 pu)}, C_F = 22 \text{ } \mu\text{F (0.023 pu)}, f_{res} = 1385 \text{ Hz.}$$

The grid side inductance of the LCL-filter is varied in simulation and experimental studies for +25% ($L_{F,G} = 1.5$ mH (0.143 pu)) and -25% ($L_{F,G} = 0.9$ mH (0.086 pu)). These new grid side inductances lead to new resonance frequencies of $f_{res} = 1314$ Hz and $f_{res} = 1496$ Hz, respectively. Both new resonance frequencies are in the range of ten times of the grid frequency and one-half of the carrier frequency ($500 \text{ Hz} < f_{res} < 2000 \text{ Hz}$). The simulation and experimental results for the influence of the grid inductance variations on the step response of the current control loop are shown in Fig. 4-53 (a) and (b), respectively. Obviously, these $\pm 25\%$ -deviations in the grid side converter do not lead to a significant change in the rise time and overshoot of the step response of the converter current.

4.7 Summary

PWM active front end converters are increasingly applied due to features such as bidirectional power flow, unity power factor, low distorted grid currents, and an adjustment of the converter dc-link voltage. Several control strategies like direct power control and voltage-oriented control as well as virtual-flux-based sensorless methods are successfully applied to

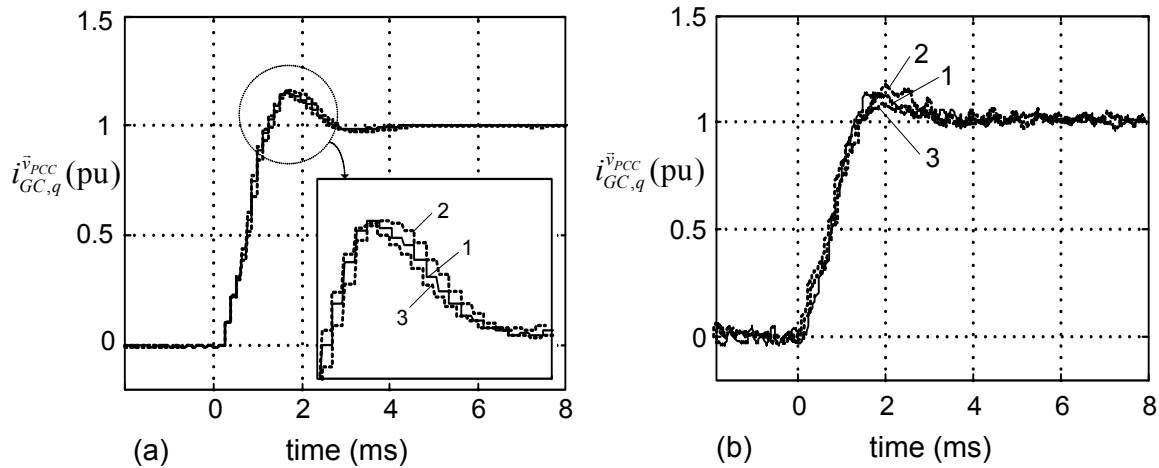


Fig. 4-53 Robustness of the current control loop of the PWM active front end converter with LCL-filter against variation of the grid side inductance: (a) simulation results; (b) experimental results: $L_{F,GC} = 1.2$ mH (0.114 pu), and $C_F = 22$ μ F (0.023 pu), 1: $L_{F,G,t} = 1.2$ mH (0.114 pu); 2: $L_{F,G,t} = 1.5$ mH (0.143 pu); 3: $L_{F,G,t} = 0.9$ mH (0.086 pu), $I_{b,G} = 99$ A

control the grid side active front end converters. Assuming symmetrical sinusoidal grid voltages and a constant dc-link voltage, the widely spread voltage-oriented controlled PWM active front end converters generate grid current harmonics in carrier bands of n times the switching frequency, which are usually sufficiently damped by moderate inductive filters in industrial grids.

However, the grid voltage at PCC is substantially distorted by the commutation of thyristors if PWM rectifiers and thyristor converters are operated in parallel. In this case, voltage-oriented controlled PWM rectifiers are not able to suppress low-order current harmonics (e.g. 5th and 7th) if conventional state-of-the-art PI current controllers are applied.

An iterative procedure to design L- and LCL-filters for active rectifiers has been proposed. The analytical expression of the converter voltage harmonics based on Bessel functions is applied to determine the filter parameters which enable a sufficient damping of the grid current harmonics (e.g. according to IEEE-519-1992).

In the case of the LCL-filter, it is shown that LCL-filters with different parameters (f_{res}, r) and components ($L_{F,GC}, L_{F,G}, C_F$) can cause identical attenuations of the grid current harmonics. Thus, various optimization criteria like minimum costs, weight, size, or stored energy of the passive components can be applied to determine optimal filter parameters. As an example, the stored energy as measure for the expense of passive components has been used to compare different filter designs and to derive optimal solution. The optimized filter of a 400V, 49kVA converter with a switching frequency of about 4 kHz features a split factor of about 1 and a resonance frequency of about 1 kHz if the dc-link voltage is $V_{dc} = 700$ V. These filter parameters remain constant for different rated grid currents and line voltages when assuming a constant voltage reserve.

The voltage oriented control including active damping is applied in the simulations and the experimental test bench. A simple design method on the basis of the modulation and processing delays for the required Lead-Lag compensator is proposed. Simulation and experimental results prove both, the accuracy of the proposed design procedure and an acceptable performance of the current control loop for different filter parameters. The

experimental investigations show that a reduction of the inductivity at high frequencies will reduce the effectiveness of LCL-filters. The drawbacks of the reactive component values deflection can be counterbalanced by choosing a properly desired amplitude of the $(m_f-2)^{\text{th}}$ grid current harmonic $\hat{I}_{G,(m_f-2),desired, \%}$ in the LCL-filter design procedure.

Chapter 5

Conclusions

In this thesis, the control of a low voltage ac/dc/ac converter for high-speed induction motor drive (HSIMD) applications has been investigated. Such a configuration can be applied, for example, in microturbines and high-speed spindles. Scalar control is usually applied for the control of high-speed drives (HSDs) especially in the case of very high-speed drives (e.g. $n_{syn} > 200,000$ rpm). RFOC and DTC are designed and compared for the control of an exemplary HSIMD in this work. The 2L VSC is the most widely applied converter for HSDs. However, the 3L-NPC VSC is an attractive topology if drastically increased switching frequencies are required. In this thesis, a detailed comparison between 2L VSC and 3L-NPC VSC as the machine side converter of the exemplary HSIMD is carried out.

VOC is applied for the control of the grid side converter. In several industrial applications PWM active front end converters commonly operate in parallel to thyristor converter fed dc drives. The behavior of the voltage-oriented controlled active front end converter with L-filter in the presence of a parallel thyristor converter is investigated in this thesis.

The design of the LCL-filter components according to the given maximum current harmonics (e.g. IEEE-519) is a complex task. So far a precise and clear design procedure has not been presented. A new procedure to design the grid side filter (L- and LCL-filter) is proposed in this thesis to achieve the compliance with the grid standard of IEEE-519. VOC with active damping is used to control the active front end converter with LCL-filter. A simple method is proposed to design the required lead-lag compensator in the active damping loop.

In an opening chapter state-of-the-art low voltage drives are investigated. Different parts of an industrial low voltage drive are described. State-of-the-art control strategies for the machine side and the grid side converter are introduced. Industrial applications of low voltage drives are briefly addressed.

Characteristics and state-of-the-art of HSDs are presented in Chapter 2. Advantages, disadvantages, power, and speed range of HSDs are addressed. Furthermore, state-of-the-art technology of HSDs regarding electric machines, converter, and control are summarized.

In Chapter 3 RFOC and DTC are designed and investigated for the control of an exemplary HSIMD ($V_{S,ll,n} = 400$ V, $I_{S,n} = 38.25$ A, $P_{mech,n} = 20$ kW, $f_{0M} = 500$ Hz). Furthermore, design and comparison of 2L VSC and 3L-NPC VSC for the HSIMD is presented in this chapter.

A comparison among different methods of FOC of IMs is presented in Section 3.4.1. Indirect RFOC is preferred compared to SFOC and MFOC control due to the features like relative simple structure and linear torque-slip characteristic at steady-state. A detailed description of the indirect RFOC and the procedure of the controller design for the HSIMD are given in Section 3.4.2. RFOC is implemented with SRS-PWM ($f_{s,cc} = f_{sw}$) and ARS-PWM ($f_{s,cc} = 2f_{sw}$). DTC and the design procedure of the control system parameters for the HSIMD are briefly described in Section 3.5. Subchapter 3.6 presents a comparison between indirect RFOC and DTC for the exemplary HSIMD. A switching frequency of 11.5 kHz ($m_f = 23$) is applied for

the RFOC. The electromechanical torque with the given frequency ratio is equal to $THD_{Tem} \approx 20\%$ for RFOC with both SRS-PWM ($f_{s,cc} = 11.5$ kHz) and ARS-PWM ($f_{s,cc} = 23$ kHz).

The sampling frequency of the torque and flux control loop for DTC is determined to 230 kHz to realize a comparable torque THD of $THD_{Tem} \approx 20\%$. In this case, the average switching frequency of DTC is 11.53 kHz.

For the applied sampling frequencies for RFOC ($f_{s,cc} = 11.5$ kHz for SRS-PWM and $f_{s,cc} = 23$ kHz for ARS-PWM) and DTC ($f_{s,DTC} = 230$ kHz), the DTC features the best load disturbance rejection capability with a disturbance rejection time of 0.5 ms. RFOC with ARS-PWM and SRS-PWM realize a disturbance rejection time of 1.5 ms and 3.5 ms, respectively.

Spectrum analysis of the electromechanical torque for the DTC shows low order harmonics while the RFOC causes well defined torque spectrum with harmonics at switching frequency and times of the switching frequency.

The main advantage of the DTC is the excellent dynamic performance which is not essential in most of the high-speed drive applications. A significantly higher sampling frequency and consequently the requirement of an expensive control platform are the disadvantages of DTC for HSDs. Furthermore, a large LC-filter is required to damp the low order harmonics of the electromechanical torque.

RFOC features a good dynamic performance for HSIMDs with a lower sampling frequency compared to DTC. Therefore, simpler control platforms can be applied. Due to the well defined behaviour of PWM in RFOC, a smaller LC-filter is required to reduce the THD of the electromechanical torque. Hence, the RFOC is more suitable for the control of HSIMDs.

A detailed comparison between the 2L VSC and the 3L-NPC VSC for the exemplary HSIMD with RFOC is presented in Subchapter 3.7. The investigations carried out within this thesis demonstrate that in the same carrier frequency of 11.5 kHz for the HSIM the power losses of the 3L-NPC VSC is about 50% lower than the power loss of the 2L VSC with a comparable installed switch power. Torque THD of the HSIMD fed by the 2L VSC is almost twice the Torque THD of the HSIMD fed by the 3L-NPC VSC. If the switching frequency of the 2L VSC is increased so that both converters generate comparable torque THD (e.g. $THD_{Tem} = 10.7\%$), the semiconductor power losses of the 2L VSC is about 166% larger than that of the 3L-NPC VSC. In this case, the installed switch power of the 2L VSC is twice the installed switch power of the 3L-NPC VSC.

In Chapter 4, control of PWM active front end converters and design of the grid side filter are investigated. A brief comparison among different control strategies of active front end converters is presented. VOC is selected for the control of the grid side converter due to advantages like constant switching frequency which leads to a smaller grid side filter to meet the IEEE-519 limits.

VOC is designed in detail in Subchapter 4.4 and well comparable simulation and experimental results are presented for the dynamic and steady-state performance.

Assuming symmetrical sinusoidal grid voltages and a constant dc-link voltage, the widely spread voltage-oriented controlled PWM active front end converters generate grid current harmonics in carrier bands of n times the switching frequency, which are usually sufficiently damped by moderate inductive filters in industrial grids. However, the grid voltage at the PCC is substantially distorted by the commutation of thyristors if the PWM active front end converters and thyristor converters are operated in parallel. The influence of the grid voltage distortions on the steady-state performance of VOC is presented in Section 4.4.6. In the case

of a grid with distorted voltage, VOC is not able to suppress low-order current harmonics (e.g. 5th and 7th) if conventional state-of-the-art PI current controllers are applied. The use of faster PI current controllers decreases the lower current harmonics (e.g. 5th and 7th) but increases the higher current harmonics (e.g. >11th). An increase in the filter inductor leads to a significant damping of all current harmonics between grid and switching frequency. However, additional costs, size, and weight of an increased inductor as well as the limitation of the maximum dc-link voltage and the dynamic performance prevent the use of large filter inductors. Obviously, the application of control schemes like individual harmonic control, overriding current controller, and multi-resonant current controllers, which are able to suppress harmonic currents at distorted grids, is the most attractive solution if sinusoidal grid currents are required in industrial applications where thyristor converters operate in parallel to self-commutated PWM active front end converters.

A new design procedure of the grid side filters (L- and LCL-filter) to meet the IEEE-519 limits is presented in Subchapter 4.5. An analytical method based on the most significant voltage harmonic of the converter output voltage is used to design the L-filter. The simulation results show that a high switching frequency is required to meet the IEEE-519 conditions when using an L-filter. As an example, for a PWM active front end converter with a grid rms line-to-line voltage of $G_{all} = 400$ V and a dc-link voltage of $V_{dc} = 700$ V, a switching frequency of $f_{sw} = 24.3$ kHz is required to limit the grid current harmonics to 0.2% of the rated current when using an L-filter with an inductance of 2.1%.

Therefore, the application of an LCL-filter can be an attractive alternative to damp the grid current harmonics. The analytical expression of the converter voltage harmonics is also applied to the development of an iterative design procedure for LCL-filters under consideration of the IEEE-519 limitations as well as the required control reserve. It is shown that the LCL-filters with different parameters (inductance split factor and resonance frequency) and various reactive components values can lead to the same damping of the grid harmonics.

Thus, various optimization criteria like minimum costs, weight, size, or stored energy of the passive components can be applied to determine optimal filter parameters. As an example, the stored energy as measure for the expense of passive components was used to compare different filter designs and to derive an optimal solution. The optimized filter of a 400V, 50kVA converter with a switching frequency of about 4 kHz features a split factor of about 1 and a resonance frequency of about 1 kHz. These filter parameters remain constant for different rated grid currents and line voltages when assuming a constant voltage reserve.

In Subchapter 4.6, control of the PWM active front end converter with LCL-filter is investigated. VOC with active damping is applied as the control strategy. Voltages of the filter capacitors are used in the active damping. Lead-lag compensators are applied to improve the transient performance. A simple design method on the basis of the modulation and processing delays for the required lead-lag compensator is proposed.

The simulation results validate the accuracy of the proposed LCL-filter designed procedure. Experimental investigations of the active front end converter with LCL-filter are also carried out. Experimental results for the dynamic performance are well comparable with simulation results. The experimental investigations show that a reduction of the inductivity at high frequencies will reduce the effectiveness of LCL-filters.

Bibliography

Books and Theses

- [1] K. J. Aström and T. Hägglund, *PID Controllers: Theory, Design, and Tuning*, 2nd Edition. North Carolina : ISA, 1995
- [2] S. Bernet, *Leistungshalbleiter als Nullstromschalter in Stromrichtern mit weichen Schaltvorgängen*. Aachen: Verlag Shaker, 1995
- [3] T. Brückner, *The active NPC Converter for Medium Voltage Drives*. Aachen: Verlag Shaker, 2006
- [4] M. Centner, *Entwurf schnelldrehender Asynchronmaschinen unter besonderer Berücksichtigung der magnetisch aktiven Materialien*. Berlin, Dissertation TU Berlin, 2009
- [5] S. S. Fazel, *Investigation and Comparison of Multi-level Converters for Medium Voltage Applications*. Berlin: Dissertation TU Berlin, 2005
- [6] R. Fischer, *Elektrische Maschinen*. München: Carl Hanser Verlag , 1999.
- [7] D. G. Holmes and T. A Lipo, *Pulse Width Modulation for Power Converters*. New York: John Wiley, 2003
- [8] M. Kazmierkowski, R. Krishnan, and F. Blaabjerg, *Control in Power Electronics–Selected Problems*. San Diego: Academic Press, 2002
- [9] W. Leonhard, *Introduction to Control Engineering and Linear Control System*. Spring International Student Edition, New Dehli, India: Allied Publishers Pvt. Ltd., 1976
- [10] W. Leonhard, *Control of Electric Drives*. New York: Springer Verlag, 1985
- [11] H. Lutz, W. Wendt, *Taschenbuch der Regelungstechnik*. Frankfurt am Main: Verlag Harri Deutsch, 2002
- [12] M. Malinowski, *Sensorless Control Strategies for Three–Phase PWM Rectifiers*. Warsaw: Warsaw University of Technology, 2001
- [13] N. Mohan, T.M. Undeland, and W.P. Robbins, *Power Electronics, Converters, Applications and Design*. New York: John Wiley, 2003
- [14] U. Nicolai, *Application manual power modules*. SEMIKRON international. Ilmenau: Verlag ISLE, 2000
- [15] J. Saari, *Thermal Analysis of High Speed Induction Machines*. Helsinki: Helsinki University of Technology, 1998
- [16] D. Schröder, *Elektrische Antriebe – Regelung von Antriebssystemen*. Berlin: Springer Verlag, 2001
- [17] P. C. Sen, *Principles of Electric Machines and Power Electronics, 2nd Edition*. John Wiley, 1997
- [18] D. Sobczuk, *Application of ANN for Control of PWM Inverter Fed Induction Motor Drives*. Warsaw: Warsaw University of Technology, 1999

- [19] P. Vas, *Sensorless Vector and Direct Torque Control*. London: Oxford University Press, 1998
- [20] M. Winkelkemper, *Reduzierung von Zwischenkreiskapazitäten in Frequenzumrichtern für Niederspannungsantriebe*. Berlin: Dissertation, TU Berlin 2005
- [21] M. Zelechowski, *Space Vector Modulation – Direct Torque Controlled Inverter – Fed Induction Motor Drive*. Warsaw: Warsaw University of Technology, 2005

Conference and Journal Papers

High-Speed Drives

- [22] B. Bae, S. Sul, J. Kwon, and J. Shin, “Implementation of sensorless vector control for super-high speed PMSM of turbo compressor,” in *Conf. Rec. IEEE-IAS Annu. Meeting*, 2001, pp. 1203–1209
- [23] S. Bernet, M. Centner, Literature study: High speed machines, TU Berlin, 2002
- [24] P. D. Chandana Perera, F. Blaabjerg, J. K. Pedersen, and P. Thøgersen, “A Sensorless, Stable V/f Control Method for Permanent-Magnet Synchronous Motor Drives,” *IEEE Trans. Ind. Applicat.* vol. 39, no. 3, pp. 783–791, May/Jun. 2003
- [25] A. Chiba, K. Chida, and T. Fukao, “Principles and characteristics of a reluctance motor with winding of magnetic bearings,” in *Conf. Rec. IPEC*, Tokyo, 1990, pp. 919–926
- [26] A. Chiba, T. Deido, T. Fukao, and M. A. Rahman, “An analysis of bearingless ac motors,” *IEEE Trans. Energy Convers.*, vol. 9, no. 1, pp. 61–68, Mar. 1994
- [27] T. Fukao, “The evaluation of motor drive technologies development of bearingless motors,” in *Conf. Rec. power electron. and motion control*, 2000, pp. 33–38
- [28] J. F. Gieras, “Comparison of high power high speed machines: Cage induction versus switched reluctance motors,” in *Conf. Rec. IEEE, AFRCON*, 1999, pp. 675–678
- [29] J. He and F. Lin, “A High frequency high power IGBT inverter drive for 45 HP 16000 rpm brushless homopolar induction motor,” in *Conf. Rec. IEEE-IAS Annu. Meeting*, 1995, pp. 9–15
- [30] L. Hertel and W. Hofmann, “Design and test results of a high speed bearingless reluctance motor,” in *Conf. Rec. EPE*, Lausanne, Switzerland, 1999
- [31] J. Hupponen and J. Pyrhönen, “Filtered PWM inverter drive for high speed solid rotor induction motors,” in *Conf. Rec. IEEE-IAS Annu. Meeting*, 2000, pp. 1942–1949
- [32] Y. Kim, S. Kim, and I. Hong, “Speed sensorless control of high speed induction motors using intelligent control algorithm,” in *Conf. Rec. IEEE, IECON*, 1998, pp. 888–892
- [33] J. K. Lähteenmäki, “Optimization of high speed motors using genetic algorithm,” in *Conf. Rec. IEE, EMD*, 1997, pp. 26–30
- [34] M. Mekhiche, J. L. Kirtley, M. Tolkas, E. Ognibene, J. Kiley, E. Holmanský, and F. Nimblett, “High speed motor drive development for industry applications, electric machines and drives,” in *Conf. Rec. IEEE-IEMDC*, 1999, pp. 244–248
- [35] L. J. J. Ofringa and J. L. Duarte, “A 1600 kW IGBT converter with inter phase transformer for high speed gas turbine power plants,” in *Conf. Rec. IEEE-IAS Annu. Meeting*, 2000, pp. 2243–2248

- [36] M. Ooshima, A. Chiba, T. Fukao, and M. A. Rahman, "Design and analysis of permanent magnet-type bearingless motors," *IEEE Trans. Power Electron.*, vol. 43, no. 2, pp. 292–299, Mar. 1996
- [37] R. Schöb and J. Bichsel, "Vector control of the bearingless motor," in *Conf. Rec. of the 4th Inter. Symp. on magnetic bearings*, 1994, pp. 327–332
- [38] W.L Soong, G.B. Kliman, R.N. Johnson, R.A. White, and J.E. Miller, "Novel high speed induction motor for a commercial centrifugal compressor," *IEEE Trans. Ind. Applicat.*, vol. 36, no. 3, pp. 706–7137, May/Jun. 2000
- [39] I. Takahashi, T. Koganezawa, G. Su, and K. Ohyama, "A super high speed PM motor drive system by a quasi-current source inverter," *IEEE Trans. Ind. Applicat.*, vol. 30, no. 3, pp. 683–690, May/Jun. 1994
- [40] L. Xu, and Ch. Wang, "Implementation and experimental investigation of sensorless control schemes for PMSM in super-high variable speed operation," in *Conf. Rec. IEEE-IAS Annu. Meeting*, pp. 483–489, 1998
- [41] Z. Yang and T. Fukao, "Direct output power control for PWM converter-based super-high-speed reluctance generator," *IEEE Trans. Ind. Applicat.*, vol. 28, no. 1, pp. 57–63, Jan./Feb. 1992

Control of High-Speed Induction Machine Drives

- [42] V. Ambrozic, G.S. Buja, and R. Menis, "Band-constrained technique for direct torque control of induction motor," *IEEE Trans. Ind. Electron.*, vol. 51, no. 4, pp. 776–784, Aug. 2004
- [43] S. Bernet, S. Ponnaluri, and R. Teichmann, "Design and loss comparison of matrix converters and voltage source converters for modern ac-drives," *IEEE Trans. Ind. Electron.*, vol. 49, no. 2, pp. 304–314, Apr. 2002
- [44] M. Bertoluzzo, G. Buja, and R. Menis, "Analytical formulation of the direct control of induction motor drives," in *Conf. Rec. IEEE Int. Symp. Ind. Electron.*, 1999, pp. 14–20
- [45] F. Blaabjerg, U. Jaeger, and M. Nielsen, "Power Losses in PWM-VSI Inverter Using NPT or PT IGBT Devices," *IEEE Trans. Power Electron.*, 1995, vol. 10, no. 3, pp. 358–367, MAY 1995
- [46] F. Blaschke, "The principle of field-orientation as applied to the transvector closed-loop control system for rotating-field machines", *Siemens Rev.*, vol. 34, pp. 217–220, 1972
- [47] G.S. Buja and M.P. Kazmierkowski, "Direct torque control of PWM inverter-fed AC motors - a survey," *IEEE Trans. Ind. Electron.* vol. 51, pp.744–756, Aug. 2004
- [48] D. Casadei, G. Grandi, G. Serra, and A. Tani, "Effects of flux and torque hysteresis band amplitude in direct torque control of induction machines," in *Conf. Rec. IEEE IECON*, 1994, pp. 299–304
- [49] D. Casadei and G. Serra, "Analytical investigation of torque and flux ripple in DTC schemes for induction motors," in *Conf. Rec. IEEE IECON*, 1997, pp. 552–556
- [50] M. Comanescu and L. Xu, "Sliding-mode MRAS speed estimators for sensorless vector control of induction Machine," *IEEE Trans. Ind. Electron.* vol. 53, pp.146–153, Feb. 2006.

- [51] M. Depenbrock, "Direct self control of inverter-fed induction machines," *IEEE Trans. Power Electron.*, vol. 3, pp. 420–429, Oct. 1988
- [52] S. S. Fazel, S. Bernet, D. Krug, and K. Jalili, "Design and comparison of 4kV Neutral Point Clamped, Flying Capacitor and Series Connected H-Bridge Multi-Level Converters," *IEEE Trans. Ind. Applicat.*, vol. 43, no. 4, pp. 1032–1040, Jul./Aug. 2007
- [53] K. Hasse, "Drehzahlregelverfahren für schnelle umkehrantriebe mit stromrichter-gespeisten asynchron-kurzschlusslaufer-Motoren," *Regelungstechnik*, vol. 20, pp. 60–66, 1972
- [54] S. J. Henriksen, R. E. Betz, and B. J. Cook, "Digital hardware implementation of a current controller for IM variable-speed drives," *IEEE Trans. Ind. Appl.*, vol. 35, no. 5, pp. 1021–1029, Sept./Oct. 1999
- [55] E. Y. Y. Ho, and P. C. Sen, "Decoupling Control of Induction Motor Drives," *IEEE Trans. Ind. Electron.*, vol. 35, no. 2, pp. 253–262, May 1988
- [56] H. Hofmann, S. R. Sanders, and C. R. Sullivan, "Stator-Flux-Based vector control of induction machines in magnetic saturation," *IEEE Trans. Ind. Appl.*, vol. 33, no. 4, pp. 935–942, Jul./Aug. 2005
- [57] K. Jalili, M. Malinowski, and S. Bernet, "Rotor flux oriented control of a high speed induction motor drive applying a two-level voltage source converter with LC-sine filter," in *Conf. Rec. EPE*, Dresden, Germany, 2005
- [58] K. Jalili, D. Krug, S. Bernet, M. Malinowski, and B.J. Cardoso Filho, "Design and Characteristics of a Rotor Flux Controlled High Speed Induction Motor Drive Applying Two-Level and Three-Level NPC Voltage Source Converters," in *Conf. Rec. IEEE-PESC 36th Annu. Meeting, Brazil*, 2005, pp. 1820–1826
- [59] J. K. Kang and S. K. Sul, "Analysis and prediction of inverter switching frequency in direct torque control of induction machine based on hysteresis band and machine parameters," *IEEE Trans. Ind. Electron.*, vol. 48, pp. 545–553, Jun. 2001
- [60] M.P. Kazmierkowski, and M.A. Dzieniakowski, "Review of current regulation techniques for three-phase PWM inverters," in *Conf. Rec. IEEE-IECON*, 5-9 Sept., 1994, pp. 1241–3485
- [61] M. P. Kazmierkowski and A. B. Kaspruwicz, "Improved direct torque and flux vector control of PWM inverter-fed induction motor drives," *IEEE Trans. Ind. Electron.*, vol. 42, pp. 344–350, Aug. 1995
- [62] M. P. Kazmierkowski, "Control philosophies of PWM inverter-fed induction motors," in *Conf. Rec. IEEE-IECON*, Nov 1997, pp. 16–26
- [63] M. P. Kazmierkowski and L. Malesani, "Current control techniques for three-phase voltage- source PWM converters: A survey," *IEEE Trans. Ind. Electron.*, vol. 45, pp. 691–703, Oct. 1998
- [64] M. P. Kazmierkowski, M. Malinowski, D. L. Sobczuk, F. Blaabjerg, and J. K. Pedersen, "Simplified stator flux oriented control," in *Conf. Rec. IEEE Int. Symp. Ind. Electron.* Vol. 2, 12-16 July 1999, pp. 474 – 479.
- [65] D. Krug, S. Bernet, S.S. Fazel, K. Jalili, and M. Malinowski, "Comparison of 2.3-kV Medium-Voltage Multilevel Converters for Industrial Medium-Voltage Drives," *IEEE Trans. Ind. Electro.*, vol. 54, no. 6, pp. 2979–2992, Dec. 2007

- [66] T Kwon, M. Shin, and D Hyun, "Speed sensorless stator flux-oriented control of induction motor in the field weakening region using luenberger observer," *IEEE Trans. Power Electron.*, vol. 20, no. 4, pp. 864–869, Jul. 2005
- [67] D. Lee, S. Sul, and M. Park, "High performance current regulator for a field-oriented controlled induction motor drive," *IEEE Trans. Ind. Appl.*, vol. 30, no. 5, pp. 1247–1257, Sept./Oct. 1994
- [68] D. Lei, Y. Dong, and L. Xiaozhong, "Speed Sensorless Control with Neuron MRAS Estimator of an Induction Machine," in *Conf. Rec. PEDS '07, 2007*, pp. 1151 – 1156.
- [69] J. Li, Y. Zhong, and H. Ren, "Speed Estimation of Induction Machines Using Square Root Unscented Kalman Filter," in *Conf. Rec. IEEE-PESC 36th Annu. Meeting, 2005*, pp. 674–679.
- [70] E. D. Mitronikas, and A. N. Safacas, "A hybrid sensorless stator-flux oriented control method for induction motor drives," in *Conf. Rec. IEEE-PESC 35th Annu. Meeting, Aachen, Germany, 2004*, pp. 3481–3485
- [71] K. Nishibata, M. Ishida, S. Doki, T. Masuzawa, and M. Fujitsuna, "Speed Estimation Method utilizing Rotor Slot Harmonics Detected from Line Current for Speed Sensorless Drive of Ultra High Speed Induction Machine," in *Conf. Rec. IEEE-ICIT, 2006*, pp. 1591–1598.
- [72] U. Schäfer, "Das Script zur Vorlesung Elektrische Antriebe II," TU Berlin
- [73] Takahashi and T. Noguchi, "A new quick-response and high efficiency control strategy of an induction machine," *IEEE Trans. Ind. Appl.*, vol. IA-22, pp. 820–827, Sept. /Oct. 1986
- [74] R. Teichmann and S. Bernet, "A comparison of three-level converters versus two-level converters for low-voltage drives, traction, and utility applications," *IEEE Trans. Ind. Appl.*, vol. 41, no. 3, pp. 855–865, May/Jun. 2005
- [75] R. Teichmann, M. Malinowski, and S. Bernet, "Evaluation of three-level rectifiers for low-voltage utility applications," *IEEE Trans. Ind. Electron.*, Vol. 52, pp.471–481, April 2005
- [76] D. Telford, M. W. Dunnigan, and B. W. Williams, "Adaptive high bandwidth current control for induction machines," *IEEE Trans. Power Electron.* , vol. 18, no. 2, pp. 527–538, Mar. 2003
- [77] N. Urasaki, T. Senjyu, K. Uezato, and T. Funabashi, "An adaptive dead-time compensation strategy for voltage source inverter fed motor drives, " *IEEE Trans. Power Electro.*, vol. 20, no. 5, pp. 1150–1160, Sept. 2005
- [78] X. Xu, R. D. Doncker, and D.W. Novotny, "Stator flux orientation control of induction machines in the field weakening region," in *Conf. Rec. IEEE-IAS Annu. Meeting, 1988*, pp. 437–443
- [79] X. Xu, R. De Doncker, and D. W. Novotny, "A stator flux oriented induction machine drive," in *Conf. Rec. IEEE PESC, Apr. 1988*, pp.870–876
- [80] M. Zelechowski, M.M. Kazmierkowski, and F. Blaabjerg, "Controller design for direct torque controlled space vector modulation (DTC-SVM) induction motor drives," in *Conf. Rec. IEEE ISIE, June 20-23, 2005* pp. 951–956

PWM Active Front End Converters

- [81] H. Akagi, "Active harmonic filters," *Proc. of the IEEE*, vol. 93, no. 2, pp. 2128–2141, Dec. 2005
- [82] L. N. Arruda, B. J. Cardoso Filho, S. M. Silva, S. R. Silva, and A. S.A.C. Diniz, "Wide bandwidth single and three-phase PLL structures for grid-tied PV systems," in *Conf. Rec., Photovoltaic Specialists Conference, IEEE*, 15-22 Sept. 2000, pp.1660 – 1663
- [83] L.N. Arruda, S.M. Silva, and B.J.C Filho, "PLL structures for utility connected systems," in *Conf. Rec., IEEE-IAS*, 2001, pp. 2655–2660
- [84] F. Blaabjerg, R. Teodorescu, M. Liserre, and A.V. Timbus, "Overview of control and grid synchronization for distributed power generation systems," *IEEE Trans. Ind. Electron.*, vol. 53, no. 5, pp. 1398–1409, Oct 2006
- [85] V. Blasko and V. Kaura, "A novel control to actively damp resonance in input LC-filter of a three-phase voltage source converter," *IEEE Trans. Ind. Appl.*, vol. 33, no. 2, pp. 542–550, Mar./Apr. 1997
- [86] V. Blasko, V. Kaura, "A new mathematical model and control of a three-phase AC-DC voltage source converter," *IEEE Trans. Power Electron.*, vol. 12, no. 1, pp. 116–123, Jan. 1997
- [87] V. Blasko, "Adaptive filtering for selective elimination of higher harmonics from line currents of a voltage source converter," in *Conf. Rec. IEEE IAS Annu. Meeting*, 1998, vol.2, pp. 1222–1228
- [88] M. Bramoulle, "Electrolytic or film capacitors," in *Conf. Rec. IEEE-IAS Annu. Meeting*, 1998, pp. 1138–1141
- [89] R. Cardenas, R. Pena, M. Perez, J. Clare, G. Asher, and F. Vargas, "Vector control of front-end Converters for variable-speed wind–diesel systems," *IEEE Trans. Ind. Electron.*, vol. 53, no. 4, pp. 1127–1136, Aug. 2006
- [90] J.M. Carrasco, L.G. Franquelo, J.T. Bialasiewicz, E. Galvan, R.C. PortilloGuisado, M.A.M. Prats, J.I. Leon, and N. Moreno-Alfonso, "Power-electronic systems for the grid integration of renewable energy sources: A survey," *IEEE Trans. Ind. Electron.*, vol. 53, no. 4, pp. 1002–1016, Aug. 2006
- [91] Y. Chen and K. Ma Smedley, "Parallel operation of one-cycle controlled three-phase PFC rectifiers," *IEEE Trans. Ind. Appl.*, vol. 54, no. 6, pp. 3217–3224, Dec. 2007
- [92] P. A. Dahono, "A control method to damp oscillation in the input LC filter of AC-DC PWM converters", in *Conf. Rec. PESC'02*, June 2002, pp. 1630–1635
- [93] R. Grinberg and P.R. Palmer, "Advanced DC link capacitor technology application for a stiff voltage-source inverter," in *Conf. Rec. IEEE Conf. on vehicle power and propulsion*, 2005, pp. 205–210
- [94] S. Hansen, M. Malinowski, F. Blaabjerg, and M. P. Kazmierkowski, "Sensorless control strategies for PWM rectifier," in *Conf. Rec., APEC-IEEE*, 2000, vol. 2, pp. 832 – 838
- [95] A. M. Hava, T. A. Lipo, and W. L. Erdman, "Utility interface issues for line connected PWM voltage source converters: a comparative study," in *Conf. Rec. APEC '95*, Mar. 1995, pp. 125–132

- [96] A.L. Heredia, H. Gaztanaga, I. Etxeberria-Otadui, S. Bacha, D. Roye, J. Guiraud, and R. Rezero, "Evaluation of stationary frame and fixed switching frequency digital current control techniques for power active filters," in *Conf. Rec., EPE, Dresden, 2005*, 11–14 Sept.
- [97] IEEE Std 519-1992, "IEEE Recommended Practices and Requirements for Harmonic Control in Electrical Power Systems", *IEEE*, 1992
- [98] K. Jalili, N. Weitendorf, S. Bernet, "Behaviour of PWM active front ends in the presence of parallel thyristor converters," *IEEE Trans. Ind. Electron.*, vol. 55, no. 3, pp.1035–1046, Mar. 2008
- [99] K. Jalili, S. Bernet, "Design of LCL-filters of active front end two-level voltage source converters," to be published in *IEEE Trans. Ind. Electron.*
- [100] H.R. Karshenas, and H. Saghafi, "Basic criteria in designing LCL filters for grid connected converters," in *Conf. Rec. IEEE ISIE, Canada, Jul. 9-12, 2006*, pp 1996–2000
- [101] V. Kaura and V. Blasko, "Operation of a phase locked loop system under distorted utility conditions," *IEEE Trans. Ind. Appl.*, vol. 33, no. 1, pp. 58–63, Jan./Feb. 1997
- [102] B. Kwon, J. Youm, and J Lim, "A line-voltage-sensorless synchronous rectifier," *IEEE Trans. Power Electron.*, vol. 14, no. 5, pp. 966–1201, Sept. 1999
- [103] W. C. Lee, D-S Hyun, and T.-K Lee, "A novel control method for three-Phase PWM rectifiers using a single current sensor," *IEEE Trans. on Power Electro.*, vol. 15, no. 5, pp. 861–870, Sept. 2000
- [104] D-C. Lee and D-S Lim, "AC voltage and current sensorless control of three-phase PWM rectifiers," *IEEE Trans. Power Electron.*, vol. 17, no. 6, pp. 883–890, Nov. 2002
- [105] M. Liserre, A. Dell'Aquila, and F. Blaabjerg, "Stability improvements of an LCL-filter based three- phase active rectifier," in *Conf. Rec., PESC, Jun. 2002*, pp. 1195–1201
- [106] M. Liserre, A. Dell'Aquila, and F. Blaabjerg, "Genetic algorithm based design of the active damping for a LCL-filter three-phase active rectifier," *IEEE Trans. Power Electron.*, vol. 19, no. 1, pp. 76–86, Jan. 2004
- [107] M. Liserre, F. Blaabjerg, and S. Hansen, "Design and control of an LCL-filter-based three-phase active rectifier," *IEEE Trans. Ind. Appl.*, vol. 41, no. 5, pp. 1281–1291, Sept./Oct. 2005
- [108] A. Lopez de Heredia, P. Antoniewicz, I. Etxeberria-Otadui, M. Malinowski, and S. Bacha, "A comparative study between the DPC-SVM and the Multi-Resonant controller for power active filter applications," in *Conf. Rec., IEEE Ind. Electron. Int. Symp.*, Volume 2, Jul. 2006, pp.1058–1063
- [109] A. Lopez de Heredia, I. Etxeberria-Otadui, M. Malinowski, S. Bacha, and D. Roye, "Comparison of integrator-based and dead-beat controllers for shunt power active filters," *IEEE Ind. Electron., IECON - 32nd Ann. Conf.*, Nov. 2006 , pp.2329–2334
- [110] M. Malinowski, M.P. Kazmierkowski, S. Hansen, F. Blaabjerg, and G. D. Marques," Virtual flux based Direct Power Control of three-phase PWM rectifier," *IEEE Trans. Ind. Appl.*, vol. 37, no. 4, pp. 1019–1027, Jul./Aug. 2001
- [111] M. Malinowski, M. P. Kazmierkowski, and A. M. Trzynadlowski, "A comparative study of control techniques for PWM rectifiers in ac adjustable speed drives," *IEEE Trans. Power Electron.* , vol. 18, no. 6, pp. 1390–1396, Nov. 2003

- [112] M. Malinowski, M. Jasinski, and M. P. Kazmierkowski, "Simple direct power control of Three-Phase PWM rectifier using space-vector modulation(DPC-SVM)," *IEEE Trans. Ind. Appl.*, vol. 51, No. 2, pp. 447–454 April 2004
- [113] M. Malinowski, M. P. Kazmierkowski, W. Szczygiel, and S. Bernet, "Simple sensorless active damping solution for three-phase PWM rectifier with LCL filter," in *Conf. Rec., IEEE IECON 2005, 32nd Annu. Conf.*, Nov. 6–10 2005, pp. 987–991
- [114] L. Moran, P.D. Ziogas, and G. Joos, "Design aspects of synchronous PWM rectifier systems under unbalanced input voltage conditions," *IEEE Trans. Ind. Appl.*, vol. 28, no. 6, pp.1268–1293, Nov./Dec.1992
- [115] T. Noguchi, H. Tomiki, S. Kondo, and I. Takahashi, "Direct power control of PWM converter without power-source voltage sensors," *IEEE Trans. Ind. Appl.*, vol. 34, pp. 473–479, May/Jun. 1998
- [116] F.-S. Pai, "An improved utility interface for microturbine generation system with stand-alone operation capabilities," *IEEE Trans. Ind. Electron.*, vol. 53, no. 5, pp. 1529–1537, Oct. 2006
- [117] S. Ponnaluri, A. Brickwedde, and R.W. De Doncker, "Overriding individual harmonic current control with fast dynamics for UPS with nonlinear loads," in *Conf. Rec., Power Electron., Drive Sys., 4th IEEE Int. Conf.*, vol. 2, 2001, pp.527–532
- [118] S. Ponnaluri and A. Brickwedde, "Overriding individual harmonic current control with fast dynamics for active filtering," in *Conf. Rec. IEEE- PESC.*, 2001, pp.1596–1601
- [119] S. Ponnaluri and A. Brickwedde, "Generalized system design of active filters", in *Conf. Rec. IEEE PESC*, vol. 3, 2001, pp. 1596–1601
- [120] R. Rioual, H. Pouliquen, and J. P. Louis, "Control of a PWM rectifier in the unbalanced state by robust voltage regulation," in *Conf. Rec., EPE 1993*, pp. 8–14
- [121] P. Rioual, H. Pouliquen, and J. P. Louis, "Regulation of the PWM rectifier in the unbalanced network state using a generalized model," *IEEE Trans. Ind. Electron.*, vol. 11, no. 3, pp.495–502, Oct. 1996
- [122] J.R. Rodriguez, J.W. Dixon, J.R. Espinoza, J. Pontt, and P. Lezana, "PWM regenerative rectifiers: state of the art", *IEEE Trans. Ind. Electron.*, vol. 52, no. 1, pp.5–22, Feb. 2005
- [123] P. Rodríguez, J. Pou, J. Bergas, I. Candela, R. Burgos, and D. Boroyevich, "Double synchronous reference frame PLL for power converters control," in *Conf. Rec., IEEE-PESC*, 2005, pp. 1415–1421
- [124] P. Rodríguez, J. Pou, J. Bergas, I. Candela, R. Burgos, and D. Boroyevich, "Decoupled double synchronous reference frame PLL for power converters control," *IEEE Trans. Power Electron.*, vol. 22, no. 2, pp. 584–592, Mar. 2007
- [125] M. Salo, H. Tuusa, "A vector controlled current-source PWM rectifier with a novel current damping method," *IEEE Trans. Power Electron.*, vol. 15, no. 3, pp 464–470, May 2000
- [126] L. A. Serpa, J. W. Kolar, S. Ponnaluri, and P. M. Barbosa, "A modified direct power control strategy allowing the connection of three-phase inverter to the grid through LCL filters," in *Conf. Rec., IEEE-IAS*, 2005, pp. 265–271

- [127] W. Tangtheerajaronwong, T. Hatada, K. Wada, and H. Akagi, "Design and Performance of a Transformerless Shunt Hybrid Filter Integrated Into a Three-Phase Diode Rectifier," *IEEE Trans. Power Electron.*, vol. 22, pp.1882–1889, Sept. 2007
- [128] D. Vincenti and H. Jin, "A three-phase regulated PWM rectifier with on-line feed forward input unbalance correction," *IEEE Trans. Ind. Electron.*, vol. 41, no. 5, pp.526–532, Oct. 1994
- [129] T. CY Wang, Zh. Ye, G. Sinha, and X. Yuan, "Output Filter Design for a Grid-interconnected Three-phase Inverter," in *Conf. Rec. IEEE PESC, 34th Annu. Meeting*, vol.2, 15-19 Jun. 2003, pp. 779–784
- [130] R. Wu, S. B. Dewan, and G. R. Slemon, "Analysis of an ac-to-dc voltage source converter using PWM with phase and amplitude control," *IEEE Trans. Ind. Appl.*, vol. 27, no. 3, pp. 355–364, Mar./Apr. 1991
- [131] E. Wu and P. W. Lehn, "Digital current control of a voltage source converter with active damping of LCL resonance," *IEEE Trans. Power Electron.* vol. 21, no. 5, pp. 1364–1373, Sept. 2006
- [132] B. Yin, R. Oruganti, S.K. Panda, and A.K.S Bhat, "A novel instantaneous power control strategy for a PWM rectifier under unbalanced input voltage conditions," *IEEE Ind. Electron. Annu. Meeting 2004*, pp.251–256

Product Information, Standards, Datasheets

- [133] ABB Automation: OPCoDe Benutzerhandbuch, ABB Switzerland Ltd., 2002
- [134] ABB low voltage AC Drives, <http://www.abb.com>
- [135] <http://www.bowman.com>, Turbogén TG50cG, Turbo Alternators
- [136] <http://www.capstone.com>, Microturbines
- [137] EPOCS AG, Aluminum Electrolytic Capacitors: General technical information, <http://www.epocs.com>
- [138] EPOCS AG, Film Capacitors: General technical information, <http://www.epocs.com>
- [139] ESR Pollmeier GmbH, applications, <http://www.esr-pollmeier.de>
- [140] <http://www.ibag.ch>
- [141] BSM50GB120DLC, BSM100GB120DLC, BSM50GB60DLC, Datasheets. Available at <http://www.infineon.com>
- [142] Infineon: New R_{thCH} data sheet values, Online document AN-2004-01, <http://www.infineon.com>
- [143] Application characterization of IGBTs, Application Note, AN-990, <http://www.irf.com>
- [144] <http://www.polaron-group.co.uk/nelco>
- [145] <http://www.rieter-basetex.com>
- [146] SIEMENS low voltage inverters, <http://www.siemens.com>
- [147] <http://www.turbec.com>, T100 Microturbine CHP System
- [148] <http://www.vem-group.com>

LEBENS LAUF

Persönliche Daten

Name	JALILI
Vorname	Kamran
Geschlecht	männlich
Staatsangehörigkeit	iranisch
Geburtstag	10. Oktober 1974
Geburtsort	Abhar / Iran
E-Mail	kamran.jalili@web.de

Ausbildung

04/2004 – 03/2008	<p>Doktorand im Fachgebiet Leistungselektronik des Institutes für Energie- und Automatisierungstechnik, Fakultät IV der Technischen Universität, Berlin</p> <ul style="list-style-type: none">– Doktorvater: Prof. Dr.-Ing. Steffen Bernet– Doktorarbeit: <i>Investigation of Control Concepts for High Speed Induction Machine Drives and Grid Side Pulse-Width Modulation Voltage Source Converters.</i>– Stipendium: DAAD
10/1997 - 03/2000	<p>Masterstudium der Elektrotechnik an der Universität Teheran</p> <ul style="list-style-type: none">– Schwerpunktfach: Elektrische Antriebstechnik– Hauptfach: Regelungstechnik– Master Thesis: <i>Sensorless Vector Control of Induction Motor Using Neural Networks.</i>
10/1992 - 02/1997	<p>Bachelorstudium der Elektrotechnik an der PWIT – Teheran</p> <ul style="list-style-type: none">– Schwerpunktfach: Elektrische Maschine– Hauptfach: Energietechnik– Studienarbeit: <i>Parameter Estimation of Single Phase and Three Phase Induction Machines.</i>
10/1988 - 07/1992	<p>Sadi – High School, Khorramdarreh, Iran.</p>